

MODERN ANALYSIS OF CORNEAL BIOMECHANICS

GABRIELE CIVIERO

Doctor of Philosophy

Aston University

June 2024

©Gabriele Civiero, 2024

Gabriele Civiero asserts their moral right to be identified as the author of this thesis

This copy of the thesis has been supplied on condition that anyone who consults it is understood to recognise that its copyright belongs to its author and that no quotation from the thesis and no information derived from it may be published without appropriate permission or acknowledgement.

Personal Acknowledgments

There are so many people I should and would like to thank, and I am sure these few lines will not be enough.

First and foremost, my supervisors: Professor Shehzad Naroo, for the countless meetings in which he tried to make sense of my strange and confused ideas, forgiving my long silences and poorly expressed concepts. Above all, I thank him for conveying enthusiasm and passion that are rare to find and for always trying to see the positive side of every situation, while granting me the enormous freedom to explore diverse fields. Professor Sunil Shah, despite much less frequent meetings, made a fundamental contribution to this research, as without him, I would not have had the opportunity to use the BOSS. Finally, Dr Mark Dunne, for the endless remote meetings, where he patiently answered my strangest questions and tried to shape the ideas that were only in my head. I have learned so much from them and feel extremely fortunate.

Secondly, all the people who became my second family in Birmingham and made the city a less grey place: Antonio, Sonia, Alberto, Silvia, Alex, Jimmy, Polina, Shital, Rohit, Ash, Jonny, and Ruth. If I have endured for so long, it is mainly thanks to you.

To my office colleagues (David, Rachel, Shree, Aya, Justin, Satyam). With a special thanks to Sunny, whose presence in the office always brought joy even if she had to endure my freak-outs. And Pete and Yas, with whom I shared countless lunch breaks, making that drab room an almost pleasant place. To all of them who shared a coffee and a break.

To my lifelong friends (Raspis, Aperitivo Categoricalo, Brigata Tonino Asta), who were always ready to celebrate each of my returns from Albion. I cannot imagine how sad my life would be without you.

To my family, who stood by me through good times and bad, suffering the difficulty of my departure and sharing the joy of spending time together living far apart for most of the year.

To a neighbour I have not yet managed to get rid of, who has the gift of being one of the few people who can bring out both the best and the worst in me and is largely responsible for this journey. Despite the 1081.17 km between us, he often makes me feel as if I had never left.

To all the members of the SOPTI Boards from 2018 to 2026, who have done an extraordinary job over the years, forgiving my absence to too many events. I keep learning from each one of you.

To all these people (and to all those I have forgotten and to whom I apologise), I owe more thanks than I can express, either in a few pages or in a lifetime.

Abstract

The measurement of corneal biomechanics has gained significant importance recently. Over the past two decades, three devices capable of quantifying biomechanical properties have become commercially available: two non-contact tonometers (ORA and Corvis ST) that record changes in corneal shape induced by an air-puff, and a third device (BOSS) that quantifies rigidity by analysing the frequency shift of light scattered within the corneal tissue, in accordance with Brillouin scattering. Due to its unique technology, the BOSS can also quantify the rigidity of the crystalline lens.

Data from ORA and Corvis ST have been employed to train supervised machine learning models for the detection of keratoconus and primary open-angle glaucoma. Various learners and strategies were used to identify the most effective model. Subsequently, another model was developed to differentiate between healthy eyes, primary open-angle glaucoma, normal-tension glaucoma, and ocular hypertension. After fine-tuning, this model was tested to determine if keratoconus (without glaucoma) could confound the labelling.

Several experiments with the BOSS were conducted, including assessments of repeatability, correlations with measurements from ORA, Corvis ST, and OCT, and investigations into changes in corneal biomechanics related to age and refractive error. The thesis concludes with incidental findings on variations in crystalline lens thickness along the same meridian.

The main findings are as follows:

- It is possible to detect keratoconus and glaucoma using corneal biomechanical data and supervised machine learning algorithms.
- Corneal biomechanics data from patients with keratoconus may confound the classification in a model designed to detect glaucoma.
- The repeatability of the BOSS is high for lens modulus, but it is quite low for corneal modulus. Other lens parameters show even lower repeatability.
- BOSS measurements do not correlate with any measurement from ORA or Corvis ST, the machines do measure different corneal features.
- The most notable change in ocular biomechanics due to age is the reduction in the Brillouin modulus (rigidity) of the crystalline lens, which is contrary to expectations.
- Myopic eyes generally exhibit weaker biomechanics compared to emmetropic eyes.
- Peripheral crystalline lens thickness varies across different meridians (considering the same eccentricity).

Keywords

Corneal biomechanics, glaucoma, keratoconus, machine learning, Brillouin modulus, crystalline lens.

Table of Content

1	Literature Review: Corneal Biomechanics.....	1
1.1	Introduction.....	1
1.2	How to measure and quantify corneal biomechanical properties.....	3
1.2.1	Ocular Response Analyser.....	3
1.2.2	Corneal Visualization Scheimpflug Technology (Corvis ST).....	5
1.2.3	Brillouin Optical Scanner System (BOSS).....	9
1.3	Corneal Biomechanics in Glaucoma	27
1.3.1	Primary Open Angle Glaucoma (POAG).....	28
1.3.2	Normal Tension Glaucoma (NTG).....	31
1.3.3	Ocular hypertension (OHT)	33
1.4	Corneal Biomechanics in Keratoconus.....	35
1.4.1	ORA.....	35
1.4.2	Corvis ST.....	36
1.5	General hypothesis.....	38
2	Detection of Keratoconus and Primary Open Angle Glaucoma with Machine Learning and Corneal Biomechanics Data	39
2.1	Introduction.....	39
2.2	Material and Methods	41
2.2.1	Basic concept in machine learning.....	41
2.2.2	Libraries.....	45
2.2.3	Metrics.....	45

2.2.4	Algorithms	46
2.2.5	Learning and hyperparameter tuning	58
2.2.6	Test	59
2.2.7	Permutation Feature Importance (PFI).....	59
2.2.8	Shapley Additive exPlanations (SHAP).....	60
2.3	Results.....	61
2.3.1	Keratoconus	61
2.3.2	Primary Open Angle Glaucoma.....	68
2.4	Discussion	85
2.4.1	Performances GridSearch vs RandomSearch	85
2.4.2	Interpretation	85
2.4.3	Support Vector Machine.....	86
2.4.4	Keratoconus	86
2.4.5	Glaucoma	89
2.5	Conclusions	92
2.6	Limitations	92
2.7	Future Studies	93
3	Impact of Keratoconus Data on Glaucoma Screening Algorithm.....	94
3.1	Introduction.....	94
3.2	Methods.....	95
3.2.1	Use of both eyes from the same research participants	95
3.2.2	Dataset A for creating models	96

3.2.3	Dataset B for investigating the impact of keratoconus on glaucoma screening	96
3.2.4	Corneal biomechanics measured using ORA and Corvis ST.....	96
3.2.5	Use of Orange Data Mining software to create the models.....	97
3.2.6	Use of Orange Data Mining software for investigating the impact of keratoconus on glaucoma screening.....	98
3.3	Results and Discussion	99
3.3.1	Main study findings.....	99
3.3.2	Model for Glaucoma	100
3.3.3	Impact of Keratoconus on Glaucoma Screening.....	102
3.3.4	Study limitations and recommended further research.....	103
3.4	Conclusions	104
4	BOSS Repeatability	106
4.1	Introduction.....	106
4.2	Material and Methods	106
4.2.1	Participants.....	106
4.2.2	Scan Pattern.....	107
4.2.3	Statistical Analysis.....	107
4.3	Results.....	108
4.3.1	Mean and Standard Deviation for all the three sets of measurements	108
4.3.2	Bland Altman Analysis and Coefficient of Variation	110
4.3.3	Is the bias proportional to value measured?	115
4.3.4	Difference in intersession repeatability due to time of the measurement.....	116

4.3.5	ICC	120
4.3.6	Repeatability of Cornea Measurements Regardless Location	121
4.4	Discussion	123
4.4.1	Ratio between means and COR interval	124
4.4.2	ICC	124
4.4.3	Time of the measurement	125
4.4.4	All Cornea Measurements together.....	126
4.5	Conclusion.....	127
5	Is BOSS interchangeable with ORA or Corvis ST?	128
5.1	Introduction.....	128
5.2	Material and Methods	130
5.3	Results.....	131
5.4	Discussion	134
5.4.1	Corneal Measurement.....	134
5.4.2	Lens Measurement.....	135
5.4.3	Confrontation between lens thickness measured using BOSS and OCT	135
5.5	Conclusions	137
6	Age-Related Changes in Corneal Biomechanics.....	138
6.1	Introduction.....	138
6.1.1	Calculus of sample size.....	138
6.2	Materials and Methods	139
6.3	Results.....	140

6.3.1	Differences between Young and Presbyopes	140
6.3.2	Correlation with age for group P.....	146
6.4	Discussion	148
6.4.1	ORA.....	148
6.4.2	Corvis ST:.....	149
6.4.3	BOSS - Cornea	150
6.4.4	BOSS - Lens	151
6.5	Conclusion.....	152
7	Corneal Biomechanics Changes related to Refractive Error	154
7.1	Introduction.....	154
7.1.1	Sample Size Calculation	154
7.2	Material and Methods	155
7.3	Results.....	156
7.3.1	Participants.....	156
7.3.2	Differences among groups	157
7.3.3	Correlation with Refractive Error	159
7.4	Discussion	163
7.4.1	ORA.....	163
7.4.2	Corvis ST.....	165
7.4.3	BOSS	168
7.4.4	OCT.....	169
7.5	Conclusions	169

7.6	Limitations	170
8	Lens Peripheral Thickness Variations.....	171
8.1	Introduction.....	171
8.2	Materials and Methods	171
8.3	Results.....	172
8.4	Discussion	174
8.5	Conclusions	176
9	Summary and Future Work.....	178
9.1	Summary of Findings.....	178
9.2	Future Research.....	180
10	Bibliography	182
11	Appendix.....	200
11.1	General Version of the ML Code	200
11.2	Results ML to detect KC and POAG	209
11.2.1	KC	209
11.2.2	POAG	210
11.3	Repeatability.....	215
11.3.1	Correlation Difference-Mean value for Intrasession Repeatability	215
11.3.2	Correlation Difference-Mean value for Intrasession Repeatability	216
11.3.3	Bland Altman analysis for time of the day	217
11.4	Relationship with other instruments.....	219
11.5	Age Analysis	222

11.6	Refractive Error Analysis	225
11.6.1	Groups.....	225
11.6.2	Continuous Distribution of Refractive Error	230

List of Equations

Eq. 1.1 Imbert-Fick Law	1
Eq. 1.2 Corneal Hysteresis Formula	4
Eq. 1.3 Corneal Resistance Factor Formula	4
Eq. 1.4 GAT-related IOP Formula	4
Eq. 1.5 Corneal Compensated IOP Formula	4
Eq. 1.6 Brillouin frequency shift	10
Eq. 1.7 Brillouin Modulus	12
Eq. 1.8 Log-Log relationship between Brillouin modulus and Young's Modulus	12
Eq. 2.1 Bayes' Theorem of conditional probability	47
Eq. 2.2 Linear Combination of Independent Variables before applying Logistic Sigmoid Function	48
Eq. 2.3 Sigmoid Function for Linear Regression	48
Eq. 2.4 Logistic Cost Function	48
Eq. 2.5 Gradient Descent Algorithm	48
Eq. 2.6 Ridge Regularisation	49
Eq. 2.7 Lasso Regularisation	49
Eq. 2.8 SVM Hyperplane Formula	51
Eq. 2.9 Condition to have the hyperplane with the widest margin possible for data separation	51
Eq. 2.10 Conditions for data not linearly separable	51
Eq. 2.11 Glni Index	53
Eq. 2.12 Entropy index	53

Eq. 2.13 Neuron Output for MLP Classifier.....	56
Eq. 2.14 Input to Output neuron.....	56
Eq. 2.15 Function to calculate probability	56
Eq. 2.16 Loss Calculation	56
Eq. 2.17 Loss Gradient	57
Eq. 2.18 Weight Update Function	57
Eq. 4.1 Bias for Bland Altman analysis	110
Eq. 4.2 Coefficient of Repeatability	110
Eq. 4.3 Within-subjects Standard Deviation (wSD).....	110

All the figures that do not have a specific attribution were created by the author of the thesis.

List of Figures

Figure 1.1 In green the intensity of the puff of air over time, in red the intensity of signal over time. The two peaks correspond to the applanations. The IOP is measured as the intensity of the air puff during the applanation.	5
Figure 1.2 Instant 0, cornea has its natural shape, the puff of air did not reach the cornea yet.	7
Figure 1.3 First applanation (A1), the puff of air is increasing in intensity and the cornea is moving inward. Time, corneal velocity and length of applanation are recorded	8
Figure 1.4 Highest concavity (HC) reached, radius, time, deformation amplitude, deflection length and displacement are measured.....	8
Figure 1.5 Second applanation (A2), the peak of the puff of air is passed and the cornea is moving outward, toward its natural shape. Time, corneal velocity and length of applanation are recorded.....	8
Figure 1.6 Test is finished, cornea has regained its normal shape.....	9
Figure 1.7 . Representation of Brillouin scattering caused by phonons. V is the velocity of the phonons in the media, n the refractive index of the media, θ the angle of scattering (Reiss, Bureau, Stachs, Guthoff, & Stolz, 2011)	10
Figure 1.8 Cross-sectional map of a IOL placed in a cuvette filled with liquid (blue) that creates lower frequency shift than the material of IOL. In the left upper part, it is possible to identify the edge of the cuvette, with a frequency shift similar to the IOL material.	13
Figure 1.9 Depth dependant frequency shift (green dots) of rabbit eye lens (left image) and porcine (right image), on the right y axis there are storage and loss moduli. AH is aqueous humour; L is lens and VH vitreous humour (Reiss et al., 2011).....	13
Figure 1.10 Depth-dependant analysis of Brillouin frequency shift measured in vivo on 42 years old male human (Scarcelli & Yun, 2012)	15
Figure 1.11 Effects of a UV light on optical adhesive polymer (Scarcelli et al., 2012).	19

Figure 1.12 Maps of corneal Brillouin frequency shift. The left map is from a 53-years old normal cornea, while the right one is from a 40-years old patient with advanced keratoconus. Sagittal and Thickness maps in the upper part (Scarcelli et al., 2015)23

Figure 1.13 ROC curves of thinnest pachymetry (red), Kmax (green) and Brillouin frequency shift (blue). The latest has the lower potential in keratoconus detection (Seiler et al., 2019).24

Figure 1.14 Current version of the Brillouin Optical Scanning System (BOSS).....25

Figure 1.15 The output of the lens measurement of the BOSS. The upper arrow is the Top Plateau, the lower one is the Bottom Plateau. The arrow on the left is the Anterior Slope, the one on the right is the Posterior Slope. On the x axis there is the depth of the scanning along the z-axis. On the y axis there is the value of the Brillouin modulus.....26

Figure 2.1 ROC Curves for Grid Search, Corvis ST including CCT in KC detection62

Figure 2.2 ROC Curves for Random Search, Corvis ST including CCT in KC detection62

Figure 2.3 PFI for Corvis ST including CCT in KC detection62

Figure 2.4 SHAP impact of each predictor on KC detection for Corvis ST including CCT data63

Figure 2.5 SHAP effect of each predictor on KC detection for Corvis ST including CCT data63

Figure 2.6 ROC Curves for Grid Search, Corvis ST excluding CCT in KC detection64

Figure 2.7 ROC Curves for Random Search, Corvis ST including CCT in KC detection64

Figure 2.8 PFI for Corvis ST excluding CCT in KC detection64

Figure 2.9 SHAP impact of each predictor on KC detection for Corvis ST excluding CCT data65

Figure 2.10 SHAP effect of each predictor on KC detection for Corvis ST excluding CCT data65

Figure 2.11 ROC Curves for Grid Search, ORA including CCT in KC detection.....66

Figure 2.12 ROC Curves for Random Search, ORA including CCT in KC detection.....66

Figure 2.13 PFI for ORA including CCT in KC detection66

Figure 2.14 SHAP impact of each predictor on KC detection for ORA including CCT data...66

Figure 2.15 SHAP effect of each predictor on KC detection for ORA including CCT data66

Figure 2.16 ROC Curves for Grid Search, ORA excluding CCT in KC detection67

Figure 2.17 ROC Curves for Random Search, ORA excluding CCT in KC detection.....67

Figure 2.18 PFI for ORA excluding CCT in KC detection67

Figure 2.19 SHAP impact of each predictor on KC detection for ORA excluding CCT data..68

Figure 2.20 SHAP effect of each predictor on KC detection for ORA excluding CCT data ...68

Figure 2.21 ROC Curves for Grid Search, Corvis ST including CCT and IOP in POAG
detection69

Figure 2.22 ROC Curves for Random Search, Corvis ST including CCT and IOP in POAG
detection69

Figure 2.23 PFI for Corvis ST including CCT and IOP in POAG detection.....69

Figure 2.24 SHAP impact of each predictor on POAG detection for Corvis ST including CCT
and IOP data.....70

Figure 2.25 SHAP effect of each predictor on POAG detection for Corvis ST including CCT
and IOP data.....70

Figure 2.26 ROC Curves for Grid Search, Corvis ST including CCT and excluding IOP in
POAG detection.....71

Figure 2.27 ROC Curves for Random Search, Corvis ST including CCT and excluding IOP in
POAG detection.....71

Figure 2.28 PFI for Corvis ST including CCT and excluding IOP in POAG detection.....71

Figure 2.29 SHAP impact of each predictor on POAG detection for Corvis ST including CCT
and excluding IOP data.....71

Figure 2.30 SHAP effect of each predictor on POAG detection for Corvis ST including CCT and excluding IOP data.....71

Figure 2.31 ROC Curves for Grid Search, Corvis ST including IOP and excluding CCT in POAG detection72

Figure 2.32 ROC Curves for Random Search, Corvis ST including IOP and excluding CCT in POAG detection72

Figure 2.33 PFI for Corvis ST including IOP and excluding CCT in POAG detection.....73

Figure 2.34 SHAP impact of each predictor on POAG detection for Corvis ST including IOP and excluding CCT data73

Figure 2.35 SHAP effect of each predictor on POAG detection for Corvis ST including IOP and excluding CCT data73

Figure 2.36 ROC Curves for Grid Search, Corvis ST excluding CCT and IOP in POAG detection74

Figure 2.37 ROC Curves for Random Search, Corvis ST excluding CCT and IOP in POAG detection74

Figure 2.38 PFI for Corvis ST excluding CCT and IOP in POAG detection.....74

Figure 2.39 SHAP impact of each predictor on POAG detection for Corvis ST excluding CCT and IOP data.....75

Figure 2.40 SHAP effect of each predictor on POAG detection for Corvis ST excluding CCT and IOP data.....75

Figure 2.41 ROC Curves for Grid Search, ORA including CCT and IOP in POAG detection 76

Figure 2.42 ROC Curves for Random Search, ORA including CCT and IOP in POAG detection76

Figure 2.43 PFI for ORA including CCT and IOP in POAG detection.....77

Figure 2.44 SHAP impact of each predictor on POAG detection for ORA including CCT and IOP data.....77

Figure 2.45 SHAP effect of each predictor on POAG detection for ORA including CCT and IOP data77

Figure 2.46 ROC Curves for Grid Search, ORA including CCT and excluding IOP in POAG detection78

Figure 2.47 ROC Curves for Random Search, ORA including CCT and excluding IOP in POAG detection78

Figure 2.48 PFI for ORA including CCT and excluding IOP in POAG detection.....78

Figure 2.49 SHAP impact of each predictor on POAG detection for ORA including CCT and excluding IOP data.....78

Figure 2.50 SHAP effect of each predictor on POAG detection for ORA including CCT and excluding IOP data.....78

Figure 2.51 ROC Curves for Grid Search, ORA including IOP and excluding CCT in POAG detection79

Figure 2.52 ROC Curves for Random Search, ORA including IOP and excluding CCT in POAG detection79

Figure 2.53 PFI for ORA including IOP and excluding CCT in POAG detection.....80

Figure 2.54 SHAP impact of each predictor on POAG detection for ORA including IOP and excluding CCT data80

Figure 2.55 SHAP effect of each predictor on POAG detection for ORA including IOP and excluding CCT data80

Figure 2.56 ROC Curves for Grid Search, ORA excluding CCT and IOP in POAG detection81

Figure 2.57 ROC Curves for Random Search, ORA excluding CCT and IOP in POAG detection81

Figure 2.58 PFI for ORA excluding CCT and IOP in POAG detection.....81

Figure 2.59 SHAP impact of each predictor on POAG detection for ORA excluding CCT and IOP data82

Figure 2.60 SHAP effect of each predictor on POAG detection for ORA excluding CCT and IOP data82

Figure 2.61 ROC Curves for Grid Search, GAT including CCT in POAG detection.....83

Figure 2.62 ROC Curves for Random Search, GAT including CCT in POAG detection.....83

Figure 2.63 PFI for GAT including CCT in POAG detection.....83

Figure 2.64 SHAP impact of each predictor on POAG detection for GAT including CCT data83

Figure 2.65 SHAP effect of each predictor on POAG detection for GAT including CCT data83

Figure 2.66 ROC Curves for Grid Search, GAT only in POAG detection84

Figure 2.67 ROC Curves for Random Search, GAT only in POAG detection.....84

Figure 2.68 SHAP effect of each predictor on POAG detection for GAT only.....84

Figure 3.1 : Orange Data Mining canvas and connected widgets used to create the ORA NB, ORA LR, Corvis ST NB and Corvis ST LR models97

Figure 3.2 : Orange Data Mining canvas and connected widgets used to create the ORA NB, ORA LR, Corvis ST NB and Corvis ST LR models99

Figure 4.1 Histograms of the mean and standard deviation for the three sets of measurements 109

Figure 4.2 Bland Altman Plot (Bias and 95% of COR interval) for the intrasession repeatability of the Brillouin modulus measured in the superior part of the cornea. 112

Figure 4.3 Bland Altman Plot (Bias and 95% of COR interval) for the intrasession repeatability of the Brillouin modulus measured in the inferior part of the cornea 112

Figure 4.4 Bland Altman Plot (Bias and 95% of COR interval) for the intrasession repeatability of the Brillouin modulus measured in the nasal part of the cornea 112

Figure 4.5 Bland Altman Plot (Bias and 95% of COR interval) for the intrasession repeatability of the Brillouin modulus measured in the temporal part of the cornea 112

Figure 4.6 Bland Altman Plot (Bias and 95% of COR interval) for the intrasession repeatability of the mean corneal Brillouin modulus 113

Figure 4.7 Bland Altman Plot (Bias and 95% of COR interval) for the intrasession repeatability of the crystalline Brillouin modulus 113

Figure 4.8 Bland Altman Plot (Bias and 95% of COR interval) for the intrasession repeatability of the top plateau..... 113

Figure 4.9 Bland Altman Plot (Bias and 95% of COR interval) for the intrasession repeatability of the bottom plateau..... 113

Figure 4.10 Bland Altman Plot (Bias and 95% of COR interval) for the intrasession repeatability of the anterior slope..... 113

Figure 4.11 Bland Altman Plot (Bias and 95% of COR interval) for the intrasession repeatability of the posterior slope 113

Figure 4.12 Bland Altman Plot (Bias and 95% of COR interval) for the intersession repeatability of the Brillouin modulus measured in the superior part of the cornea 114

Figure 4.13 Bland Altman Plot (Bias and 95% of COR interval) for the intersession repeatability of the Brillouin modulus measured in the inferior part of the cornea 114

Figure 4.14 Bland Altman Plot (Bias and 95% of COR interval) for the intersession repeatability of the Brillouin modulus measured in the nasal part of the cornea 114

Figure 4.15 Bland Altman Plot (Bias and 95% of COR interval) for the intersession repeatability of the Brillouin modulus measured in the temporal part of the cornea 114

Figure 4.16 Bland Altman Plot (Bias and 95% of COR interval) for the intersession repeatability of the mean corneal Brillouin modulus 114

Figure 4.17 Bland Altman Plot (Bias and 95% of COR interval) for the intersession repeatability of the crystalline Brillouin modulus 114

Figure 4.18 Bland Altman Plot (Bias and 95% of COR interval) for the intersession repeatability of the top plateau..... 115

Figure 4.19 Bland Altman Plot (Bias and 95% of COR interval) for the intersession repeatability of the bottom plateau..... 115

Figure 4.20 Bland Altman Plot (Bias and 95% of COR interval) for the intersession repeatability of the anterior slope..... 115

Figure 4.21 Bland Altman Plot (Bias and 95% of COR interval) for the intersession repeatability of the posterior slope..... 115

Figure 4.22 Bland Altman plots for TimeD subgroups for Brillouin modulus measured in the nasal part of the cornea 119

Figure 4.23 Bland Altman plots for TimeDABS subgroups for Brillouin modulus measured in the superior part of the cornea..... 120

Figure 4.24 Bland Altman plots for Intrasession Repeatability of all corneal measurements (excluding Mean) regardless location 122

Figure 4.25 Bland Altman plots for Intersession Repeatability of all corneal measurements (excluding Mean) regardless location 122

Figure 4.26 Correlation between average of the measurements and difference between the measurements for intrasession repeatability of Brillouin modulus for all corneal measurements (excluding Mean) regardless location 122

Figure 4.27 Correlation between average of the measurements and difference between the measurements for intersession repeatability of Brillouin modulus for all corneal measurements (excluding Mean) regardless location 123

Figure 4.28 Time difference between the measurements and difference of Brillouin modulus measured in the nasal part of the cornea 125

Figure 5.1 Correlation between Brillouin Modulus measured in the inferior part of the corneal and time of the first applanation (Corvis ST)..... 133

Figure 5.2 Correlation between Brillouin Modulus measured in the inferior part of the corneal and biomechanically corrected IOP (Corvis ST) 133

Figure 5.3 Correlation between Brillouin Modulus measured in the inferior part of the corneal and corneal resistance factor (ORA)..... 133

Figure 5.4 Correlation between Brillouin Modulus measured in the inferior part of the corneal and non-corrected IOP (Corvis ST) 133

Figure 5.5 Correlation between crystalline lens Brillouin Modulus and central lens thickness (OCT) Figure 5.6 Correlation between bottom plateau and central lens thickness (OCT) .. 133

Figure 5.7 Correlation between posterior slope central lens thickness (OCT)..... 134

Figure 5.8 Correlation between top plateau and central lens thickness (OCT) 134

Figure 5.9 Bland Altman Plot Central Lens Thickness (OCT) vs Bottom Plateau..... 136

Figure 5.10 Bland Altman Plot Central Lens Thickness (OCT) vs Top Plateau 136

Figure 6.1 Refractive error distribution in terms of Spherical Equivalent for group Y and P 141

Figure 6.2 Boxplot for Refractive Error (SphEq) for groups P and Y 141

Figure 6.3 Boxplot for Length of First Applanation (Corvis ST)..... 144

Figure 6.4 Boxplot of Velocity at First Applanation (Corvis ST) 144

Figure 6.5 Boxplot of Velocity at Second Applanation (Corvis ST) 144

Figure 6.6 Boxplot of Deformation Amplitude during Highest Concavity (Corvis ST) 144

Figure 6.7 Boxplot of Biomechanically Corrected IOP (Corvis ST)..... 144

Figure 6.8 Boxplot of Whole-Eye-Movement (Corvis ST)..... 144

Figure 6.9 Boxplot of Brillouin modulus of the crystalline lens (BOSS) 145

Figure 6.10 Boxplot of Top Plateau (BOSS) 145

Figure 6.11 Boxplot of Bottom Plateau (BOSS) 145

Figure 6.12 Boxplot of Posterior Slope (BOSS)..... 145

Figure 6.13 Boxplot of Central Lens Thickness (OCT) 145

Figure 6.14 Age distribution of P Group..... 146

Figure 6.15 Scatterplot, Regression Line and 95% Confidence Interval for Age and Time of Second Applanation (Corvis ST)..... 147

Figure 6.16 Scatterplot, Regression Line and 95% Confidence Interval for Age and Brillouin modulus measured in the temporal cornea (BOSS) 147

Figure 6.17 Scatterplot, Regression Line and 95% Confidence Interval for Age and Mean Corneal Brillouin modulus (BOSS)..... 147

Figure 6.18 Scatterplot, Regression Line and 95% Confidence Interval for Age and Crystalline Lens Brillouin Modulus (BOSS)..... 147

Figure 6.19 Scatterplot, Regression Line and 95% Confidence Interval for Age and Anterior Slope (BOSS) 147

Figure 7.1 Boxplot of differences in Length at First Applanation across Refractive Error groups (Corvis ST)..... 158

Figure 7.2 Boxplot of differences in Radius at Highest Concavity across Refractive Error groups (Corvis ST)..... 158

Figure 7.3 Boxplot of differences in Inverse Radius across Refractive Error groups (Corvis ST) 159

Figure 7.4 Boxplot of differences in Stress-Strain Index across Refractive Error groups (Corvis ST)..... 159

Figure 7.5 Boxplot of differences in Integrated Radius across Refractive Error groups (Corvis ST) 159

Figure 7.6 Boxplot of differences in Crystalline Lens Modulus across Refractive Error groups (BOSS)..... 159

Figure 7.7 Refractive error distribution..... 160

Figure 7.8 Scatterplot and regression line of Refractive Error and Length of First Applanation (Corvis ST)..... 161

Figure 7.9 Scatterplot and regression line of Refractive Error and Highest Concavity Time (Corvis ST)..... 161

Figure 7.10 Scatterplot and regression line of Refractive Error and Highest Concavity Radius (Corvis ST)..... 162

Figure 7.11 Scatterplot and regression line of Refractive Error and Deflection Amplitude (Corvis ST).....	162
Figure 7.12 Scatterplot and regression line of Refractive Error and Deflection Amplitude Ratio (Corvis ST)	162
Figure 7.13 Scatterplot and regression line of Refractive Error and Deformation Amplitude Ratio (Corvis ST)	162
Figure 7.14 Scatterplot and regression line of Refractive Error and Inverse Radius (Corvis ST)	162
Figure 7.15 Scatterplot and regression line of Refractive Error and Whole-Eye-Movement (Corvis ST).....	162
Figure 7.16 Scatterplot and regression line of Refractive Error and Stress-Strain Index (Corvis ST).....	162
Figure 7.17 Scatterplot and regression line of Refractive Error and Integrated Radius (Corvis ST)	162
Figure 8.1 Box plot of lens thickness according to location. CLT (Central Lens Thickness) Inferiorly (I), Superiorly (S), Nasally (N) and Temporally (T).	174

List of Tables

Table 1.1 values of swelling and frequency shift at different times after wake.....	18
Table 1.2 Thickness, value of hydration and Brillouin frequency shift for specimens in different solutions. Corneal hydration is measured as grams of water per gram of dry tissue.	18
Table 2.1 Size of datasets used for the current experiment.....	43
Table 2.2 Performances of the models on Keratoconus detection	61
Table 2.3 Performances of different combinations of Corvis ST data in POAG detection	68
Table 2.4 Performances of different combinations of ORA data in POAG detection	75
Table 2.5 Performances of different combinations of GAT data in POAG detection	82
Table 2.6 Findings of other studies in terms of AUC in Keratoconus detection	89
Table 2.7 Findings of other studies in terms of AUC in POAG detection	91
Table 3.1 The performance of all four models (ORA NB, ORA LR, Corvis ST NB and Corvis ST LR) ranked in order of best to worst in terms of the area under the ROC curve (AUROC) averaged over all classes (Normal, OHT, NTG and POAG), after 10-fold stratified cross validation.....	100
Table 3.2 The relative importance of the 12 Corvis ST and 3 ORA corneal biomechanical parameters according to the ORA NB, ORA LR, Corvis ST NB and Corvis ST LR models. Were applicable, IOP and CCT are highlighted in red	101
Table 3.3 Baseline performance of the ORA NB, ORA LR, Corvis ST NB and Corvis ST LR models that had been trained on Dataset A (as shown in the Orange Data Mining canvas of Figure 1). Values show, for each model, the percentage (and frequency) of the predicted Normal that were correct (green: as these were Normal in reality) and incorrect (red: as these were POAG, OHT or NTG in reality).	101
Table 3.4 The impact of keratoconus on glaucoma screening is revealed by observing the performance of the ORA NB, ORA LR, Corvis ST NB and Corvis ST LR models, that had been trained on dataset A (as shown in the Orange Data Mining canvas of Figure 1) that had been used to make predictions on Dataset B containing Normal without and with	

keratoconus. Values show, for each model, the percentage (and frequency) of the predicted Normal that were correct (green: as these were Normal in reality) and incorrect (red: as these were POAG, OHT or NTG in reality) in eyes with and without keratoconus. P-values (from Chi-square tests) are shown for the comparison of predictions made in eyes without and with keratoconus by each model.....	102
Table 4.1 Mean, Standard Deviation and Coefficient of Variation for the three sets of measurements	108
Table 4.2 Intrasession Repeatability	111
Table 4.3 Intersession Repeatability Table.....	111
Table 4.4 Correlation between TimeD and differences in BOSS measurements.....	117
Table 4.5 Correlation between TimeDABS and differences in BOSS measurements	117
Table 4.6 Results of Normality test (Shapiro Wilk) and for differences between groups in TimeD subgroups.....	118
Table 4.7 Results of Normality test (Shapiro Wilk) and for differences between groups in TimeDABS subgroups	118
Table 4.8 ICC for Intrasession repeatability	120
Table 4.9 ICC for Intersession repeatability	121
Table 4.10 Bland Altman analysis for all corneal measurements (excluding Mean) regardless location.....	121
Table 4.11 Correlation between mean value and Bias for all corneal measurements (excluding Mean) regardless location	122
Table 4.12 ICC for all corneal measurements (excluding Mean) regardless locations	123
Table 5.1 Demographics of participants; Mean and SD of clinical measurements	131
Table 5.2 Statistically significant correlations between BOSS measurements and parameters measured by ORA, Corvis ST and OCT	132
Table 6.1 Demographics	140

Table 6.2 Mean, SD and results of normality test (Shapiro Wilk) for refractive error for groups Y and P	141
Table 7.1 Demographics of participants divided in groups according to the refractive error	157
Table 8.1 Demographics of participants.....	172
Table 8.2 Mean, SD and Shapiro Wilk results for normality.....	173
Table 8.3 Results of post hoc analysis, with differences along meridians	173
Table 11.1 Corvis ST considering CCT	209
Table 11.2 Corvis ST excluding CCT	209
Table 11.3 ORA including CCT	210
Table 11.4 ORA excluding CCT	210
Table 11.5 Corvis ST including Central Corneal Thickness and IOP	211
Table 11.6 Corvis ST including Central Corneal Thickness, but not IOP	211
Table 11.7 Corvis ST including IOP, but not Central Corneal Thickness.....	211
Table 11.8 Corvis ST excluding IOP and Central Corneal Thickness	212
Table 11.9 ORA including IOP and Central Corneal Thickness	212
Table 11.10 ORA including Central Corneal Thickness, excluding IOP	213
Table 11.11 ORA including IOP, excluding Central Corneal Thickness.....	213
Table 11.12 ORA excluding IOP and Central Corneal thickness	213
Table 11.13 GAT including central corneal thickness.....	214
Table 11.14 GAT excluding Central corneal thickness.....	214
Table 11.15 Correlation tested according to Kolmogorov Smirnov test	215
Table 11.16 Correlation tested according to Shapiro Wilk test.....	215
Table 11.17 Correlation tested according to Kolmogorov Smirnov test	216

Table 11.18 Correlation tested according to Shapiro Wilk test.....	216
Table 11.19 Bland Altman analysis results for TimeD subgroups	217
Table 11.20 Bland Altman analysis results for TimeDABS subgroups	217
Table 11.21 Results of Normality test (Shapiro Wilk) for clinical measurements	219
Table 11.22 Correlations between measurements from different instruments	219
Table 11.23 Results of normality test, mean/median, SD/IQR, and test for differences between groups Y and P.	222
Table 11.24 Correlation between age and parameters measured with ORA, Corvis ST, BOSS and OCT for group P.....	223
Table 11.25 Results of Normality test, Mean and SD for groups	225
Table 11.26 Results of test among groups.....	229
Table 11.27 Correlation between Refractive Error and parameters measured by ORA, Corvis ST, BOSS, OCT	230

1 Literature Review: Corneal Biomechanics

1.1 Introduction

Biomechanics refer to the mechanical properties of living tissues. Corneal biomechanics are important because they can alter the measurement of intraocular pressure (IOP).

Goldmann Applanation Tonometry (GAT) (Goldmann and Schmidt 1957) is considered the gold standard for measuring IOP, but it suffers from limitations because it does not account for corneal features such as rigidity, elasticity, and thickness. The operating principle of GAT is quite simple: it is based on the Imbert-Fick Law (Markiewitz 1960) which states that the force required to applanate an external part of a sphere filled with liquid is directly proportional to the pressure of the fluid in the sphere (as shown in Eq. 1.1). GAT, the goal is to achieve the applanation of a fixed portion of the cornea (a circular area with a diameter of 3.06 mm, A) using a probe. By adjusting the force applied (F) by the probe, it is possible to achieve applanation. Once this is reached, the instrument indicates the value of IOP (P).

$$P = \frac{F}{A}$$

Eq. 1.1 Imbert-Fick Law

The Imbert-Fick Law is valid only for dry, spherical, perfectly elastic surfaces with infinitely thin membranes. However, GAT is calibrated for a central corneal thickness (CCT) of 500-520 μm , even though it has been shown that CCT can range between 427 and 670 μm in healthy eyes (Ku, Danesh-Meyer et al. 2006). Even if formulae were proposed to correct GAT measurements according to CCT, the results would remain dubious due to the poor correlation between CCT and GAT (Kotecha 2007), suggesting that a more appropriate correction factor should include corneal biomechanical properties.

It is possible to trace back the birth of the study of corneal biomechanical properties to the tentative of correction of IOP measurements, when researchers tried to calculate and corneal contribute to tonometry (Liu and Roberts 2005). Initially, the research about corneal biomechanics mainly focused on static parameters, on central corneal thickness and corneal curvature. Soon, it was clear that static parameters alone were not sufficient to predict how the cornea would respond to dynamic stressors such as IOP fluctuations or surgical manipulation. Being a living tissue, it is not possible to perform on a cornea all the tests that would be performed on an ex vivo or during an in vitro experiment. Therefore, during the

last 20 years the analysis of corneal biomechanics was done through the use of special non-contact tonometers, developed for the analysis of parameters that are not usually considered during tonometry.

The main corneal biomechanical properties are:

- **Stiffness:** the ability to resist deformation when subjected to external force. It is influenced by the collagen fibres network, that provides mechanical stability. It is crucial to maintain curvature and optical function. (Kling and Hafezi 2017)
- **Elasticity:** the ability of the tissue to return to its original shape after the deformation. It depends on the organisation and density of collagen fibrils. A higher elasticity allows the cornea to better withstand IOP fluctuations without permanent deformation. It is believed to protect the eye from sudden forces. (Marinescu, Dascalescu et al. 2022)
- **Viscoelasticity:** it is a combination of elastic (reversible deformation) and viscous (time-dependant flow) properties that enable corneas to absorb mechanical energy and slowly dissipate it. (Gatzioufas and Seitz 2015)
- **Resistance:** the ability of the tissue to withstand mechanical loads without structural failures, even for long periods of time. It prevents ectasia, it can be weakened by refractive surgery but can be enhanced by cross-linking.(Rahmati, Razaghi et al. 2021)

Measuring corneal biomechanical properties is particularly important not only to achieve a more accurate intraocular pressure (IOP) reading — one that incorporates these biomechanical characteristics — but also because pathologies such as corneal ectasia and glaucoma demonstrably alter corneal biomechanical parameters (Komninou, Seiler et al. 2024). Detecting such alterations may enable earlier diagnosis and intervention. Moreover, assessing corneal biomechanics is a non-invasive procedure that can be performed rapidly while providing a wealth of clinically relevant information.

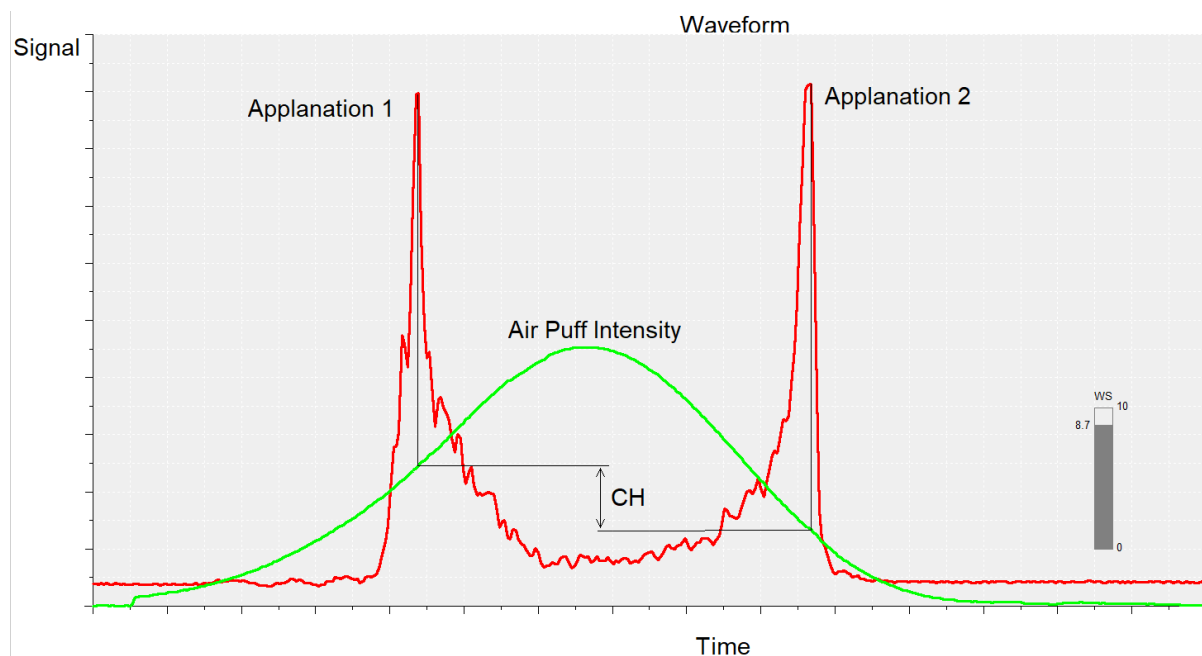
1.2 How to measure and quantify corneal biomechanical properties

Currently, two devices that can measure corneal biomechanics in vivo and provide IOP corrected according to measured properties are commercially available. These are the Ocular Response Analyzer (ORA), by Reichart (Depew, NY, USA), and Corneal Visualization Scheimpflug Technology (Corvis ST), by Oculus (Wetzlar, Germany). A third device, Brillouin Optical Scanner System (BOSS), by Intelon (Woburn, MA, USA) analyses the frequency shift of the light that is backscattered by a tissue, to compute the longitudinal elastic modulus.

1.2.1 Ocular Response Analyser

ORA, launched in 2005, is a non-contact tonometer that measures intraocular pressure IOP and some corneal biomechanical properties, adjusting IOP values accordingly (Luce 2005).

The intensity of the puff of air used by the ORA follows a Gaussian profile over time (30 ms), meaning that the intensity increases linearly to a peak and then decreases with the same slope, as shown in Figure 1.1



Thanks to the IR system, the ORA can detect the two applanations, which correspond to peaks in IR intensity measured by the detector. In a completely elastic material, the two applanations would occur at the same level of air pressure. However, due to the difference in air pressure intensity between the two applanations, the cornea can be described as a viscoelastic material. In a viscoelastic material, resistance to external stress depends on the velocity of the applied force. The intensity of the puff of air during the second applanation is always lower than during the first due to the dissipation of energy during the process of returning to its original shape, known as damping.

From several parameters measured during the two applanations, the ORA provides some clinical outputs:

- **Corneal Hysteresis (CH)**: the difference in the intensity of the puff of air between the first and second applanation. CH describes the cornea's ability to dissipate energy, which is transformed into heat.

$$CH = k1(P1 - P2) + k2$$

Eq. 1.2 Corneal Hysteresis Formula

- **Corneal Resistance Factor (CRF)**: describes the overall rigidity of the cornea. It is similar to CH but is more related to P1 and, therefore, to CCT.

$$CRF = k3(P1 - 0.7 \times P2) + k4$$

Eq. 1.3 Corneal Resistance Factor Formula

- **IOPg**: a measurement of IOP that correlates to GAT.

$$IOPg = k5(P1 + P2) + k6$$

Eq. 1.4 GAT-related IOP Formula

- **IOPcc**: the corneal-compensated IOP, a corrected measurement of IOP that considers corneal biomechanical properties.

$$IOPcc = k7(P2 - 0.43 \times P1) + k8$$

Eq. 1.5 Corneal Compensated IOP Formula

Wavefront Score (WS) was introduced in the second generation of ORA. WS, providing an analysis of IR signal features, helps the operator evaluate the quality of the measurement. It is composed of seven parameters (derived using principal component analysis) that can

have values between 0 and 10, with 10 being the ideal score for a perfect analysis. Over the past ten years, it has been shown that measurements associated with a WS lower than 3.5 should be rejected (Lam, Chen et al. 2010), that measurements with a WS higher than 6 have good inter-operator reproducibility even if the operators are inexperienced (Mandalos, Anastasopoulos et al. 2013), and that a WS higher than 7 is associated with good agreement between GAT and IOPg (Ayala and Chen 2012).

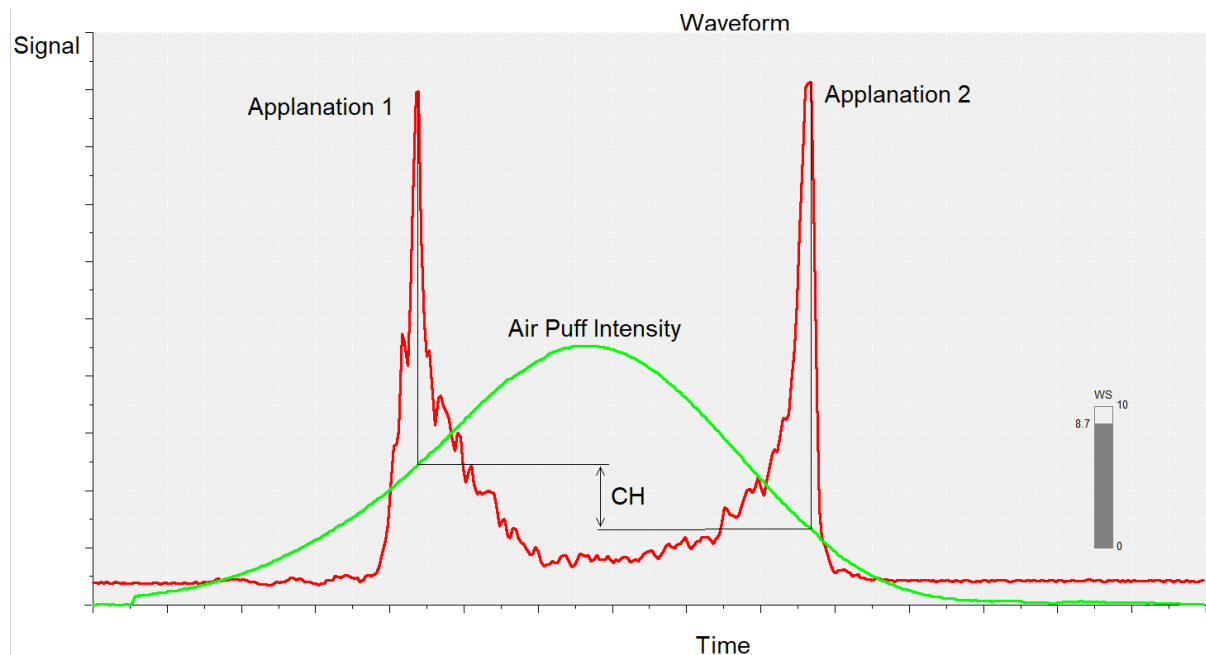


Figure 1.1 In green the intensity of the puff of air over time, in red the intensity of signal over time. The two peaks correspond to the applanations. The IOP is measured as the intensity of the air puff during the applanation.

1.2.2 Corneal Visualization Scheimpflug Technology (Corvis ST)

The second device capable of providing clinical measurements of corneal biomechanical properties is the Corvis ST, launched in 2013 (Hon and Lam 2013). The major difference between the ORA and the Corvis ST is that the latter uses a high-speed Scheimpflug camera that records 140 images in 30 ms to examine an 8-mm horizontal arc of the cornea during the puff of air. The air pulse lasts 25 ms and has a Gaussian distribution in terms of intensity, with a peak of 25 kPa.

Through the analysis of recorded images, the Corvis ST detects the two applanations (A1 and A2) and the highest concavity (HC). Corvis ST calculates several parameters from the analysis of photographs. The clinical outputs provided by Corvis ST are:

- **IOP**: Intraocular pressure.
- **biOP**: Biomechanically corrected intraocular pressure.
- Pachymetry.
- **A1V**: Velocity of the cornea during the first applanation.
- **A1T**: Time frame of the first applanation.
- **A1L**: Length of the applanated cornea during the first applanation.
- **A2V**: Velocity of the cornea during the second applanation (negative).
- **A2T**: Time frame of the second applanation.
- **A2L**: Length of the applanated cornea during the second applanation.
- **Highest Concavity Time (HCT)**: Time frame between the start of the puff of air and the highest concavity.
- **Highest Concavity Peak Distance (PD)**: Distance between the two surrounding peaks at the highest concavity.
- **Highest Concavity Radius (HCR)**: Corneal radius during the highest concavity.
- **Highest Concavity Deformation Amplitude (DefoAm)**: Maximal displacement of the corneal apex between the normal corneal shape and the highest concavity. It is defined as the vertical movement of the corneal apex over time and is the sum of the deflection amplitude and the whole eye movement.
- **Deflection Amplitude (DeflAm)**: The movement of the corneal apex compared to the superimposed cornea in its initial state. To consider corneal movement only, the whole eye movement is compensated.
- **Deflection Amplitude Ratio (DeflAmR)**: The ratio between the deflection amplitude at the apex and the deflection amplitude at 2 mm.
- **Deflection Area (DeflAr)**: The area of the cornea in the horizontal sectional plane that is displaced.
- **Deformation Amplitude Ratio (DefAR)**: The ratio between the deflection amplitude at the apex and the deflection amplitude at 2 mm.
- **Highest Concavity Inverse Radius (InvRad)**: The maximum value of the inverse of the concave radius measured during the concave phase of the deformation.
- **Whole-Eye Movement (WEM)**: The movement of the whole eye in the vertical direction, determined by the movement of the edge points of the cornea in the periphery.

- **Stress-Strain Index (SSI):** Derived from an algorithm that uses a combination of parameters measured by Corvis ST. It is designed to be independent of central corneal thickness and IOP and represents corneal rigidity (Eliasy, Chen et al. 2019).
- **Stiffness Parameter at first applanation (SP-A1):** Calculated as the ratio between the applied load and the displacement, representing corneal rigidity during the first applanation (Roberts, Mahmoud et al. 2017).
- **Ambrosio Relational Thickness horizontal (ARTh):** Combines the central corneal thickness and corneal deformability, useful in keratoconus screening and diagnosis (Vinciguerra, Ambrósio et al. 2016).
- **Integrated Radius (IntRad):** The area under the Inverse Radius curve.
- **Corneal Biomechanical Index (CBI):** Based on a logistic regression formula, calculated from five different biomechanical parameters measured by Corvis ST (A1V, A2V, PD, HCR, DefoAm), representing the risk for corneal ectasia (< 0.25 low risk; between 0.25 and 0.5 moderate risk; above 0.5 high risk) (Vinciguerra, Ambrósio et al. 2016).
- **Tomographic and Biomechanical Index (TBI):** integrates data from corneal tomography and biomechanical analysis to detect ectasia. A random forest algorithm is employed to compute the TBI, which provides a continuous output ranging from 0 to 1. In the study that presented the TBI, it achieved an AUC of 0.996 for discriminating ectatic from healthy corneas, and a cut-off value of 0.79 yielded 100% sensitivity and specificity for identifying clinically evident ectasia (Ambrósio, Lopes et al. 2017).

Figure 1.2-1.6 illustrate the different stages of a Corvis ST measurement.

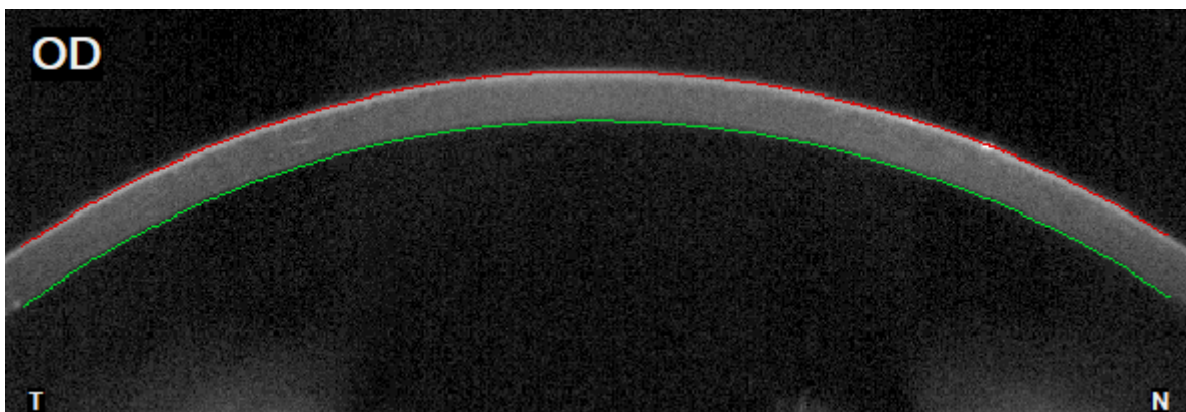


Figure 1.2 Instant 0, cornea has its natural shape, the puff of air did not reach the cornea yet.

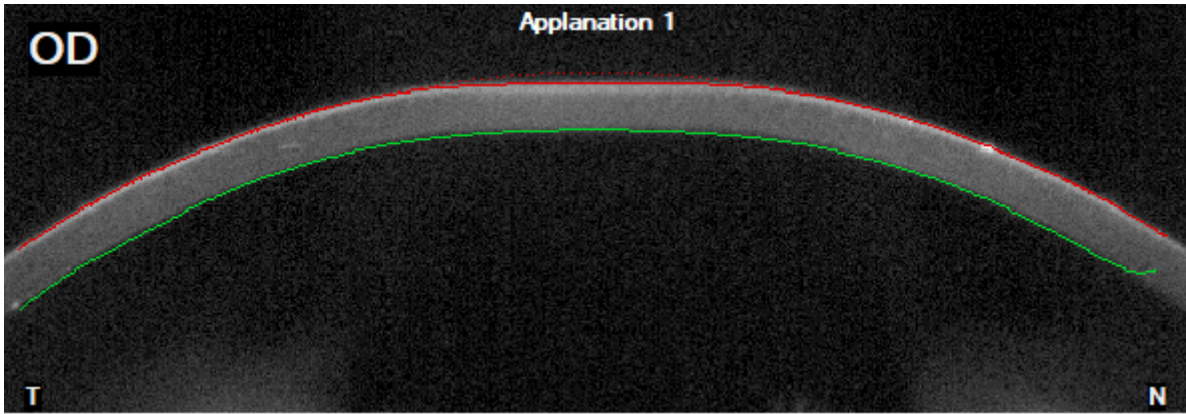


Figure 1.3 First applanation (A1), the puff of air is increasing in intensity and the cornea is moving inward. Time, corneal velocity and length of applanation are recorded

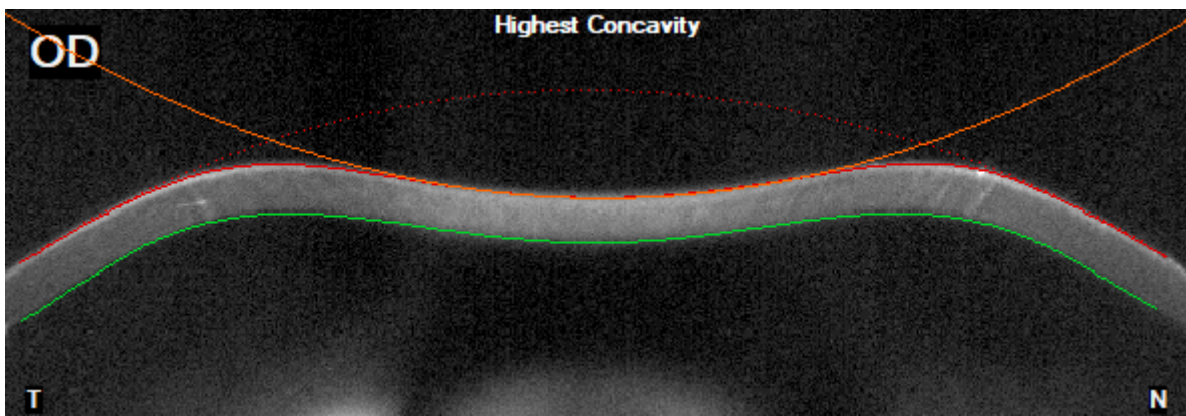


Figure 1.4 Highest concavity (HC) reached, radius, time, deformation amplitude, deflection length and displacement are measured.

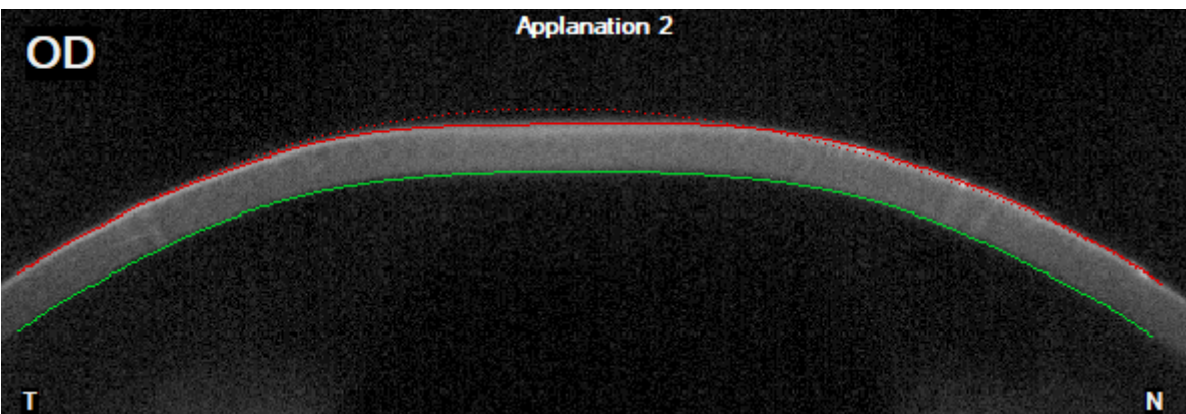


Figure 1.5 Second applanation (A2), the peak of the puff of air is passed and the cornea is moving outward, toward its natural shape. Time, corneal velocity and length of applanation are recorded.

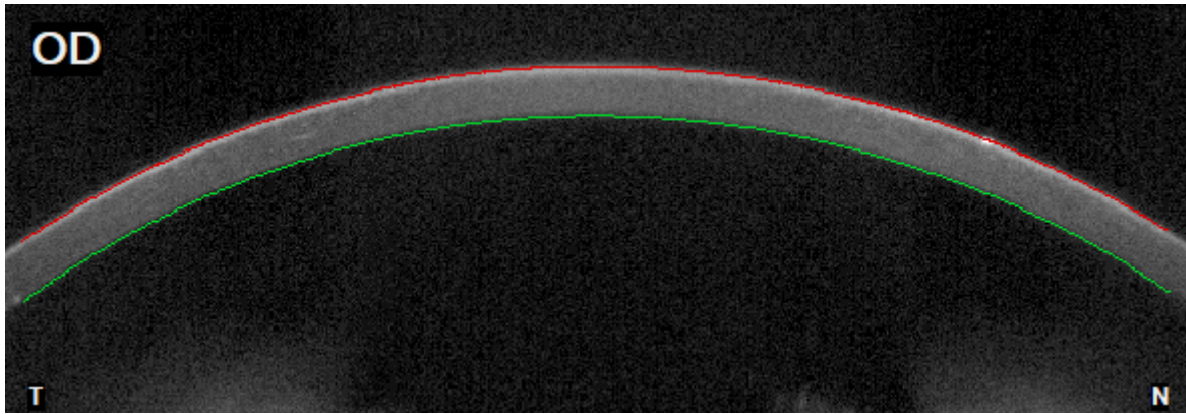


Figure 1.6 Test is finished, cornea has regained its normal shape.

1.2.3 Brillouin Optical Scanner System (BOSS)

The BOSS is an innovative instrument that uses Brillouin confocal microscopy to assess the biomechanical properties of tissue. The BOSS analyses Brillouin scattering to calculate the longitudinal elastic modulus of a transparent tissues. The instrument comprises a laser, essential for its high coherence and monochromatic wavelength, and a virtually imaged phase array (VIPA) spectrometer.

When a single photon passes through the cornea, it interacts with phonons—the elementary vibrations in tissues caused by the oscillation of atoms and molecules at a single frequency due to thermodynamic variations. The photon that interacts with phonons scatters inelastically, transferring energy. By analysing the backscattered light, it is possible to obtain information about phonons, which are related to the biomechanical properties of the tissue.

The development of Brillouin confocal microscopy over the last fifteen years has enabled the use of this promising technology to create a map of the corneal longitudinal modulus. Several clinical applications of this type of instrument are yet to be investigated.

1.2.3.1 Historical perspective and development

In 1922, Léon Brillouin described the scattering caused by thermal acoustic longitudinal waves at the atomic or molecular level on coherent light, typically observed at a 90° angle, as show in Figure 1.7 (Brillouin 1922). It is important to note that the scattering described by Brillouin is an inelastic scattering process, where the total energy is not maintained because part of it causes a frequency shift between the incident and scattered light.

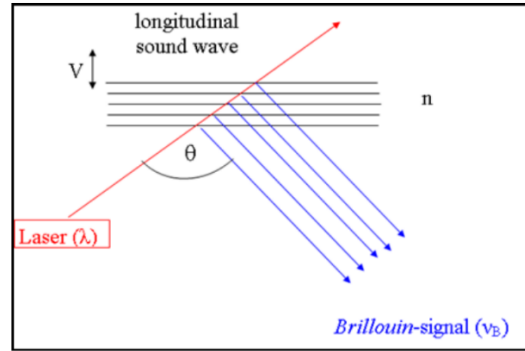


Figure 1.7 . Representation of Brillouin scattering caused by phonons. V is the velocity of the phonons in the media, n the refractive index of the media, θ the angle of scattering (Reiss, Burau, Stachs, Guthoff, & Stolz, 2011)

Knowing the frequency shift, it is possible to calculate certain properties of the medium through which the light is passing, as there is a mathematical relation between the frequency shift and the thermal acoustic wave that scatters the light (phonons). Such vibrations, also known as lattice vibrations or phonons, are present in all media and are related to various features of the material, such as density and elastic modulus.

When the phonons create constructive interference, it is called spontaneous Brillouin scattering. The use of a spectrometer allows the investigation of the spectral changes of the scattered light (spectrometry), which depends on the frequency of the incident light and the vibrations of the molecules around their equilibrium point. Depending on the frequency shift, which can be higher or lower, it is possible to detect Stokes and anti-Stokes Brillouin frequency shifts. Half the frequency difference between the Stokes and anti-Stokes spectral peaks is the Brillouin frequency shift. The Brillouin frequency shift depends on the phonon velocity, wavelength of incident radiation, and refractive index, as shown in Eq. 1.6 Brillouin frequency :

$$\nu_B = \pm \frac{2n}{\lambda} V \cos(\theta/2)$$

Eq. 1.6 Brillouin frequency shift

Differentiating Brillouin scattering from Rayleigh and Raman scatterings represents a significant challenge because both Rayleigh and Raman scatterings are several orders of magnitude more intense. Moreover, Brillouin scattering typically occurs at frequencies in the range of a few GHz.

Rayleigh scattering happens when light interacts with particles smaller than the wavelength of light, resulting in scattering without a change in wavelength. This scattering is responsible

for the blue sky and red sky during sunrise and sunset. Raman scattering, which is completely inelastic, occurs when light interacts with the vibrational modes of molecules, causing a wavelength shift proportional to the vibration. It is commonly used in molecular identification (Park, Min et al. 2002).

Another issue arises from the wavelength of the electromagnetic wave used, typically a laser. To minimise the negative effects of the laser on the tissue, a laser with a high wavelength is preferred. However, increasing the wavelength of the laser reduces the shift of the inelastically scattered light (Reiss, Bureau et al. 2011).

Brillouin scattering, occurring at GHz frequencies, is often too small to be resolved using conventional spectrometers and to be distinguished from Raman and Rayleigh scatterings. To address this challenge, several methods have been developed: multiple-scanning Fabry-Perot interferometers (Lindsay, Anderson et al. 1981), optical beating methods (Tanaka and Sonehara 1995) and monochromators (Benassi, Eramo et al. 2005) as scanning approaches, or non-scanning parallel approaches using angle-dispersive Fabry-Perot interferometers (Itoh 1998). The main limitation of these methods is that their efficiency is constrained by the inverse of the finesse coefficient of the Fabry-Perot interferometer.

In the early 1980s, Brillouin frequency shift was measured in ex vivo corneas and lenses, but the imaging process was extremely time-consuming (Vaughan and Randall 1980, Randall and Vaughan 1982).

In 2007, a new spectrometer was developed based on a virtually imaged phased array (VIPA) with a free spectral range of 33.3 GHz, higher finesse (up to 56), and efficiency up to 80%. This new spectrometer, used with a confocal microscope, achieved a three-dimensional resolution of $6 \times 6 \times 60 \mu\text{m}$ (on x, y, and z axes, respectively) with an integration time of one second instead of minutes (Scarcelli and Yun 2007). In 2012, a resolution of $1 \times 1 \times 5 \mu\text{m}$ (x, y, z) was achieved (Scarcelli, Pineda et al. 2012).

The VIPA consists of a single transparent plate with two semi-reflecting surfaces and an anti-reflecting coating on one side. The light (laser) enters through a fissure on the edge and is reflected several times between the two semi-reflecting surfaces. After each reflection, part of the light passes through the surface, creating several parallel beams of light with different angles. The constructive and destructive interference creates an interference pattern that depends on the wavelength and beam angle.

Recently, Zhang and colleagues (Zhang, Tatham et al. 2016) utilised parallel detection to scan hundreds of points simultaneously, reducing the acquisition time from hours to seconds.

Brillouin Modulus (M) is calculated using the Eq. 1.7 Brillouin Modulus:

$$M = \frac{v_B^2 \lambda^2 \rho}{4n^2 \cos^2\left(\frac{\theta}{2}\right)}$$

Eq. 1.7 Brillouin Modulus

The Brillouin Modulus describes the rigidity of a material in terms of its elastic properties, specifically its resistance to deformation under stress along the direction of wave propagation. The Brillouin Longitudinal Modulus and Young's Modulus (E) differ in magnitude due to their definitions and the scale of pressure modulation (GHz for phonons, MHz for mechanical stress). Consequently, these moduli are not interchangeable because they originate from different types of measurements. However, as shown in Eq. 1.8 there is a good log-log relationship between them (Scarcelli, Kim et al. 2011):

$$\log(M) = a \log(E) + b$$

Eq. 1.8 Log-Log relationship between Brillouin modulus and Young's Modulus

In a recent paper, Ambekar and colleagues compared the Brillouin frequency shift (for the longitudinal modulus) and Optical Coherence Elastography (for Young's modulus), confirming the log-log relationship in Eq. 1.8 Log-Log relationship between Brillouin modulus and Young's Modulus (Ambekar, Singh et al. 2020).

1.2.3.2 Lens

Randall and Vaughan measured the Brillouin frequency shift of lenses from various animals, including humans, in ex vivo conditions. They found a value of 4.71 GHz, with no difference between the centre and the periphery of the lens. This was the first attempt to measure Brillouin frequency shift in ocular tissue (Randall and Vaughan 1982).

In 2007, Scarcelli and Yun mapped the Brillouin frequency shift of a mouse lens in a cuvette filled with viscous polymer. The imaging provided a cross-sectional map of the elastic modulus of the intraocular lens (IOL), with colour coding based on the frequency shift: dark red in the centre (14.6 GHz) of the lens and blue for the surrounding optical medium (11.5 GHz), as shown in Eq. 1.8 (Scarcelli and Yun 2007).

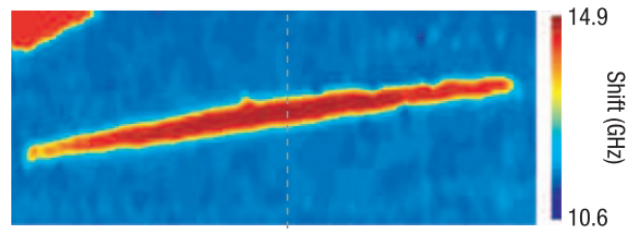


Figure 1.8 Cross-sectional map of a IOL placed in a cuvette filled with liquid (blue) that creates lower frequency shift than the material of IOL. In the left upper part, it is possible to identify the edge of the cuvette, with a frequency shift similar to the IOL material.

Using Scarcelli's configuration, in 2011 Reiss and colleagues (Reiss, Burau et al. 2011) measured in vitro the rheological properties of extracted lenses from rabbits, pigs, and humans, and in situ the rheological properties of pig and rabbit eyes. Measurements were taken with eyes placed in a cuvette filled with saline, and measurements were performed as an axial scan along the optic axis of the eye.

Measurements performed on both rabbit and pig lenses showed higher values of Brillouin frequency shift in the central part of the lens (7.9 GHz for rabbit and 6.5 GHz for pig) than in the cortex. It was even possible to distinguish between different media (aqueous humour, crystalline lens, and vitreous humour) during data collection, due to the scattering at the anterior and posterior capsules of the lens, which correspond to slopes in the graphs, as shown in Figure 1.9. From the obtained measurements, researchers hypothesised that the nucleus has greater toughness than the cortex because the modulus in the cortex is lower than in the nucleus. Once the lenses (human, rabbit, and pig) were extracted, the storage and loss moduli were measured from the lateral positions, revealing higher moduli in the nucleus than in the cortex, as well as higher bulk viscosity and volume elasticity.

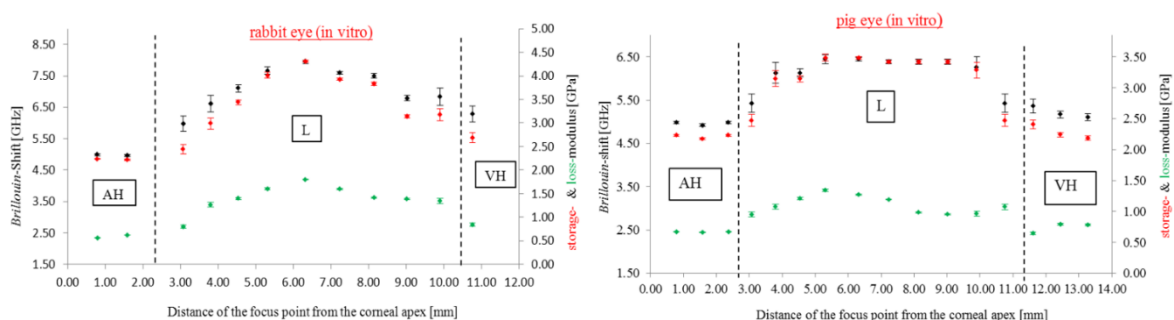


Figure 1.9 Depth dependant frequency shift (green dots) of rabbit eye lens (left image) and porcine (right image), on the right y axis there are storage and loss moduli. AH is aqueous humour; L is lens and VH vitreous humour (Reiss et al., 2011)

In 2011, Scarcelli and colleagues (Scarcelli, Kim et al. 2011), measured *ex vivo* the rheological properties of porcine lenses and, for the first time *in vivo*, the age-related changes in the crystalline lens of anaesthetised mice using Brillouin frequency shift. They found that the peak in Brillouin shift is higher in older mice lenses (up to 16 GHz compared to 11 GHz for younger mice). Weekly measurements correlated with data collected on same-age mice, showing higher values of the Brillouin frequency shift and a peak shifted toward the centre of the lens in older animals.

Authors also measured the Brillouin frequency shift *ex vivo* on young and old porcine (< 1 month, 6 months) and bovine corneas (< 1 month, 1-2 years). In porcine lenses, they observed a similar but less pronounced age-dependent increase in shift compared to mice, and the formation of a plateau in the centre of the crystalline lens, which loses the typical bell shape. In bovine lenses, besides measuring the Brillouin frequency shift, they performed a quasi-static stress-strain test to measure Young's modulus and dynamic shear rheometry for shear moduli, comparing the results with the Brillouin longitudinal modulus calculated from the Brillouin frequency shift. The results showed a significant age-related increase with all methods: Brillouin longitudinal modulus increased from 3.5 GPa for young to 4.5 GPa for old, Young's modulus from 1 kPa for young to 30 kPa for old, and shear modulus from 2 kPa for young to 100 kPa for old, with significant differences in the order of magnitude of measurement units due to differences in measurement procedures.

In 2012 it was demonstrated that degeneration effects in specimens of porcine crystalline lenses were observable from 5 hours post-mortem. Five measurements were taken between the moment of extraction and 25.5 hours later. The deviation between values of frequency shift increased (from zero up to 3 GHz) as signal intensity decreased over time, likely related to a loss of transparency and regularity of the tissue (Rei, Sperlich et al. 2012).

In the same year, the first pilot study on the human crystalline lens *in vivo* was conducted (Scarcelli and Yun 2012). The data showed a classic bell shape for the lens frequency shift, with a central plateau of about 6.05 GHz corresponding to the nucleus of the lens, as shown in Figure 1.10. The calculated modulus ranged from 2.38 to 3.1 GPa for the lens. This study was conducted on a single subject aged 42 years.

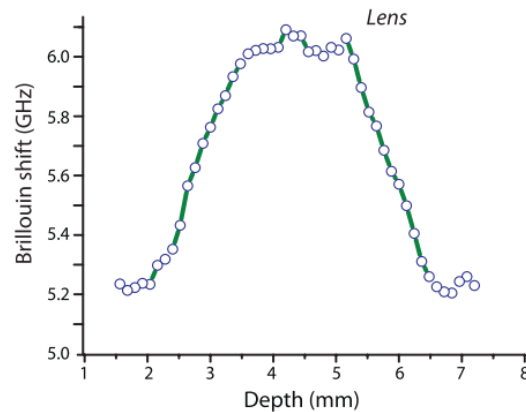


Figure 1.10 Depth-dependant analysis of Brillouin frequency shift measured in vivo on 42 years old male human (Scarcelli & Yun, 2012)

Besner and colleagues in 2016 investigated age-related changes in the longitudinal modulus of the crystalline lens in healthy patients (Besner, Scarcelli et al. 2016). Their data showed that the aqueous and vitreous humours have a mean Brillouin longitudinal modulus of 2.4 GPa, with small variations within the instrument's accuracy for all subjects. They observed steeper slopes in the cortices, given by changes in the moduli (both anterior and posterior), and a central plateau (defined as the top 98% of the longitudinal modulus, around 3.3 GPa) anatomically identifiable with the nucleus of the lens, which has the highest values of modulus. The extent of this plateau is age-dependent and increases with age. No statistically significant differences in the longitudinal modulus were found between the right and left eyes (regardless of age), while significant variability was measured between individuals of the same age. Between 19 and 63 years of age, the lens thickness increased at a rate of around 30 μm per year, but only in the stiff central region, while the periphery remained unchanged. The moduli of the vitreous and aqueous humours, as well as the central lens region, were stable until the age of 45, after which there was a linear decrease of -4.5 MPa per year, though the central lens region remained stiffer than the cortices.

Significant differences in the orders of magnitude between the shear modulus (measured in kPa using rheometry) and Brillouin moduli (measured in GPa) are expected, given the incompressibility of water, but a strong correlation between the two moduli was observed (Reiss, Bureau et al. 2011).

In 2020, Ambekar and colleagues compared two methods to determine the ex vivo elastic properties of the crystalline lens: Brillouin frequency shift (for longitudinal modulus) and Optical Coherence Elastography (OCE, for Young's modulus). They derived the coefficients

for Eq. 1.8 ($a = 0.13$, $b = 9.13$) and calculated the Brillouin longitudinal moduli for the anterior, central, and posterior parts of the lens: respectively 3.43 ± 0.18 GPa, 4.33 ± 0.13 GPa, and 3.59 ± 0.16 GPa (Ambekar, Singh et al. 2020).

1.2.3.3 Cornea

In 2012, Scarcelli and colleagues measured the Brillouin modulus of bovine cornea samples. They found that the Brillouin frequency shift varied depending on the depth of the tissue, with higher shifts in the epithelium (8.6 GHz, corresponding to 2.96 GPa) and lower shifts toward the endothelium (7.8 GHz, corresponding to 2.43 GPa). This discrepancy can be explained by the organization of stromal lamellae, which are interwoven in the anterior part and mostly parallel to the corneal anterior surface in the inner part. The mean longitudinal modulus measured in the four samples was 2.70 ± 0.02 GPa (Scarcelli, Pineda et al. 2012).

During the same year, the same group began in vivo measurements of the cornea and anterior segment in humans using a 780 nm laser. They found a decline in the Brillouin shift from 5.6 GHz in the anterior stroma to 5.25 GHz in the posterior portion of the cornea, a change marked within about 200 μm of corneal thickness. It was difficult to analyse the first 70 μm of the cornea due to confocal resolution and Fresnel reflection from the anterior corneal surface. The aqueous humour appeared to have a uniform Brillouin frequency shift (5.25 GHz), similar to water due to its chemical composition, with variations within the aqueous humour being about 30 MHz. The calculated values for the Brillouin longitudinal modulus ranged from 2.82 to 2.5 GPa for the cornea, depending on the depth of the measurement. Differences from previous values in the literature were attributed to variations among subjects and the values of the index and density of ocular tissues. This pilot study had only one participant (Scarcelli and Yun 2012).

In 2014, Scarcelli and colleagues measured the Brillouin shift in 6 healthy patients, finding a mean of 5.74 GHz for the anterior portion of the 5x5 mm central corneal zone, with a resulting Brillouin modulus of 2.83 GPa (Scarcelli, Besner et al. 2014)

A 2019 paper by Gouveia and colleagues Brillouin microscopy could verify that the limbus has a lower Brillouin frequency shift than the central cornea (Gouveia, Lepert et al. 2019). Researchers measured the in vivo Brillouin frequency shift of various portions of the anterior segment:

- Central corneal epithelium (50-60 μm of depth): 6.37 ± 0.09 GHz
- Bowman's membrane: 6.66 ± 0.04 GHz

- Anterior central stroma: 6.53 ± 0.04 GHz
- Limbal epithelium (40-60 μm of depth): 6.34 ± 0.14 GHz
- Extracellular matrix: 6.24 ± 0.09 GHz
- Corneal stroma under the limbus: 6.40 ± 0.14 GHz

The data indicated that the highest shift occurs in Bowman's membrane and that the corneal layers produce higher shifts than the limbus. Corneal layers also have more defined biomechanical properties, identified by precise shifts, than the limbus, likely due to the presence of Palisades of Vogt, focal stromal projections, and limbal crypts. This study used a 671 nm laser, which may explain the differences in the magnitude of the Brillouin frequency shift.

In 2019, Seiler and colleagues measured an average Brillouin frequency shift of 5.72 ± 0.01 GHz (2.81 ± 0.01 GPa) in vivo in the central corneal region of healthy subjects. They found that the frequency shift increased by 4 MHz per decade, with no differences based on gender and bilateral symmetry between the right and left eyes within the instrument's resolution (Seiler, Shao et al. 2019).

Another study reported a similar increase of about 3 MHz per decade, but this correlation was not statistically significant. The mean measurement for the central corneal shift was 5.73 ± 0.03 GHz, with remarkable symmetry between the two eyes of the same subject, showing an inter-subject difference of ± 15 MHz within the same age group (Shao, Eltony et al. 2019).

Recently, Brillouin confocal microscopy has been used to assess the presence of Fuchs Endothelial Corneal Dystrophy (FECD) in vivo in humans. This was possible because the increased water content in FECD decreases the Brillouin frequency shift from 5.73 ± 0.02 GHz in healthy subjects to 5.65 ± 0.04 GHz in FECD subjects. Additionally, an increase in central corneal thickness was measured in FECD subjects (Eltony, Clouser et al. 2020).

Data from several studies on healthy corneas seem to agree on a Brillouin frequency shift value around 5.72 ± 0.02 GHz using a 780 nm laser, corresponding to 2.81 ± 0.01 GPa.

1.2.3.4 Hydration

The influence of hydration, calculated as the percentage of water in the total weight of a tissue, has been investigated both in vitro on porcine corneal samples and in vivo on humans after waking (Shao, Seiler et al. 2018). The animal model revealed an inverse

relationship between hydration and Brillouin frequency shift: after soaking, the specimens were left to dry, and the frequency shift increased by 200 MHz in 20 minutes. Additionally, there was an inverse relationship between central corneal thickness (CCT) and Brillouin frequency shift. In humans, the inverse relationship with CCT was confirmed by measuring the Brillouin frequency shift and CCT just after waking up and at intervals of 1, 2, 3, and 9 hours. The results showed that an increase in CCT, caused by physiological overnight swelling, is associated with a lower Brillouin frequency shift, as shown in Table 1.1.

Differences in terms of Brillouin shift between 2 and 9 hours after waking up were not significant, but it is interesting to note that the complete recovery to the normal range does not occur within one hour.

Table 1.1 values of swelling and frequency shift at different times after wake

	0 h	1 h	2 h	9 h
CCT	$17 \pm 8 \mu\text{m}$	$5 \pm 4 \mu\text{m}$	$1 \pm 4 \mu\text{m}$	$0 \pm 3 \mu\text{m}$
Brillouin Frequency shift	$-25 \pm 12 \text{ MHz}$	$-10 \pm 13 \text{ MHz}$	$-3 \pm 7 \text{ MHz}$	$0 \pm 8 \text{ MHz}$

On ex vivo rabbit corneas immersed in a Dextran solution, similar results were found: higher hydration and increased thickness led to lower Brillouin frequency shifts, even when the hydration levels were greater than in the previous study (Seiler, Shao et al. 2018) as can be seen in Table 1.2.

Table 1.2 Thickness, value of hydration and Brillouin frequency shift for specimens in different solutions. Corneal hydration is measured as grams of water per gram of dry tissue.

	5% detran	10% dextran	15% dextran	20% dextran
Minimal Centra Pachymetry [μm]	600 ± 31	473 ± 28	330 ± 10	305 ± 13
Corneal hydration	4.57 ± 0.26	3.47 ± 0.24	2.23 ± 0.09	2.02 ± 0.11
Brillouin frequency shift [GHz]	5.33 ± 0.01	5.49 ± 0.01	5.63 ± 0.01	5.79 ± 0.01

1.2.3.5 Retina

In 2020, the Brillouin longitudinal modulus was measured on murine retinas ex vivo (Ambekar, Singh et al. 2020). The collected data indicated a longitudinal modulus of around 2.50 GPa. Researchers were able to differentiate between retinal layers, finding that the inner and outer nuclear layers had the highest moduli (2.53 ± 0.02 GPa), while the outer plexiform layer had the lowest modulus (2.48 ± 0.02 GPa). This difference is likely due to the density of cell bodies in the nuclear layers, with higher density corresponding to a higher modulus.

Unfortunately, this function is not yet available on the commercially available version of the Brillouin Optical Scanner System (BOSS).

1.2.3.6 Cross-Linking

One of the first uses of the new generation of Brillouin microscopy was monitoring the dynamic changes induced by a Cross-Linking (CXL) procedure on an optical adhesive polymer that responds to UV light, simulating a CXL procedure (Scarcelli and Yun 2007). The changes in Brillouin shift (left y-axis) and elastic modulus (right y-axis) during the process and after 24 hours can be observed, as shown in Figure 1.11.

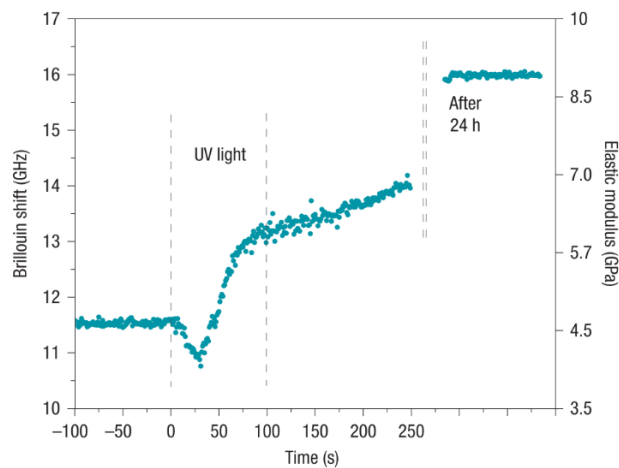


Figure 1.11 Effects of a UV light on optical adhesive polymer (Scarcelli et al., 2012).

In 2012, Scarcelli and colleagues measured the changes in the Brillouin modulus of bovine corneas following a Cross-Linking (CXL) procedure. The corneas were soaked for 5 minutes with a 0.1% riboflavin solution and then exposed to 460 nm light at 15 mW/cm² for 20 minutes. The results revealed that the Brillouin modulus increased in the stroma after the

CXL treatment, while the epithelium removal and riboflavin treatment alone had no effect. The Brillouin modulus increased by 10% (from 2.70 ± 0.03 GPa to 2.98 ± 0.03 GPa) compared to a greater than 200% increase in Young's modulus (from 0.4 ± 0.1 MPa to 0.9 ± 0.2 MPa) (Scarcelli, Pineda et al. 2012).

Results revealed that Brillouin modulus increased in stroma and that the treatment is effective only after blue light, the epithelium removal and riboflavin treatment does not have any effect. As expected, the differences in terms of Brillouin modulus between the measurements control and Cross-Linking group were clear: 10% of increase in Brillouin modulus (from 2.70 ± 0.03 GPa to 2.98 ± 0.03 GPa) against a gain higher than 200% in Young's modulus (from 0.4 ± 0.1 MPa to 0.9 ± 0.2 MPa).

In 2013 Brillouin Microscopy was used to assess the efficacy of different CXL protocols on porcine corneas in vitro. They found that compared to the classical Dresden protocol (30 minutes of pre-soaking and 30 minutes of UV exposure), epi-off procedures with reduced pre-soaking or UV exposure times resulted in lower corneal stiffening effects (35% to 65% less than the Dresden procedure). The pre-soaking alone significantly stiffened the cornea, likely due to dehydration. The epi-on procedure had about one-third the effect of the classical procedure, with most stiffening in the anterior stroma. Epi-off procedures cause corneal dehydration, increasing Brillouin frequency shift and modulus, while epi-on procedures cause swelling, decreasing these metrics (Scarcelli, Kling et al. 2013).

It was proven, that temperature differences between room temperature (22°C) and body temperature (37°C) do not affect shift measurements. However, in crosslinked specimens, UV irradiation for 12 minutes at 30 mW/cm^2 increased the Brillouin shift by 0.7-0.9 GHz (Bukshab, Paranjape et al. 2015).

In 2017 (Randleman, Su et al. 2017) the outcome of rapid Cross-Linking (Kanellopoulos 2012) procedure on porcine corneas on which a LASIK flap was created was investigated in vitro. After creating the flap, the rapid CXL procedure was performed as follows: the corneas were soaked with riboflavin, avoiding contact between the riboflavin and the flap, and then rinsed off the excess riboflavin. The flap was then repositioned, and the cornea was irradiated with UV-A at 30 mW/cm^2 for 80 seconds. Following the rapid CXL procedure, the Brillouin frequency shift was slightly higher than the one measured after the flap creation (0.002 ± 0.019 GHz for the anterior, 0.006 ± 0.010 GHz for the central, and 0.009 ± 0.011 GHz for the posterior part). However, these differences were not statistically significant in any part of the cornea and were still lower than those of the untreated (virgin) cornea. The

impact on the modulus was minimal, indicating that the rapid CXL procedure did not significantly strengthen the corneal tissue.

In 2017, Brillouin frequency shift was used to analyse the outcomes of different Cross-Linking procedures on porcine corneas *in vitro*, modifying the intensity and duration of exposure (Webb, Su et al. 2017). After 30 minutes of soaking with riboflavin, various procedures were performed on the corneal samples: each cornea was split into two samples, one for treatment and the other as a control. This strategy allowed for the assessment of the stiffness gained from the procedure for each cornea. The Cross-Linking procedures involved 30 minutes at 3 mW/cm², 10 minutes at 9 mW/cm², 2.65 minutes at 34 mW/cm², and 1.80 minutes at 50 mW/cm², ensuring the same total energy on each sample (5.4 J/cm²). The results showed that all the procedures produced a statistically significant increase in corneal stiffness compared to controls, but with lower efficacy compared to the classical procedure (30 minutes at 3 mW/cm²). The classical procedure induced significantly higher stiffness than the 34 and 50 mW/cm² procedures (5.3% increase in Brillouin modulus compared to 1.2% and 1.1%, respectively), and the 9 mW/cm² procedure created significantly higher stiffness than the 50 mW/cm² procedure (3.6% compared to 1.1%), while the 34 and 50 mW/cm² procedures did not differ in induced stiffening. Additional differences were measured between 3 and 9 mW/cm², with a similar effect in the anterior part of the cornea and statistically lower stiffening in the central and posterior cornea for the latter irradiation. To strengthen the experiment, researchers measured the Young's modulus of samples and compared it with the Brillouin modulus; the results showed that the relationship between the percentage differences in the two moduli is almost linear, with lower effects for higher irradiation conditions.

In 2019, Zhang and colleagues (Zhang, Roozbahani et al. 2019) compared the efficacy of the classical Cross-Linking procedure with Contact Lens Assisted Cross-Linking (CACXL) using Brillouin frequency shift *ex vivo* on porcine eyes. Both stress tests and Brillouin frequency shift results confirmed that the CACXL procedure produced lower stiffness results than the classical Cross-Linking procedure. The increases in Brillouin longitudinal modulus were 7.8%, 1.7%, and -0.7% for the anterior, central, and posterior cornea in Cross-Linking, while in CACXL the increases were 5.5%, 1.2%, and -0.4%. Again, the classical Cross-Linking procedure proved to be the most effective.

Recently, Zhang et al. investigated *in vitro* the efficacy of Cross-Linking performed over or under a LASIK flap on porcine corneas (Zhang, Roozbahani et al. 2020). The main difference was in the soaking procedure: in the “over” procedure, corneas were soaked with

riboflavin with the flap attached (over flap), while in the “under” procedure, the riboflavin was applied while the flap was reflected, and then the flap was repositioned once soaking was completed; the corneas were then irradiated with 3 mW/cm^2 UV for 30 minutes. The results showed different outcomes for the anterior and central portions of the cornea: the “over” procedure induced a higher frequency shift in the anterior section ($8.29 \pm 0.04 \text{ GHz}$ against $8.17 \pm 0.03 \text{ GHz}$), which was statistically significant; while the “under” procedure induced a higher frequency shift in the middle portion of the cornea ($8.06 \pm 0.04 \text{ GHz}$ against $8.05 \pm 0.05 \text{ GHz}$), but this was not statistically significant. No effect was measured in the posterior region.

It is clear that Brillouin frequency shift is a useful tool for evaluating the efficacy of Cross-Linking treatments and comparing different procedures. However, there are currently no published papers measuring changes in human corneas in vivo before and after treatment.

1.2.3.7 Keratoconus

In 2014, Scarcelli and colleagues investigated the biomechanics of ex vivo healthy and keratoconic corneas (Scarcelli, Besner et al. 2014). Tissue samples were taken from patients who underwent Descemet’s stripping endothelial keratoplasty (DSEK), as this procedure requires only the posterior part of the cornea, leaving the anterior and central parts available for research. Differences in Brillouin cross-sectional images between healthy and cone zones of keratoconic corneas were clear: the cone zone showed a lower shift ($7.99 \pm 0.10 \text{ GHz}$) than healthy corneas ($8.17 \pm 0.06 \text{ GHz}$), while shifts measured in non-cone portions of keratoconic corneas ($8.19 \pm 0.04 \text{ GHz}$) were not significantly different from those measured in healthy samples. These results suggest that the weakening is limited to the cone zone. It is interesting to note that the authors did not calculate the Brillouin modulus because they did not know the density and refractive index of the tissue samples due to the swelling caused by the lack of endothelium.

The first in vivo study on patients with advanced keratoconus was conducted in 2015 (Scarcelli, Besner et al. 2015). This study showed that the cone zone has a lower Brillouin shift ($5.67 \pm 0.02 \text{ GHz}$) than normal corneas ($5.74 \pm 0.01 \text{ GHz}$), and the difference was statistically significant. A statistically significant difference was also measurable between the cone and the areas outside the cone zone ($5.73 \pm 0.03 \text{ GHz}$), as shown in Figure 1.12. The differences from the previous study can be attributed to the wavelength of the laser used (780 nm instead of 520 nm).

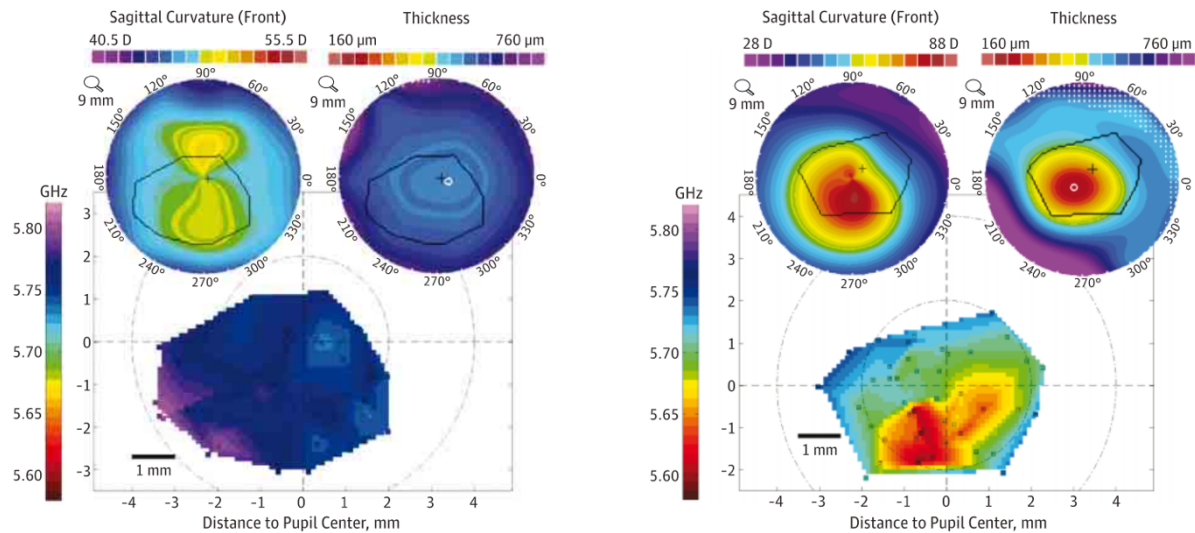


Figure 1.12 Maps of corneal Brillouin frequency shift. The left map is from a 53-years old normal cornea, while the right one is from a 40-years old patient with advanced keratoconus. Sagittal and Thickness maps in the upper part (Scarcelli et al., 2015)

A lower Brillouin frequency shift in ectatic corneas (5.70 ± 0.02 GHz) compared to healthy ones (5.72 ± 0.01 GHz) was measured at the thinnest point (Seiler, Shao et al. 2019). Researchers highlighted that the frequency shift measured at the maximum posterior elevation had the best correlation with other clinical parameters related to keratoconus, such as minimal thickness and maximal keratometry. Despite the statistically significant difference in frequency shift, the authors stated that a single measurement would be insufficient to discriminate between healthy and keratoconic corneas. This is because the technology of the instrument used (Brillouin Optical Scanner System, Intelon Optics, Lexington, USA) was neither specific nor sensitive enough, as demonstrated by the Receiver Operating Characteristic (ROC) curves in Figure 1.13. These curves indicate that the potential of Brillouin frequency shift is lower than that of maximum keratometry and thickness in detecting keratoconus.

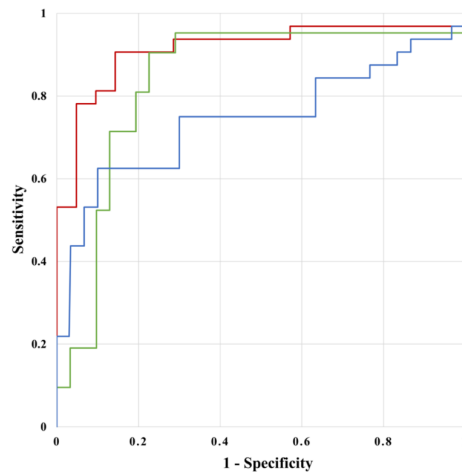


Figure 1.13 ROC curves of thinnest pachymetry (red), K_{max} (green) and Brillouin frequency shift (blue). The latest has the lower potential in keratoconus detection (Seiler et al., 2019).

Using an improved version of the instrument with enhanced sensitivity and stability of eye tracking, Shao and colleagues (Shao, Eltony et al. 2019) measured the Brillouin frequency shift in keratoconic corneas, categorising them into four sub-groups according to the Amsler-Krumeich classification (Amsler 1946). Stages III and IV (advanced stages of ectatic disorder) exhibited less uniformity than normal and stage I corneas, with Brillouin frequency shift values 100-200 MHz lower than those of healthy corneas. Compared to normal corneas, stage I and II corneas had shifts lowered by 3 and 7 MHz, respectively, but these differences were not statistically significant. The authors calculated ROC curves for stage I keratoconus, which demonstrated good sensitivity and specificity for Brillouin frequency shift in the cone zone, the regional difference in Brillouin frequency shift, maximum keratometry, and minimum thickness. It is important to note that the Area Under the Curve (AUC) for Brillouin frequency shift in the cone zone and the regional difference in Brillouin frequency shift were similar to or higher than those for maximum keratometry and minimum thickness.

Keratoconus causes a lowering in Brillouin frequency shift, localised in cone zone, that depends on the stage of pathology.

1.2.3.8 Refractive surgery

The effects of LASIK flap creation were analysed ex vivo on porcine eyes (Randleman, Su et al. 2017). Measurements taken before and after flap creation revealed a reduction in Brillouin frequency shift, suggesting a weakening in the anterior cornea (-0.104 ± 0.024 GHz), coinciding with the flap. No significant differences in Brillouin modulus were measured in the central (-0.029 ± 0.012 GHz) and posterior corneas (-0.005 ± 0.009 GHz). Similarly,

Zhang and colleagues (Zhang, Roozbahani et al. 2020) found a weaker area in the anterior cornea due to the flap creation for LASIK.

1.2.3.9 Glaucoma

It has been demonstrated that using etalon filters, it is possible to determine the Brillouin shift in the conjunctiva and sclera of ex vivo porcine eyes (Shao, Besner et al. 2016). The conjunctiva (5.7 GHz) and sclera (6.4 GHz) showed higher values of Brillouin shift compared to the cornea (5.5 GHz). This finding is promising, considering the role of the sclera in glaucoma pathogenesis (Jia, Yu et al. 2016). To date, no papers have investigated changes in Brillouin modulus or frequency shift in glaucoma.

1.2.3.10 BOSS

The current version of the BOSS, showed in Figure 1.14, measures the Brillouin Modulus at different corneal locations, with a scan every 100 μm along the z-axis. For each corneal location, the mean value is calculated, and a map is created based on the calculated values for each location. It takes up to 30 seconds to measure each location, so the duration of the entire corneal scan depends on the number of locations scanned.



Figure 1.14 Current version of the Brillouin Optical Scanning System (BOSS)

For the lens, the modulus is usually measured at a single location due to pupillary restrictions, and this measurement takes up to a minute. The lens scan provides data about the modulus, including the top plateau (where the Brillouin modulus is relatively stable), the bottom plateau, and the anterior and posterior slopes, from the graph with a classic bell shape, as shown in Figure 1.15.

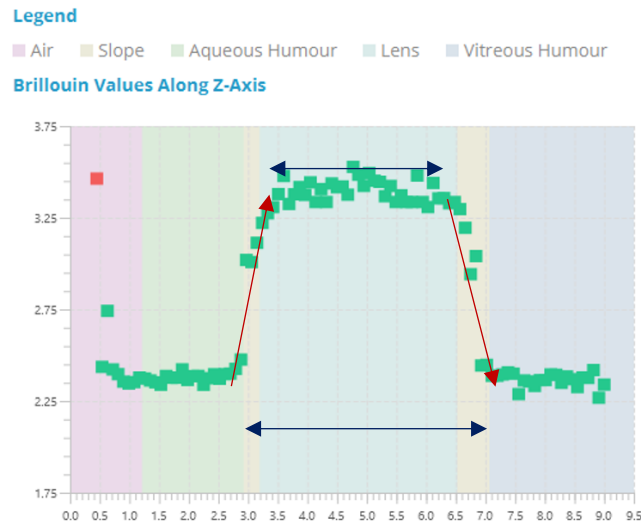


Figure 1.15 The output of the lens measurement of the BOSS. The upper arrow is the Top Plateau, the lower one is the Bottom Plateau. The arrow on the left is the Anterior Slope, the one on the right is the Posterior Slope. On the x axis there is the depth of the scanning along the z-axis. On the y axis there is the value of the Brillouin modulus.

1.3 Corneal Biomechanics in Glaucoma

Glaucoma is a group of ocular pathologies characterised by progressive damage to the optic nerve, often associated with raised intraocular pressure (IOP). This damage can lead to irreversible vision loss, which typically begins in the periphery of the visual field, preserving good central vision until the advanced stages of the disease. This preservation of central vision presents a challenge, as most people are unaware of peripheral vision loss and only notice visual impairment when it is too late to halt the disease. In later stages, glaucoma can cause tunnel vision and ultimately complete loss of vision. The diagnosis of glaucoma involves several tests, including tonometry to measure IOP, gonioscopy to assess whether the iridocorneal angle is obstructed, visual field tests to quantify peripheral vision loss, fundus examination to inspect the back of the eye for signs of damage, and Optical Coherence Tomography (OCT) to detect damage to the optic nerve and retinal nerve fibre layer.

There are several types of glaucoma. Primary open-angle glaucoma (POAG) is the most common type, where the iridocorneal angle is open, but there is an imbalance between the production and outflow of aqueous humour, often due to obstruction in the trabecular meshwork. Its progression is slow and asymptomatic in the early stages. Closed-angle glaucoma is less common but more acute, with the iridocorneal angle closed, causing a rapid increase in IOP and symptoms such as headaches, ocular pain, glare, and nausea. This type can quickly lead to vision loss. Normal tension glaucoma involves damage to the optic disc and visual field despite normal IOP, with the mechanism not yet fully understood. Secondary glaucoma results from an outflow obstruction caused by a systemic or ocular condition such as uveitis, trauma, surgery, or drugs. Ocular hypertension is a condition where IOP is raised without clear signs of glaucomatous damage but is a crucial risk factor for developing glaucoma (Kass, Heuer et al. 2002).

The primary goal of glaucoma treatment is the reduction of IOP. Research has shown that even a reduction of 1 mmHg can slow the progression of the disease (Jayaram 2020). Understanding and early detection of glaucoma are critical for effective management and prevention of vision loss.

1.3.1 Primary Open Angle Glaucoma (POAG)

1.3.1.1 ORA

Patients with POAG showed lower values of CH (Sullivan-Mee, Billingsley et al. 2008, Mangouritsas, Morphis et al. 2009, Abitbol, Bouden et al. 2010, Kaushik, Pandav et al. 2012, Costin, Fleming et al. 2014, Hussnain, Alsberge et al. 2015, Pillunat, Hermann et al. 2016, Tejwani, Devi et al. 2016) and CRF (Sullivan-Mee, Billingsley et al. 2008, Pillunat, Hermann et al. 2016, Tejwani, Devi et al. 2016) compared to healthy controls. CH is lower, but CRF is higher in POAG patients compared to NTG (Ang, Bochmann et al. 2008, Shah, Laiquzzaman et al. 2008, Kaushik, Pandav et al. 2012). Lower CH and CRF may indicate that the abilities to dissipate energy and overall corneal resistance in POAG are lower than in healthy subjects and have been suggested as risk factors in potential POAG patients.

Weak to moderate positive correlations between CCT and CH (Shah, Laiquzzaman et al. 2008, Mangouritsas, Morphis et al. 2009, Abitbol, Bouden et al. 2010, Narayanaswamy, Su et al. 2011, De Moraes, Hill et al. 2012, Prata, Lima et al. 2012, Dascalescu, Corbu et al. 2015) and between CH and CRF (Khawaja, Chan et al. 2013, Lee, Kim et al. 2019) were found, suggesting that thicker corneas have higher damping and are less compliant to mechanical stress.

In unilateral and asymmetric POAG, the eye with the worst visual field has lower values of CH and slightly lower values of CRF (Anand, De Moraes et al. 2010, Hirneiss, Neubauer et al. 2011). No differences were detected in CCT (Anand, De Moraes et al. 2010); some authors reported no significant differences once the samples were corrected for IOP (Hirneiss, Neubauer et al. 2011).

Among different ethnicities, African POAG patients have lower values of CH, CRF, and CCT than Caucasian POAG patients. These parameters also showed differences even in healthy controls (Detry-Morel, Jamart et al. 2012), suggesting an ethnic dependence. In the Chinese POAG population, CH was measured to be similar to that in Caucasian POAG patients (Narayanaswamy, Su et al. 2011).

Patients with POAG suffer from a significantly greater decrease in CH values over time (-0.11 ± 0.73 mmHg per year) compared to healthy subjects (0.07 ± 2.31 mmHg per year) (Hussnain, Alsberge et al. 2015). This finding may suggest a relationship between the decrease in CH, the increase in IOP, and the progression of the pathology.

Patients with POAG have been associated with higher dIOP (the difference between IOPcc and IOPg) than healthy subjects (Sullivan-Mee, Billingsley et al. 2008). IOPcc may help differentiate between POAG and glaucoma suspect patients (Sullivan-Mee, Billingsley et al. 2008, Tejwani, Devi et al. 2016).

In unilateral and asymmetric glaucoma, IOPcc is higher in eyes with a worse visual field, but no significant differences were detected when measuring IOP with Goldmann Applanation Tonometry (GAT) (Anand, De Moraes et al. 2010, Hirneiss, Neubauer et al. 2011). IOPg and IOPcc correlate strongly, but both have poor correlation with CH and CRF (Khawaja, Chan et al. 2013).

Differences in GAT measurements between POAG and healthy subjects were not significant, while IOPcc showed a statistically significant difference, being 3.4 ± 2.7 mmHg higher than GAT (Costin, Fleming et al. 2014). A negative correlation was found between CH and GAT, as well as between CH and IOPcc, suggesting an important role of CH in dissipating high IOP (Narayanaswamy, Su et al. 2011, Dascalescu, Corbu et al. 2015).

Patients with POAG exhibit significantly lower values of CH and CRF compared to healthy controls, suggesting reduced ability to dissipate energy and overall corneal resistance. IOPcc has been measured being a more significant metrics to detect POAG than IOPg.

In terms of diagnostic performance, a study (Ehrlich, Radcliffe et al. 2012) found that IOPcc exhibited a higher AUC of 0.93, with both sensitivity and specificity at 0.85, compared to GAT, which showed an AUC of 0.78 in detecting glaucomatous optic neuropathy. Although these findings are promising, the diagnosis of POAG cannot rely solely on data from corneal biomechanics. Instead, these biomechanical parameters provide supplementary information that may enhance the clinician's ability to more accurately assess glaucoma risk and progression, beyond what is offered by IOP measured using GAT or CCT. Nonetheless, the precise clinical utility and significance of CH and CRF in the diagnosis of POAG require further investigation and clarification.

1.3.1.2 Corvis ST

A study that investigated repeatability, used Intraclass Correlation Coefficient and demonstrated that the inter- and intra-examiner precision of Corvis ST measurements was excellent for CCT, IOP, A1time, A2time, DA, and HCradius, good for A1velocity, A2velocity, and HCtime, and moderate to poor for A1length, A2length, and PD in both POAG and healthy patients. The POAG group showed higher values of A1time and lower values of

A1velocity, A2time, A2velocity, and DA than healthy controls. Researchers found that IOP affects the measurement of biomechanical parameters more than CCT. Biomechanical features measured by Corvis ST were evaluated to have similar or lower power in discriminating between POAG and healthy eyes compared to GAT. The Area Under the Curve (AUC) of ROC analysis for corneal biomechanical parameters was between 0.51 and 0.72, while it was 0.73 for GAT, suggesting comparable to lower sensitivity and specificity in discriminating between conditions. The analysis of biomechanical parameters suggested that POAG patients have a less deformable cornea than healthy controls, which the authors attributed to high IOP or the use of glaucoma medications (Salvetat, Zeppieri et al. 2015).

DA, A1velocity, and A2time were measured to be lower in POAG than in healthy controls, whereas A1time, A2velocity, and PD were higher in POAG than in controls. In both POAG and controls, all the aforementioned parameters, excluding PD and DA, were positively related to IOP, while PD and DA were inversely related to IOP, suggesting that corneal compliance is inversely related to IOP (Wang, Du et al. 2015).

A2velocity and PD were found to be higher in POAG than in controls, while HCtime was lower. A2velocity and PD correlated moderately with IOP and CCT, while HCtime appeared to be the most promising risk factor to differentiate between POAG and controls, because of its independence from IOP and CCT (Lee, Chang et al. 2016).

A1velocity, A2time, and PD were measured to be lower in POAG than in controls, while DA was higher. A significant correlation was found between DA and GAT in both POAG and controls. ROC curve analysis found that A2time had the highest AUC (0.797), while other parameters performed worse (PD: 0.724; DA: 0.695; A1velocity: 0.657). Combining all biomechanical parameters resulted in an AUC of 0.876, better than any single parameter (Tian, Wang et al. 2016).

Compared to the normal control group, patients with POAG had lower values of DA. When POAG patients were divided by disease severity, the group with more advanced POAG showed higher values of DA and DefIA than the early-stage group, while HCradius values were higher in the early group than in more advanced stages. Interestingly, the relationship of DA with CCT was negative in normal and early groups but became positive in moderate and severe groups. This change could be due to the prolonged use of antiglaucoma medication or prolonged high IOP (Hirasawa, Matsuura et al. 2017).

A1velocity and DA were measured to be lower in POAG than in controls, while HCradius was higher. IOP can be considered a predictive factor for DA in POAG. All these parameters indicated a less deformable cornea in POAG than in controls (Jung, Park et al. 2020).

In current literature, there is an agreement about certain Corvis ST values: POAG eyes have lower values of A1velocity, A2time, and DA, whereas they show higher values of A1time and A2velocity. These findings suggest that POAG eyes are less compliant to the air puff and exhibit higher rigidity: the first applanation occurs later, with lower velocity, the overall deformation is lower, and the second applanation occurs earlier with higher velocity. The role of raised IOP in these corneal biomechanical alterations is yet to be fully established.

1.3.2 Normal Tension Glaucoma (NTG)

1.3.2.1 ORA

In NTG patients, CH was found to be lower than in healthy subjects (Kaushik, Pandav et al. 2012, Morita, Shoji et al. 2012, Shin, Lee et al. 2015, Park, Shin et al. 2018) but higher than in POAG. CRF was found to be lower in NTG than in POAG and controls (Kaushik, Pandav et al. 2012, Morita, Shoji et al. 2012, Shin, Lee et al. 2015, Park, Shin et al. 2018). IOPg and IOPcc were been measured to be lower (Kaushik, Pandav et al. 2012) to comparable to healthy levels, but lower than POAG (Ang, Bochmann et al. 2008, Grise-Dulac, Saad et al. 2012). IOPcc was measured to be higher than GAT, while IOPg and GAT were not statistically different from healthy (Morita, Shoji et al. 2012). GAT, as expected, was measured lower than in POAG and comparable to healthy (Ang, Bochmann et al. 2008, Grise-Dulac, Saad et al. 2012). CCT was found thinner or comparable to in NTG than in healthy controls (Kaushik, Pandav et al. 2012, Morita, Shoji et al. 2012, Shin, Lee et al. 2015)

Some authors suggested that in NTG patients IOP measurement is more affected by CRF than CH, and not affected at all by CCT (Kaushik, Pandav et al. 2012). ORA IOP indices may be useful in distinguishing between healthy and NTG (Morita, Shoji et al. 2012)

In NTG, CRF and CCT were significantly different from those in POAG and OHT, while CH only differed from OHT. The difference between GAT and IOPg was significant between POAG and OHT. CCT positively correlates with CH and CRF, as well as CH with CRF (Shah, Laiquzzaman et al. 2008).

Values of VFI, PSD, and MD were found to be lower in NTG than in controls (Shin, Lee et al. 2015, Park, Shin et al. 2018). The intraclass correlation coefficient was found to be good between IOPcc, IOPg, GAT, and iCare. Significant differences between NTG and healthy were not measured, but there were differences among tonometers in the NTG group, with IOPcc markedly higher than others (Shin, Lee et al. 2015). Authors suggested that, because it does not consider corneal biomechanics, iCare may underestimate IOP values as GAT does in NTG patients. CH positively correlates with rim area and volume, and negatively with C/D ratio. It is also associated with RNFL thickness, VFI, and MD. CRF correlates positively with rim area and is associated with MD and VFI, while CCT positively correlates with rim area and negatively with C/D ratio (Park, Shin et al. 2018).

Dividing NTG patients by CH levels, it was found that the group with lower CH had thinner CCT, lower CRF, lower IOPcc, and thinner RNFL in the inferior quadrant compared to the group with higher CH. No differences were found in the progression of VF damage between groups: two-thirds showed progression in VF damages, while one-third did not. CH showed moderate correlation with CCT and IOPcc, and weak correlation with RNFL thickness (Park, Jun et al. 2015).

In asymmetric NTG, worse eyes have lower CH, lower CRF, and higher IOPcc values. CH and CRF negatively correlate with MD, while the CH-CRF difference positively correlates with MD and IOPcc. A correlation was found between lower IOPcc, higher CH and CRF, smaller C/D ratio, and low MD (Helmy, Leila et al. 2016).

Comparing slow and rapid progression of NTG patients (according to VF changes in the last 3 years), it was found that, compared to the slow progression group, the rapid progression group had lower CH, lower CRF (not statistically significant), higher IOPcc, and higher IOPg. No differences were measured in CCT. Differences in MD, PSD, and VF were significant between the two groups, and the rate of change in MD positively correlated with CH, IOPcc, and the difference between IOPcc and GAT (Hong, Shoji et al. 2016).

1.3.2.2 Corvis ST

Using Corvis ST in asymmetric NTG, worse eyes were associated with lower A1time, A1length, A2length, PD, HCradius, and higher A1velocity and DA. Parameters such as A2time, A2velocity, and HCtime did not show a lack of asymmetry. A1time had a strong correlation with IOP but only a moderate correlation with CCT. Findings suggest that worse eyes are more compliant and easier to deform (Li, Cai et al. 2017).

Between NTG and controls, only A1velocity was statistically higher (0.15 ± 0.02 m/s) than in controls (0.14 ± 0.02 m/s). All other parameters measured by Corvis ST were not significantly different between controls and NTG. The increment of at least 0.01 m/s in A1velocity is 1.15 times more likely in patients with NTG compared to controls (Hong, Wong et al. 2019).

Lower values of A1time, A2time, HCradius, and higher values of PD, DAR1 (ratio between DA on the corneal apex and the mean of two points that are 1 mm lateral to the apex) and Iradius (reciprocal of HCradius) were measured in NTG compared to controls. These values suggest that untreated NTG corneas are softer and more deformable than healthy ones (Miki, Yasukura et al. 2020).

Based on parameters measured by Corvis ST, NTG corneas are softer and more compliant than those in controls, OHT, and POAG (Vinciguerra, Rehman et al. 2020).

1.3.3 Ocular hypertension (OHT)

1.3.3.1 ORA

RF was measured to be significantly higher in OHT than in healthy subjects, and therefore higher than in NTG and POAG. No statistically significant differences were measured in CH between OHT and normal subjects, but values were higher than in NTG and POAG. In a recent paper, after adjusting CH and CRF for age, CCT, and IOP, no significant differences were measured in terms of CH and CRF between OHT and POAG patients. This can be explained because only a minority of OHT patients were receiving treatment to control IOP, which may have misled previous studies with too small and often non-treated samples of OHT patients. (Shah, Laiquzzaman et al. 2008, Grise-Dulac, Saad et al. 2012, Kaushik, Pandav et al. 2012, Nessim, Mollan et al. 2013, Pillunat, Hermann et al. 2016, Murphy, Pokrovskaya et al. 2017).

GAT and IOPg correlate well, with no significant differences between measurements reported. IOPcc was measured to be higher in OHT than in POAG, NTG, and healthy subjects (Grise-Dulac, Saad et al. 2012, Kaushik, Pandav et al. 2012, Nessim, Mollan et al. 2013, Hoccoğlu, Kara et al. 2020). CCT values in OHT were found to be significantly higher than in NTG and POAG, and they correlate positively with CH and CRF (Shah, Laiquzzaman et al. 2008, Nessim, Mollan et al. 2013, Murphy, Pokrovskaya et al. 2017).

In post-PRK patients with steroid-induced ocular hypertension, CH and IOP were measured to be higher than in control (post-PRK patients who used steroids but did not develop OHT), while CRF and CCT were lower than in controls (Yülek, Gerçeker et al. 2015).

1.3.3.2 Corvis ST

Using Corvis ST, GAT and bIOP (biomechanically corrected IOP) were compared: GAT values were higher (5.6 mmHg on average) than in normal, NTG, and POAG subjects. bIOP values were within normal limits (< 21 mmHg), and the mean difference between OHT and controls was 3.6 mmHg. Biomechanical parameters derived from Corvis ST analysis did not show any significant differences between OHT and controls (Vinciguerra, Rehman et al. 2020). The authors suggested that the use of bIOP, which data indicate as a more accurate measure of IOP, may help differentiate between patients with high and low risk of glaucoma progression and VF defect.

High values of CH and CRF in OHT may play a role in preventing the onset of POAG due to the damping effect provided by corneal viscoelasticity in energy dissipation.

1.4 Corneal Biomechanics in Keratoconus

Keratoconus is a progressive corneal ectasia that causes thinning of the cornea and changes in both anterior and posterior curvatures, leading to distorted vision, particularly irregular astigmatism. The thinning results from the degeneration of proteoglycans in the stromal collagen fibrils, which weakens the collagen fibrils, sometimes causing breakage and a reduction in the number of lamellae, whose distribution is already altered. These changes compromise the structure and regularity of the cornea, leading to the formation of a cone shape (Meek, Tuft et al. 2005, Alkanaa, Barsotti et al. 2019).

Keratoconus is currently diagnosed using a combination of tests, including retinoscopy, clinical observation of signs, best-corrected visual acuity, keratometry, aberrometry, topography, and tomography. Older studies emphasised clinical signs, scissor reflex during retinoscopy, and distorted keratometry mires as diagnostic standards, but these methods were more effective at detecting advanced stages of the disease. Today, the introduction of topography and tomography allows for the detection and diagnosis of early stages (Santodomingo-Rubido, Carracedo et al. 2022). Early detection enables prompt intervention with cross-linking, a surgical procedure that increases the rigidity and stability of the corneal tissue by creating new chemical links among collagen molecules within the stroma using riboflavin and UV-A (Santhiago and Randleman 2021).

Measurable changes in corneal biomechanics have been found in several studies using both ORA and Corvis ST.

1.4.1 ORA

Several studies have revealed that corneal hysteresis and corneal resistance factor are lower in eyes with keratoconus compared to normal eyes (Alain, Lteif et al. , Fontes, Ambrósio et al. , Hurmeric, Şahin et al. , Johnson, Myhanh et al. , Kirwan, Donal et al. , Piñero, Alio et al. , Shah, Laiquzzaman et al.). Some authors found that despite statistically significant differences, hysteresis and resistance factor lack the predictive accuracy needed to be used as tools for detecting and diagnosing early stages of the pathology. They argue that biomechanical data are not sensitive or specific enough to detect or diagnose keratoconus on their own but should be integrated into clinical routine (Fontes, Ambrósio et al. , Johnson, Myhanh et al.).

Forme-fruste keratoconus shows significantly lower corneal hysteresis and corneal resistance factor, but the data often overlap with those from normal eyes, preventing clear discrimination between conditions (Johnson, Myhanh et al. , Kirwan, Donal et al.). The same happens with suspected keratoconus (Alain, Lteif et al.). Some studies investigated the diagnostic ability of ORA parameters in detecting keratoconus founding that CH has an AUC of 0.824 (sensitivity 87%, specificity 65%) for mild keratoconus (Fontes, Ambrósio et al. 2010), and an AUC of 0.894 (sensitivity 80.7%, specificity 84.7 %) for frank (clinical) keratoconus (Sedaghat, Momeni-Moghaddam et al. 2018). Although it can be considered a good result, it is lower than index from topographic maps that have an AUC of 0.985 (sensitivity 93.8%, specificity 99.3 %) (Sedaghat, Momeni-Moghaddam et al. 2018).

1.4.2 Corvis ST

In the last 10 years several studies investigated differences in terms of Corvis ST parameters between keratoconus and healthy eyes.

Deformation Amplitude was the parameters that more often showed statistically significative differences, with greater values in eyes with diagnosis of keratoconus (Mercer, Waring et al. , Ye, Yu et al. , Bak-Nielsen, Pedersen et al. 2014, Yang, Xu et al. 2019), although there was some overlap with normal eyes that could complicate detection (Tian, Yifei et al.). Despite this overlap, DA had a good AUROC value (0.770) (Ali, Patel et al.). Other parameters that showed significant differences included the time of the first applanation, the radius at the highest concavity, and the lengths of the first and second applanations. However, these parameters alone did not allow for a diagnosis based entirely on Corvis ST measurements (Peña-garcía, Peris-Martínez et al. , Roghiyeh, Jafarzadehpur et al. , Steinberg, Katz et al. , Ye, Yu et al. , Bak-Nielsen, Pedersen et al. 2014) or for the detection of subclinical stages of keratoconus (Steinberg, Katz et al.).

Since 2016, new indices such as the Cornea Biomechanical Index (CBI) have been introduced, showing excellent capabilities in differentiating pathology from healthy corneas (specificity = 98.4%, sensitivity = 100%) and even detecting subclinical stages (sensitivity = 94.1%, specificity 100%) (Shengwei, Liyan et al. , Vinciguerra, Renato et al.).(Salomão, Hofling-Lima et al. 2018)

SP-A1 is significantly lower in keratoconus (Kaili, Liyan et al. , Mercer, Waring et al. , Shengwei, Liyan et al.) and can be used to detect subclinical stages of the disease (AUC = 0.753) (Abdelgawad, Elnaggar et al. 2024) or forme-fruste from healthy eyes (AUC = 0.927,

sensitivity = 83.4 %, specificity = 100%) (Yang, Qi et al. 2024) and to monitor the progression of the disease (Yu, Yang et al.)

TBI showed high repeatability and great ability in discriminating between normal and keratoconic corneas (Kaili, Liyan et al. , Koç, Aydemir et al.), with a AUC of 0.996 and 100% in terms of sensitivity and specificity for cutoff values of 0.79 (Vinciguerra, Ambrósio et al. 2016).

In terms of repeatability, measurements are generally more repeatable on healthy corneas, but the differences were not statistically significant (Shengwei, Liyan et al. , Ye, Yu et al.).

1.5 General hypothesis

In light of the technological advancements, the use of data from corneal biomechanics gained importance in the clinical setting.

This research project is grounded in the hypothesis that corneal biomechanical parameters — measured using advanced technologies such as the ORA, Corvis ST, and BOSS — provide informative and clinically relevant data that can enhance the early screening of ocular diseases such as keratoconus and glaucoma through supervised machine learning models. However, it is further hypothesized that the presence of coexisting pathological conditions — specifically keratoconus — may act as a confounding factor in the automatic classification of different types of glaucoma, potentially compromising the specificity and accuracy of predictive models.

Moreover, the clinical validity and interpretability of biomechanical parameters are expected to be influenced by interindividual variability related to demographic (e.g., age) and refractive (e.g., myopia, hyperopia) factors. These sources of variability must be accounted for in the design of robust and generalizable diagnostic algorithms. Finally, it is hypothesized that the integration of novel imaging technologies such as BOSS may provide complementary or superior biomechanical measurements compared to established devices, provided that such measurements demonstrate adequate repeatability and show consistent correlations with well-validated biomechanical metrics.

2 Detection of Keratoconus and Primary Open Angle Glaucoma with Machine Learning and Corneal Biomechanics Data

2.1 Introduction

The detection and diagnosis of ocular diseases such as primary open-angle glaucoma (POAG) and keratoconus have significantly advanced due to recent developments in optometric instrumentation, machine learning algorithms and computational resources. POAG, the prevalent form of glaucoma, is characterised by progressive optic neuropathy, leading to irreversible vision loss if not promptly diagnosed and treated. Keratoconus, on the other hand, is a degenerative disorder resulting in thinning and conical deformation of the cornea, causing significant visual impairment. Traditional diagnostic methods for these conditions, while effective, often rely on clinical observations and basic imaging techniques that may not capture the subtle biomechanical changes in the cornea indicative of early disease stages.

This chapter presents a comprehensive analysis of several experiments utilising corneal biomechanics data to improve the detection accuracy of POAG and keratoconus. The corneal biomechanics data used in this study were acquired using the Corvis ST and the Ocular Response Analyzer (ORA).

It is well-documented that both POAG and keratoconus cause distinctive changes in corneal biomechanical properties. For instance, studies using the ORA have shown that keratoconic corneas exhibit altered biomechanical responses, such as reduced corneal hysteresis and corneal resistance factor, compared to healthy corneas (Luce 2005, Shah, Laiquzzaman et al. 2009). Similarly, the Corvis ST has demonstrated that keratoconus is associated with increased corneal deformation amplitude and altered dynamic response parameters (Eliasy, Chen et al. 2019). In the context of POAG, reduced corneal hysteresis measured by the ORA has been associated with the progression of glaucomatous damage (Wells, Garway-Heath et al. 2008, Medeiros, Meira-Freitas et al. 2013), while the Corvis ST can reveal changes during corneal deformation that may be indicative of early glaucomatous alterations (Aoki, Kiuchi et al. 2020).

In recent years, the use of machine learning models has grown dramatically in the fields of optometry and ophthalmology. Techniques have been developed for the early detection of refractive errors and for predicting the future progression of myopia, as well as for refining spectacle prescriptions and contact lens fittings, and for screening tools in strabismus and amblyopia (Krishnan, Dutta et al. 2025) (Alnahedh and Taha 2024). Another application of machine learning is in natural language processing (NLP) for the analysis of patient records to identify patterns that can lead to more efficient and accurate clinical decisions (Santos, Sánchez-Tena et al. 2025).

Ophthalmology, with its heavy reliance on imaging and complex diagnostic procedures, has seen a surge in the application of machine learning for a wide array of conditions. Several applications involve the detection and grading of diabetic retinopathy, particularly through the analysis of standardized fundus images in combination with convolutional neural networks (CNNs) for automatic detection in screening tools, forecasting disease progression, early diagnosis, monitoring treatment, and assisting in overall disease management (Jin and Ye 2022) (Labib, Ghumman et al. 2024).

Machine learning has also been employed to analyse various data from patients with glaucoma, including optical coherence tomography (OCT) scans, visual field plots, and fundoscopic images. In many cases, models have been developed for early glaucoma risk assessment to identify individuals who may benefit from early intervention. The use of machine learning algorithms also reduces intra- and inter-observer bias in diagnosis (Labib, Ghumman et al. 2024). Additionally, machine learning plays a role in the early detection, classification, and progression prediction of AMD (Li, Wang et al. 2023), as well as in cataract detection, pre-operative assessment, and post-surgical recovery monitoring. ML is also used to optimize surgical processes to improve patient outcomes, even though cataract surgery is already a highly successful procedure (Labib, Ghumman et al. 2024).

The primary focus of this research is the application of machine learning algorithms to corneal biomechanics data to develop predictive models for POAG and keratoconus. Machine learning, with its ability to handle large and complex datasets, is particularly suited to identifying patterns and features that may not be apparent through conventional analysis. By training algorithms on labelled datasets of corneal biomechanics measurements, the aim is to create models that can accurately distinguish between healthy eyes and those affected by POAG or keratoconus.

The aim of this experiment is to demonstrate the feasibility and effectiveness of integrating corneal biomechanics data with machine learning algorithms for the detection of primary open-angle glaucoma (POAG) and keratoconus. To this end, six different learning techniques were employed, using two methods of hyperparameter optimization under various experimental conditions (with and without central corneal thickness or IOP).

In summary, this chapter describes the methodology and results of these experiments, introducing a novel approach to ocular disease detection that combines advanced corneal biomechanics measurements with state-of-the-art machine learning techniques. Through this research, the ultimate goal is to improve diagnostic accuracy and patient outcomes for POAG and keratoconus. To the best of the authors' knowledge, this marks the first attempt to (1) employ machine learning on data from the ORA to detect keratoconus and POAG, (2) compare the performance of the ORA and Corvis ST, and (3) train and test a broad range of supervised learning algorithms.

2.2 Material and Methods

2.2.1 Basic concept in machine learning

Some of the concepts introduced in this chapter might not be very familiar to a clinician, so here are the most common terms used:

- **Model:** A mathematical representation of a real-world condition, it is created using data to train an algorithm. It can be used to make predictions in classification or regression.
- **Learner (algorithm):** A mathematical function that builds the model learning from the data.
- **Hyperparameters:** A set of one or more parameters that drive the learning process, assigning weights and penalties to the data.
- **Training set:** A portion of the entire dataset used to train the learner, usually between 70% and 90% of the data.
- **Test set:** The remaining part of the dataset, used to test the performance of the learner, typically between 10% and 30% of the original dataset. The learner is not trained on this portion of the data; otherwise, performance measurements would not be accurate as the learner would already know the data, and might have a perfect score, not reflecting the performances on real-world data.

- **Underfitting:** Occurs when the learning rate is poor and not generalisable. The model is too simple, does not capture the patterns and has poor performance.
- **Overfitting:** Occurs when the learning is too specific; the model perfectly mimics the dataset but is not generalisable because it is influenced by the noise (random variations or errors) in the data. Usually, performance on the training data is excellent, but it might be poor when tested on unseen data.
- **Instances:** Individual samples from which the model learns. Each instance is represented by a set of features. In this chapter, the instances are the eyes of the patients.
- **Features:** The data (properties or characteristics) associated with each instance. These are used as input to the model. In this chapter, they are the clinical measurements of the eyes.
- **Labels (target):** The output variable that the model predicts. Each instance is associated with a label that the model uses to classify data. In this chapter the label is the diagnosis (normal, keratoconus or POAG).

The purpose of this chapter is to create a machine learning model using several supervised learning algorithms to detect cases of keratoconus and primary open-angle glaucoma from healthy eyes. The model searches for the optimal hyperparameters during training on the training set and then, once identified, is tested on the test set. Among all the learners, the one with the best performance on the test set is analysed to determine the importance of each feature.

The general version of the code can be found in Appendix 11.1

The code developed follows the following structure:

- 1) Load of the libraries needed to execute the code.
- 2) Definition of the metrics to evaluate the models' performances:
 - a. Accuracy, F1, precision, AUROC, confusion matrix, sensitivity and specificity
- 3) Load the dataset:
 - a. Creation of the train and test set.
- 4) Definition of the algorithms used in the models:
 - a. Naïve Bayes, Logistic Regression, Support Vector Machine, Decision Tree, Random Forest, Multi-Layer Perceptron Classifier.
- 5) Definition of the cycle to run the models:
 - a. Hyperparameter tuning with GridSearch and RandomSearch.

- 6) Selection of the model with highest performances (AUC).
- 7) Run of the best model on the Test set.
- 8) Interpretation of the best model:
 - a. Permutation Feature Importance
 - b. SHAP.

2.2.1.1 Dataset

The dataset was provided by Professors Naroo and Shah and consists of anonymized data collected by Dr. Haslina during her PhD. Data were collected at the corneal and glaucoma clinics of the Birmingham and Midland Eye Centre, City Hospital, Birmingham, where patients already diagnosed with keratoconus or glaucoma were selected by an independent ophthalmologist for inclusion in the study. Further classification based on disease severity was not possible, as no topographies, anterior segment images, clinical records, OCT scans, visual field data, or fundus photographs were included in the dataset. Moreover, because the dataset was fully anonymised it was impossible to retrieve patient detail or access their clinical records. The current analysis extends the work conducted by Dr Haslina, who initially examined differences in corneal biomechanics across various conditions. Because the size of the dataset varies among experimental groups, it is summarized in Table 2.1. Since all data were already collected and available, no formal sample size calculation was conducted. Instead, it followed the principle that a larger sample more accurately represents the diversity of the condition, and therefore yields more robust results (Althnian, ALSaeed et al. 2021).

Table 2.1 Size of datasets used for the current experiment.

	Condition (KC/POAG)	Normal
KC_ORA	86	333
KC_Corvis ST	114	365
POAG_ORA	92	314
POAG_Corvis ST	167	314

POAG_GAT	172	314
----------	-----	-----

Corneal parameters measured with ORA included central cornea thickness using an ultrasound probe (CCT.US), corneal compensated IOP (IOPcc), Goldmann-correlated IOP (IOPg), corneal hysteresis (CH), and corneal resistance factor (CRF). Parameters measured using Corvis ST were velocity at the first applanation (A1velocity), length of first applanation (A1length), time of the first applanation (A1time), velocity at the second applanation (A2velocity), length of second applanation (A2length), time of the second applanation (A2time), time of highest concavity (HCtime), highest concavity radius (HCradius), highest concavity peak distance (HCpeak.distance), highest concavity deformation amplitude (HCdef.amplitude), central corneal thickness measured using the Scheimpflug camera (CCTcor), and IOP (IOPcor). Only instances with all features measured by an instrument were considered.

From the initial database, two different datasets were created, one per experiment. In the first dataset (normal and keratoconus), there were data from ORA and Corvis ST. In the second dataset (normal and POAG), there were measures from GAT, ORA, and POAG. Each dataset was further divided into two separate sets: the training set (80%) and the test set (20%). The training and test sets were stratified to ensure proportional representation of both classes. This step is crucial to avoid circularity, ensuring models are tested on data not used for training, thereby avoiding overly optimistic results that would not generalise to new real-world data.

The significance of corneal thickness in keratoconus detection is well established (Ahmadi Hosseini, Mohidin et al. 2013), and it has also been shown to function as a confounding factor for CH and CRF (Galletti, Pfortner et al. 2012). Accordingly, four experimental conditions were tested in this study: (1) Corvis ST data including corneal thickness, (2) Corvis ST data excluding corneal thickness, (3) ORA data including corneal thickness, and (4) ORA data excluding corneal thickness. Given the recognised importance of corneal thickness as a potential confounding variable, the models were evaluated both with and without this parameter in the training and test sets. It is hypothesized that omitting corneal thickness from the dataset may reduce the accuracy of keratoconus detection.

For the glaucoma experiment, ten different conditions were tested: Corvis ST data including IOP and corneal thickness, Corvis ST data including IOP but excluding corneal thickness, Corvis ST data including corneal thickness but excluding IOP, Corvis ST data excluding

corneal thickness and IOP, ORA data including corneal thickness and IOPs, ORA data including corneal thickness but excluding IOPs, ORA data including IOPs but excluding corneal thickness, ORA data excluding both IOP and corneal thickness, GAT and corneal thickness data, and GAT alone. This approach was chosen because IOP impacts POAG diagnosis, and corneal thickness data might help determine whether high IOP is due to the cornea.

2.2.2 Libraries

The creation of the model to detect keratoconus and glaucoma was coded in Python using the JupyterLab environment and several libraries: pandas, numpy, matplotlib, seaborn, and scikit-learn. Pandas is a library designed to handle and analyse data and datasets; it is commonly used to load, clean, and preprocess data. Numpy is designed for mathematical operations, scientific calculations, and data transformation. Matplotlib and seaborn are used to create graphs and visualise results. Scikit-learn is a machine learning library built on numpy, pandas, and matplotlib; it stores algorithms and tools to optimise their performance for classification, regression, clustering, dimensionality reduction, and model selection tasks.

2.2.3 Metrics

To evaluate the performances of each algorithm, several metrics were used:

- Confusion matrix: this is a table that allows the visualisation the performances of a model's classification. It is based on the following data:
 - TP: True Positive, the condition is present and is correctly identified by the model.
 - TN: True Negative, the condition is not present, and the model does not detect the condition.
 - FP: False Positive, the model identifies the condition, even if it is not present.
 - FN: False Negative, the model does not detect the condition, that is present.

	Positive prediction	Negative Prediction
Positive condition	TP	FN
Negative condition	FP	TN

Using this matrix, it is possible to calculate several metrics to evaluate performance:

- **Accuracy:** is defined as the ratio between the sum of TP and TN and the total number of cases.

$$Accuracy = \frac{TP + TN}{TP + TN + FP + FN}$$

- **Precision:** is the ratio between the TP and all the positive outcomes

$$Precision = \frac{TP}{TP + FP}$$

- **Sensitivity (Recall):** is the ratio between TP and the total of positives (TP and FN). It represents the ability of the model of detecting the positive instances.

$$Sensitivity = \frac{TP}{TP + FN}$$

- **Specificity:** is the ratio between TN and the total of negative (TN and FP). It is the ability of the model of detecting the negative instances.

$$Specificity = \frac{TN}{TN + FP}$$

- **F1:** is the harmonic mean of precision and sensitivity. It is useful for unbalanced classes.

$$F1 = 2 \times \frac{Precision \times Sensitivity}{Precision + Sensitivity}$$

- **AUROC:** is the Area Under the Receiver Operative Characteristics Curve. It is a measure of the quality of prediction of a classifier. It is plotted as the function of 1 – Specificity on the x axis and Sensitivity on the y axis. The higher the AUROC value, the better the model's performance: a value of 1 indicates a perfect classifier, while a value of 0.5 indicates a random classifier.

2.2.4 Algorithms

Several supervised learning algorithms have been used in this experiment. The following list explore them with a basic mathematical description about the working principles.

The following algorithms were selected because they are among the most frequently used in supervised machine learning research (Raju, Manasa et al. 2023). K-nearest neighbors (KNN) was excluded because it relies on instance-based learning rather than a standard learning method. In KNN, each classification task requires calculating the distance between the test instance and each of the training instances, rendering the algorithm less efficient on large datasets, not readily scalable, and more demanding in terms of computational resources (Taunk, De et al. 2019). XGBoost and AdaBoost were also omitted, as they involve ensemble learning—a technique that combines multiple algorithms and lies beyond the scope of this study.

2.2.4.1 Naïve Bayes

It is based on Bayes' theorem of conditional probability, assuming that features are independent (naïve) of each other. This assumption simplifies the calculations. Bayes' theorem allows us to calculate the probability that a hypothesis is true given a set of conditions. The theorem states that:

$$P(H|E) = \frac{P(E|H) \cdot P(H)}{P(E)}$$

Eq. 2.1 Bayes' Theorem of conditional probability

Where $P(H|E)$ is the probability of hypothesis H considering that E has been observed, $P(E|H)$ is the probability of observing E if H is true, $P(H)$ is the a priori probability of hypothesis H and $P(E)$ is the probability observing E . For this experiment, the Gaussian variant of Naïve Bayes was used, as the features are continuous variables.

For classification purposes, Naïve Bayes calculates the probability that an instance belongs to any of the classes and then assigns the instance to the class with the highest probability. It is one of the simplest algorithms for classification, as it does not have any hyperparameters to tune and is computationally efficient even with large datasets containing several features. The effectiveness of Naïve Bayes decreases when the features are not independent of each other.

2.2.4.2 Logistic Regression

It is a linear algorithm that calculates the probability that an instance belongs to a class. It performs well when used for binary classification. The output is a number between 0 and 1, which can be converted into the prediction of belonging to one class or another. The usual

threshold is 0.5 (above it is assigned to class 1, below to class 0). The probability is calculated considering the features of the dataset ($X = (x_1, x_2, \dots, x_n)$). These features are combined in a linear function:

$$z = \beta_0 + \beta_1 x_1 + \beta_2 x_2 + \dots + \beta_n x_n$$

Eq. 2.2 Linear Combination of Independent Variables before applying Logistic Sigmoid Function

Where β are the coefficients of the model. Using the sigmoid function:

$$\sigma(z) = \frac{1}{1 + e^{-z}}$$

Eq. 2.3 Sigmoid Function for Linear Regression

it is possible to calculate a probability (p), between 0 and 1. The function $\sigma(z)$ approaches 0 when z is toward $-\infty$ (since the denominator becomes very large, making the fraction approach 0), and approaches 1 as z approaches $+\infty$ (since the denominator approaches 1, making the fraction approach 1). Once the probability is calculated, it is possible to classify the instance according to the set threshold (usually 0.5), attributing it to class 0 or 1.

During the training the goal is to find the β coefficients that minimise the differences between the calculated probabilities and the real labels. This is achieved using the logistic cost function:

$$J(\beta) = -\frac{1}{m} \sum_{i=1}^m [y_i \log(p_i) + (1 - y_i) \log(1 - p_i)]$$

Eq. 2.4 Logistic Cost Function

Where m is the number of the instances in the dataset, y_i is the label of the i -th and p_i is the probability calculated of the i -th instance. The cost function measures the fit of the model to the data. Minimisation of the cost function is performed through the gradient descent algorithm, which iteratively updates the parameters of the model:

$$\beta = \beta - \alpha \nabla J(\beta)$$

Eq. 2.5 Gradient Descent Algorithm

Where α is the learning rate and $\nabla J(\beta)$ is the gradient of the β function.

To avoid overfitting, regularisation can be introduced in logistic regression. There are two types of regularisation:

- **L2 or Ridge Regularisation**, this transforms the cost function $J(\beta)$ into:

$$J(\beta) = \frac{-1}{m} \sum_{i=1}^m [y_i \log(p_i) + (1 - y_i) \log(1 - p_i)] + \frac{\lambda}{2m} \sum_{j=1}^n \beta_j^2$$

Eq. 2.6 Ridge Regularisation

- **L1 or Lasso Regularisation**, this transforms the cost function $J(\beta)$ into:

$$J(\beta) = \frac{-1}{m} \sum_{i=1}^m [y_i \log(p_i) + (1 - y_i) \log(1 - p_i)] + \frac{\lambda}{m} \sum_{j=1}^n |\beta_j|$$

Eq. 2.7 Lasso Regularisation

Where λ is the regularisation strength (often known as C), which controls the penalisation on the parameters to make the model simpler to avoid overfitting. The division by m or $2m$ normalises the penalisation based on the total number of instances, n is the number of the features of the model and β_j is the value of the j -th feature.

Ridge regularisation penalises the sum of the squares of the coefficients, reducing the importance of features with higher values but keeping all β parameters in the model, even if with very small values. This is useful if all the features have some importance, and it can reduce the impact of features with multicollinearity.

Lasso regularisation penalises the sum of the absolute values of the coefficients, potentially bringing some coefficients to zero and excluding some features, thus automatically selecting variables. This is useful when there are many features, some of which might be irrelevant. Lasso typically creates simpler models with fewer features.

The functions that manage the minimisation of the cost function are called solvers. In the scikit-learn library that runs logistic regression in Python, there are four different solvers:

- **liblinear**: Uses coordinate descent to optimise the cost function, supports both L1 and L2 regularisation, and is particularly efficient for small and medium-sized datasets.
- **newton-cg**: Uses the Newton-conjugate gradient and supports L2 regularisation only. It is used for datasets with high dimensionality. The Newton-conjugate gradient combines the Newton method (using both first and second derivatives, the Hessian matrix) and the conjugate gradient, which does not require the inversion of the Hessian matrix.

- **Lbfgs**: Uses the Limited-memory Broyden-Fletcher-Goldfarb-Shanno algorithm and supports L2 regularisation only. It does not keep the entire approximation matrix of the Hessian in memory but saves a limited series of updated vectors from recent iterations. It is particularly efficient and useful for large datasets.
- **saga**: Uses Stochastic Average Gradient algorithm and supports both L1 and L2. It combines the advantages of Stochastic Gradient Descent (updating the parameters of the model using a single example per time) and Batch Gradient Descent (calculates the gradient using the entire dataset), minimising the noise (errors or random variability in data) and improving the velocity of convergence (the optimisation process to get to a stable solution, that corresponds to the minimum of the cost function). It calculates the partial gradients, then the average and update them.

Logistic regression is a powerful classifier that works well with linear data and calculates the probability of belonging to a class. It is quite easy to interpret (Osl, Baumgartner et al. 2008), typically exhibits low variance, and is less prone to overfitting (Westreich, Lessler et al. 2010). Its main limitations are the assumption of linearity between model features and the susceptibility to imbalanced data, where the class distribution is not uniform (Abd Rahman and Yap 2016).

2.2.4.3 Support Vector Machine (SVM)

It is an algorithm that creates separation hyperplanes in the data space to efficiently separate data belonging to different classes. In a bidimensional space (two features describing the instance), the hyperplane is a line. In a three-dimensional space (three features), it is a plane. In datasets with higher dimensionality (more than three features), it is called a hyperplane and cannot be visualised. The main goal of SVM is to maximise the margins between the separation plane and the closest training instances. Maximising the decision boundaries minimises generalisation errors in classification tasks.

The support vectors are the data points (instances) on the boundaries that guide the position, shape, and structure of the hyperplanes. SVM only uses these data points, ignoring the others.

Considering a hyperplane described by the following equation:

$$w \cdot x - b = 0$$

Eq. 2.8 SVM Hyperplane Formula

Where w is the vector of the coefficients, b is the bias and x is the feature. The goal is to find the values of w and b that maximise the margins. Considering a support vector per class, one with label +1 and one with label -1, the hyperplanes become:

$$w \cdot x_+ - b = 1$$

$$w \cdot x_- - b = -1$$

It can be easily demonstrated that the margin width is $\frac{2}{\|w\|}$, where $\|w\|$ is the norm of the vector w (it represents the length of the vector). The goal is to maximise $\frac{2}{\|w\|}$ minimising $\frac{1}{2}\|w\|^2$. The rationale behind is that ensures that all the instances of one class fall on one side of the hyperplane and all the instances of the other class fall on the opposite side. This concept can be expressed through the following formula:

$$y_i(w \cdot x_i - b) \geq 1 \quad \forall i$$

Eq. 2.9 Condition to have the hyperplane with the widest margin possible for data separation

Where y_i is the label of the class [+1; -1] for a binary classification of the i -th feature; $(w \cdot x_i)$ is the scalar product between w and the i -th feature and represents the projection of the data point x_i on the hyperplane defined by w , and $\forall i$ is the condition that must be true for all the i considered.

If data cannot be perfectly separated, it is possible to consider an error introduced by slack variables (ξ_i), so the generalised formula becomes:

$$\frac{1}{2}\|w\|^2 + C \sum_{i=1}^n \xi_i$$

$$y_i(w \cdot x_i - b) \geq 1 - \xi_i \quad \forall i$$

$$\xi_i \geq 0 \quad \forall i$$

Eq. 2.10 Conditions for data not linearly separable

Where C is the regularisation parameter that controls the penalisation for misclassification and is one of the hyperparameters that can be tuned in SVM. Another hyperparameter is the

kernel, which transforms data into a higher-dimensional space to make data linearly separable. There are four different kernels in SVM:

- **Linear Kernel:** add the dot product of the vectors in the original space. It is commonly used when data are already linearly separable.

$$K(x_i, x_j) = x_i \cdot x_j$$

- **Polynomial Kernel:** expands the dimensionality with a large number of variables to overcome data that are not linearly separable. c is a constant and d is the degree of the polynomial.

$$K(x_i, x_j) = (x_i \cdot x_j + c)^d$$

- **Radial Basis Function (RBF) Kernel:** is the default kernel of SVM, widely used for non-linearly separable data. The parameter γ determines the amplitude of the function. A high value of γ decreases the effect of a single instance on the model, increasing the risk of overfitting. Conversely, a low value of γ makes the model more influenced by single instances, increasing the risk of underfitting. It can be set to "auto" (reciprocal of the number of features), "scale" (considering the variance and number of features), or a fixed number.

$$K(x_i, x_j) = e^{(-\gamma|x_i-x_j|)^2}$$

- **Sigmoid Kernel:** is not commonly used, it mimics the sigmoid activation function of neural networks, making it useful for non-linearly separable data. α controls the slope of the sigmoid function and c shifts the function along the x-axis.

$$K(x_i, x_j) = \tanh(\alpha x_i \cdot x_j + c)$$

SVM main advantages are its strong statistical foundations that allow for generalisation even with limited training datasets (Hearst, Dumais et al. 1998), its effectiveness with high-dimensional data spaces (Moguerza and Muñoz 2006) and the ability to use kernels to adapt to different types of data, even detecting non-linearly separable data without complex transformations (Steinwart and Christmann 2008). However, results can be difficult to interpret, especially for high-dimensional datasets (Navia-Vazquez, Gutierrez-Gonzalez et al. 2006). SVMs are not highly scalable and large datasets may require significant computational power (Suthaharan, Suthaharan et al. 2016). Additionally, choosing the right kernel can be challenging (Yang, Wu et al. 2004)

2.2.4.4 Decision Tree

It is a supervised learning algorithm used for both classification and regression. It has a tree structure: it starts from the root node, choosing the feature that best separates the classes. The root node contains the entire dataset, and all following nodes contain subsets of the initial dataset. These decisions are made using either the Gini index or entropy. The Gini index measures the impurity of the split: if all points belong to the same class, the split is pure (p_i is the proportion of elements that belong to the class i).

$$Gini = 1 - \sum_{i=1}^n p_i^2$$

Eq. 2.11 Gini Index

Entropy is a measure of the disorder at a split or its uncertainty. It is defined by the following formula:

$$Entropy = - \sum_{i=1}^n p_i \log_2 (p_i)$$

Eq. 2.12 Entropy index

After selecting the best feature to divide the data, the data is split accordingly, creating two branches (if it is a binary tree) leading to two new nodes. Each node represents a decision based on a single feature. This process is repeated for each node, each time choosing the best feature to separate the remaining data. The algorithm stops when one of these conditions is met:

- Reaches the maximum number of levels (max depth).
- All the instances in a node belong to the same class, forming leaves or terminal nodes.
- Further splitting does not improve the classification performances.

The other hyperparameters that can be tuned are:

- **Splitter**: choose between "best" (the feature that best splits the remaining instances) and "random" (the feature is selected randomly). A random choice can avoid overfitting but might reduce model performance.
- **Maximum depth**: the maximum depth of the tree. Limiting the depth prevents overfitting, but a too shallow tree might underfit.

- **Minimum samples per split:** sets the minimum number of instances required to split a node. It can be an integer or a float (percentage of total samples). If a node has fewer samples than the minimum required, it is not split and becomes a leaf node. Preventing splits with very few samples reduces overfitting and makes the model more generalisable.
- **Minimum samples per leaf:** Sets the minimum number of samples required to form a leaf. If a split results in a leaf with fewer samples than the minimum, the split is discarded, and the node is not split again. A high value for this parameter avoids overfitting, while a lower value may lead to underfitting.

The main advantages of decision trees are their interpretability and visualisation, even for people without a background in data science or statistics. The tree maps are immediate and easy to understand (Safavian, Landgrebe et al. 1991). Decision trees can easily handle non-linear relationships, analyse smaller data spaces, and do not require data transformation or preprocessing (Swain and Hauska 1977, Sethi 1997).

On the downside, the risk of overfitting is quite high, and strategies must be used to avoid creating a model that is not generalisable (Hashemi, Yang et al. 2008). Decision trees are also highly sensitive to small variations in the dataset, which can lead to completely different tree maps. This problem can be mitigated using ensemble learning models (such as random forests). Additionally, decision trees do not handle large datasets with a high number of features well, as they require significant computational power (Pal and Mather 2002, Yu, Zhong-liang et al. 2009).

2.2.4.5 Random Forest

Random Forest is an ensemble learning algorithm based on multiple decision trees (estimators), merged to provide more accurate and stable predictions. Instead of selecting the most important feature to divide the dataset, each tree works on a portion of the dataset and uses a random subset of features to find the best threshold to separate the data (this process is called bootstrap sampling). Consequently, many trees are trained in a weak manner, each specialising in a small portion of the dataset. Once all the trees have been built, the algorithm aggregates the predictions. For classification, the aggregation process is based on majority vote: each tree makes an independent prediction for a sample, and the class that receives the majority of votes is chosen as the final prediction.

Therefore, the number of trees is crucial for Random Forest performance: too few trees result in poor performance, while too many trees require high computational power. All the other hyperparameters considered in a Decision Tree are present as well, except for the splitter, with the separation criterion being Gini by default. The number of randomly selected features is by default the square root of the total number of features.

The hyperparameters that can be set are:

- **Number of estimators:** is the number of trees build.
- **Maximum depth:** is the maximum depth that each tree can get.
- **Minimum samples per split:** set the minimum number of instances to split a node.
- **Minimum samples per leaf:** set the minimum number of samples to form a leaf.

The main advantages of Random Forest are its ability to manage high-dimensional datasets and its robustness to noise and overfitting, which overcomes the main disadvantages of Decision Trees (Scornet, Biau et al. 2015). On the other hand, the models tend to be more complex and less interpretable than Decision Trees, and a high number of estimators requires significant computational power and time, especially for larger datasets (Breiman 2001, Genuer, Poggi et al. 2010).

2.2.4.6 Multi-Layer Perceptron Classifier (MLP)

MLP (Multilayer Perceptron) is a type of artificial neural network used in supervised learning classification tasks. Like any other neural network, it consists of nodes (neurons). The particularity of MLP is that neurons are organised in multiple layers, with each layer connected to both the previous and the following ones. The typical architecture of an MLP includes:

- **Input Layer:** each neuron in the input layer represents a feature of the dataset.
- **Hidden Layer(s):** There can be one or more hidden layers (in which case it is called a deep neural network). Each layer consists of multiple neurons that process the input, extract features, and pass the information to the output layer. Each neuron applies a weighted sum, adds bias, and then applies an activation function.
- **Output layer:** it has one layer per class to produce the prediction.

It is possible to identify three main steps in the MLP functions:

- 1) **Forward Propagation:** After the input layer receives the data, the information is passed to the hidden layer. The input values are multiplied by the associated weights, summed together, and bias is added. The results pass through a non-linear activation function to avoid linearity within the network. Considering two neurons (i, j) in two different layers the function is:

$$a_j = f\left(\sum_{i=1}^n w_{ij} x_i + b_j\right)$$

Eq. 2.13 Neuron Output for MLP Classifier

Where a_j is the output of the neuron j ; w_{ij} are the weight that connect the neuron i to the neuron j ; x_i are the input values, b_j is the bias of the neuron j ; f is the activation function. This process is repeated for all neurons in the hidden layers. After the last hidden layer, the outputs pass through the output layer, where each neuron represents a class. For binary classification, the output layer will have one neuron that quantifies the probability of belonging to the positive class. Neurons in the output layer use a softmax activation function, while a sigmoid function is used for binary classification. In the output layer, the argument of the function is called z (the input to the output neuron) and is used to calculate the probability σ .

$$z = \sum_{j=1}^n w_j a_j + b_j$$

Eq. 2.14 Input to Output neuron

$$\sigma(z) = \frac{1}{1 + e^{-(\sum_j w_j a_j + b_j)}}$$

Eq. 2.15 Function to calculate probability

- 2) **Loss Calculation:** The next step is to calculate the error of the prediction compared to the actual labels. The categorical cross-entropy loss function is used, defined as:

$$L = - \sum_{i=1}^N \sum_{k=1}^M y_{ik} \log(o_{ik})$$

Eq. 2.16 Loss Calculation

Where N is the number of the samples, M is the number of the classes, y_{ik} is a binary indicator (0; 1) if label (k) is correct or not the i -th example, o_{ik} is the predicted probability to belong to class k .

- 3) **Backpropagation:** This process updates the weights of the network to reduce and minimise the loss. The loss function is used to calculate the gradient for each weight in the network:

$$\frac{\delta L}{\delta z_j} = o - y$$

Where o is the predicted label and y is the true label. The weights are adjusted in the opposite direction of the gradient:

$$\delta_j = \frac{\delta L}{\delta z_j} = \left(\sum_k \delta_k w_{jk} \right) f'(z_j)$$

Eq. 2.17 Loss Gradient

Where δ_k is the loss gradient with respect to the output of the neuron k in the following layer, w_{jk} is the weight between neuron j and k and $f'(z_j)$ is the derivative of the activation function applied to z_j . The weights are updated using the calculated gradients:

$$w_{ij}^{new} = w_{ij} - \eta \frac{\delta L}{\delta w_{ij}}$$

Eq. 2.18 Weight Update Function

Where η is the learning rate that controls the update.

This whole process is controlled by the optimisation algorithm, which iteratively updates the weights to minimise the loss function until convergence is reached.

The hyperparameters that can be set are:

- **Hidden layer size:** the number of neurons in the hidden layer. In this experiment a maximum of two layers was set.
- **Activation function of neurons in the hidden layers:**
 - o **Rectified Linear Unit (relu):** this whole process is controlled by the optimisation algorithm, which iteratively updates the weights to minimise the loss function until convergence is reached.
 - o **Hyperbolic tangent (tanh):** maps input values between -1 and 1, centring data around 0, which might improve learning. Gradients might vanish in deep networks, causing some neurons not to activate.
 - o **Logistic:** maps input values between 0 and 1. The output can be interpreted binarily but may not be efficient in deep networks.

- **Identity**: does not transform the input, commonly used for regression tasks.
- **Solver**: the optimisation algorithm
 - **Adaptive moment estimation (adam)**: calculates adaptive learning rates for all parameters. It quickly converges, especially with high noise and complex optimisation but might be computationally expensive.
 - **Stochastic Gradient Descent**: updates the weights using the gradient of the loss function on single instances or small batches. It is computationally efficient but may be slow if the learning rate is not optimised.
- **Learning rate**: sets the initial value of the learning rate
- **Maximum number of iterations**: the maximum number of iterations (epochs) for the optimisation algorithm.

Despite the flexibility of the MLP Classifier in managing complex non-linear relationships and providing high performance compared to other classifiers (Windeatt 2008, Bonaccorso 2018, Raschka and Mirjalili 2019), it has some drawbacks. Tuning hyperparameters can be time-consuming and computationally expensive (Windeatt 2006, Windeatt 2008) and if there is insufficient data, the model might overfit (training that does not generalise to real-world data due to extensive recursive iterations between layers) (Chi 1995).

2.2.5 Learning and hyperparameter tuning

The hyperparameter tuning was carried out using two different techniques: GridSearch (GridSearchCV in the scikit-learn library) and RandomSearch (RandomizedSearchCV in the scikit-learn library). GridSearchCV creates a grid with all possible combinations of hyperparameters and then calculates the learning performance, in terms of AUROC, for each combination. RandomizedSearchCV tries a fixed number (50 in this experiment) of random combinations of hyperparameters, being computationally less expensive than GridSearchCV.

The rationale behind RandomSearch is that only a fraction of the hyperparameters significantly impact the algorithm's performance. Therefore, it can be inefficient to try all combinations, as many will likely yield similar or poor results (e.g., very high or very low values of the cost function). This is especially true in contexts with a high number of hyperparameters. RandomSearch is equally effective with no computational restriction, and it has been shown that, given the same computational budget as GridSearch, RandomSearch tends to find better patterns due to its ability to explore a larger, less

promising configuration space effectively, avoiding the rigidity of the default grid (Bergstra and Bengio 2012).

Learning occurs using cross-validation techniques: the whole dataset is divided into a fixed number of folds (k). The folds are stratified to maintain the proportion between classes. A cycle runs k times, and during each run, the algorithm learns from $k-1$ folds and is tested on the fold left out. Using this approach, the model is tested each time on unseen data, avoiding overfitting and confounding results. The AUROC of each run is stored, and the performance is expressed as the average of all the runs.

2.2.6 Test

The best configuration of hyperparameters was then tested on the test set. The label assigned by each algorithm was compared with the actual label, the confusion matrix was computed, and all the previously described metrics were calculated. The learner with the highest AUROC on the test set was chosen as the best algorithm. Feature importance was then assessed using Permutation Feature Importance and SHAP values.

2.2.7 Permutation Feature Importance (PFI)

It is a technique that provides information about the importance of each variable in the model. Once the model has been trained and tested, it is run again on the test set, but this time the values of a specific feature are randomly shuffled. This process breaks the relationship between the feature and the output label, while the other variables remain unchanged. The importance of each feature is calculated as the difference in terms of performance (AUROC) between the original run on the test set and the new run with the shuffled feature. This operation is repeated for all the features. A positive score indicates that the shuffling lowered the performance by the amount specified by the value, while a score very close to zero indicates that the feature has low importance, ideally a negative result may occur, implying that the shuffle improved the performance of the model. It is important to note that Permutation Feature Importance (PFI) does not provide information about the direction of the contribution of each variable, but only about the importance of the feature to the model (Altmann, Toloşi et al. 2010).

2.2.8 Shapley Additive exPlanations (SHAP)

It is an advanced and novel method to explain the predictions of machine learning models. It is based on Shapley values, derived from game theory. SHAP values represent the contribution of each individual feature to the final prediction (Nohara, Matsumoto et al. 2022). SHAP values are computed by considering the marginal contribution of each feature's value to the outcome. This is determined by altering the feature's value and evaluating the change in the prediction.

A pool of instances from the test set is passed through SHAP, which determines both the importance and the direction of each feature in the final prediction for each instance. In this sense, SHAP analysis provides local explanations but can be useful to identify trends in the prediction and determine the contribution of a single feature. After calculating SHAP values, two different outputs were created:

Bar Graph: This graph represents the impact of each feature on the output. Data are divided by class and ranked vertically, with the most important feature at the top. The horizontal axis represents the absolute scale of the SHAP value: the higher the SHAP value, the greater the impact of the feature on the outcome. It is important to note that this analysis does not provide information about the direction of the outcome, only about the importance of the feature for the model. The data are aggregated, so it is not possible to analyse individual instances or features.

Scatterplot: On the vertical axis features are ranked by their importance (the same rank as in the bar graph). The horizontal axis represents the SHAP values, indicating the impact of that feature on the prediction. Each analysed instance is plotted as a coloured dot, where the colour depends on the value of the feature (high is red, low is blue). Points are distributed along the horizontal axis according to the impact and the direction of the prediction. This graph is analysed for one class only; for the other class, the value is the same but in the opposite direction (the graph is reversed).

SHAP values analysis is particularly useful as it can be applied to all learners tested in this experiment. However, it is computationally expensive, especially for complex models with high dimensionality and large datasets. Moreover, interpreting the results of SHAP is not immediate or precise and can only provide a trend. It is also quite sensitive to outliers. For all these reasons SHAP graphs provide an overall representation of the trends, but nothing too specific.

2.3 Results

Results of all the learners are in Appendix 11.2. Only the single algorithm that works best for each experimental condition is discussed in this section.

2.3.1 Keratoconus

Results on test set for KC models are listed in Table 2.2

Table 2.2 Performances of the models on Keratoconus detection

Algorithm	CST_CCT	CST_noCCT	ORA_CCT	ORA_noCCT
NaiveBayes_grid	0.957	0.945	0.947	0.894
LogisticRegression_random	0.977	0.952	0.904	0.842
LogisticRegression_grid	0.977	0.971	0.905	0.845
SVM_random	0.990	0.983	–	–
SVM_grid	0.987	0.985	–	–
DecisionTree_random	0.917	0.938	0.824	0.767
DecisionTree_grid	0.921	0.938	0.828	0.758
RandomForest_random	0.980	0.977	0.829	0.782
RandomForest_grid	0.980	0.983	0.828	0.766
MLPClassifier_random	0.975	0.984	0.845	0.718
MLPClassifier_grid	0.970	0.946	0.904	0.772

2.3.1.1 Corvis ST

2.3.1.1.1 Corvis ST including Central Corneal Thickness.

The algorithm with the best AUROC on the test set was SVM with Random Search ($C = 4.60$, $\gamma = \text{auto}$, kernel = rbf, AUROC = 0.990, with a sensitivity of 0.870 and specificity of 0.959), which can be considered exceptionally good. The performance on the test set was excellent for all the learners, which reached AUROC values above 0.91. Compared to the learning score (the average AUROC at the end of cross-validation), all the algorithms exhibited better performance on the test set. The learner with the best score during training was Random Forest with GridSearch (AUROC 0.962).

Analysing the performance of the SVM with Random Search using PFI, it is evident that the most important feature for the model is the radius at highest concavity (HCradius, 0.10 ± 0.02), while corneal thickness (CCTcor, 0.03 ± 0.01) is the second most important feature.

This finding is confirmed by the SHAP bar graph. The scatter plot shows that a lower value of HCradius is typical in keratoconic eyes, as well as a reduced corneal thickness.

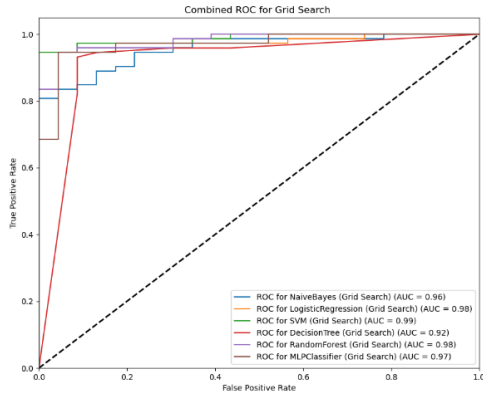


Figure 2.1 ROC Curves for Grid Search, Corvis ST including CCT in KC detection

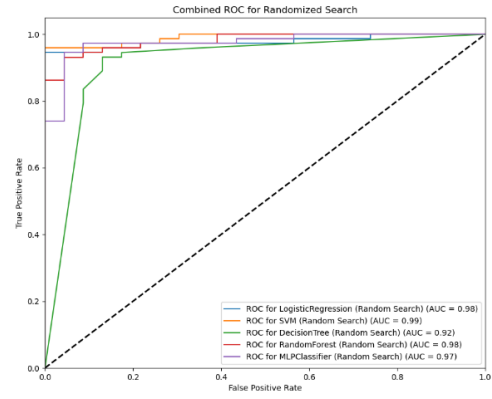


Figure 2.2 ROC Curves for Random Search, Corvis ST including CCT in KC detection

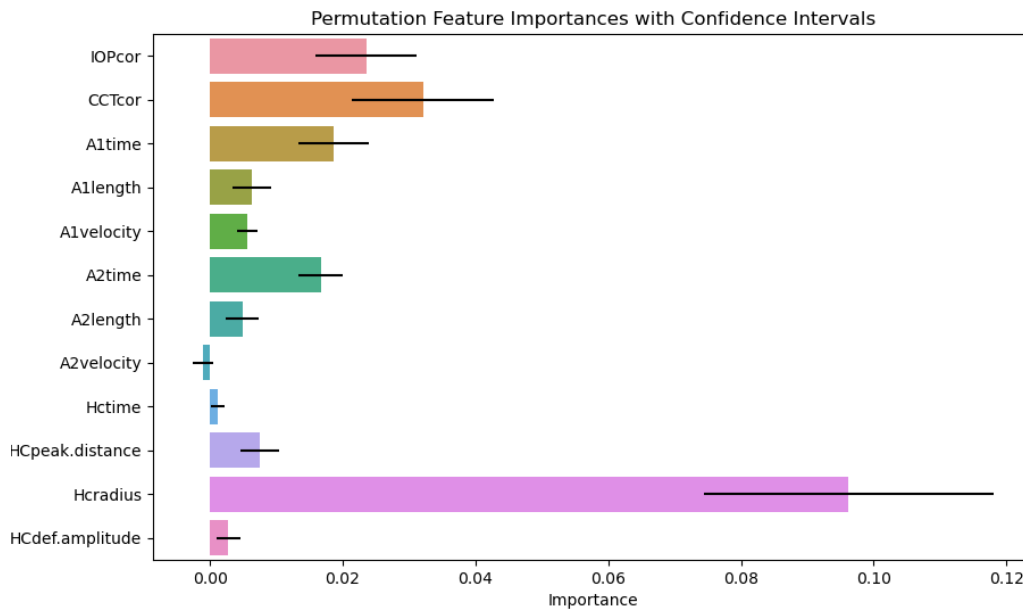


Figure 2.3 PFI for Corvis ST including CCT in KC detection

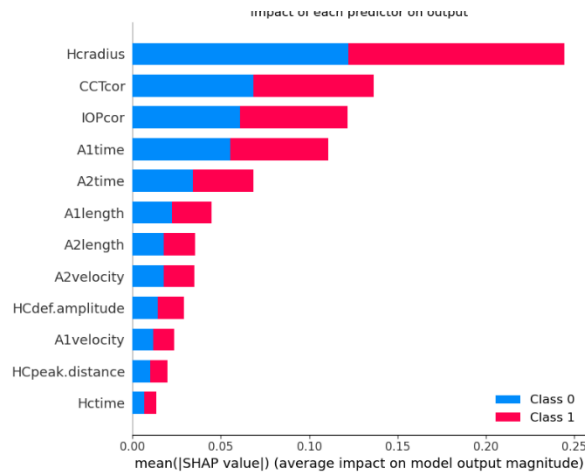


Figure 2.4 SHAP impact of each predictor on KC detection for Corvis ST including CCT data

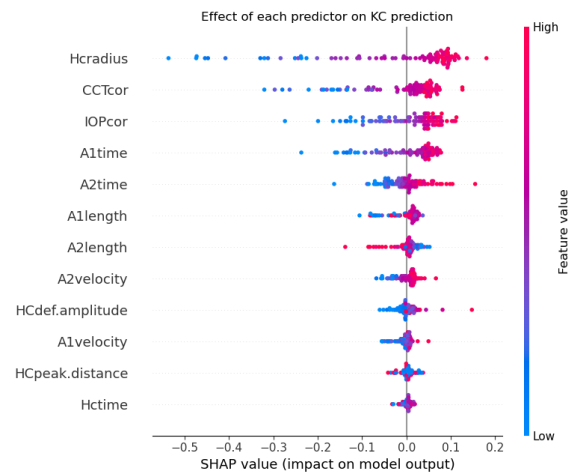


Figure 2.5 SHAP effect of each predictor on KC prediction for Corvis ST including CCT data

2.3.1.1.2 Corvis ST excluding Central Corneal Thickness

The algorithm with the highest AUROC on the test set was again SVM, but this time using GridSearch ($C = 10$, $\gamma = 0.1$, kernel = rbf, AUROC = 0.985, specificity = 0.945, sensitivity = 0.826). All the performances on the test set were very good, exceeding an AUROC value of 0.930. Again, the AUROCs on the test set were better than the performances during training (except for the MLP Classifier with GridSearch, which had an AUROC of 0.953 during training and 0.946 during testing). The learner with the highest AUROC during training was Random Forest (GridSearch) with 0.959.

Analysing the PFI, the contribution of HCRadius is crucial (0.20 ± 0.04), even higher than in the previous experimental condition, likely due to the absence of CCTcor. Following HCRadius, the most important features are IOPcor (0.07 ± 0.01) and A1Time (0.04 ± 0.01). SHAP analysis confirmed the importance of HCRadius for both classes and highlighted those lower values of HCRadius, IOPcor, A1Time, and A2Time influence the final outcome.

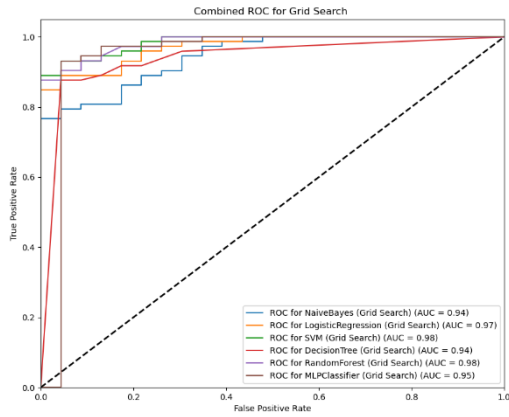


Figure 2.6 ROC Curves for Grid Search, Corvis ST excluding CCT in KC detection

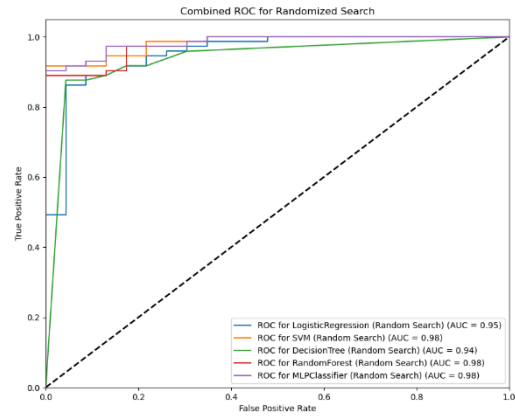


Figure 2.7 ROC Curves for Random Search, Corvis ST including CCT in KC detection

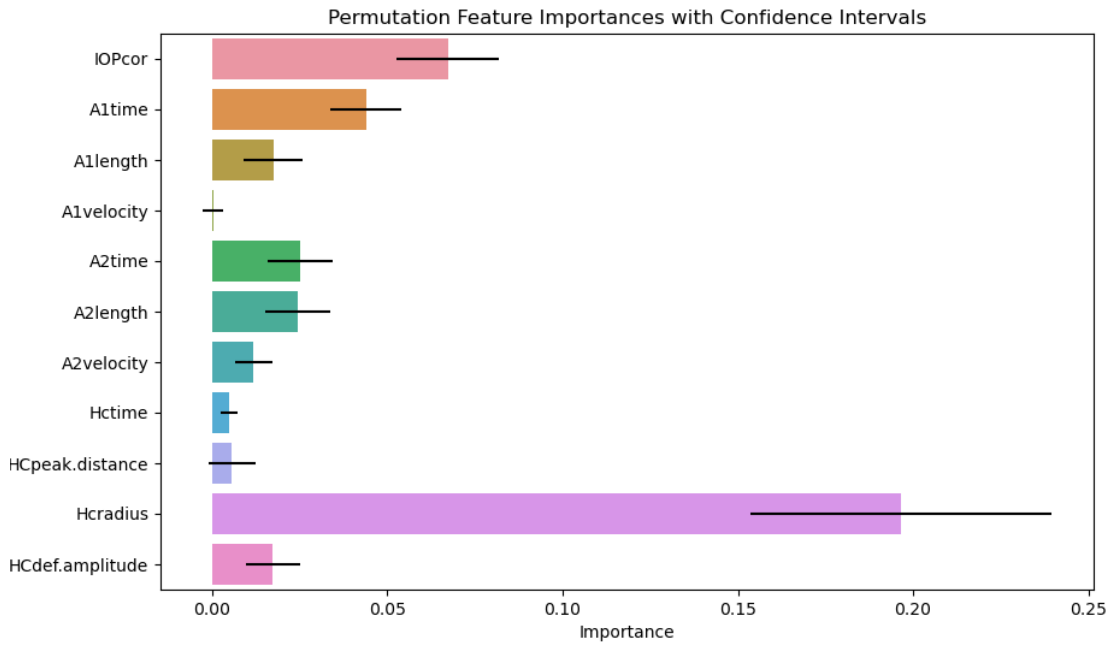


Figure 2.8 PFI for Corvis ST excluding CCT in KC detection

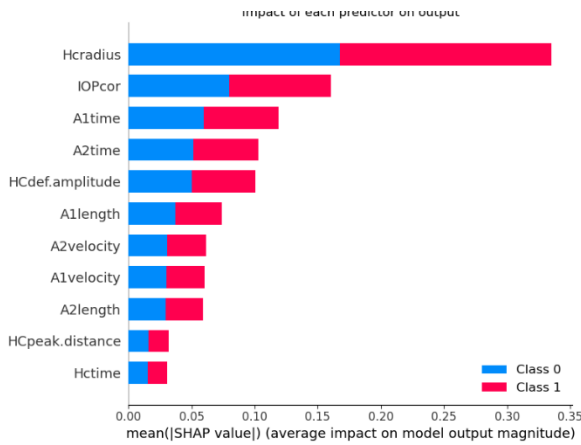


Figure 2.9 SHAP impact of each predictor on KC detection for Corvis ST excluding CCT data

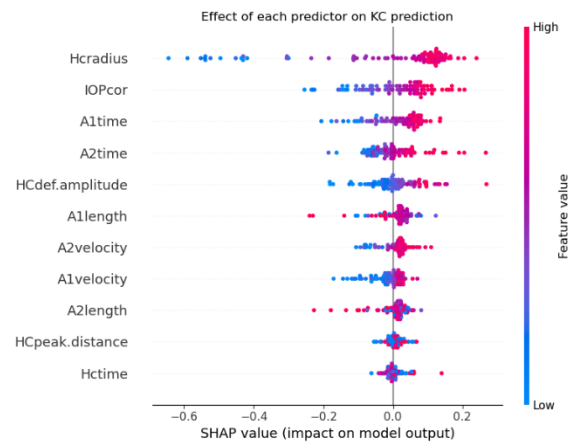


Figure 2.10 SHAP effect of each predictor on KC detection for Corvis ST excluding CCT data

2.3.1.2 ORA

2.3.1.2.1 ORA including Central Corneal Thickness

The algorithm with the highest AUROC value on the test set was Naïve Bayes (AUROC = 0.947). The performances on the test set were good, but generally lower than those of Corvis ST. The learner with the highest AUROC was Random Forest (GridSearch) with 0.924.

Analysing the PFI, it is clear how important corneal thickness is (0.12 ± 0.02), followed by corneal hysteresis (0.09 ± 0.02) and the corneal resistance factor (0.05 ± 0.02). SHAP analysis partially confirmed this: corneal thickness remains the most important, but the corneal resistance factor and IOPg have the same impact on the model output, which is greater than that of corneal hysteresis and IOPcc. In terms of effect on prediction, lower values of all the parameters measured by ORA tend to indicate the keratoconus label.

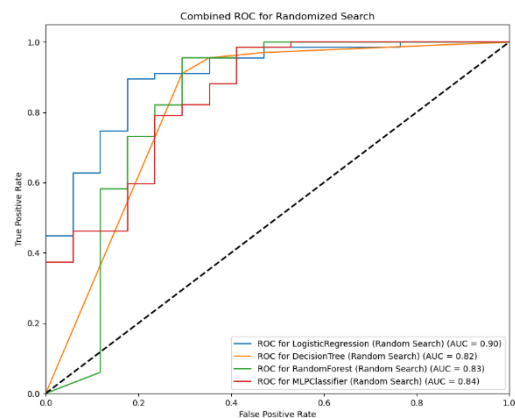
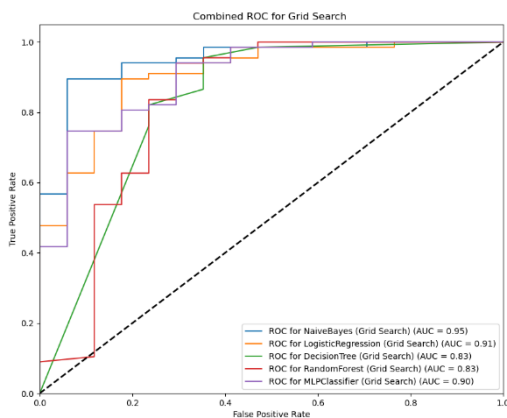


Figure 2.11 ROC Curves for Grid Search, ORA including CCT in KC detection

Figure 2.12 ROC Curves for Random Search, ORA including CCT in KC detection

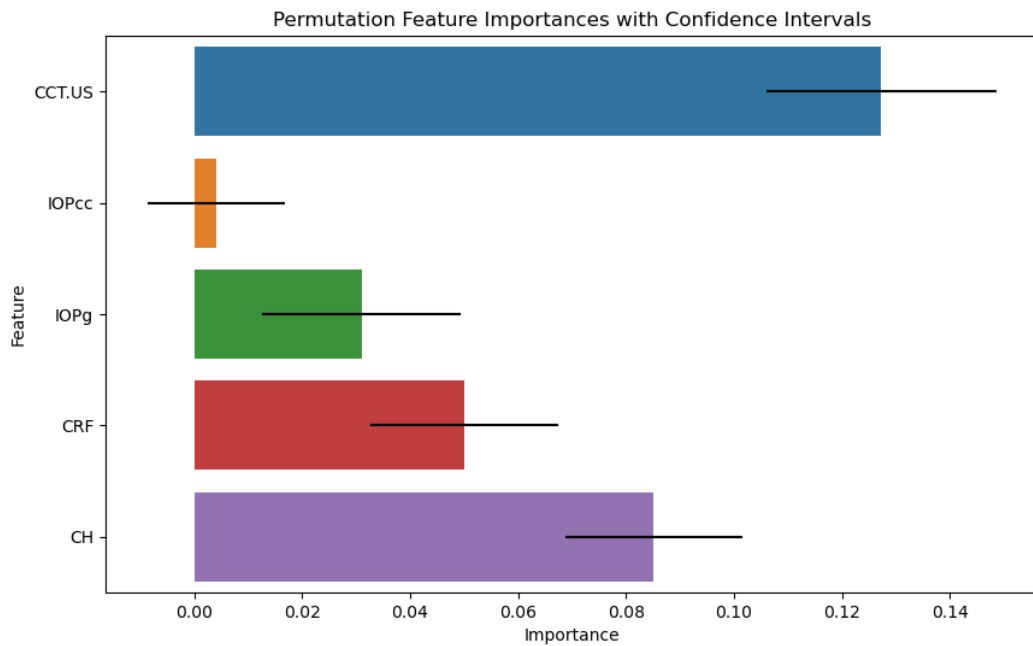


Figure 2.13 PFI for ORA including CCT in KC detection

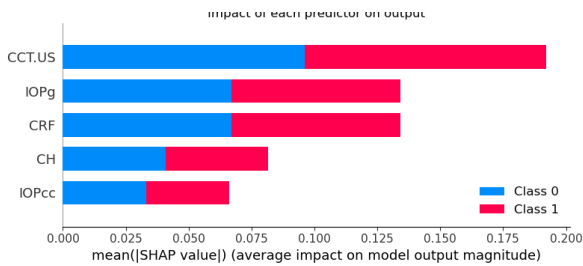


Figure 2.14 SHAP impact of each predictor on KC detection for ORA including CCT data

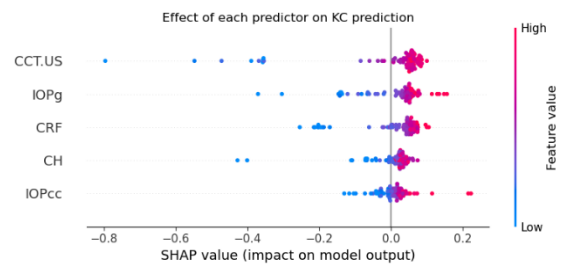


Figure 2.15 SHAP effect of each predictor on KC detection for ORA including CCT data

2.3.1.2.2 ORA excluding Central Corneal Thickness

The algorithm with the highest AUROC value on the test set was Naïve Bayes (AUROC = 0.894, sensitivity = 0.818, specificity = 0.890). The performances on the test set were lower than those of the ORA with corneal thickness among the features. The learner with the highest AUROC was Random Forest (GridSearch) with 0.924.

Analysing the PFI, the most important feature is IOPg (0.10 ± 0.04), followed by corneal hysteresis (0.08 ± 0.02) and the corneal resistance factor (0.06 ± 0.03). SHAP analysis did not confirm this: the corneal resistance factor is the most important, similar to IOPg, while

CH and IOPcc have limited impact. In terms of effect on prediction, lower values of all the parameters measured by ORA tend to indicate the keratoconus label.

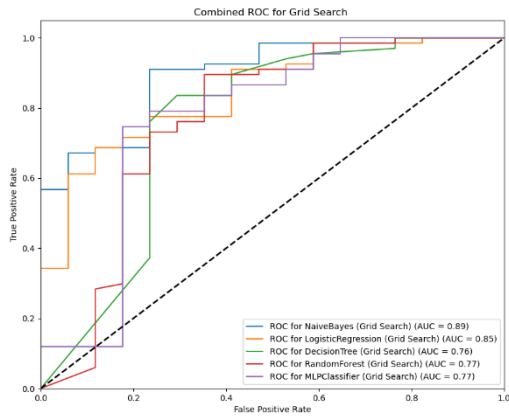


Figure 2.16 ROC Curves for Grid Search, ORA excluding CCT in KC detection

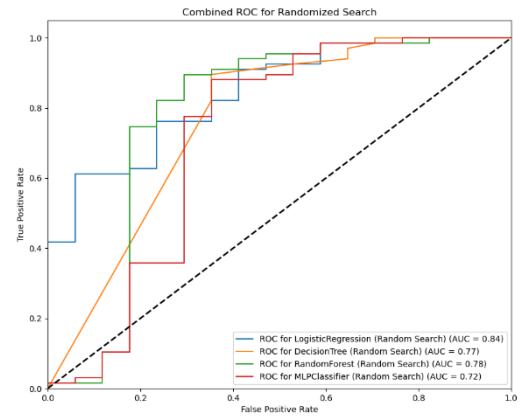


Figure 2.17 ROC Curves for Random Search, ORA excluding CCT in KC detection

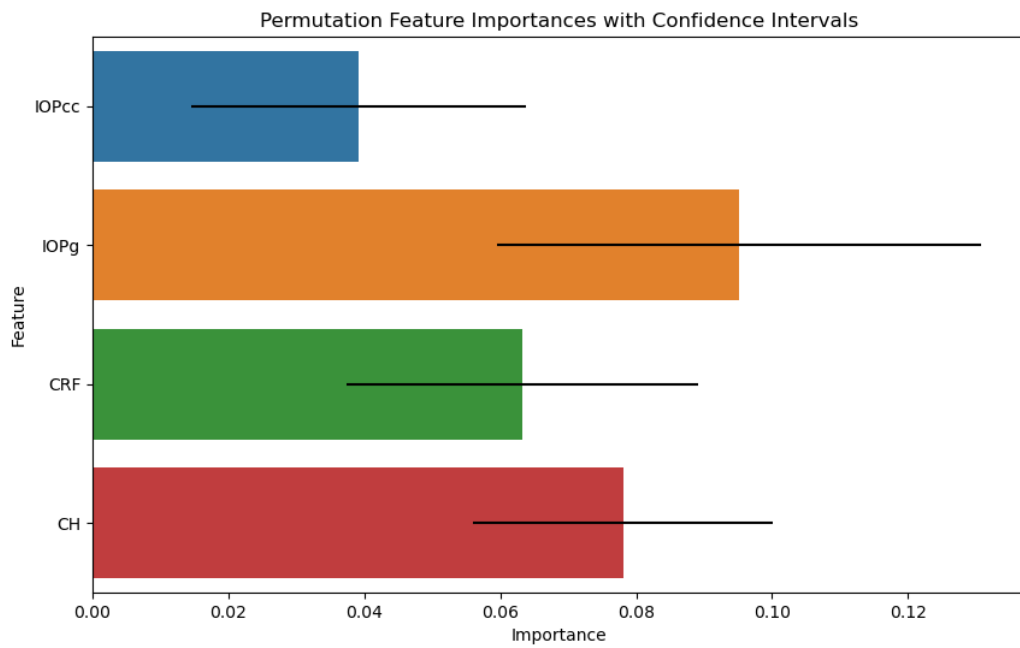


Figure 2.18 PFI for ORA excluding CCT in KC detection

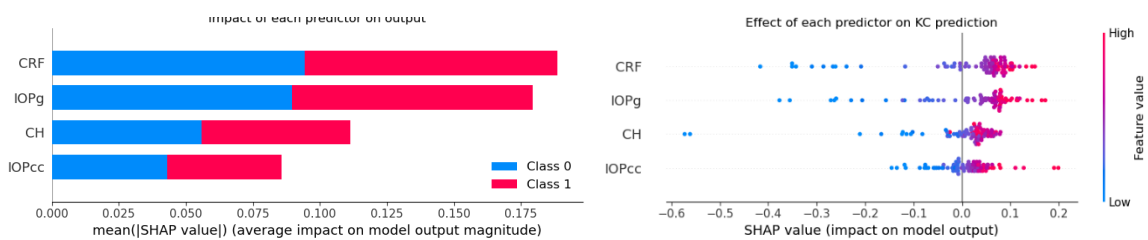


Figure 2.19 SHAP impact of each predictor on KC detection for ORA excluding CCT data

Figure 2.20 SHAP effect of each predictor on KC detection for ORA excluding CCT data

2.3.2 Primary Open Angle Glaucoma

Results on test set for all the combination with Corvis ST are listed in Table 2.3.

Table 2.3 Performances of different combinations of Corvis ST data in POAG detection

	CCT_IOP	CCT_no_IOP	IOP_no_CCT	noIOP_no_CCT
NaiveBayes_grid	0.779	0.777	0.773	0.771
LogisticRegression_random	0.759	0.716	0.772	0.741
LogisticRegression_grid	0.758	0.718	0.773	0.745
SVM_random	0.824	0.808	0.830	0.817
SVM_grid	0.830	0.809	0.831	0.813
DecisionTree_random	0.746	0.690	0.699	0.699
DecisionTree_grid	0.746	0.690	0.736	0.699
RandomForest_random	0.803	0.803	0.811	0.802
RandomForest_grid	0.796	0.803	0.822	0.814
MLPClassifier_random	0.803	0.805	0.823	0.810
MLPClassifier_grid	0.807	0.791	0.811	0.818

2.3.2.1 Corvis ST

2.3.2.1.1 Corvis ST including Central Corneal Thickness and IOP

The algorithm with the best AUROC was SVM with GridSearch ($C = 1000$, $\gamma = 0.001$, kernel = rbf, AUROC = 0.830, sensitivity = 0.625, specificity = 0.842). The algorithm that performed best during training was Random Forest with GridSearch (AUROC = 0.896).

The PFI analysis showed that for POAG classification, the two most important parameters were A2Time (0.23 ± 0.03) and IOPcor (0.16 ± 0.04), followed by A1Time (0.06 ± 0.02).

SHAP analysis confirmed these findings. The calculation of the effect of each predictor on the final outcome revealed that high A2Time and IOPcor point towards POAG, while for A1Time, it was the opposite.

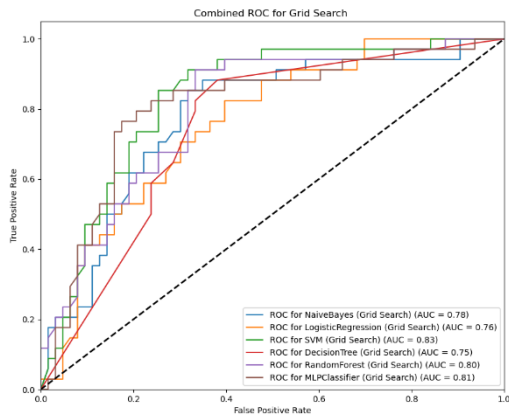


Figure 2.21 ROC Curves for Grid Search, Corvis ST including CCT and IOP in POAG detection

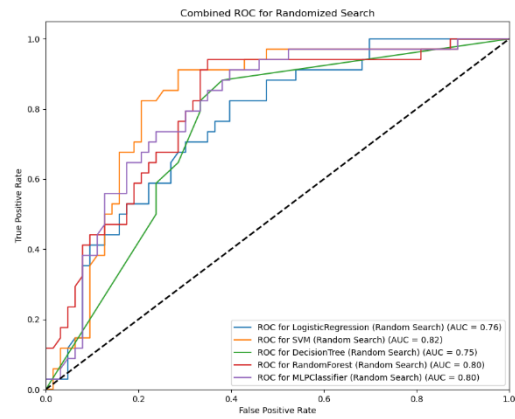


Figure 2.22 ROC Curves for Random Search, Corvis ST including CCT and IOP in POAG detection

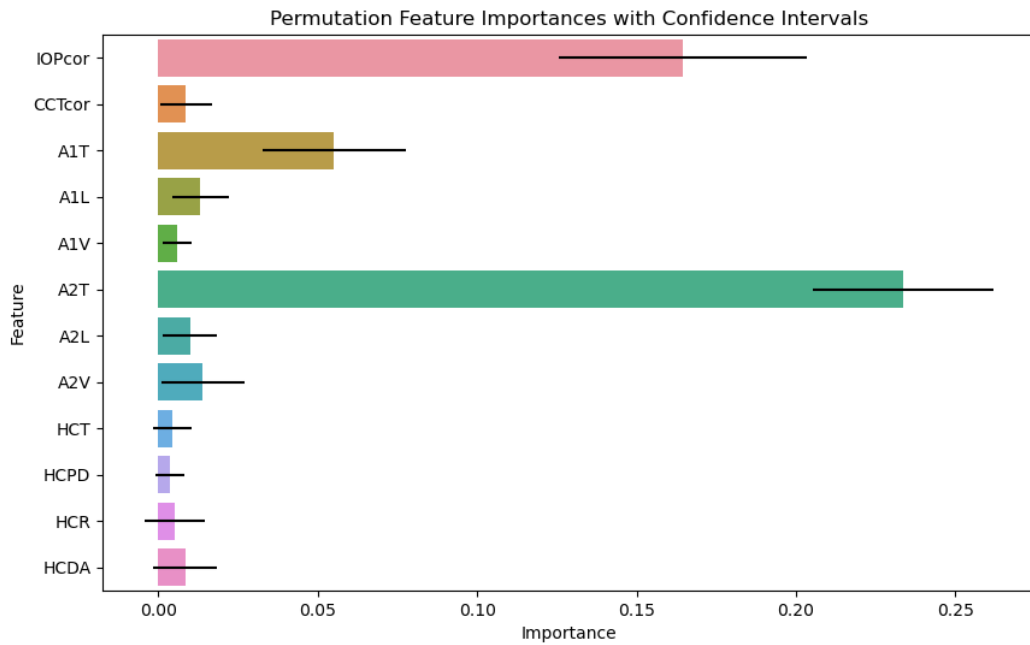


Figure 2.23 PFI for Corvis ST including CCT and IOP in POAG detection

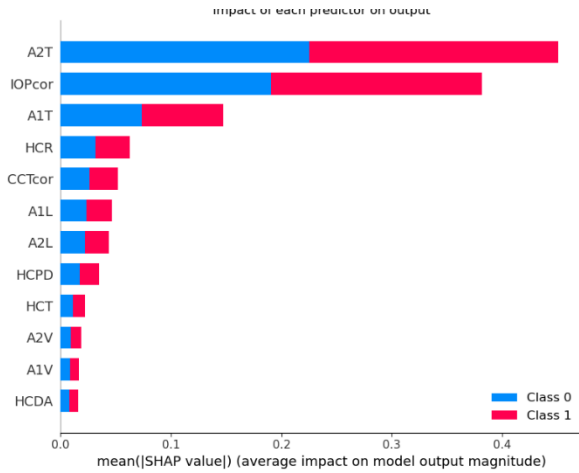


Figure 2.24 SHAP impact of each predictor on POAG detection for Corvis ST including CCT and IOP data

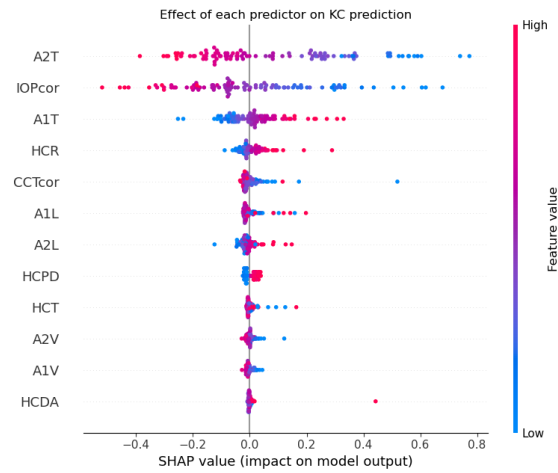


Figure 2.25 SHAP effect of each predictor on POAG detection for Corvis ST including CCT and IOP data

2.3.2.1.2 Corvis ST including Central Corneal Thickness, excluding IOP

The algorithm with the highest AUROC on the test set was SVM with GridSearch (C = 1, γ = scale, kernel = rbf, AUROC = 0.809, sensitivity = 0.860, specificity = 0.650). The best learner during training was Random Forest with GridSearch.

According to PFI analysis, the most important feature was A2Time (0.14 ± 0.1), followed by A1Time (0.06 ± 0.02) and A1Length (0.04 ± 0.02). The calculation of SHAP values confirmed these findings: a high value of A2Time or A1Time points towards POAG, while the interpretation for A1Length is less clear.

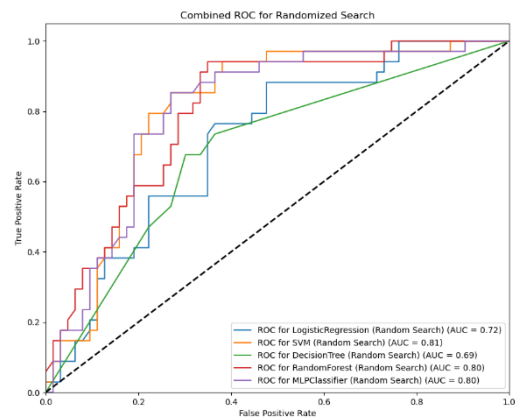
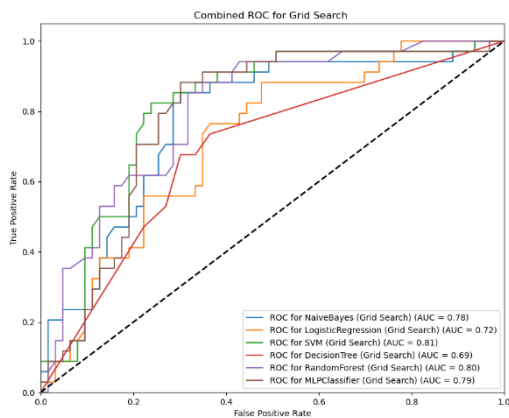


Figure 2.26 ROC Curves for Grid Search, Corvis ST including CCT and excluding IOP in POAG detection

Figure 2.27 ROC Curves for Random Search, Corvis ST including CCT and excluding IOP in POAG detection

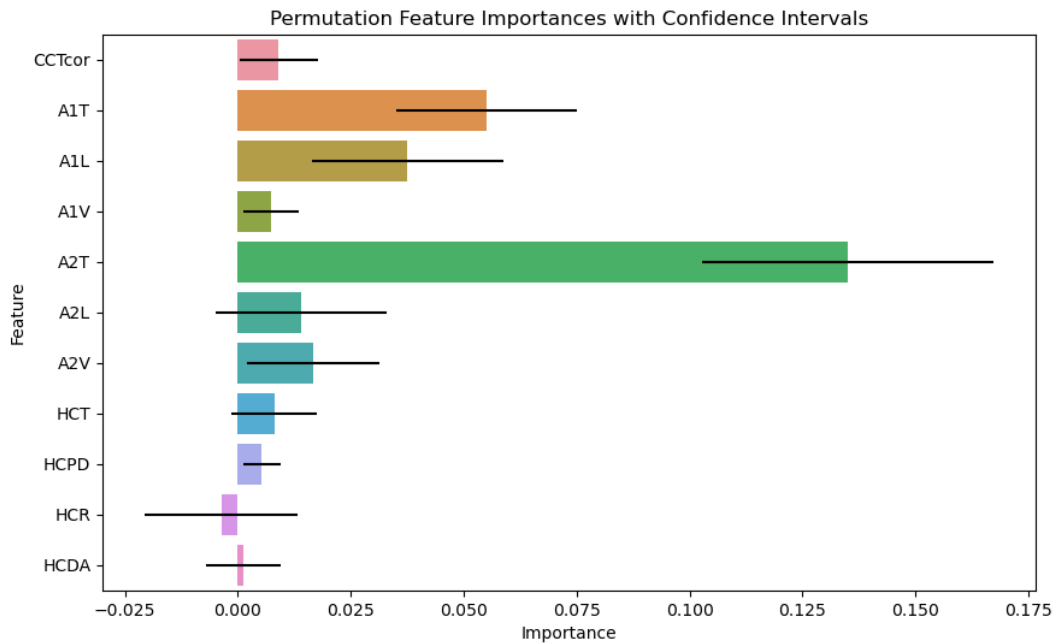


Figure 2.28 PFI for Corvis ST including CCT and excluding IOP in POAG detection

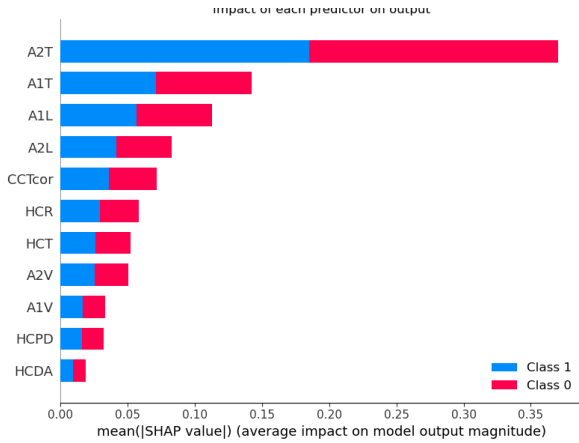


Figure 2.29 SHAP impact of each predictor on POAG detection for Corvis ST including CCT and excluding IOP data

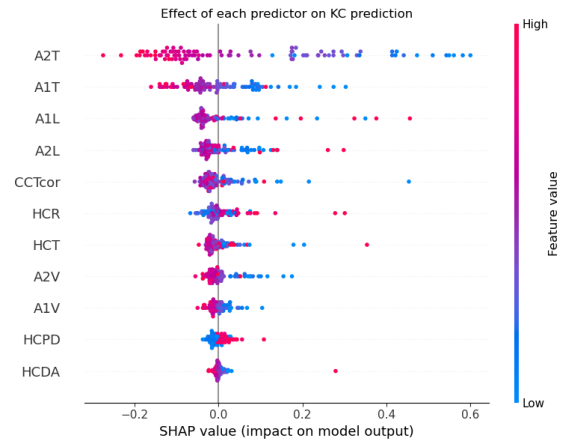


Figure 2.30 SHAP effect of each predictor on POAG detection for Corvis ST including CCT and excluding IOP data

2.3.2.1.3 Corvis ST including IOP, excluding Central Corneal Thickness

The algorithm with the highest AUROC on the test set is SVM with GridSearch (C = 1, γ = 0.1, kernel = rbf, AUROC = 0.831, sensitivity = 0.889, specificity = 0.651). All the learners

showed lower AUROC values on the test set than during training. The best learner during training was Random Forest with GridSearch (AUROC = 0.892).

The PFI analysis shows that the feature with the highest importance is A2Time (0.17 ± 0.03), followed by IOPcor (0.06 ± 0.02) and A1Length (0.03 ± 0.02). The SHAP analysis confirmed the PFI findings, indicating that high values of A2Time and IOPcor point towards POAG classification, while the interpretation of A1Length is less clear due to the lack of a distinct separation.

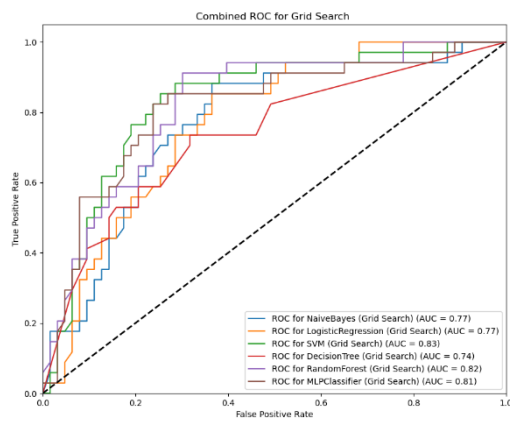


Figure 2.31 ROC Curves for Grid Search, Corvis ST including IOP and excluding CCT in POAG detection

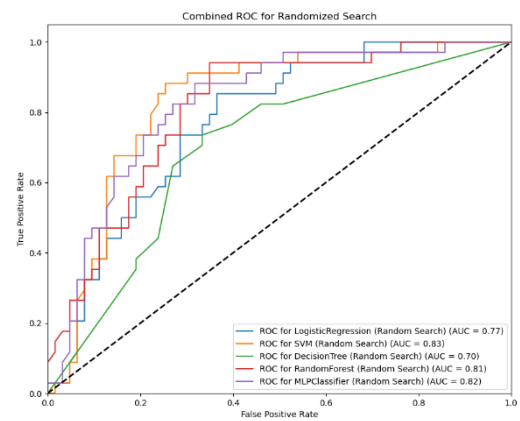


Figure 2.32 ROC Curves for Random Search, Corvis ST including IOP and excluding CCT in POAG detection

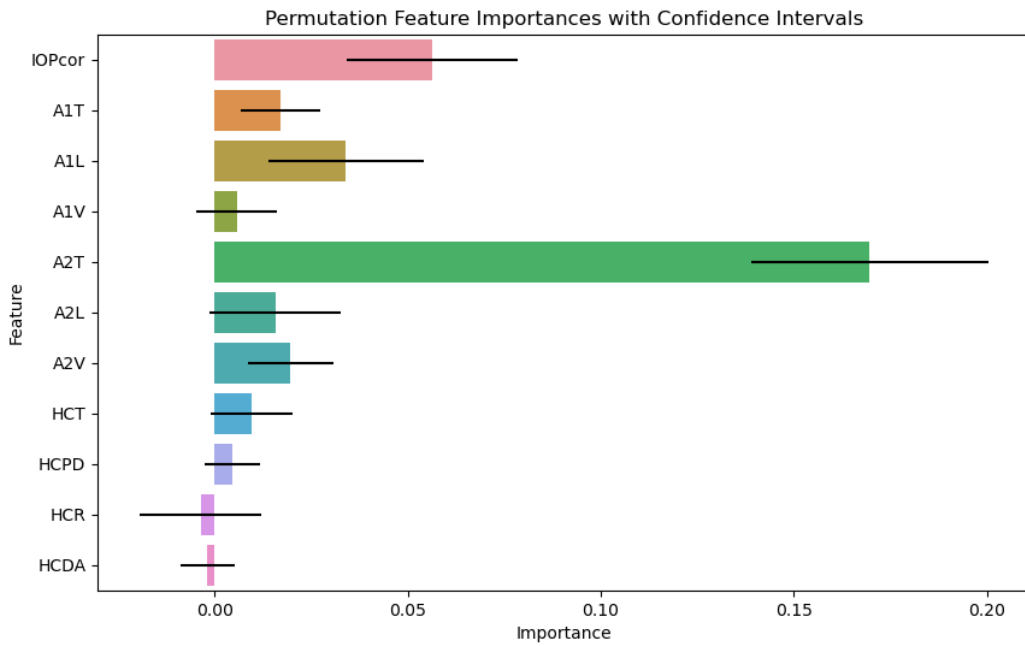


Figure 2.33 PFI for Corvis ST including IOP and excluding CCT in POAG detection

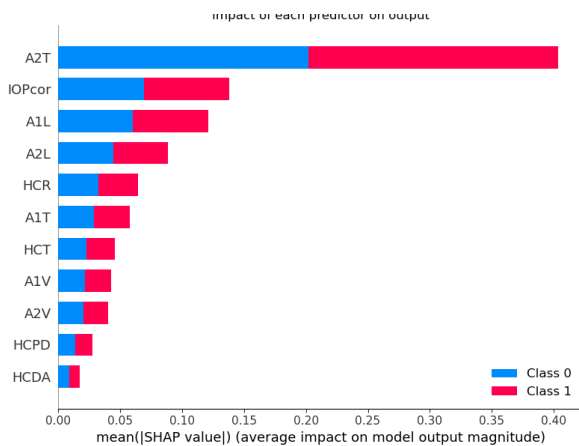


Figure 2.34 SHAP impact of each predictor on POAG detection for Corvis ST including IOP and excluding CCT data

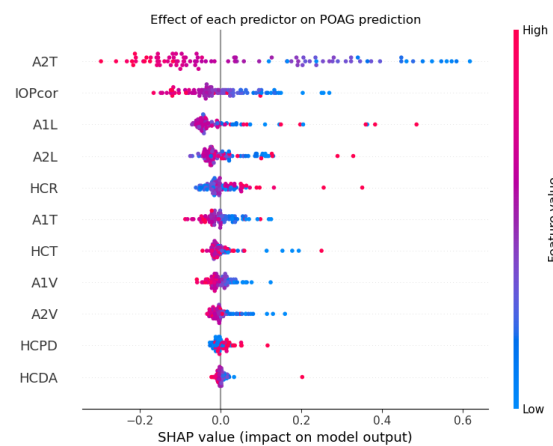


Figure 2.35 SHAP effect of each predictor on POAG detection for Corvis ST including IOP and excluding CCT data

2.3.2.1.4 Corvis ST excluding IOP and Central Corneal Thickness

The last analysis, which excluded corneal thickness and IOP, had the lowest results. The algorithm with the highest AUROC was MLP Classifier (activation: tanh, hidden layer sizes: 50, 50, learning rate = 0.01, maximum iterations = 300, solver = sgd, AUROC = 0.818, sensitivity = 0.831, specificity = 0.632). Again, the performances on the test set were lower

than during training. The learner with the highest score during training was Random Forest using GridSearch (AUROC = 0.898).

The permutation feature importance analysis identified A2Time as the most important predictor (0.22 ± 0.03), followed by A1Time (0.08 ± 0.03). The other predictors showed lower scores. SHAP analysis confirmed that A2Time and A1Time have the major impact on the output. High values of both features are associated with an increased likelihood of POAG.

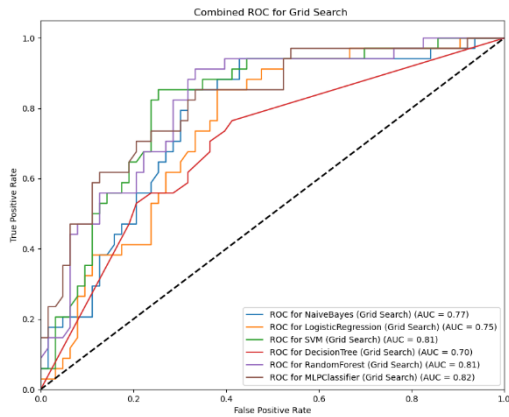


Figure 2.36 ROC Curves for Grid Search, Corvis ST excluding CCT and IOP in POAG detection

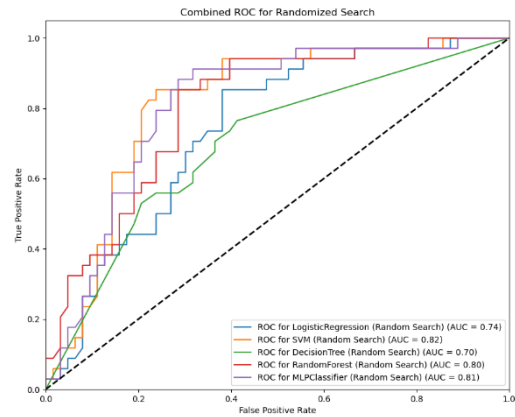


Figure 2.37 ROC Curves for Random Search, Corvis ST excluding CCT and IOP in POAG detection

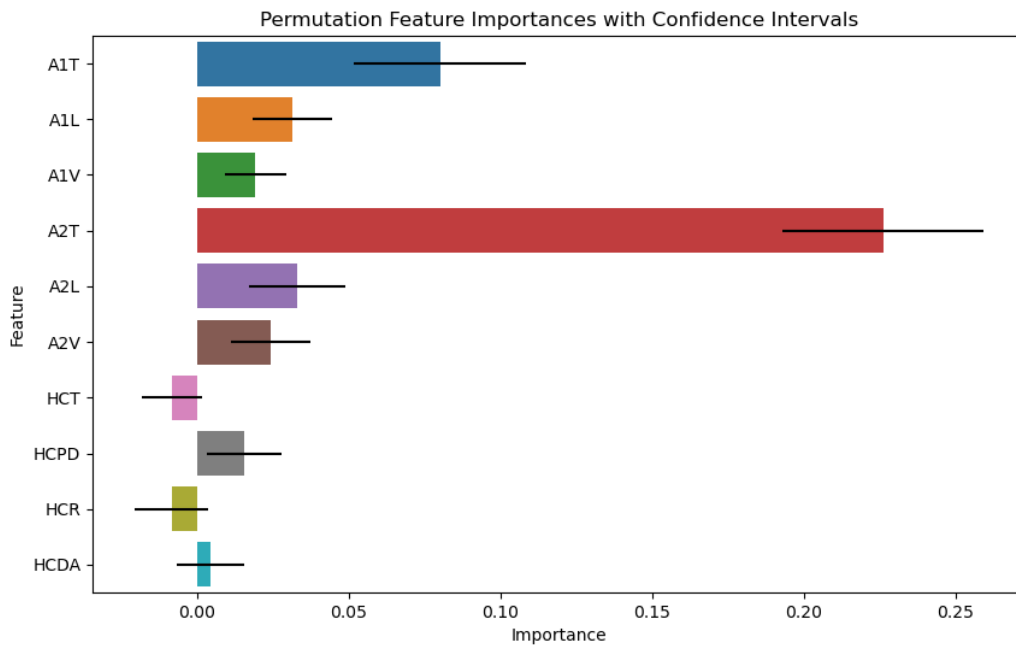


Figure 2.38 PFI for Corvis ST excluding CCT and IOP in POAG detection

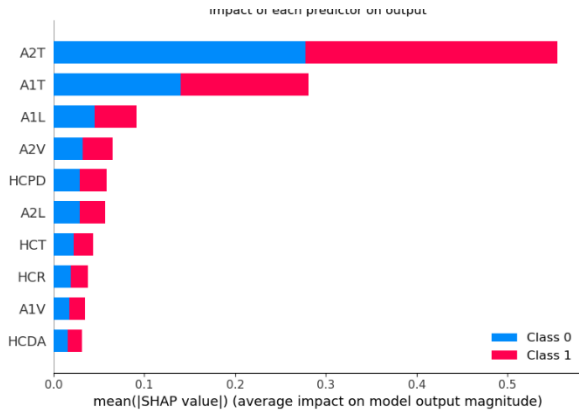


Figure 2.39 SHAP impact of each predictor on POAG detection for Corvis ST excluding CCT and IOP data

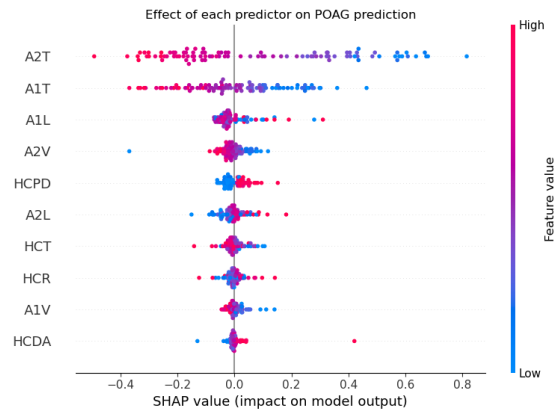


Figure 2.40 SHAP effect of each predictor on POAG prediction for Corvis ST excluding CCT and IOP data

2.3.2.2 ORA

Results on test set for all the combination with ORA are listed in Table 2.4

Table 2.4 Performances of different combinations of ORA data in POAG detection

	CCT_IOP	CCT_no_IOP	IOP_no_CCT	noIOP_no_CCT
NaiveBayes_grid	0.858	0.804	0.856	0.822
LogisticRegression_random	0.892	0.846	0.894	0.875
LogisticRegression_grid	0.893	0.846	0.894	0.876
DecisionTree_random	0.701	0.754	0.770	0.719
DecisionTree_grid	0.701	0.779	0.745	0.758
RandomForest_random	0.790	0.759	0.828	0.787
RandomForest_grid	0.797	0.767	0.835	0.793
MLPClassifier_random	0.827	0.834	0.882	0.850
MLPClassifier_grid	0.845	0.833	0.876	0.858

2.3.2.2.1 ORA including Central Corneal Thickness and IOP

The algorithm with the highest AUROC value on the test set was Logistic Regression with hyperparameters set using GridSearch (C = 100, regularisation = L1, solver = liblinear, AUROC = 0.893, sensitivity = 0.894, specificity = 0.750). Logistic Regression performance with parameters found using RandomSearch was very similar (AUROC = 0.892), despite the hyperparameters being completely different (C = 35, regularisation = L2, solver = lbfgs). The learner with the best score on the training set was the MLP Classifier (AUROC = 0.812).

Analysing PFI, the feature with the highest importance was corneal hysteresis (0.529 ± 0.05), followed by IOPg (0.22 ± 0.03) and the corneal resistance factor (0.17 ± 0.04). The contributions of IOPcc and corneal thickness were considered marginal. SHAP analysis confirmed the significant impact of corneal hysteresis and, to a lesser extent, the corneal resistance factor but swapped the importance of the IOPs, considering IOPcc to have a higher impact on prediction than IOPg. The SHAP scatterplot highlights the opposite importance of corneal hysteresis and the corneal resistance factor (high hysteresis and low resistance factor towards POAG). The same applies to the IOPs (high IOPcc and low IOPg towards POAG).

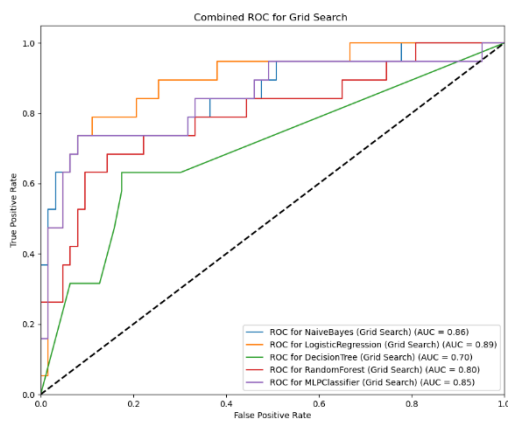


Figure 2.41 ROC Curves for Grid Search, ORA including CCT and IOP in POAG detection

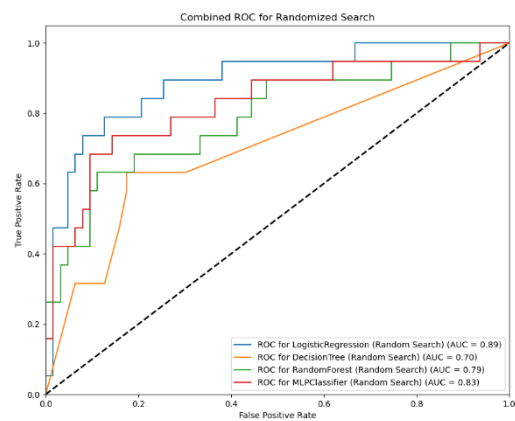


Figure 2.42 ROC Curves for Random Search, ORA including CCT and IOP in POAG detection

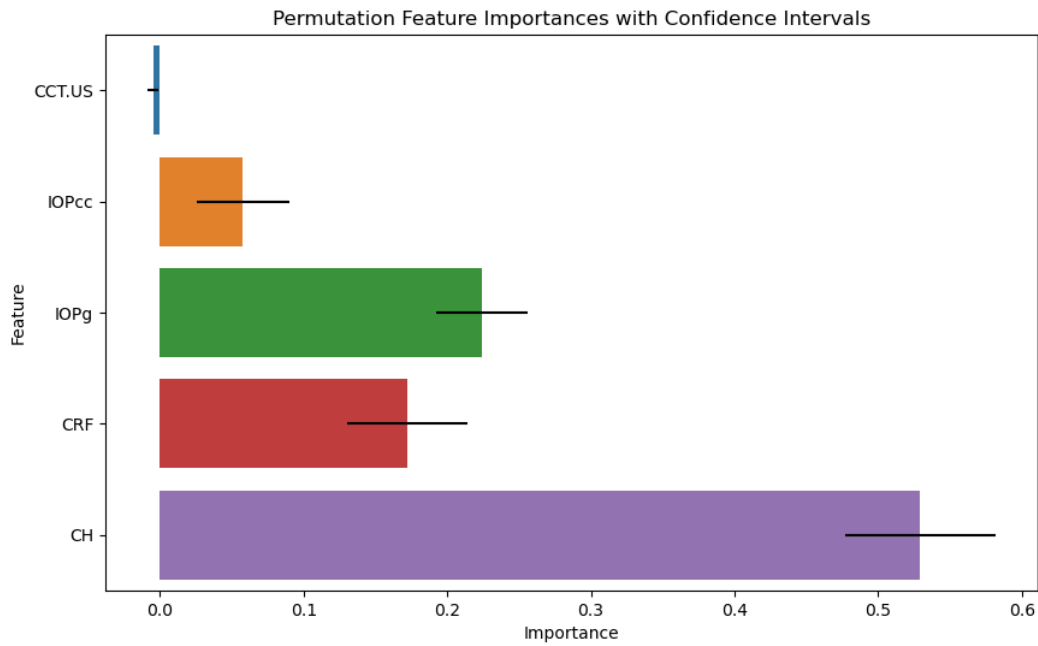


Figure 2.43 PFI for ORA including CCT and IOP in POAG detection

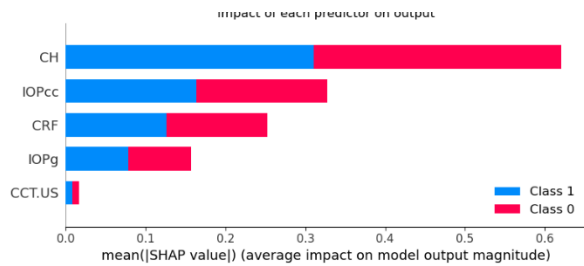


Figure 2.44 SHAP impact of each predictor on POAG detection for ORA including CCT and IOP data

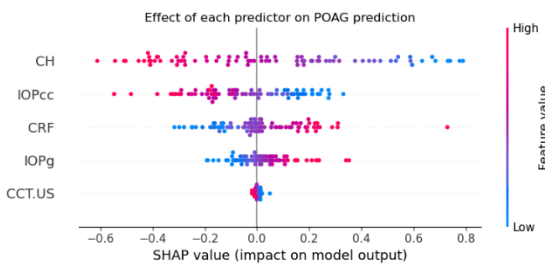


Figure 2.45 SHAP effect of each predictor on POAG detection for ORA including CCT and IOP data

2.3.2.2.2 ORA Including Central Corneal Thickness, excluding IOP

Not considering IOP, the algorithm with the highest AUROC is Logistic Regression, which achieved the same learning (AUROC = 0.846, sensitivity = 0.822, specificity = 0.667) and test score with both GridSearch (C = 0.1, regularisation = L1, solver = liblinear) and RandomSearch (C = 0.2, regularisation = L1, solver = saga), both in less than 2 seconds. The best learner during training was the MLP Classifier with GridSearch (AUROC = 0.813).

From PFI analysis, it appears the only important feature is corneal hysteresis (0.34 ± 0.06), which is confirmed by the SHAP analysis. The SHAP scatterplot suggests that a high value of corneal hysteresis can positively influence the prediction of POAG.

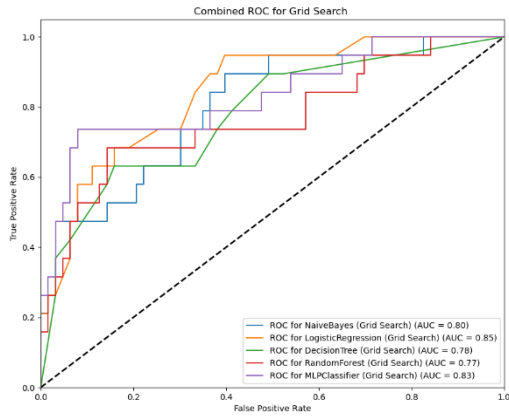


Figure 2.46 ROC Curves for Grid Search, ORA including CCT and excluding IOP in POAG detection

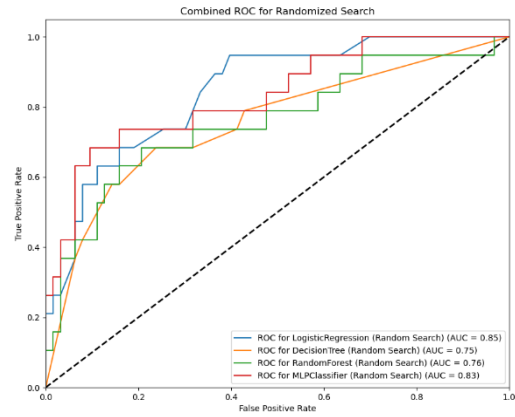


Figure 2.47 ROC Curves for Random Search, ORA including CCT and excluding IOP in POAG detection

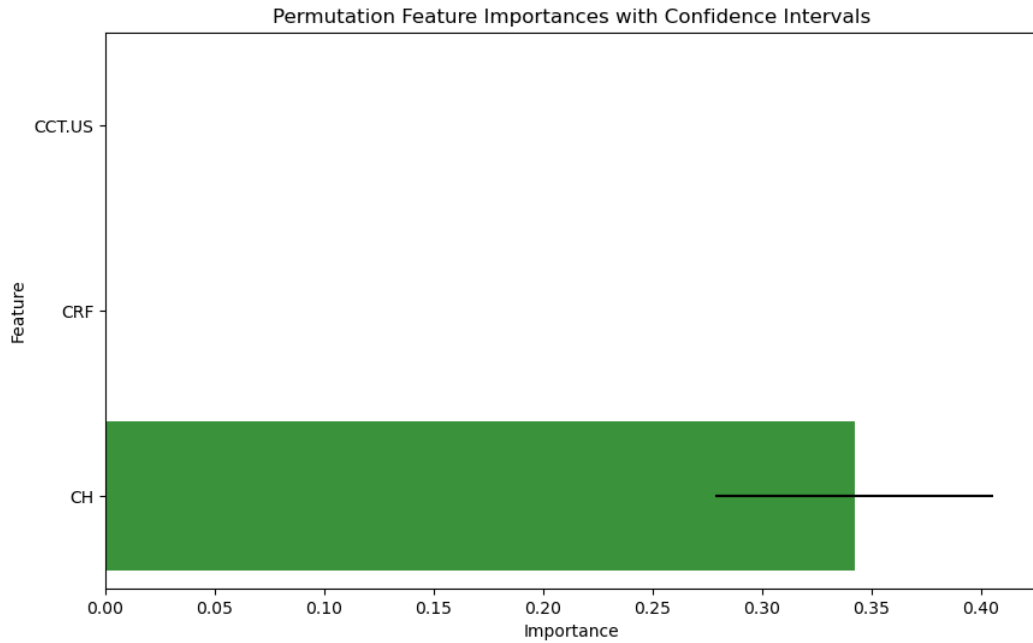


Figure 2.48 PFI for ORA including CCT and excluding IOP in POAG detection

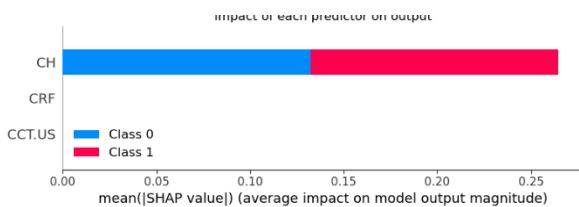


Figure 2.49 SHAP impact of each predictor on POAG detection for ORA including CCT and excluding IOP data

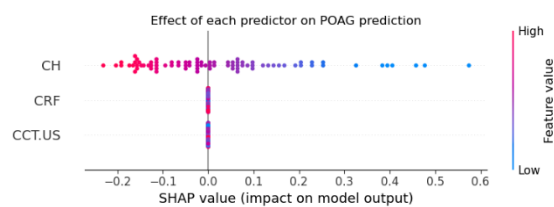


Figure 2.50 SHAP effect of each predictor on POAG detection for ORA including CCT and excluding IOP data

2.3.2.2.3 ORA including IOP, excluding Central Corneal Thickness

Not including corneal thickness, the situation was very similar. The algorithm with the best performance on the test set was Logistic Regression (AUROC = 0.894, sensitivity = 0.894, specificity = 0.750), regardless of whether GridSearch (C = 10, regularisation = L1, solver = saga) or RandomSearch (C = 14, regularisation = L2, solver = saga) was used. The learner with the best performance during training was the MLP Classifier (AUROC = 0.808).

Corneal hysteresis was the most important parameter (0.53 ± 0.05) according to PFI, followed by IOPg (0.20 ± 0.03) and CRF (0.17 ± 0.04). SHAP confirmed the importance of corneal hysteresis but swapped the importance of the IOPs: IOPcc is more important than IOPg. According to the scatterplot, high hysteresis and high IOPcc influence the decision towards POAG, while the opposite is true for the corneal resistance factor and IOPg.

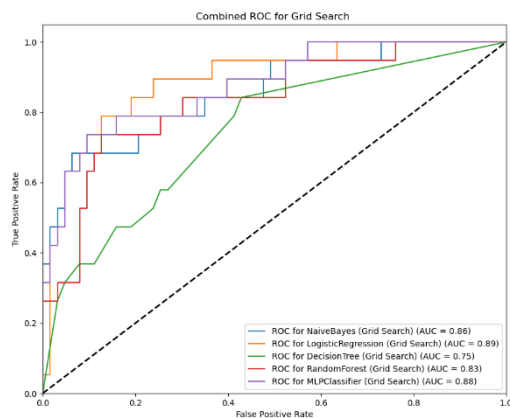


Figure 2.51 ROC Curves for Grid Search, ORA including IOP and excluding CCT in POAG detection

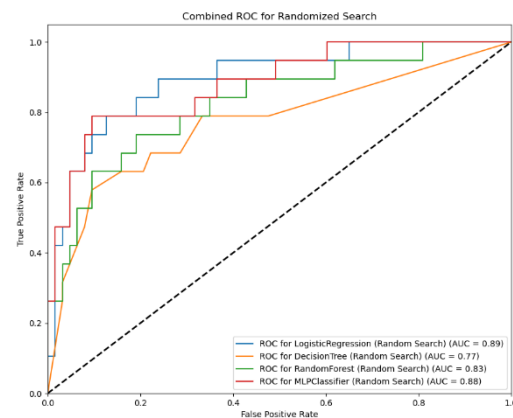


Figure 2.52 ROC Curves for Random Search, ORA including IOP and excluding CCT in POAG detection

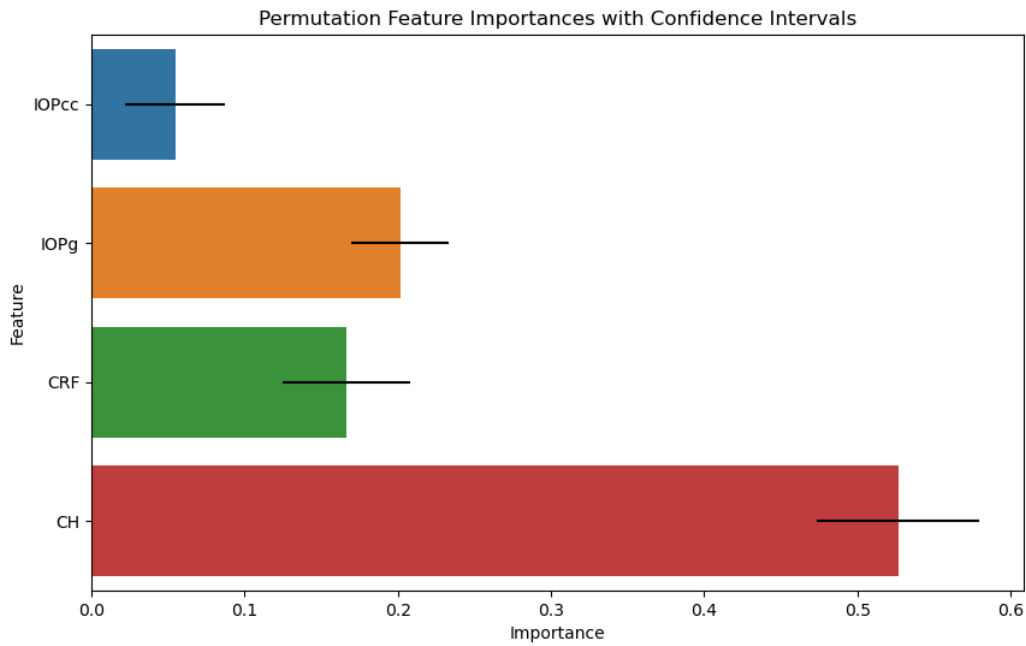


Figure 2.53 PFI for ORA including IOP and excluding CCT in POAG detection

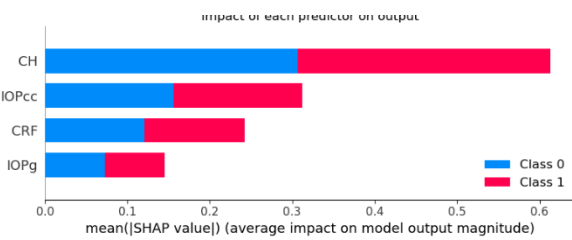


Figure 2.54 SHAP impact of each predictor on POAG detection for ORA including IOP and excluding CCT data

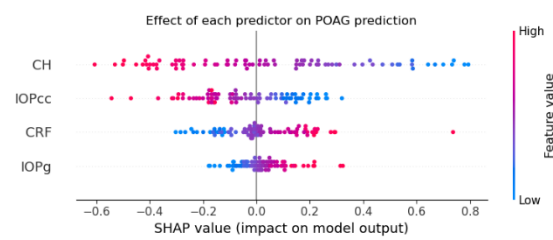


Figure 2.55 SHAP effect of each predictor on POAG detection for ORA including IOP and excluding CCT data

2.3.2.2.4 ORA excluding IOP and Central Corneal Thickness

For the last experimental condition, only corneal hysteresis and corneal resistance factor were considered. The algorithm with the best AUROC was again Logistic Regression (AUROC = 0.876, sensitivity = 0.881, specificity = 0.733) with GridSearch (C = 10, regularisation = L2, solver = newton-cg). RandomSearch gave very similar results (AUROC = 0.875, with the same specificity and sensitivity). The learner with the best performance during training was the MLP Classifier (AUROC = 0.796).

PFI analysis showed that corneal hysteresis has great importance in the model output (0.37 ± 0.06), followed by corneal resistance factor (0.06 ± 0.02). The SHAP graph confirmed that

a high value of hysteresis influences the output towards POAG, while the opposite is true for the corneal resistance factor.

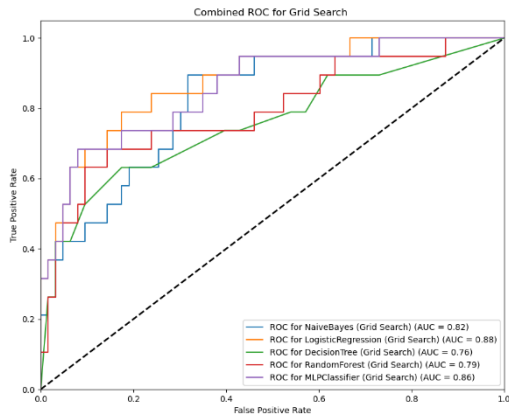


Figure 2.56 ROC Curves for Grid Search, ORA excluding CCT and IOP in POAG detection

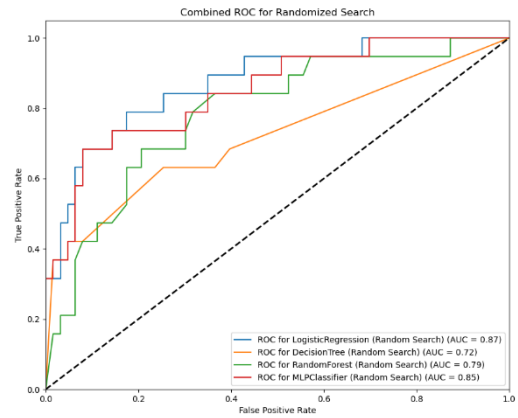


Figure 2.57 ROC Curves for Random Search, ORA excluding CCT and IOP in POAG detection

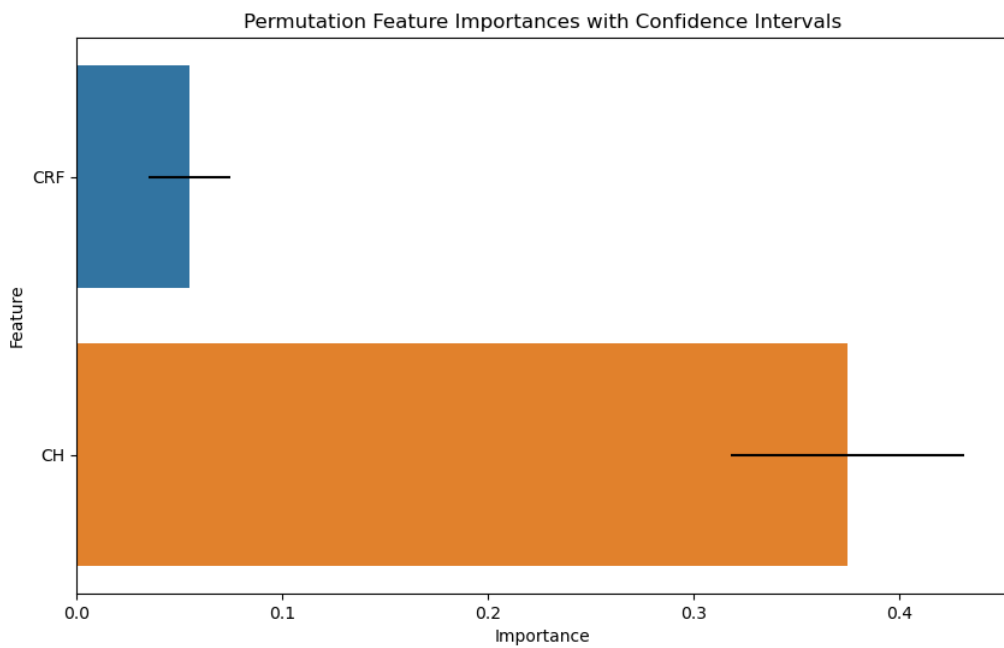


Figure 2.58 PFI for ORA excluding CCT and IOP in POAG detection



Figure 2.59 SHAP impact of each predictor on POAG detection for ORA excluding CCT and IOP data

Figure 2.60 SHAP effect of each predictor on POAG detection for ORA excluding CCT and IOP data

2.3.2.3 GAT

Results for GAT combinations are listed in Table 2.5

Table 2.5 Performances of different combinations of GAT data in POAG detection

	CCT	no_CCT
NaiveBayes_grid	0.634	0.535
LogisticRegression_random	0.636	0.500
LogisticRegression_grid	0.637	0.500
DecisionTree_random	0.624	0.575
DecisionTree_grid	0.624	0.575
RandomForest_random	0.696	0.591
RandomForest_grid	0.631	0.572
MLPClassifier_random	0.678	0.560
MLPClassifier_grid	0.674	0.590

2.3.2.3.1 GAT including Central Corneal Thickness

Using only tonometry and pachymetry data, the performance of the models decreased drastically. The best learner during training was the MLP Classifier (AUROC = 0.694), while the algorithm that showed the best performance on the test set was Random Forest (AUROC = 0.696, specificity = 0.625, sensitivity = 0.667) with RandomSearch (11 estimators, minimum samples split = 41, minimum samples leaf = 9, maximum depth = 52).

From PFI analysis, it is evident that pachymetry (0.07 ± 0.06) is more important than tonometry (0.04 ± 0.04). This finding is confirmed by SHAP bar plots. The SHAP scatterplot suggests that higher values of pachymetry drive the output towards POAG, as do tonometry values, although the latter is less clear.

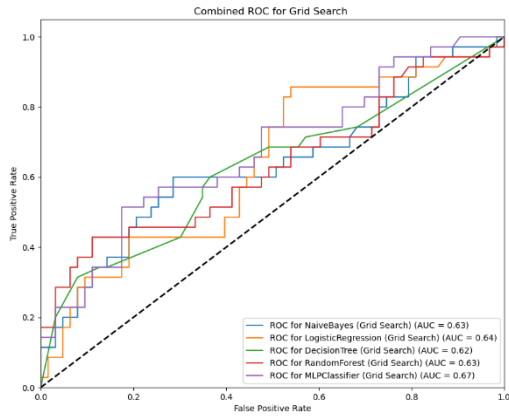


Figure 2.61 ROC Curves for Grid Search, GAT including CCT in POAG detection

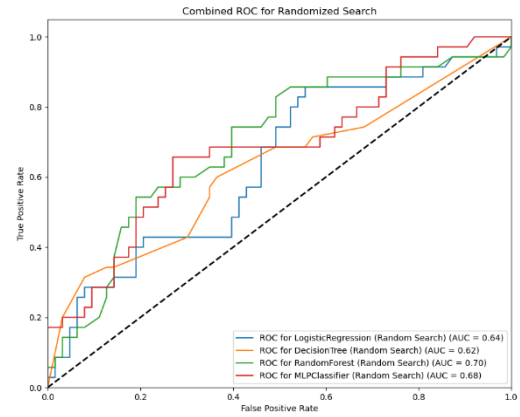


Figure 2.62 ROC Curves for Random Search, GAT including CCT in POAG detection

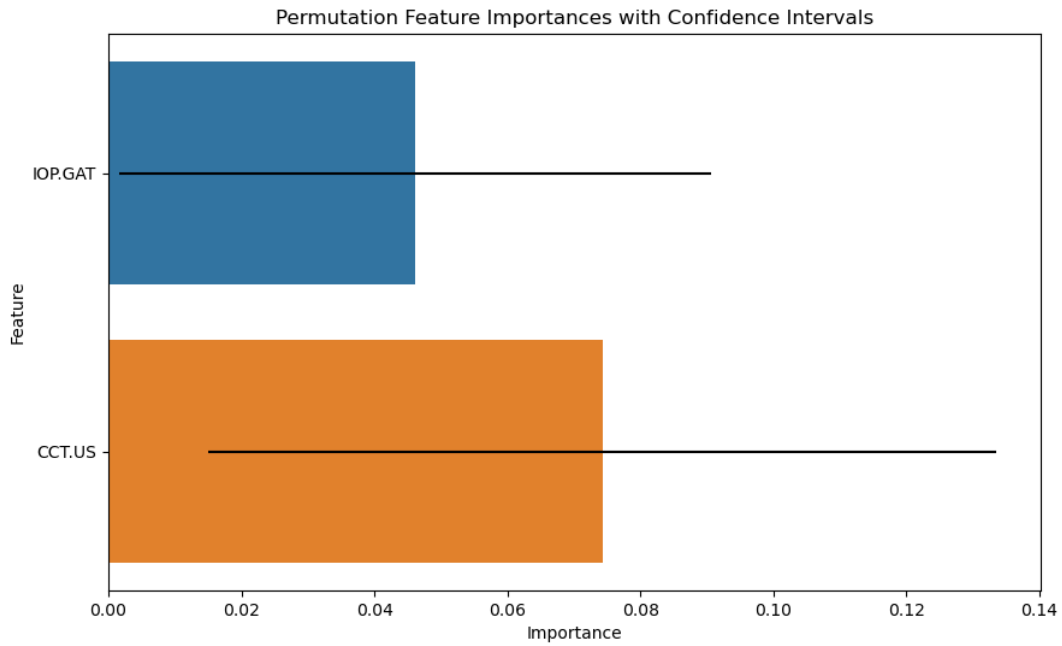


Figure 2.63 PFI for GAT including CCT in POAG detection

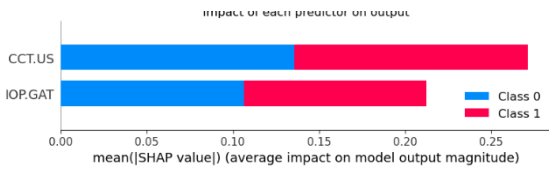


Figure 2.64 SHAP impact of each predictor on POAG detection for GAT including CCT data

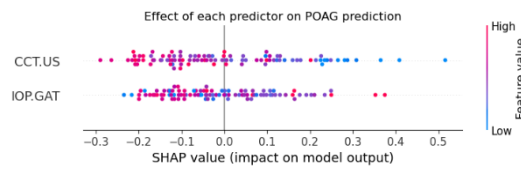


Figure 2.65 SHAP effect of each predictor on POAG detection for GAT including CCT data

2.3.2.3.2 GAT excluding Central Corneal Thickness

The performance of the models showed a further decrease when removing central corneal thickness from the features, as shown in the ROC curves. The algorithm with the best AUROC (0.591, specificity 0.800, sensitivity 0.667) is Random Forest with RandomSearch (11 estimators, minimum samples split = 41, minimum samples leaf = 9, maximum depth = 52), while the best learner during training was the MLP Classifier with RandomSearch (AUROC = 0.610).

As expected, PFI suggests that the only parameter influencing the outcome is GAT. The SHAP scatterplot suggests that high values of IOP are associated with POAG predictions, although this relationship is less clear than expected.

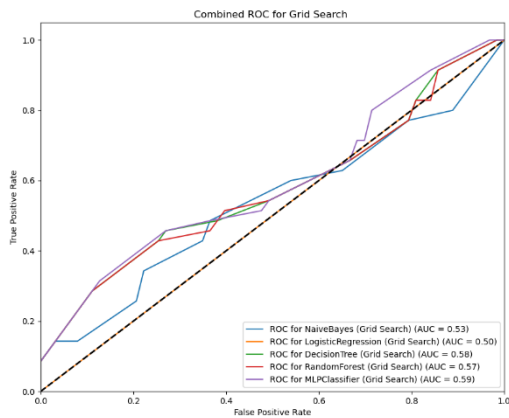


Figure 2.66 ROC Curves for Grid Search, GAT only in POAG detection

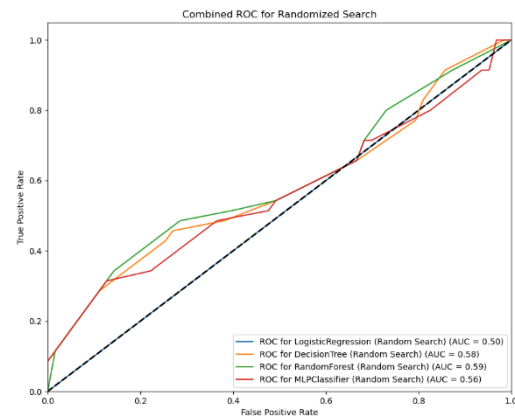


Figure 2.67 ROC Curves for Random Search, GAT only in POAG detection

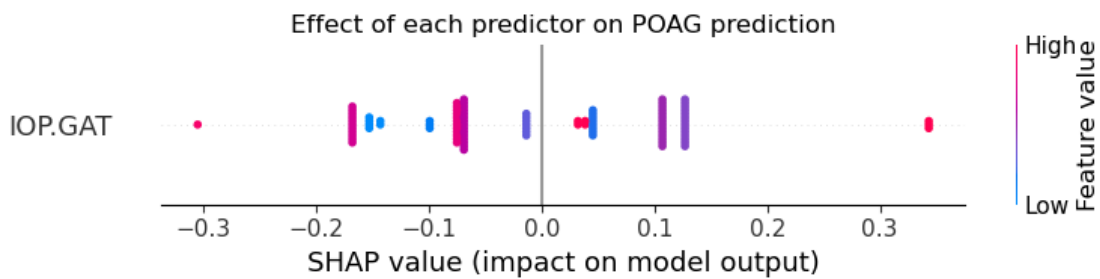


Figure 2.68 SHAP effect of each predictor on POAG detection for GAT only

2.4 Discussion

A total of 14 experimental conditions were analysed: 4 for keratoconus detection and 10 for primary open angle glaucoma detection. The metric chosen to compare the models was the area under the receiver operating characteristic curves (AUROC). The major advantage of using AUROC is that it is not affected by class imbalance and is considered a good indicator of a model's performance in discrimination (Fawcett 2006). Any score above 0.8 is considered good, and anything above 0.9 is excellent. A score of 1.0 represents perfect performance but can sometimes indicate overfitting or circularity in training and testing. A performance of 0.5 is considered random, meaning the model is unable to discriminate between the two conditions and the label is randomly assigned.

2.4.1 Performances GridSearch vs RandomSearch

As can be seen from the table results in the Appendix 11.2, the performances on the test set obtained with hyperparameter tuning using GridSearch and RandomSearch are similar. The performances of algorithms using hyperparameters found with GridSearch rarely are better than those with hyperparameters found with RandomSearch. The major difference lies in the time required to find the best combination of hyperparameters, which depends on the number of hyperparameters to be tuned and, consequently, the number of combinations to try. For some algorithms, the differences in time are minimal (Logistic Regression, Decision Tree, and Random Forest take roughly the same time, with differences of only a few seconds). For others, the differences in time are substantial (SVM and MLP Classifier, up to ten times longer) with minimal performance improvement. RandomSearch does not try all possible combinations, making it more computationally and time efficient, as described in the paper that proposed the technique (Bergstra and Bengio 2012).

2.4.2 Interpretation

Permutation Feature Importance (PFI) and SHAP can lead to different interpretations of the model's features. This occurs because the two methods are intrinsically different: PFI quantifies the importance of each feature by calculating the variation in the model's performance when the feature's values are randomly shuffled. SHAP values, calculated using Shapley values from game theory, reflect the contribution of each feature to the prediction of each instance in the test set and better represent interactions between different features. If there are several interactions among features, SHAP values more accurately

reflect the importance of each feature. Moreover, PFI can be influenced by the permutations if the data are highly correlated, potentially overestimating or underestimating the importance of individual features. If the model is non-linear or very complex, PFI can provide unreliable results, whereas SHAP has more robust theoretical foundations (Hooker and Mentch 2019, Aas, Jullum et al. 2021).

2.4.3 Support Vector Machine

SVM was not used with ORA or GAT data, as it could not handle these datasets. The reason is unknown to the author, but the code crashed every time it was run. A possible explanation lies in the handling of the small dataset. SVMs are efficient in classification and regression tasks but might have limitations when used on low-dimensional datasets. If there are too few features, SVMs tend to overestimate the feature space using kernels to separate data that would not be linearly separable. With too few features, it may be difficult to find a good separating hyperplane due to the high complexity induced by the kernel. Conversely, SVMs work well with high-dimensional dataset (Cortes and Vapnik 1995). Similar conditions have already been reported in literature (Burges and discovery 1998) and a possible solution suggested is to have a minimum number of features that is at least the natural logarithm of the number of instances (Hastie, Tibshirani et al. 2009). Using this approach, it is evident that for the dataset used in this experiment (more than 400 instances), the minimum number of features is 6, while ORA had a maximum of 4 or 5 features, and GAT had 2.

2.4.4 Keratoconus

Performance in keratoconus detection using Corvis ST data has consistently outperformed ORA, both with and without corneal thickness as a parameter. This is anticipated because the Corvis ST evaluates a broader array of dynamic corneal parameters compared to the ORA. For instance, while the ORA primarily provides metrics such as corneal hysteresis and corneal resistance factor that are related to the viscoelastic behaviour of the cornea, the Corvis ST captures additional details—including deformation amplitude, applanation times, and other dynamic responses to an air puff. These extra parameters enable a more nuanced assessment of the cornea's biomechanical behaviour under stress, thereby allowing for a more comprehensive evaluation of corneal biomechanical alterations.

Performance significantly improved when corneal thickness was included among the features, irrespective of the instrument or algorithm used. Exceptions were noted with the MLP Classifier using RandomSearch and Random Forest with GridSearch, both utilising

Corvis ST data, where classification performance was higher without corneal thickness data. The improved performance of algorithms with corneal thickness data aligns with expectations, as corneal thickness is a critical parameter in keratoconus diagnosis, alongside corneal curvature, clinical signs, and best corrected visual acuity, which were not included in the models for this experiment.

Although corneal thickness is typically considered one of the most important parameters in keratoconus detection and diagnosis, analysis of PFI and SHAP graphs indicates it is not the most crucial among Corvis ST measurements. The most important feature is the radius at highest concavity, with an impact two (SHAP) to three (PFI) times that of corneal thickness. This finding is confirmed by some authors (Tian, Huang et al. 2014, Wu, Li et al. 2018), although most literature reports that the greatest differences are found in deformation amplitude at highest concavity (Ali, Patel et al. 2014, Bak-Nielsen, Pedersen et al. 2014, Tian, Huang et al. 2014), In the models created for the experiment, deformation amplitude at highest concavity showed limited importance. According to SHAP analysis, the larger the radius, the smaller the impact on the keratoconus label. This can be explained by the fact that a smaller radius indicates a less rigid cornea, whereas a flatter radius at highest concavity suggests smaller deformation due to increased corneal rigidity. Radius at highest concavity remained the most informative parameter even when corneal thickness was excluded.

Among ORA parameters, corneal thickness was the most important for both PFI and SHAP, as expected. Notably, there is a difference in the analysis of other parameters between SHAP and PFI. In order of importance, PFI ranked the parameters as corneal hysteresis, corneal resistance factor, IOPg, and IOPcc, whereas SHAP ranked them as IOPg, CRF, CH, and IOPcc. This indicates that the contribution of IOP corrected for corneal biomechanical features (corneal hysteresis and corneal resistance factor) is minimal.

Interestingly, SHAP interpretation shows that high values of any parameters measured by ORA negatively impact keratoconus labelling. This aligns with well-established literature from the past 15 years, indicating that eyes with keratoconus exhibit lower values of corneal hysteresis and corneal resistance factor (Ortiz, Piñero et al. 2007, Shah, Laiquzzaman et al. 2007, Galletti, Pfortner et al. 2012).

In recent years, several papers have been published on detecting keratoconus using machine learning and corneal biomechanics, all utilising data from Corvis ST and none from ORA. Castro-Luna et al. investigated the performance of a Random Forest algorithm in

detecting subclinical keratoconus (corneal thickness > 490 μm , mild topographical signs, mean corneal curvature < 46.5 D, no clinical signs such as Fleischer's ring or Vogt's striae). The authors used data from both Corvis ST and Pentacam, achieving an AUROC of 0.992 (sensitivity = 94.2%, specificity = 98.8%) (Castro-Luna, Jiménez-Rodríguez et al. 2021).

Another study aimed to predict keratoconus severity (healthy, mild, moderate, and advanced keratoconus) using Corvis ST data, Linear Discriminant Analysis, and Random Forest algorithms. The Random Forest model demonstrated excellent performance (AUC of 0.97, 0.88, 0.89, and 0.95, respectively) and was considered capable of predicting keratoconus severity without keratometric data (Herber, Pillunat et al. 2021). This study utilised an updated version of Corvis ST software that provided more corneal biomechanical parameters than the version used when data for this experiment were collected.

A large recent study, including 3,886 eyes from 25 different centres, aimed to create an index (TBIv2) using random forest to distinguish normal from keratoconic corneas, using data from both Pentacam and Corvis ST. The dataset included normal and keratoconic corneas, as well as two additional groups with very asymmetric ectatic patients: eyes with normal topography and ectatic unoperated eyes. The results were excellent for normal versus all keratoconic (AUC = 0.985), exceptionally good for normal versus keratoconic and very ectatic corneas (AUC = 0.999), and acceptable for ectatic corneas with normal topography (AUC = 0.899). This study incorporated measurements from Pentacam, and all new parameters measured with Corvis ST (Ambrósio, Machado et al. 2023).

Ren and colleagues built a model to detect clinical and subclinical keratoconus in adolescents using data from Corvis ST and Pentacam. Researchers created several models using multivariate logistic regression. The best model (Model 3) included corneal posterior elevation, deformation amplitude measured 2 mm from the corneal centre and stiffness parameter at the first applanation. Such model reached good performances between different classes (AUC 0.909, sensitivity 0.904, specificity = 0.769) (Ren, Yang et al. 2023).

In the most recent study, authors used Corvis ST images to detect fruste form keratoconus, which is asymptomatic. Data were used to train and validate two different learners: Naïve Bayes and Random Forest. Then, a model based on a majority voting system was built. A majority vote is an ensemble learning technique where each learner predicts the probability of an instance belonging to a class, then the average of all probabilities is calculated, and the label is assigned accordingly. Despite the already excellent performance of the Random Forest on the validation set (AUC = 0.99, specificity = 0.92, sensitivity = 1.00), the voting

system's performance was even better (AUC = 1.00, specificity = 0.75, sensitivity = 1.00). This approach, based solely on Corvis ST images, was found to be highly effective in detecting fruste form keratoconus (Yang, Qi et al. 2024).

Results of the present study and results found in literature are summarised in Table 2.6

Table 2.6 Findings of other studies in terms of AUC in Keratoconus detection

Study	Instrument	Algorithm	AUC
Current	Corvis ST	SVM	0.990
(Castro-Luna, Jiménez-Rodríguez et al. 2021)	Corvis ST	Random Forest	0.992
(Herber, Pillunat et al. 2021)	Corvis ST	Random Forest	0.97
(Ambrósio, Machado et al. 2023)	Corvis ST + Pentacam	Random Forest	0.999
(Ren, Yang et al. 2023)	Corvis ST + Pentacam	Logistic Regression	0.909
(Yang, Qi et al. 2024)	Corvis ST images	Naïve Bayes + Random Forest	0.999/1.00

The results of this experiment align with the literature, with some differences: most studies included data from topography or tomography (Pentacam), while the Corvis ST data used in this study are limited compared to the number of parameters that can be measured with current Corvis ST technology. Moreover, in this study, the absence of proper keratoconus staging precluded further analysis in terms of severity.

2.4.5 Glaucoma

Performance of models in detecting POAG was consistently lower than those for keratoconus. Among the models developed with Corvis ST measurements, the best-performing one did not utilise all the data but excluded central corneal thickness (SVM with GridSearch, AUC = 0.831), slightly better than the model including all measurements (SVM, GridSearch, AUC = 0.830). Excluding IOP from the features markedly reduced performance, as demonstrated by lower AUC values for conditions excluding IOP. Regarding feature importance, IOP was never the most important, ranking behind the time of the second applanation (for both SHAP and PFI). In models excluding IOP, the most important predictors were the times of the first and second applanation.

From SHAP analysis, it was observed that in all developed models, higher values of the time of the second applanation tended to lead to POAG classification. This finding contradicts the literature, which indicates higher values of the time of the second applanation in healthy patients, while POAG patients show lower values. Such differences were statistically significant in a meta-analysis (Wang, Du et al. 2015).

The impact of the time of the first applanation varied: it was marginal in the model including IOP but excluding corneal thickness and showed different directions across models. In the first model (including IOP and corneal thickness), higher values of the time of the first applanation indicated normality, contrary to other models and existing literature (Wang, Du et al. 2015, Lee, Chang et al. 2016), (Salvetat, Zeppieri et al. 2015).

Discrepancies between the impact of individual features and the literature can be attributed to several causes: the overall healthy and POAG groups did not show statistically significant differences in the times of first and second applanations, but the groups created to train and test the model might not be stratified for all features, causing an imbalance and potential bias. It is important to note that SHAP analysis does not explain the model's functioning but calculates the impact of each feature value on the prediction, showing trends but not explanations.

Few studies have recently investigated the use of Corvis ST data and machine learning to detect glaucoma. A study from Brazil compared several supervised learners in myopia (low and high) and glaucoma detection, applying feature selection based on the information provided by each feature. The best learner was the gradient boosting classifier, with performance in terms of accuracy, recall, precision, and F1 comparable to this experiment's results (Leite, Campelos et al. 2022). Another study investigated glaucoma detection in myopic patients using a selection of eight highly informative features, achieving an AUROC of 0.917, with 0.947 for high myopia and 0.857 for non-myopic eyes (Baptista, Ferreira et al. 2024). A third study investigated the detection of glaucoma using densitometry, from Corvis ST Scheimpflug camera. Images were exported, to be segmented and modelled to highlight pixel distribution. Through this analysis two parameters were calculated α (scale parameter, corneal clarity) and β (shape parameter, corneal tissue homogeneity). Authors reached a very good AUROC on the test set (0.94) with Decision Tree using only the first 20 frames (García-Jiménez and Consejo 2022).

Analysing the results of ORA models, performance was lower compared to models using Corvis ST data. The impact of corneal thickness was minimal, as performance did not

decrease when this parameter was excluded (AUROC = 0.893 vs AUROC = 0.894). However, excluding IOP significantly reduced performance; interestingly, excluding both corneal thickness and IOP yielded better performance than excluding only IOP, indicating that corneal thickness might be a confounding factor. In all models, corneal hysteresis was the most important feature for both SHAP and PFI. Unexpectedly, high values of corneal hysteresis drove the decision towards POAG, despite literature documenting lower corneal hysteresis in glaucoma patients and the dataset showing similar trends (CH Normal = 10.2 ± 1.5 mmHg, CH POAG = 8.3 ± 1.9 mmHg). Conversely, a reduction in corneal resistance factor increased the probability of POAG classification, consistent with the dataset distribution (POAG CRF = 8.7 ± 1.9 mmHg; CRF Normal = 9.9 ± 1.6 mmHg). The opposite interpretation of IOPs was also interesting: high IOP_{cc} indicated POAG, while high IOP_g indicated normality, even though both were higher in POAG (IOP_{cc} = 17.6 ± 4.7 mmHg; IOP_g = 16.2 ± 4.2 mmHg) than in healthy patients (IOP_{cc} = 15.1 ± 3.0 mmHg; IOP_g = 14.3 ± 3.0 mmHg). No machine learning model based on ORA data has been published to the author's knowledge.

Machine learning has been extensively used in glaucoma detection with other technologies: OCT (Burgansky-Eliash, Wollstein et al. 2005, Xiong, Li et al. 2022) or fundus photographs (Ramesh, Subramaniam et al. 2022, Wu, Huang et al. 2024), predicting disease progression (Dixit, Yohannan et al. 2021, Mohammadzadeh, Wu et al. 2024) or onset (Singh, Smith et al. 2024) from the visual field.

The performances of the best models developed in this experiment to detect POAG are worse than other techniques that are currently used clinically. Previous research found that the analysis of RNFL thickness showed an AUC of 0.88 (Elbendary and Mohamed Helal 2013) and 0.91 (Medeiros, Zangwill et al. 2005). A recent meta-analysis showed that the performance in detecting is extremely high using fundus photography (AUC = 0.97, sensitivity = 0.92, specificity = 0.93) or OCT (AUC = 0.96, sensitivity = 0.90, specificity = 0.91) in combination with ML (Wu, Nishida et al. 2022). In terms of visual field, the AUC is between 0.88 and 0.93 for 24-2 and between 0.91 and 0.94 for 10-2 (Nishijima, Hosaka et al. 2024). Considering tonometry alone, the AUC drops to 0.78 (Ehrlich, Radcliffe et al. 2012).

Results are summarised in Table 2.7

Table 2.7 Findings of other studies in terms of AUC in POAG detection

Study	Technique	AUC
Current	Corneal Biomechanics + ML	0.831
(Elbendary and Mohamed Helal 2013)	RNFL	0.88
(Medeiros, Zangwill et al. 2005)	RNFL	0.91
(Wu, Nishida et al. 2022)	OCT + ML	0.96
(Wu, Nishida et al. 2022)	Fundus photo + ML	0.97
(Nishijima, Hosaka et al. 2024)	Visual field (24-2)	0.88-0.93
(Nishijima, Hosaka et al. 2024)	Visual field (10-2)	0.91-0.94
(Ehrlich, Radcliffe et al. 2012)	Tonometry	0.78

The confounding findings of some models analysed in this chapter highlight the lack of control over learning processes and the need for explainable AI. Explainable AI refers to the ability to describe, understand, and explain the working principles of an AI model, which are typically considered black boxes. Explainable AI is crucial for building trust in AI, especially in healthcare (Saraswat, Bhattacharya et al. 2022).

2.5 Conclusions

The models created in this chapter exhibit performances that are in line with other studies published. The performance in keratoconus detection is notably better than in POAG detection, and models using Corvis ST data outperform those using ORA data. These results are promising, suggesting that with further refinement, it may be possible to develop a robust index for the early detection of both keratoconus and glaucoma. The superior performance with Corvis ST data can be attributed to its ability to measure a broader range of corneal biomechanical parameters, which provides a more comprehensive understanding of the corneal structure and behaviour.

2.6 Limitations

The major limitation of this study is the unavailability of all Corvis ST parameters, as the data were collected using an older version of the firmware. This restriction may have hindered the full potential of the models. Another significant limitation is the lack of a separate and independent test set, which is crucial for validating the generalizability of the models. Additionally, the selection of the best features was not performed rigorously due to the

already limited number of features available. These constraints highlight the need for more comprehensive datasets and rigorous validation methodologies in future research.

2.7 Future Studies

Future research should aim to address these limitations by incorporating a separate test set to validate the models independently. Rerunning the models with datasets containing updated measures from the latest version of Corvis ST would provide a more accurate assessment of their performance. Furthermore, developing a staging system based on clinical measurements for different pathologies — such as clinical signs and topographies for keratoconus, and visual field, retinal images, and OCT for POAG — would enhance the diagnostic accuracy. Expanding the research to include other ocular pathologies could also provide valuable insights and improve the general applicability of the models. This broader approach could lead to more comprehensive screening tools capable of early detection across a range of eye conditions, ultimately benefiting clinical practice and patient outcomes.

3 Impact of Keratoconus Data on Glaucoma Screening Algorithm

3.1 Introduction

Glaucoma is a leading cause of irreversible blindness worldwide, and early detection is critical for preventing progressive vision loss. Optometrists screen for glaucoma by measuring IOP, with the diagnosis subsequently confirmed through OCT, fundus examinations, and visual field tests (Shah, Bowd et al. 2006, Thomas, Loibl et al. 2011, Michelessi, Lucenteforte et al. 2015). However, IOP measurements are significantly influenced by corneal biomechanics (Tian, Huang et al. 2014, Herber, Vinciguerra et al. 2020). Since conditions such as keratoconus alter these biomechanical properties, they may confound the screening process.

Recent advancements have shown that machine learning (ML) algorithms can detect glaucomatous damage and keratoconic alterations in corneal biomechanics (see previous chapter). Despite these promising results, it remains unclear whether an ML model trained to detect glaucoma might produce false-positive results when screening patients with keratoconus but without glaucoma. Therefore, the primary rationale of this study is to investigate whether altered corneal biomechanics in non-glaucomatous keratoconic eyes adversely impact the diagnostic accuracy of ML-based glaucoma screening. Clarifying this issue is essential for refining screening protocols and ensuring reliable diagnosis in populations with corneal biomechanical abnormalities.

Orange Data Mining is an open-source software platform that provides a visual programming interface for building and comparing machine learning models without requiring extensive coding skills. Orange was selected for the current analysis because it allows for rapid prototyping and transparent workflow construction, which is particularly advantageous when integrating data from instruments such as the Ocular Response Analyzer (ORA) and Corvis ST. Its user-friendly interface facilitates the exploration and optimization of multiple algorithms, thus enhancing reproducibility and interpretability—key factors in clinical research (Demšar, Curk et al. 2013). This approach enables researchers with limited programming expertise to efficiently develop and test models aimed at predicting the absence of glaucoma.

The hypothesis was that if keratoconus significantly affected glaucoma screening, the model would show a statistically significant reduction in correctly identifying non-glaucomatous eyes among those with keratoconus compared to those without. Supporting this hypothesis would suggest that the variation in corneal biomechanics in non-glaucomatous eyes, with or without keratoconus, is a contributing factor.

Additionally, this study aimed to determine (a) whether corneal biomechanics measured with ORA or Corvis ST were more susceptible to these errors, and (b) whether two different models, Naïve Bayes (NB) or Logistic Regression (LR), would yield consistent results. These models were selected because they can highlight the relative importance of ORA or Corvis ST parameters, offering 'white box' solutions that address explanatory issues often encountered with machine learning algorithms. Consequently, the models developed in this study can provide clinically interpretable decision support, enabling clinicians to understand the reasoning behind the model's outputs rather than relying solely on its predictions.

3.2 Methods

3.2.1 Use of both eyes from the same research participants

Both eyes from the same subjects were included in this study, considering previous research that highlights the asymmetric nature of glaucoma (Rodríguez-Robles, Verdú-Monedero et al. 2023) and keratoconus (Zadnik, Steger-May et al. 2002). Thus, both eyes of each participant were analysed in the present study. By analysing both eyes, the aim was to capture the full spectrum of intra-subject variability, which may enhance the sensitivity of the machine learning models. This approach reflects the clinical reality and provides additional insights that could improve the model's performance, while any potential bias introduced by the non-independence of eyes will be addressed in subsequent studies.

Consistent with the previous chapter, data were collected by Dr Haslina at Birmingham and Midland Eye Centre, City Hospital, Birmingham during her PhD. Although a formal sample size calculation was not performed, it is common in data science to utilise the entire available dataset rather than pre-defining a sample size, as it mimics the "all-inclusive" approach allowed us to maximize the real-world data available.

While the current dataset did not include detailed demographic information or precise severity metrics for glaucoma and keratoconus, the primary focus of the study was on

leveraging a large, diverse set of clinical data to develop robust predictive models. It is important to note that all data were anonymized for privacy reasons, which prevented the retrieval of detailed patient identifiers or additional demographic information.

3.2.2 Dataset A for creating models

Dataset A, used for creating models, consisted of 409 eyes without keratoconus from approximately half that number of participants. Among these eyes, 253 were classified as normal, 47 had ocular hypertension (OHT), 19 had normal tension glaucoma (NTG), and 90 had primary open-angle glaucoma (POAG). These classifications were made by an ophthalmologist, ensuring that all models were based on eyes without the corneal biomechanical changes associated with keratoconus.

3.2.3 Dataset B for investigating the impact of keratoconus on glaucoma screening

Dataset B was utilised to explore the impact of keratoconus on glaucoma screening. It included 150 eyes without glaucoma, of which 78 had keratoconus. The models needed to correctly identify all 150 eyes as free of glaucoma. By comparing the number of errors in eyes with and without keratoconus, the impact of keratoconus on glaucoma screening could be determined. It is crucial to note that the eyes labelled as normal in Dataset B were not present in Dataset A. Dataset B was created by extracting 72 eyes from the normal group and merging them with the keratoconic eyes.

3.2.4 Corneal biomechanics measured using ORA and Corvis ST

Separate models were developed using the corneal biomechanical parameters measured by ORA and Corvis ST. Since it is uncommon for clinics to have access to both instruments, a single model combining measurements from both was deemed irrelevant to clinical practice. Additionally, one of the study's objectives was to determine which device was more affected by the corneal biomechanical properties of keratoconic eyes.

ORA provided four measurements: corneal-corrected IOP (IOP_{cc}), Goldmann-correlated IOP (IOP_g), corneal hysteresis (CH), and corneal resistance factor (CRF).

Corvis ST provided twelve measurements, including IOP based on the first applanation response, central corneal thickness (CCT), time to the first applanation (A1T), cord length of the cornea during the first applanation (A1L), velocity of the first applanation (A1V), equivalent measurements for the second applanation (A2T, A2L, and A2V), the amplitude of corneal movement at the highest corneal concavity deformation (DA), the radius of corneal curvature at the highest corneal concavity deformation (HcR), the distance of the most anterior point of the anterior corneal surface during the highest corneal concavity deformation (HcD), and the time to reach the highest corneal concavity deformation (HcT).

3.2.5 Use of Orange Data Mining software to create the models

Free and open-source Orange Data Mining software (version 3.37.0), developed by the Bioinformatics Laboratory at the University of Ljubljana in Slovenia (Demšar, Curk et al. 2013), was utilised to create the models. This software is specifically designed for individuals without a background in computer science, enabling any clinician to replicate this analysis if desired.

Figure 3.1 illustrates the virtual canvas with connected widgets used in this part of the processing.

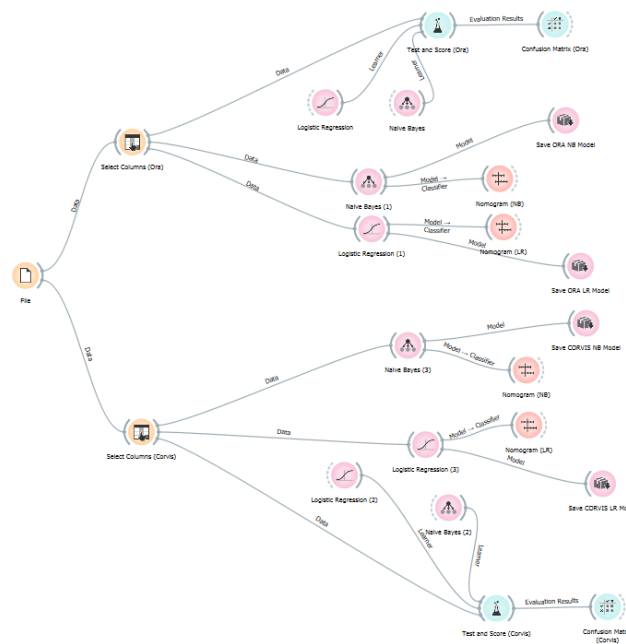


Figure 3.1 : Orange Data Mining canvas and connected widgets used to create the ORA NB, ORA LR, Corvis ST NB and Corvis ST LR models

The File widget was used to upload Dataset A. The Select Columns widgets enabled the assignment of independent variables (corneal biomechanics measurements) and dependent variables (diagnosis categories: normal, OHT, NTG, and POAG) for the ORA and Corvis ST models. The upper part of Figure 1 represents the ORA models, while the lower part represents the Corvis ST models, with identically connected widgets.

Naive Bayes (NB) and Logistic Regression (LR) widgets were employed to perform two types of conventional supervised machine learning. Logistic regression is more complex as it can be hyperparameter tuned for optimal performance by adjusting its Lasso regularisation strength. Lasso regularisation offers the advantage of eliminating redundant independent variables, which is explained in greater detail in Chapter 2.

Connections between these widgets and the Test and Score widget facilitated hyperparameter tuning and comparison of model performance based on the Area Under the Receiver Operating Characteristic Curve (AUROC), averaged across all classes (normal, OHT, NTG, and POAG) after 10-fold stratified cross-validation.

The Confusion Matrix widgets were connected to allow observation of correct and incorrect class predictions made by each model. This study focused on predictions where normal eyes were either correctly identified or incorrectly classified as OHT, NTG, or POAG.

Nomogram widgets were connected to display the relative absolute importance of corneal biomechanical parameters in identifying normal eyes. The Save widgets were utilised to store the four created models (ORA NB, ORA LR, Corvis ST NB, and Corvis ST LR) for future use.

3.2.6 Use of Orange Data Mining software for investigating the impact of keratoconus on glaucoma screening

Figure 3.2 shows the virtual canvas with connected widgets that carried this part of the processing.

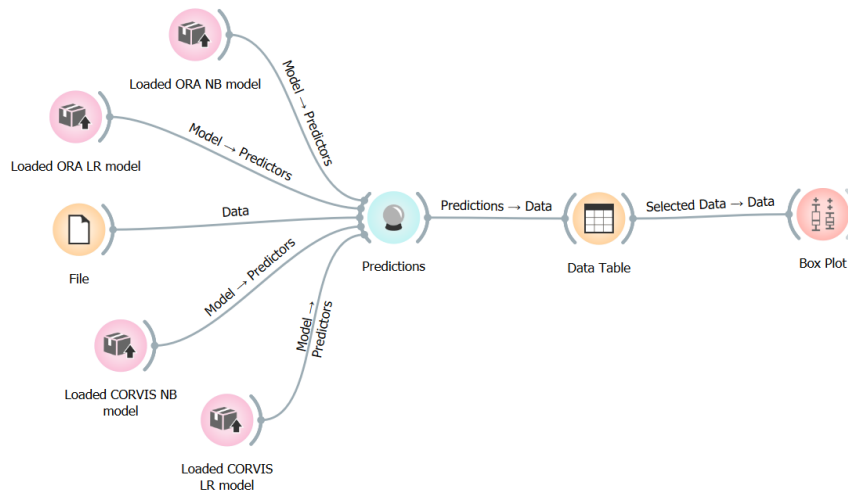


Figure 3.2 : Orange Data Mining canvas and connected widgets used to create the ORA NB, ORA LR, Corvis ST NB and Corvis ST LR models

The File widget was used to upload Dataset B. The Load Model widgets retrieved the four previously stored models (ORA NB, ORA LR, Corvis ST NB, and Corvis ST LR). Predictions made by all four models applied to Dataset B were passed through the Predictions and Data Table widgets to the Box Plot widget. Here, the Chi-square test was employed to determine whether any of the four models showed a statistically significant reduction in correctly identifying normal (non-glaucomatous) eyes in cases with and without keratoconus.

3.3 Results and Discussion

3.3.1 Main study findings

This study utilised machine learning models to investigate how keratoconic alterations in corneal biomechanics affect glaucoma screening outcomes based on measurements from the Ocular Response Analyzer (ORA) and Corvis ST.

To avoid the risk of overfitting, cross-validation, hyperparameter tuning, and a separate test dataset were employed.

Cross-validation helps minimise overfitting, as implemented via the Test and Score widget shown in Figure 1. This method splits the training data into stratified folds, ensuring that a model is never tested on the same data it was trained on. Stratified folds maintain the same proportion of classes (Normal, POAG, OHT, and NTG). Using 10 folds means that 10 versions of each model were tested, providing a realistic estimate of model performance.

Hyperparameter tuning optimises model complexity to prevent overfitting (high variance) and underfitting (high bias). This tuning process involves assigning weights to each predictor (independent) variable in the form of log odds ratios in NB and LR models. The complexity of the models is at its maximum when these log odds ratios exert their maximum cumulative effect on each predicted (dependent) variable. LR models have the advantage of hyperparameter tuning through a regularisation strength parameter (C), which adjusts the cumulative effect of each log odds ratio, thereby reducing model complexity to achieve the bias-variance trade-off.

In this study, hyperparameter tuning required regularisation values of $C = 25$ for the ORA LR model and $C = 1$ for the Corvis ST LR model, both using Lasso regularisation.

3.3.2 Model for Glaucoma

Table 3.1 displays the AUROC values of all four models. The Corvis ST LR model (AUROC = 0.807) outperformed the others, whose AUROC values ranged from 0.780 to 0.753. This data, obtained from the Test and Score widgets shown in Figure 1, indicates that the hyperparameter-tuned LR models generally performed better than the NB models. However, the performance difference was relatively marginal. According to D'Agostino et al. (2013), an AUROC below 0.7 is considered suboptimal, 0.7 to 0.8 is good, and above 0.8 is excellent (D'Agostino, Pencina et al. 2013).

Table 3.1 The performance of all four models (ORA NB, ORA LR, Corvis ST NB and Corvis ST LR) ranked in order of best to worst in terms of the area under the ROC curve (AUROC) averaged over all classes (Normal, OHT, NTG and POAG), after 10-fold stratified cross validation

Model	AUROC
Corvis ST LR	0.807
ORA LR	0.780
Corvis ST NB	0.771
ORA NB	0.753

Table 3.2 illustrates the relative importance of the corneal biomechanical parameters measured by ORA and Corvis ST in predicting normal eyes without keratoconus, as determined by the ORA NB, ORA LR, Corvis ST NB, and Corvis ST LR models. This part of the study examines the consistency with which the two machine learning models evaluated relative importance. This information was derived from the Nomogram widgets connected to

each of the four models shown in Figure 1. Where applicable, IOP and CCT are highlighted in red to indicate their relative importance. It is noteworthy how many corneal biomechanical parameters were deemed more important than IOP and CCT for glaucoma screening. Table 2 indicates that there were considerable inconsistencies between models regarding the relative importance of corneal biomechanical parameters. However, Table 1 showed that the performance of all models ranged from good to excellent.

Table 3.2 The relative importance of the 12 Corvis ST and 3 ORA corneal biomechanical parameters according to the ORA NB, ORA LR, Corvis ST NB and Corvis ST LR models. Where applicable, IOP and CCT are highlighted in red

Model	Corneal biomechanical parameters listed in order of most to least important
Corvis ST LR	A2T > HcR > IOP > A2V > A1T > CCT > A1L > HCPD > HCT > A2L > DA > A1V
Corvis ST NB	A2T > A2L > A1L > DA > A2V > A1T > A1V > IOP > HcR > HcT > HCPD > CCT
ORA LR	CRF > IOP _{cc} > IOP _g > CH
ORA NB	IOP _g > IOP _{cc} > CH > CRF

None of the models perfectly predicted cases free of glaucoma (Normal). This is illustrated in Table 3.3, which shows the baseline performance in terms of errors associated with each model's predictions of Normal. This information was obtained from the Confusion Matrix widgets connected to each of the four models in Figure 1. Table 3 may be of interest as it displays the percentages of correct (Normal) and incorrect (POAG, OHT, and NTG) predictions, focusing on predictive values rather than sensitivity.

Table 3.3 Baseline performance of the ORA NB, ORA LR, Corvis ST NB and Corvis ST LR models that had been trained on Dataset A (as shown in the Orange Data Mining canvas of Figure 1). Values show, for each model, the percentage (and frequency) of the predicted Normal that were correct (green: as these were Normal in reality) and incorrect (red: as these were POAG, OHT or NTG in reality).

Model	Normal	POAG	OHT	NTG
Corvis ST LR	70.5% (241)	18.1% (62)	6.4% (22)	5.0% (17)
Corvis ST NB	81.1% (167)	14.1% (29)	2.9% (6)	1.9% (4)
ORA LR	72.7% (240)	17.0% (56)	5.8% (19)	4.5% (15)
ORA NB	78.5% (193)	13.4% (33)	3.7% (9)	4.5% (11)

3.3.3 Impact of Keratoconus on Glaucoma Screening

Table 1.1 Table 3.4 presents the results of investigations into the impact of keratoconus on glaucoma screening. The ORA NB, ORA LR, Corvis ST NB, and Corvis ST LR models, trained on Dataset A (as depicted in the Orange Data Mining canvas in Figure 3.1), were used to make predictions on Dataset B, which included Normal eyes with and without keratoconus. It is crucial to note that Dataset A contained no cases of keratoconus, meaning that none of the four models had been trained on data exhibiting the corneal biomechanical properties of keratoconic eyes.

The application of these models to Dataset B, which comprised eyes without glaucoma but about half of which had keratoconus, was designed to identify any confounding effects on predictions due to the corneal biomechanical properties associated with keratoconus. Table 4 shows, for each model, the percentage (and frequency) of correctly (green) and incorrectly (red) predicted Normal cases in eyes with and without keratoconus. P-values from Chi-square tests compare the predictions made in eyes with and without keratoconus by each model.

These analyses, derived from the Box Plot widget in the Orange Data Mining canvas in Figure 3.2, reveal a consistent, statistically significant decrease in the percentage of correctly classified non-glaucomatous eyes in cases with keratoconus (66.7 - 100% depending on the model) compared to those without keratoconus (24.4 – 94.9% depending on the model). Table 4 also indicates an increase in the number of normal eyes misclassified as having POAG (0 - 11.1% in eyes without keratoconus compared to 2.3 - 51.3% in eyes with keratoconus, depending on the model) or NTG (0 - 15.1% in eyes without keratoconus compared to 0 - 65.4% in eyes with keratoconus, depending on the model).

Table 3.4 The impact of keratoconus on glaucoma screening is revealed by observing the performance of the ORA NB, ORA LR, Corvis ST NB and Corvis ST LR models, that had been trained on dataset A (as shown in the Orange Data Mining canvas of Figure 1) that had been used to make predictions on Dataset B containing Normal without and with keratoconus. Values show, for each model, the percentage (and frequency) of the predicted Normal that were correct (green: as these were Normal in reality) and incorrect (red: as these were POAG, OHT or NTG in reality) in eyes with and without keratoconus. P-values (from Chi-square tests) are shown for the comparison of predictions made in eyes without and with keratoconus by each model

Model	Normal without keratoconus				Normal with keratoconus				P-value (Chi ² , df)
	Normal	POAG	OHT	NTG	Normal	POAG	OHT	NTG	
Corvis ST LR	98.6% (71)	1.4% (1)	0% (0)	0% (0)	80.8% (63)	14.1% (11)	0% (0)	5.1% (4)	0.002 (12.59, 2)
Corvis ST NB	66.7%	6.9%	11.1%	15.3%	24.4%	10.3%	0%	65.4%	<0.001

	(48)	(5)	(8)	(11)	(19)	(8)	(0)	(51)	(46.89, 3)
ORA LR	100%	0%	0%	0%	94.9%	2.6%	2.6%	0%	0.150
	(72)	(0)	(0)	(0)	(74)	(2)	(2)	(0)	(3.79, 2)
ORA NB	77.8%	11.1%	11.1%	0%	46.2%	51.3%	2.6%	0%	<0.001
	(56)	(8)	(8)	(0)	(36)	(40)	(2)	(0)	(29.09, 2)

These findings suggest that alterations in corneal biomechanical properties due to keratoconus may confound glaucoma screening, potentially increasing false positives. This information will be of particular interest to primary care clinicians who use ORA and Corvis ST machines for screening keratoconus or glaucoma. It may also be of interest to manufacturers of these machines, who might want to develop corrective algorithms to address these issues when screening for glaucoma in keratoconic eyes.

The potential impact of keratoconic biomechanical alterations on glaucoma screening has been hypothesised by some authors (Cohen and Myers 2010, Curatolo, Birkenfeld et al. 2020) but this effect has not been quantified until now.

To that end, the limitations of this study are now discussed followed by recommendations for further study that might lead to the desired corrective algorithms.

3.3.4 Study limitations and recommended further research

- (1) The study revealed that corneal biomechanical parameters potentially confound glaucoma screening when using Corvis ST and ORA machines.
- (2) Although previous studies have documented that glaucomatous damage and keratoconus exhibit asymmetry between eyes, the current analysis included both eyes from each participant. This methodological choice could introduce bias due to the non-independence of observations from the same individual. It is clear that including both eyes might lead to an overestimation of the effective sample size and potentially affect the precision of our estimates; therefore, this represents a limitation of the study.
- (3) One limitation of the study is the unequal number of cases in each subgroup, which can distort the findings of machine learning models. To address this, Datasets A and B should be reconstructed to contain equal numbers in each subgroup before re-

running the analysis. However, this re-analysis would result in less data for the machine learners to train on, as all subgroups would be limited to the size of the smallest group (e.g., only 19 cases in the OHT group).

- (4) Keratoconic eyes were not included in Dataset A. If excluding them reduces the confounding observed in Table 4, this approach could provide a corrective algorithm beneficial for users and manufacturers of ORA and Corvis ST. This supports the continued use of 'white box' machine learning models like NB and LR, as both reveal the log odds ratios that form their models.
- (5) Although 'white box' machine learning methods like NB and LR are recommended, other methods such as decision trees (available in Orange Data Mining) should also be considered. Furthermore, 'black box' methods, including support vector machines, neural networks, random forests, and various boosting methods available in Orange Data Mining, can be explored. These models can be created and saved using the Save Model (Figure 1) and Load Model (Figure 2) widgets. However, Orange Data Mining currently lacks functions like Grid Search or Random Search for hyperparameter optimization, making hyperparameter tuning time-consuming.
- (6) Newer versions of the Corvis ST software include novel indices that were not available when the dataset was collected. It would be worthwhile to rerun the entire experiment, incorporating these newer indices.

3.4 Conclusions

The findings of this study suggest that keratoconic alterations to corneal biomechanical properties may confound glaucoma screening, potentially leading to an increased rate of false positives. This is of significant concern for ophthalmologists and optometrists, as accurate glaucoma screening is critical for early detection and management of the disease. These results will be particularly relevant to users and manufacturers of the ORA and Corvis ST, both of which are commonly employed in clinical settings to assess corneal biomechanics.

Moreover, the study highlights the utility of Orange Data Mining, a powerful tool developed at the University of Ljubljana, which is especially beneficial for individuals lacking advanced coding skills. Orange Data Mining allows users to engage in data mining by simply connecting widgets, thereby making complex data analysis more accessible through its intuitive interface and comprehensive tutorials. This democratization of data analysis tools is

crucial in fostering a broader understanding of data science principles among researchers and clinicians alike.

The integration of Orange Data Mining or similar software into undergraduate programmes is strongly recommended. Providing students with hands-on experience in these tools will enable them to grasp the basics of machine learning and data analysis. Such knowledge is increasingly essential given the profound transformations occurring in scientific research and the anticipated advancements in clinical practices. Equipping the next generation of professionals with these skills will be pivotal in ensuring they are prepared to leverage emerging technologies and methodologies in their respective fields.

By incorporating these tools into educational curricula, institutions can better prepare students for the demands of modern research and clinical environments, ultimately enhancing their ability to contribute to advancements in healthcare and other scientific domains.

Following the exploration of machine learning algorithms for the diagnosis of KC and POAG, attention now shifts towards a new instrument capable of quantifying ocular biomechanical properties: the Brillouin Optical Scanner System (BOSS), whose functioning and development were discussed in Chapter 1. Due to its recent introduction, clinical research on the BOSS is quite limited. Therefore, the following chapters will investigate the repeatability of its measurements, the relationships between measurements from the BOSS, ORA, and Corvis ST, as well as the effects of age-related and refractive errors on ocular biomechanics.

4 BOSS Repeatability

4.1 Introduction

The concept of repeatability represents a fundamental aspect of scientific measurements for multiple reasons. Firstly, repeatability is a crucial indicator of an instrument's reliability and accuracy, reflecting its ability to provide stable and consistent results when the same sample or condition is assessed multiple times under identical conditions (Bartlett and Frost 2008). Ensuring high repeatability is essential for data reproducibility, as it guarantees consistency over time and across different instruments, thus supporting comparability and validity of experimental outcomes (Atkinson and Nevill 1998). High repeatability also minimizes variability within identical measurement conditions, which is vital for establishing the precision and trustworthiness of obtained data, especially in clinical settings where measurement consistency directly impacts decision-making and patient outcomes (Koo and Li 2016). Moreover, repeatability can be viewed as a critical component of the broader concept of reproducibility, which pertains to the capability of obtaining the same or similar results when key conditions such as operators, instruments, time-points, or laboratories are varied (Goodman, Fanelli et al. 2016). Assessing and documenting repeatability thus not only confirms the internal reliability of instruments but also strengthens confidence in subsequent interpretations and applications of scientific and clinical findings.

In this experiment the intra-session and inter-session repeatability of the Brillouin Optical Scanner System (BOSS, Intelon Optics, Woburn, MA, USA) were assessed. Intra-session is defined as the repeatability within the same session, so different measurements separated by few minutes, while for inter-session is meant that the two measurements are usually taken days or weeks apart. To date, this is the first study that investigates the BOSS repeatability.

4.2 Material and Methods

4.2.1 Participants

67 participants were enrolled in the study: all 67 completed the intrasession experiment, 63 completed the both the visits to assess intersession repeatability. Each participant chose the eye that had to be measured (52 OD, 15 OS) and underwent three different scans for both cornea and lens, the first as baseline measurement, the second time 15 minutes after the first one (intra-session repeatability), and the third two 14 days apart (inter-session

repeatability). The inclusion criteria were the absence of ocular pathology and not to have worn contact lenses in the 24 hours prior to the experiment. Only one BOSS machine, operated by the same skilled researcher, was utilised in this study.

4.2.2 Scan Pattern

The cornea scan strategy used was the 4-dots scan, where four different locations of the cornea are scanned. Scanned points were located 2 mm upper (BSup), lower (BInf), nasally (BNas), and temporally (BTem) to the detected centre of the pupil, the mean of the four measurements was included in the analysis too (Mean). The BOSS has a specific function that detects the centre of the pupil, that is indicated by four green arrows. The centre of the pupil is calculated using the pupil itself as reference for the creation of a circle and the centre is calculated and displayed live on the screen. To be accepted, each scanned point had to be assessed as “GOOD” by the quality index, if the level had any other indication (“LOW” or “AVERAGE”) the scan was repeated, until the measure was good enough.

The lens scan was done 1 mm temporally to the centre of the pupil, as it is not possible to carry out a measurement in the centre of the lens (or of the cornea), due to the reflection caused by the front surface of the tissue that lowers the quality of the measurement. The distance of 1 mm was chosen considering that the average pupil diameter is unlikely to be smaller than 3 mm (Kobashi, Kamiya et al. 2012), no vertical offset was considered. Any lens scan must have a quality index score lower than 3 to be accepted. The BOSS quality index for the lens scan has a reverse scale, where the higher score means lower quality and a score of 0 means that the measurement was optimal.

Both the quality indices (cornea and lens) are based on the number of points on the z-axis not properly scanned by the BOSS.

4.2.3 Statistical Analysis

The data analysis was carried out using JupyterLab from Anaconda, using the following packages: pandas, numpy, matplotlib, scipy, seaborn, statsmodels and sklearn. The repeatability was assessed creating Bland Altman plots, correlation (Pearson and Spearman), regression, within subject standard deviation (wSD), coefficient of variation (CV) and coefficient of variation within-subject (CVwS).

4.3 Results

4.3.1 Mean and Standard Deviation for all the three sets of measurements

Alongside mean and standard deviation of the three sets of measurements, in the Table 4.1 is shown the CV, defined as the ratio between SD and mean, and that can be considered an expression of the spread of the data around the mean (Lovie 2005). In Figure 4.1 there are histograms with the values of average and SD for the three sets of measurements.

Table 4.1 Mean, Standard Deviation and Coefficient of Variation for the three sets of measurements

Measurement	Mean	SD	CV (%)	Measurement	Mean	SD	CV (%)
BSup#1	2.831	0.051	1.81	BLens#1	3.381	0.057	1.67
BSup#2	2.827	0.053	1.88	BLens#2	3.387	0.048	1.43
BSup#3	2.832	0.063	2.22	BLens#3	3.365	0.132	3.93
BNas#1	2.819	0.057	2.01	TopPlat#1	2.811	0.521	18.53
BNas#2	2.820	0.067	2.38	TopPlat#2	2.809	0.498	17.73
BNas#3	2.810	0.067	2.39	TopPlat#3	2.822	0.592	20.97
BInf#1	2.811	0.064	2.26	BotPlat#1	4.223	0.583	13.81
BInf#2	2.807	0.062	2.21	BotPlat#2	4.316	0.568	13.17
BInf#3	2.797	0.068	2.44	BotPlat#3	4.258	0.600	14.08
BTem#1	2.824	0.059	2.09	AntSI#1	1.563	0.423	27.03
BTem#2	2.809	0.061	2.17	AntSI#2	1.567	0.462	29.49
BTem#3	2.789	0.059	2.11	AntSI#3	1.628	0.539	33.12
BMean#1	2.821	0.038	1.36	PostSI#1	-1.546	0.564	36.49
BMean#2	2.816	0.044	1.57	PostSI#2	-1.354	0.491	36.24
BMean#3	2.807	0.044	1.57	PostSI#3`	-1.443	0.451	31.28

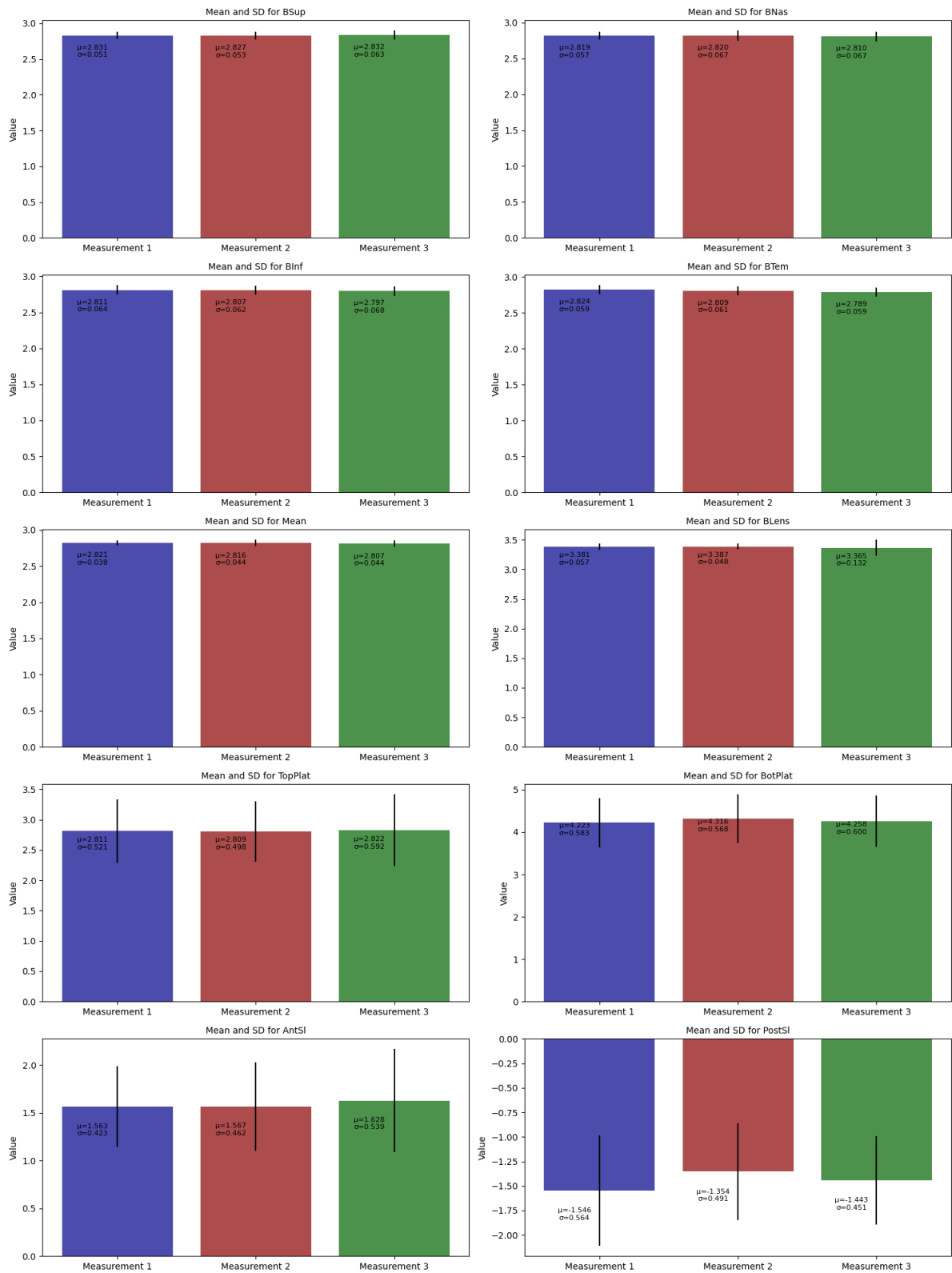


Figure 4.1 Histograms of the mean and standard deviation for the three sets of measurements

4.3.2 Bland Altman Analysis and Coefficient of Variation

The use of Bland Altman plots (Bland and Altman 1986) allowed the calculation of the bias (B), that is defined as the mean of the differences between the two measurements:

$$B = \frac{1}{n} \sum_{i=1}^n (x_{i1} - x_{i2})$$

Eq. 4.1 Bias for Bland Altman analysis

and the Coefficient of Repeatability (COR), defined as:

$$COR = B \pm (1.96 \times SD)$$

Eq. 4.2 Coefficient of Repeatability

The interval within COR limits is the range where lie the 95% of the differences between the two measurements (Bland and Altman 1996).

Within-subject standard deviation (wSD) represents the variability within a single participant and is defined in

$$wSD = \sqrt{\frac{1}{2} \times \frac{\sum_{i=1}^n ((x_{i1} - x_{i2}) - \bar{x})^2}{n - 1}}$$

Eq. 4.3 Within-subjects Standard Deviation (wSD)

The Coefficient of Variation within Subjects ($CVwS$) is a percentage defined as the ratio between the within-subjects standard deviation and the mean of the measurement for each subject. It is dimensionless and allows for the comparison between different variables or scales, in this case it represents the average of the ratio between the within-subjects standard deviation and the average of the two measurements calculated for every single participant.

Table 4.2 and Table 4.3 contain the results of the Bland Altman analysis for intrasession and intersession repeatability.

Table 4.2 Intrasession Repeatability

Measure	Bias	Lower COR limit	Upper COR limit	COR Interval	Ratio (Mean/ Interval)	wSD	CVwS (%)
BSup [GPa]	0.004	-0.119	0.128	0.247	0.09	0.044	1.14
BNas [GPa]	0.003	-0.160	0.166	0.326	0.12	0.056	1.59
BInf [GPa]	0.005	-0.156	0.166	0.321	0.11	0.059	1.63
BTem [GPa]	0.014	-0.156	0.183	0.340	0.12	0.060	1.63
BMean [GPa]	0.006	-0.091	0.104	0.196	0.07	0.034	0.99
BLens [GPa]	-0.002	-0.083	0.079	0.163	0.05	0.035	0.60
TopPlat [mm]	0.007	-0.766	0.780	1.546	0.55	0.287	7.77
BotPlat [mm]	-0.090	-1.142	0.963	2.106	0.49	0.388	6.89
AntSI [GPa/mm]	0.002	-1.214	1.218	2.432	0.09	0.450	20.69
PostSI [GPa/mm]	-0.183	-1.445	1.078	2.523	0.12	0.468	20.55

Table 4.3 Intersession Repeatability Table

Measure	Bias	Lower COR limit	Upper COR limit	COR Interval	Ratio (Mean/ Interval)	wSD	CVwS (%)
BSup [GPa]	-0.002	-0.158	0.154	0.312	0.11	0.079	1.45
BNas [GPa]	0.009	-0.171	0.189	0.360	0.13	0.092	2.08
BInf [GPa]	0.014	-0.174	0.202	0.376	0.13	0.096	1.93
BTem [GPa]	0.034	-0.120	0.188	0.308	0.11	0.079	1.65
BMean [GPa]	0.014	-0.103	0.131	0.234	0.08	0.060	1.21
Lens [GPa]	0.004	-0.100	0.108	0.208	0.06	0.139	0.77
TopPlat [mm]	-0.010	-0.806	0.786	1.592	0.57	0.406	8.87
BotPlat [mm]	-0.035	-1.047	0.978	2.024	0.48	0.516	6.80
AntSI [GPa/mm]	-0.065	-1.438	1.309	2.747	1.72	0.701	21.79
PostSI [GPa/mm]	-0.103	-1.307	1.101	2.408	1.61	0.614	22.20

The Bias (red line) and the 95% Coefficient of Repeatability Interval (green lines) are plotted in the following graphs for both intra and inter session repeatability: on the x axis is plotted the mean between the two variables, while on the y axis is plotted the difference between the two variables.

4.3.2.1 Bland Altman Intrasession Repeatability plots

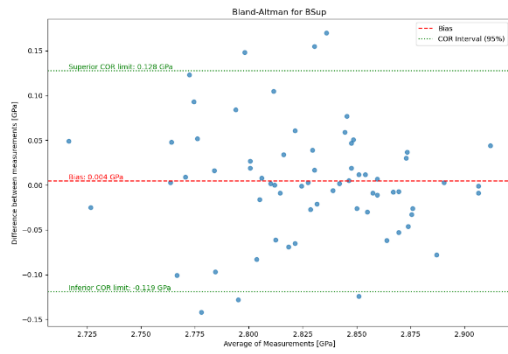


Figure 4.2 Bland Altman Plot (Bias and 95% of COR interval) for the intrasession repeatability of the Brillouin modulus measured in the superior part of the cornea.

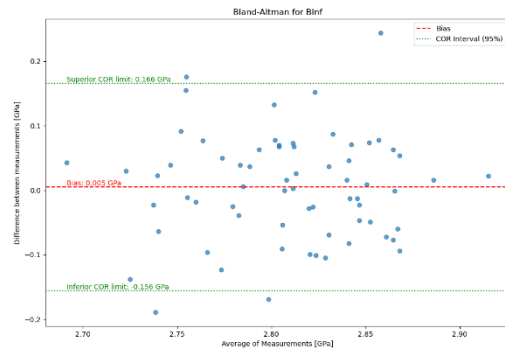


Figure 4.3 Bland Altman Plot (Bias and 95% of COR interval) for the intrasession repeatability of the Brillouin modulus measured in the inferior part of the cornea

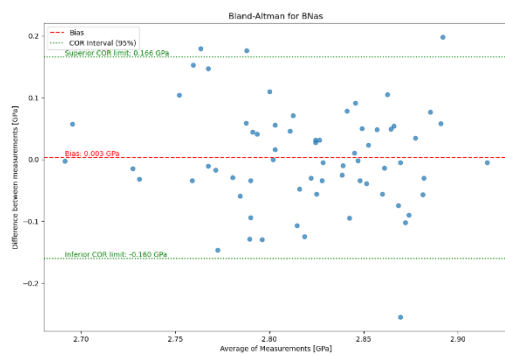


Figure 4.4 Bland Altman Plot (Bias and 95% of COR interval) for the intrasession repeatability of the Brillouin modulus measured in the nasal part of the cornea

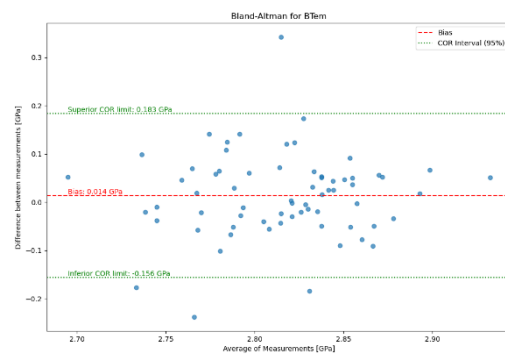


Figure 4.5 Bland Altman Plot (Bias and 95% of COR interval) for the intrasession repeatability of the Brillouin modulus measured in the temporal part of the cornea

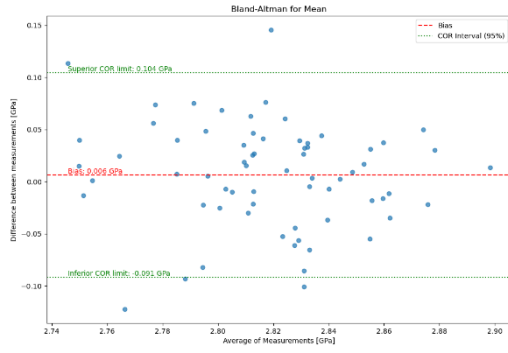


Figure 4.6 Bland Altman Plot (Bias and 95% of COR interval) for the intrasession repeatability of the mean corneal Brillouin modulus

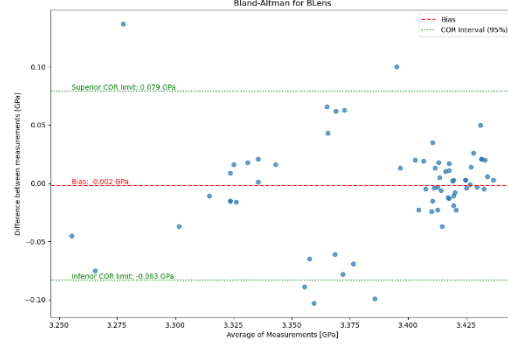


Figure 4.7 Bland Altman Plot (Bias and 95% of COR interval) for the intrasession repeatability of the crystalline Brillouin modulus

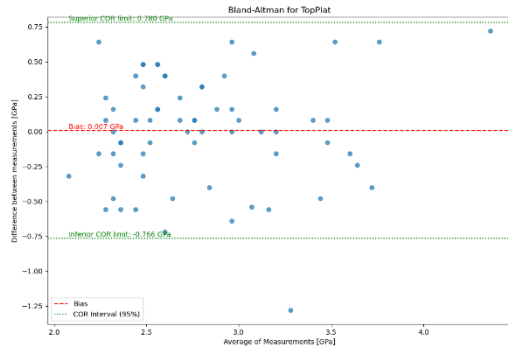


Figure 4.8 Bland Altman Plot (Bias and 95% of COR interval) for the intrasession repeatability of the top plateau

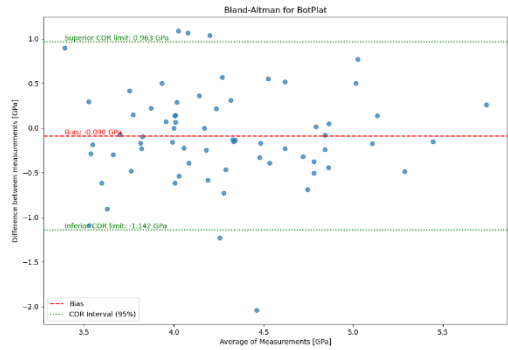


Figure 4.9 Bland Altman Plot (Bias and 95% of COR interval) for the intrasession repeatability of the bottom plateau

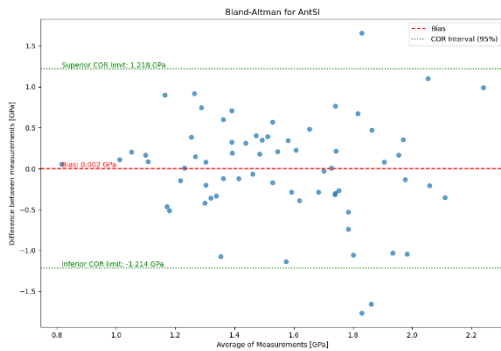


Figure 4.10 Bland Altman Plot (Bias and 95% of COR interval) for the intrasession repeatability of the anterior slope

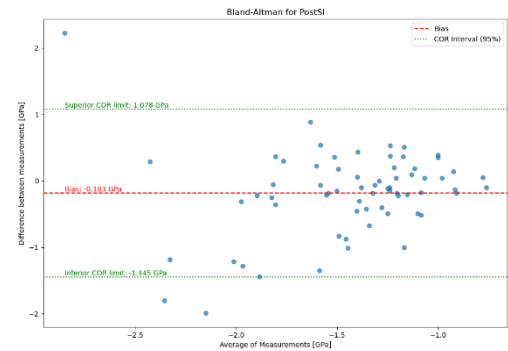


Figure 4.11 Bland Altman Plot (Bias and 95% of COR interval) for the intrasession repeatability of the posterior slope

4.3.2.2 Bland Altman Intersession repeatability plots:

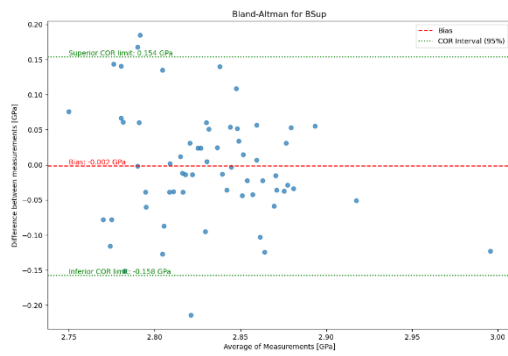


Figure 4.12 Bland Altman Plot (Bias and 95% of COR interval) for the intersession repeatability of the Brillouin modulus measured in the superior part of the cornea

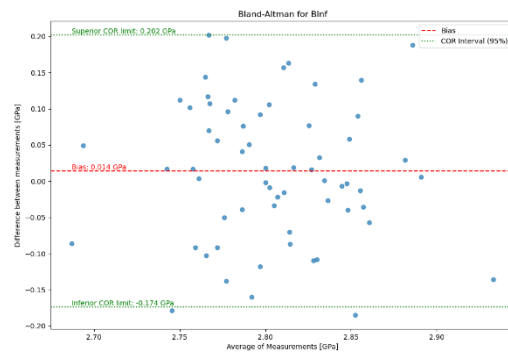


Figure 4.13 Bland Altman Plot (Bias and 95% of COR interval) for the intersession repeatability of the Brillouin modulus measured in the inferior part of the cornea

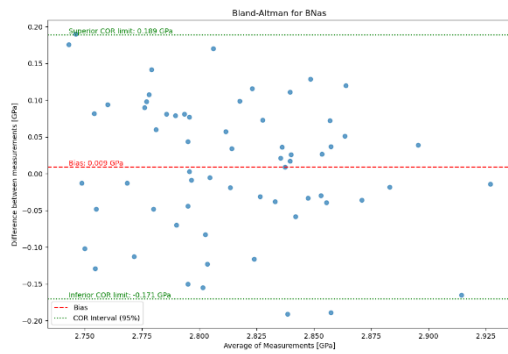


Figure 4.14 Bland Altman Plot (Bias and 95% of COR interval) for the intersession repeatability of the Brillouin modulus measured in the nasal part of the cornea

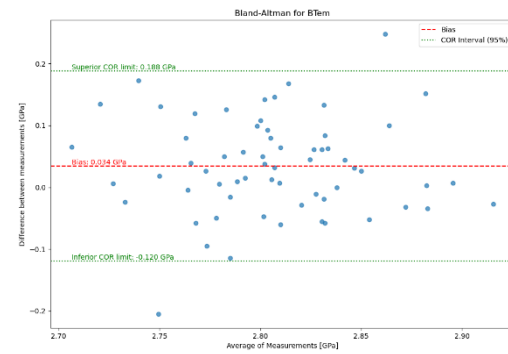


Figure 4.15 Bland Altman Plot (Bias and 95% of COR interval) for the intersession repeatability of the Brillouin modulus measured in the temporal part of the cornea

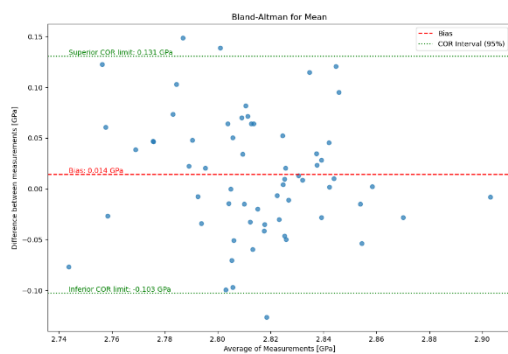


Figure 4.16 Bland Altman Plot (Bias and 95% of COR interval) for the intersession repeatability of the mean corneal Brillouin modulus

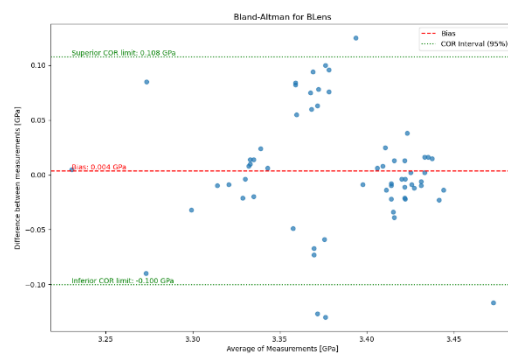


Figure 4.17 Bland Altman Plot (Bias and 95% of COR interval) for the intersession repeatability of the crystalline Brillouin modulus

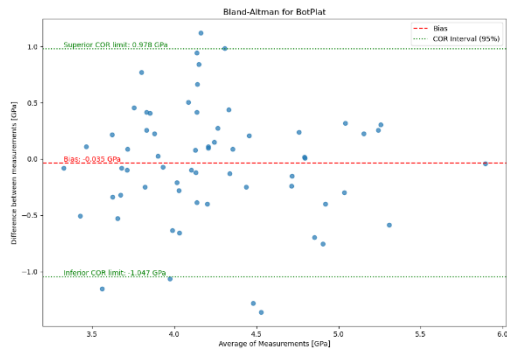


Figure 4.18 Bland Altman Plot (Bias and 95% of COR interval) for the intersession repeatability of the top plateau

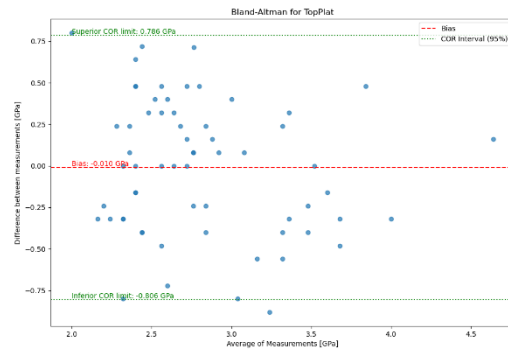


Figure 4.19 Bland Altman Plot (Bias and 95% of COR interval) for the intersession repeatability of the bottom plateau

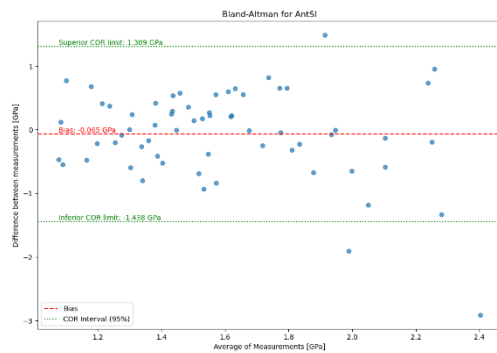


Figure 4.20 Bland Altman Plot (Bias and 95% of COR interval) for the intersession repeatability of the anterior slope

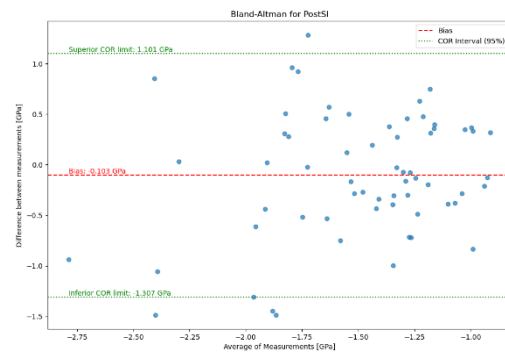


Figure 4.21 Bland Altman Plot (Bias and 95% of COR interval) for the intersession repeatability of the posterior slope

4.3.3 Is the bias proportional to value measured?

Using the same plotted data (mean vs difference) correlations (r , p , and R^2) and regression lines were calculated to determine whether the bias increases or decreases linearly with the measurement. To test for correlation the first step was to check that mean and differences were normally distributed. Kolmogorov-Smirnov and Shapiro Wilk tests were used because the size of the sample could not assure that one test would have been more accurate than the other: some authors report that the power of Shapiro-Wilk test decreases when the sample size is larger than 50 (Mendes, Pala et al. 2003), while other authors state that Kolmogorov-Smirnov is more powerful than Shapiro-Wilk only when the sample size is larger than 100 (Steinshog, Tjøstheim et al. 2007, Razali, Wah et al. 2011). If Mean and Difference

were normally distributed ($p < 0.05$) Pearson correlation was used, in any other case Spearman correlation was used.

The results of the tests can be found in Tables Table 11.15-18:

The analysis of the results presented in these tables reveals no statistically significant correlation among the measured parameters, indicating a consistent bias that does not vary with changes in the magnitude of these parameters. This consistency in bias, devoid of proportional fluctuations relative to the measured parameters, is a positive outcome, suggesting reliability in the measurement process. The findings affirm the stability of the bias across varying measurement conditions, negating the presence of a systematic relationship between the bias and the parameter magnitudes. This stability is crucial for the integrity of the measurement process, warranting the absence of any linear or predictable variation in bias with changes in the parameters.

4.3.4 Difference in intersession repeatability due to time of the measurement

It is well known that the water content of the stroma can influence the measurement of the Brillouin modulus (Silverman, Patel et al. 2009) (Shao, Seiler et al. 2018), and that the water content changes throughout the day (Harper, Boulton et al. 1996). To examine this effect, the variation in the time of day between the first and third measurements was considered, while the second measurement was excluded from this analysis due to its occurrence merely 15 minutes after the first and can be assumed that water content does not change in such small timeframe. Consequently, two additional analyses were conducted to further explore this aspect:

- 1) For each single parameter, the difference in terms of time of the day between the first and third measurements was plotted against the difference in terms of value. In this case were considered both the relative difference (positive, when the third measure was taken earlier than the first one, or negative, when it was taken later, TimeD analysis) and the absolute value of the difference (TimeDABS analysis). Both TimeD and TimeDABS considered the difference in terms of time of the day as a continuous measurement.
- 2) A series of Bland Altman plots, dividing the data according to the time difference with data divided in groups according to the time difference, between measurement 1 and 3.
3. For the relative difference data were divided in three groups: A (< -3 hours

difference), B (between -0,5 and 0,5 hours difference), and C (> 3 hours difference), so in the group A the second measure was taken at least three hours before the first (if the first was taken at 4 pm, the first was taken at 1 pm at the latest), in the group B roughly at the same time (half an hour earlier or later) and in the group C three hours later (if the first measure was taken at 11 am the second one was taken at least at 2 pm). For the absolute difference the data were divided in two groups: A (up to half an hour difference) and B (at least three hours difference).

The results for the experiment 1 are plotted in Table 4.4-5:

Table 4.4 Correlation between TimeD and differences in BOSS measurements

Variable	SW stat	SW p	Correlation test	r	Corr p	R ²
BSup	0.984	0.595	Pearson	-0.031	0.812	0.001
BNas	0.980	0.395	Pearson	0.362	0.004	0.131
BInf	0.985	0.661	Pearson	0.135	0.239	0.018
BTem	0.987	0.749	Pearson	-0.001	0.996	0.000
Mean	0.992	0.961	Pearson	-0.200	0.117	0.040
BLens	0.949	0.012	Spearman	-0.140	0.272	0.020

Table 4.5 Correlation between TimeDABS and differences in BOSS measurements

Variable	SW stat	SW p	Correlation test	r	Corr p	R ²
BSup	0.984	0.595	Spearman	-0.212	0.095	0.045
BNas	0.980	0.395	Spearman	-0.130	0.308	0.017
BInf	0.985	0.661	Spearman	-0.052	0.688	0.003
BTem	0.987	0.749	Spearman	-0.143	0.264	0.020
Mean	0.992	0.961	Spearman	-0.200	0.117	0.040
BLens	0.949	0.012	Spearman	-0.099	0.440	0.010

It worths noting that TimeD variable is normally distributed (Shapiro-Wilk test $W = 0.980$, $p = 0.302$), while TimeDABS is not (Shapiro-Wilk test $W = 0.911$, $p = 0.000$).

The observed statistical analysis revealed a sole statistically significant correlation ($p = 0.004$), albeit weak ($r = 0.364$), between the relative difference in time of the day (TimeD) and the variation of the Brillouin Modulus measured in the inferior part of the cornea (BInf).

No statistically significant correlations were found between TimeDABS and any measurement taken by the BOSS.

The second analysis based on time involved the creation of three different groups for the TimeD classification and two for the TimeDABS and testing them to verify the presence of differences in repeatability due to different time of the measurements. The size of the groups created for TimeD were A = 13, B = 22 and C = 6, while the groups for TimeDABS were A = 22 and B = 19.

For the TimeD analysis the difference between groups were tested using ANOVA and Kruskal-Wallis (KW), while to test for differences between TimeDABS groups were used t-test and Mann-Whitney U. The choice of the test was based on the outcome of the normality test conducted on all subgroups.

The results of the tests for normality of distribution and differences between groups are listed in Table 4.5-6.

Table 4.6 Results of Normality test (Shapiro Wilk) and for differences between groups in TimeD subgroups

	Shapiro Group A	Shapiro A p value	Shapiro Group B	Shapiro B p value	Shapiro Group C	Shapiro C p value	Test	Test Stat	P value
BSup	0.966	0.844	0.948	0.282	0.962	0.836	ANOVA	2.021	0.146
BNas	0.938	0.432	0.985	0.975	0.963	0.841	ANOVA	2.999	0.062
BInf	0.953	0.645	0.978	0.879	0.963	0.841	ANOVA	1.478	0.241
BTem	0.975	0.950	0.953	0.365	0.693	0.005	KW	0.507	0.776
Mean	0.976	0.956	0.940	0.194	0.940	0.658	ANOVA	1.903	0.163
BLens	0.959	0.736	0.933	0.144	0.930	0.579	ANOVA	0.005	0.995

Table 4.7 Results of Normality test (Shapiro Wilk) and for differences between groups in TimeDABS subgroups

	Shapiro Group A	Shapiro A p value	Shapiro Group B	Shapiro B p value	Test	Test Statistics	P value
BSup	0.948	0.282	0.970	0.771	t-test	2.009	0.052
BNas	0.985	0.975	0.950	0.398	t-test	1.064	0.294
BInf	0.978	0.879	0.980	0.942	t-test	0.482	0.632
BTem	0.953	0.365	0.933	0.198	t-test	0.987	0.330

Mean	0.940	0.194	0.981	0.955	t-test	1.550	0.130
BLens	0.933	0.144	0.934	0.209	t-test	0.084	0.934

From the above tables it is possible to see that the groups of the TimeD analysis are all normally distributed, except for the group C (> 3 hours difference) of the measurement of the Brillouin modulus in the temporal part of the cornea (BTem). It is important to consider that Group C of TimeD analysis only has 6 members and that being so small is more prone to distribution shifts. The statistical analysis revealed that the differences between the distributions of the three groups were not statistically significant, the only parameter that had subgroups that were close to be statistically different was the measurement of Brillouin modulus in the nasal portion of the cornea (Bias BNas Group A: -0.029 ± 0.088 GPa; Bias BNas Group B: 0.019 ± 0.068 GPa; Bias BNas Group C: -0.032 ± 0.064 GPa; $p = 0.062$).

All the subgroups created for TimeDABS analysis were normally distributed, the t-test revealed no statistically significant differences between groups A and B. The only parameter that was close to be statistically significant different was the measurement of Brillouin modulus in the superior part of the cornea (Bias BSup Group A: 0.019 ± 0.068 GPa; Bias BSup Group B: -0.030 ± 0.081 GPa, $p = 0.052$).

The experimental conditions that were close to be statistically significant different are BNas for Time D and BSup for TimeDABS. Figure 4.22-23 show the differences between groups with Bland Altman plots.

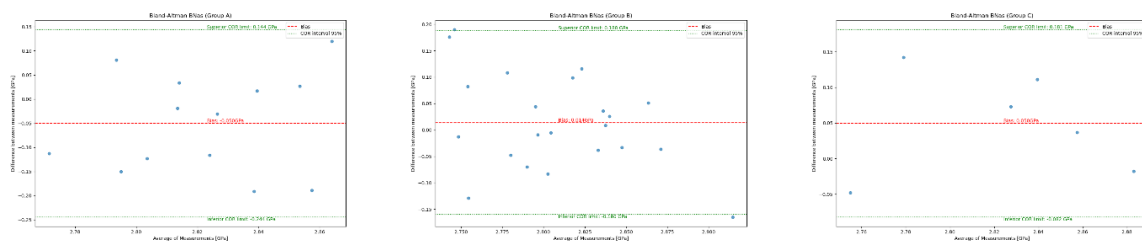


Figure 4.22 Bland Altman plots for TimeD subgroups for Brillouin modulus measured in the nasal part of the cornea

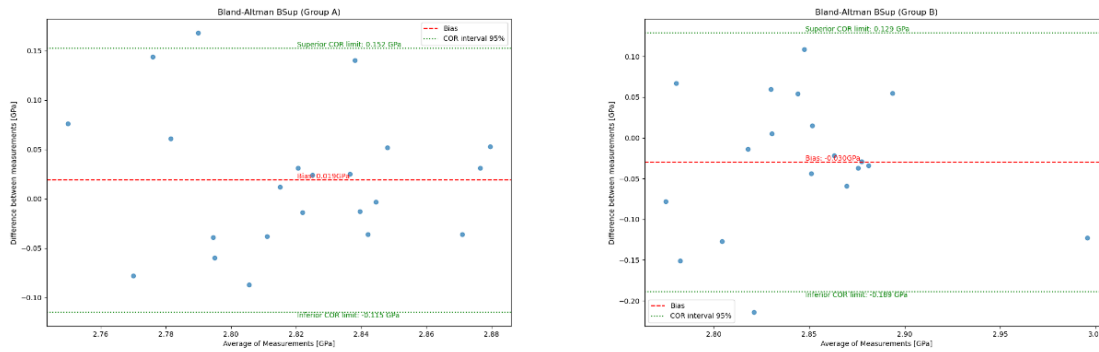


Figure 4.23 Bland Altman plots for TimeDABS subgroups for Brillouin modulus measured in the superior part of the cornea

Tables with all the data for Bland Altman plots for TimeD and TimeDABS are in Table 11.19 and Table 11.20.

4.3.5 ICC

Intraclass Correlation Coefficient (ICC) was calculated for intra and intersession repeatability. Due to the nature of the experiment, it was used Cronbach’s Alpha (Tavakol and Dennick 2011), a two ways mixed model (Koo and Li 2016) to test absolute agreement between average measures (McGraw and Wong 1996). The results for the ICC for the Brillouin Modulus measurements are in the following Tables.

4.3.5.1 ICC Intrasection

Table 4.8 ICC for Intrasection repeatability

	ICC	Superior CI Limit	Inferior CI limit	F Test	p-value
BSup	0.423	0.030	0.477	1.725	0.014
BNas	0.246	-0.235	0.538	1.322	0.130
BInf	0.199	-0.310	0.510	1.246	0.187
BTem	0.050	-0.535	0.414	1.054	0.416
Mean	0.440	0.091	0.655	1.787	0.010
BLens	0.722	0.548	0.829	3.589	<0.001

4.3.5.2 ICC Intersession

Table 4.9 ICC for Intersession repeatability

	ICC	Superior CI Limit	Inferior CI limit	F Test	p-value
BSup	0.075	-0.214	0.285	1.080	0.382
BNas	-0.198	-0.991	-0.277	0.836	0.759
BInf	-0.128	-0.859	0.316	0.886	0.683
BTem	0.179	-0.257	0.478	1.256	0.186
Mean	-0.086	-0.752	0.333	0.918	0.632
BLens	0.710	0.522	0.825	3.441	<0.001

4.3.6 Repeatability of Cornea Measurements

Regardless Location

Another analysis was carried out considering all corneal measurements, regardless position, and location. Such analysis can be considered more general and related to the quality of the measurement provided by the technology.

4.3.6.1 Bland Altman Analysis

Table 4.10 Bland Altman analysis for all corneal measurements (excluding Mean) regardless location

	Bias	Lower COR	Upper COR	COR Interval	Ratio	wSD	CVwSD
Intrasession	0.006	-0.148	0.161	0.309	0.11	0.042	1.49
Intersession	0.014	-0.157	0.185	0.342	0.12	0.050	1.77

The significance of the differences was tested using Z test for matched pairs: the intrasession bias is 0.115 ± 0.604 GPa lower than the intersession Bias ($p = 0.002$), the intra session within- subjects SD is -0.008 ± 0.050 GPa lower than the inter session one ($p = 0.012$) and the coefficient of variation within subjects is $0.28 \pm 1,78$ % lower than the intersession one ($p = 0.011$).

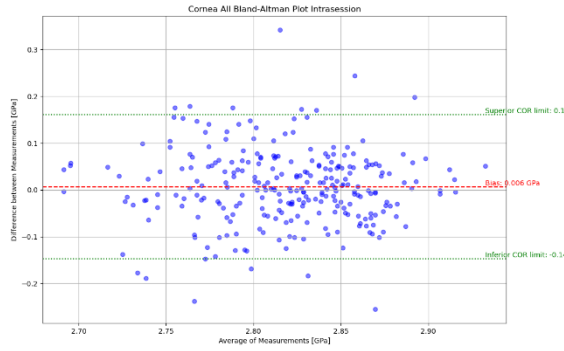


Figure 4.24 Bland Altman plots for Intrasession Repeatability of all corneal measurements (excluding Mean) regardless location

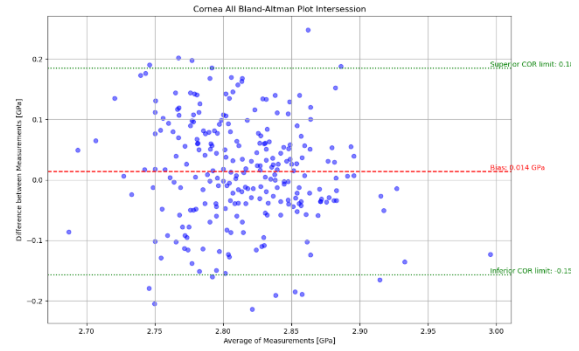


Figure 4.25 Bland Altman plots for Intersession Repeatability of all corneal measurements (excluding Mean) regardless location

4.3.6.2 Correlation between Value and Bias

The correlation between the difference in terms of magnitude of the corneal Brillouin modulus value is statistically significant, albeit very weak (correlation coefficient = - 0.131), only for the intersession repeatability, but not within the same session.

Table 4.11 Correlation between mean value and Bias for all corneal measurements (excluding Mean) regardless location

	Normality p Mean	Normality p Difference	Method	Correlation Coefficient	Correlation p value
Intrasession	<0.001	0.30	Spearman	-0.048	0.431
Intersession	<0.001	0.48	Spearman	-0.131	0.038

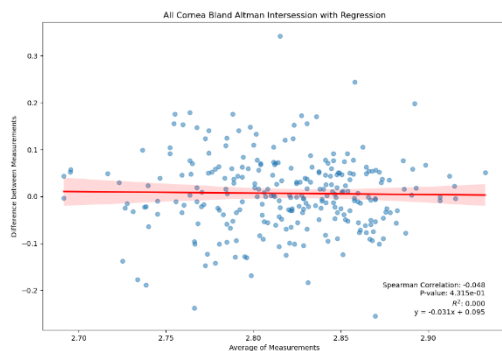
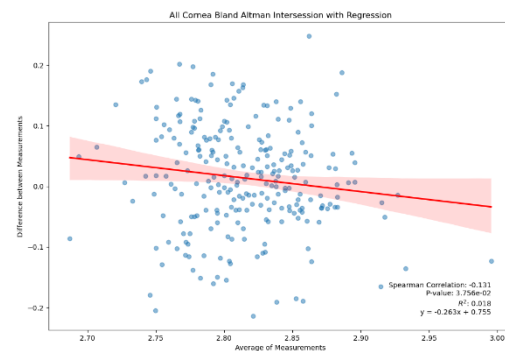


Figure 4.26 Correlation between average of the measurements and difference between the measurements for intrasession repeatability of



Brillouin modulus for all corneal measurements (excluding Mean) regardless location

Figure 4.27 Correlation between average of the measurements and difference between the measurements for intersession repeatability of

Brillouin modulus for all corneal measurements (excluding Mean) regardless location

4.3.6.3 ICC

Table 4.12 ICC for all corneal measurements (excluding Mean) regardless locations

	ICC	Superior CI limit	Inferior CI limit	F Test	P value
Intrasession	0.239	0.032	0.401	1.314	0.013
Intersession	0.045	-0.217	0.251	1.048	0.356

The calculation of ICC is relevant and statistically significant, albeit low, only for measurement within the same session. Measurements take in separate sessions are less repeatable.

4.4 Discussion

Within the array of parameters quantified by the BOSS, the Brillouin modulus emerges as the most consistent in terms of repeatability. This assertion is substantiated by the data presented in the Bland-Altman plots and further corroborated by the calculated coefficients, specifically the coefficient of variation (CV), the within-subject coefficient of variation (CVwS), and the coefficient of repeatability (COR).

The reproducibility of values associated with plateaus and slopes is notably lower. This variability is largely ascribable to their computation being based on transitional zones between the lens cortexes and the nucleus. The BOSS precludes central crystalline lens measurements due to pronounced reflections, necessitating an established offset of 1 mm towards the temporal side for practical measurement. The BOSS does not have an intrinsic mechanism to adjust for ocular movements. Thus, the practitioner must compensate for any patient-related ocular or head movement during the examination. The final offset, quantified in both y and x coordinates, is computed as the arithmetic mean of the offsets recorded throughout the duration of the measurement, taking the calculated pupillary centre as the reference point.

Results from correlations clearly show that Bias is not dependent on the Brillouin modulus. This is evident from the lack of strong and statistically significant correlations between the

average and difference in measurements for both intra and inter session repeatability. This conclusion holds regardless of whether the Shapiro-Wilk or Kolmogorov-Smirnov test is used to assess the normality of the distribution.

4.4.1 Ratio between means and COR interval

The comparative analysis between the Coefficient of Repeatability (COR) Interval and the mean average of Brillouin modulus measurements (utilising the first and second measurements for intra-session, and the first and third for inter-session) reveals that the COR intervals account for approximately 10% of the average in corneal measurements. This percentage varies, ranging from 9 to 12% in intra-session and 11 to 13% in inter-session evaluations. In a marked contrast, lens modulus measurements demonstrate significantly lower percentages, with 5% for intra-session and 6% for inter-session. This difference can be primarily attributed to the denser scanning frequency in the lens area, involving several tens of points at 0.1 mm intervals, thereby yielding greater consistency. In comparison, corneal measurements typically do not exceed four points (also at 0.1 mm intervals), a limitation often imposed by the corneal detection system's capabilities. The lower number of points measured within each scan increases variability and decreases repeatability, because the influence of a single outlier is higher.

It is noteworthy that the ratios were consistently slightly lower in intra-session analyses and moderately higher in inter-session analyses. In contrast, for other parameters, the ratio between the average and the COR interval was significantly higher, approximately 50% for TopPlat and BotPlat, and surpassing 100% for AntSI and PostSI.

4.4.2 ICC

The analysis of ICC results confirms that corneal Brillouin modulus measurements are less repeatable than lens Brillouin modulus measurements. In intrasession repeatability BSup (ICC = 0.423, $p = 0.014$) and Mean (ICC = 0.440, $p = 0.010$) are the only corneal measurements associated with a significant p value, while all the other corneal parameters have lower values of ICC and non-significant p values. In the intersession analysis no one of the corneal measurement had a statistically significant value of ICC. In both the analysis the lens modulus showed good values of ICC (intra ICC = 0.722, p value < 0.001; inter ICC = 0.710, p value < 0.001), confirming that, using BOSS, the measurement of the lenticular modulus is more repeatable than the corneal one.

A post hoc analysis was conducted using Monte Carlo simulations. Specifically, 1000 datasets were simulated under the assumption of the desired ICC (0.75), which represents the minimally acceptable reliability threshold for clinical acceptability (Koo and Li 2016)). For each simulated dataset, ICC values and their associated 95% confidence intervals were computed. Power was estimated as the proportion of simulations in which the upper bound of the ICC's 95% confidence interval fell below the desired ICC threshold. The resulting power estimates were very low (range: 0.01 to 0.03). Such extremely low power values indicate that, given the current sample sizes ($n = 67$ and $n = 63$), the study had minimal ability to statistically confirm that the observed ICC was significantly lower than the desired ICC threshold of 0.75. Consequently, the observed poor repeatability values likely reflect genuinely low reliability rather than inadequate sample sizes. Therefore, it can be stated that the sample size is adequate and future studies can use similar sample size.

4.4.3 Time of the measurement

The only statistically significant correlation found between the absolute time difference (TimeD) and BNas suggests a potential, albeit minimal (the trendline has an equation of $y = 0.014x + 0.016$), impact of time of the measurement on corneal stiffness measured value, as showed in Figure 4.28.

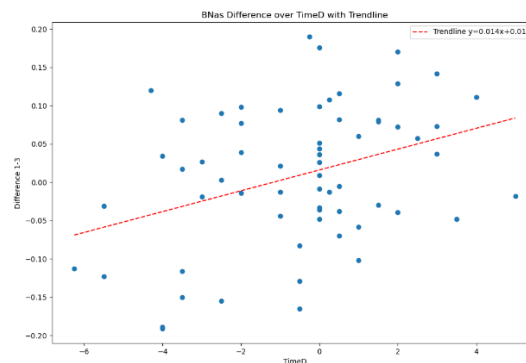


Figure 4.28 Time difference between the measurements and difference of Brillouin modulus measured in the nasal part of the cornea

However, no other strong or statistically significant correlation was detected between the time of day and the stiffness of either the cornea or the lens, as well as between the absolute difference in time (TimeDABS) and intersession measurement differences. The results collectively suggest that, based on the data gathered, the time of day does not have a noticeable impact on the measurement outcomes.

Differences in terms of repeatability were not found during the groups analysis. Therefore, it is possible to state that repeatability is not influenced by the time difference (relative or absolute) between the two visits.

Two studies explored how corneal hydration affects Brillouin measurements. A recent paper (Seiler, Shao et al. 2018) conducted in vitro research on rabbit corneas and discovered that hydration levels positively influence the Brillouin frequency shift, particularly in the anterior stroma. They observed that the shift ranged from 2.499 to 2.904 GPa with hydration levels varying between 5% and 20%. For corneas with normal hydration (around 13%), the longitudinal Brillouin modulus was determined to be approximately 2.673 GPa. On the other hand, Another study (Shao, Seiler et al. 2018) observed that changes in the Brillouin frequency due to sleep were fully reversed within 2 hours after opening the eyes. They noted that from 2 to 9 hours post-awakening, the Brillouin frequency deviations from the average value had a standard deviation of 7.2 MHz, indicating stable hydration levels during this period and negligible variation in the Brillouin frequency shift, and hence the Brillouin modulus. Consequently, the authors recommended measuring the corneal modulus at least two hours after waking up to ensure accuracy.

It is important to note that this study does not focus on the variation during the time of the day, but on the repeatability of the measurements taken during different part of the day. The experiment's limitation pertains to the constrained time frame for measurements, which were solely conducted between 9 am and 5 pm. This limitation excludes data from early morning and late-night periods, potentially impacting the comprehensiveness of the results. However, it is important to note that this time span aligns with the usual operational hours of clinical settings, thereby reflecting the practical realities of routine examinations.

4.4.4 All Cornea Measurements together

From the analysis of all the corneal measurements together, regardless the location, it is clear that the intrasession repeatability is higher than the intersession repeatability, as Bias, within subjects SD and Coefficient of Variability within subjects are statistically significantly lower. The ratio between the mean and the COR interval is similar between intra and intersession analysis. Bias and mean negatively correlate in intersession analysis, but the correlation coefficient, albeit statistically significant, is weak. This finding may suggest that the influence of magnitude of the measured value does not influence the bias at least with measurements taken few minutes apart, that can be considered a positive finding. Such relationship cannot be confirmed for measurements take days or weeks apart and further

studies are needed, as the technology is innovative and there might be several factors that could influence the measured value.

4.5 Conclusion

The aggregated data clearly indicate that crystalline lens modulus measurements obtained with the BOSS exhibit good repeatability. Conversely, repeatability for corneal modulus measurements is considerably lower, despite intra-session repeatability being consistently higher than inter-session repeatability. Furthermore, additional lens parameters such as plateaus and slopes show inherently greater variability due to the intrinsic characteristics of the quantification process. This variability underscores the need for caution when interpreting and applying these specific parameters clinically.

Following a recent update, the company reduced the step size between measurement points along the z-axis, enabling more focused and precise data acquisition within the cornea (previously, only two or three points were typically scanned at each location). This refinement significantly decreases the time spent unnecessarily analysing the aqueous humour, thus enhancing measurement efficiency and potentially improving repeatability.

In the following Chapter the comparison with other instruments' indices that quantify corneal biomechanical properties (ORA and Corvis ST) is investigated, to understand if the measurements overlap.

5 Is BOSS interchangeable with ORA or Corvis ST?

5.1 Introduction

The precise assessment of corneal biomechanics has become increasingly critical in the diagnosis and management of various ocular conditions, including keratoconus, glaucoma, and postoperative refractive surgery. Traditionally, the Ocular Response Analyzer (ORA, Reichert, Inc., Depew, NY, USA) and Corneal Visualization Scheimpflug Technology (Corvis ST, OCULUS Optikgeräte GmbH, Wetzlar, Germany) have served as pivotal tools in this domain, each offering unique methodologies and insights. Recently, Brillouin Optical Scanning System (BOSS, Intelon Optics, Woburn, MA, USA) was introduced in clinical settings offering a different analysis of corneal biomechanics, as it is able to measure the longitudinal elastic modulus (here called Brillouin modulus) in several locations on the cornea and can create a map of the distribution of the modulus.

Several studies have examined the correlations between measurements obtained from the ORA and the Corvis ST. A study reported that while many Corvis ST parameters showed significant correlations with CH measured by ORA, the strength of these correlations ranged from weak to moderate. Specifically, parameters such as deformation amplitude ratio ($R = -0.51$), stiffness parameter at first applanation (SP-A1, $R = 0.41$), and inverse radius ($R = -0.44$) exhibited significant correlations with CH. An optimal model for explaining CH using Corvis ST measurements included the first and second applanation times, deformation amplitude at maximum concavity, and central corneal thickness, achieving a determination coefficient of $R^2 = 0.67$ (Fujishiro, Matsuura et al. 2020).

Another study compared biomechanical parameters measured with ORA and Corvis ST in glaucomatous eyes. Their results showed that while many Corvis ST parameters were significantly correlated with CH and CRF measured by ORA, the strength of these correlations remained weak to moderate. Similarly, the best predictive model for CH included the first and second applanation times, deformation amplitude at maximum concavity, and central corneal thickness, with a determination coefficient of $R^2 = 0.67$ (Matsuura, Hirasawa et al. 2016).

Furthermore, Salouti et al. (2018) compared ORA, Corvis ST, and GAT in healthy children. Their findings indicated significant correlations between various CST parameters and CH, CRF, IOPg, and IOPcc as measured by ORA. However, correlations between IOP measurements obtained using the three devices (GAT, ORA, and Corvis ST) were weak or negligible (Salouti, Alishiri et al. 2018).

Despite these observed correlations, it is important to highlight that ORA and Corvis ST assess different biomechanical properties of the cornea. ORA primarily provides measurements of CH and CRF, which are dynamic indicators of corneal viscoelasticity and its ability to absorb and dissipate energy. These parameters are influenced by both the elastic and viscous components of the corneal tissue.

Conversely, Corvis ST evaluates corneal biomechanics based on high-speed Scheimpflug imaging of corneal deformation in response to an air pulse. It provides parameters such as deformation amplitude, applanation times, and stiffness-related metrics, which describe the mechanical response of the cornea in terms of structural deformation rather than energy dissipation. While Corvis ST and ORA share the goal of assessing corneal biomechanics, their methodologies and measured properties differ fundamentally, making their results complementary rather than interchangeable.

While ORA and Corvis ST provide valuable but distinct biomechanical insights, BOSS is an emerging technology capable of directly measuring intrinsic corneal stiffness at the microscale through non-contact Brillouin light scattering. Unlike ORA and Corvis ST, which rely on external forces (air-puff-based deformation), BOSS provides a spatially resolved measurement of the corneal elastic modulus, offering a fundamentally different perspective on corneal biomechanics.

Given that ORA and Corvis ST exhibit only moderate correlations, it remains unclear whether BOSS measurements will overlap with either device or provide independent, complementary information. If BOSS parameters correlate strongly with ORA-derived CH and CRF, this may indicate a shared sensitivity to viscoelastic properties. Conversely, if BOSS shows stronger correlations with Corvis ST parameters such as stiffness parameter (SP-A1) or deformation amplitude, this may suggest greater sensitivity to structural corneal rigidity rather than energy dissipation properties.

Despite the established utility of these instruments, comparative analyses in existing literature often fall short in addressing the relative efficacy under identical clinical conditions. This chapter embarks on a novel investigation aimed at juxtaposing these three devices, with a specific emphasis on their comparative performance, reliability, and diagnostic potential when utilised concurrently in a controlled experimental setting.

In this pioneering study, the biomechanical parameters obtained from ORA, Corvis ST, and BOSS across a diverse cohort of patients are evaluated and correlated. By doing so, the intent is to unveil nuanced differences and potential synergies among these instruments.

In summary, this correlation study represents a significant stride towards optimising corneal biomechanical assessments by leveraging the distinct capabilities of ORA, Corvis ST, and BOSS.

5.2 Material and Methods

Participants were required to be at least 18 years old, able to read and understand the informed consent and without the diagnosis of any ocular condition. Moreover, if contact lens wearer, they were asked to not to use contact lenses for the 24 hours before the experiment, to avoid any confounding factor.

One eye only, right or left was at patients' discretion, of 67 participants was examined using ORA, Corvis ST and BOSS, and Anterior OCT (OCT, Heidelberg Engineering GmbH, Heidelberg, Germany). The order of the instrument was randomly generated using a Python script, to avoid any possible bias. During the BOSS measurement the four dots pattern was used for corneal measurements: each measured point was 2 mm away from corneal centre, up, bottom, nasal and temporal. For crystalline lens measurement a single axial scan with a 1 mm offset from the lens centre was done. The distance of 1 mm was chosen as rarely the pupil diameter is smaller than 3 mm (Kobashi, Kamiya et al. 2012).

ORA measurements had to have a waveform score of 7 out of 10, to be considered reliable. Corvis ST measurements had display OK as quality specification. BOSS corneal measurements had to be "GOOD", "LOW" or "AVERAGE" measurements were not accepted. BOSS lens scan had to have a score lower than 3 (the scale is reverse and 0 is the optimum).

The collected data were analysed for normality and then correlations were tested, according to normality results. Normality was tested with Shapiro Wilk. Correlations were tested among

corneal measurements performed with different instruments: BOSS against ORA, BOSS against Corvis ST, BOSS against central corneal thickness with OCT. Correlations between BOSS lens and OCT measurements were calculated as well. Correlations were tested using Pearson or Spearman correlation, depending on the results of the normality test, considering the classical alpha level (0.05). Due to the high number of correlations, two levels of Bonferroni correction were applied. A first one that considered the correlation between couples of instruments independent, so the Bonferroni correction was strictly calculated for the single couple of instruments. Using this method three different p-values were obtained: BOSS vs ORA (20 correlations, $p = 2.5 \times 10^{-3}$), BOSS vs Corvis ST (125 correlations, $p = 4 \times 10^{-4}$) and BOSS vs OCT (10 correlations, $p = 5 \times 10^{-3}$). Then, the classic and more conservative one, that considered all the correlations computed in this experiment (155 test, $p = 3.2 \times 10^{-4}$) was included.

5.3 Results

The mean and the standard deviation of the measurements are in Table 5.1. The results of the normality test are in the Table 11.21 in Appendix 11.4.

Table 5.1 Demographics of participants; Mean and SD of clinical measurements

	Age	Eye	SphEq	VA	IOPcc	IOPg	CH	CRF	A1L
Mean	29.8	(RE) 52	-0.77	-0.03	15.9	14.9	10.0	9.9	2.24
SD	15.0	(LE) 15	2.40	0.13	3.5	3.7	1.6	1.8	0.35
	A1V	A1T	A2L	A2V	A2T	HCT	HCPD	HCR	HCDefoAm
Mean	0.15	7.16	1.98	-0.27	21.48	16.76	4.80	7.40	1.02
SD	0.02	0.35	0.32	0.03	0.39	0.42	0.27	0.93	0.11
	CCTcor	IOPnct	ArcL	DeflAm	DeflAmR	DeflAr	DefAR	InvRad	WEM
Mean	524	15.3	-0.13	0.86	6.12	3.04	4.67	0.16	0.33
SD	37	2.5	0.02	0.10	0.77	0.46	0.49	0.02	0.09
	SSI	SP-A1	ARTh	IntRad	CBI	biOP	BSup1	BNas1	BInf1
Mean	1.20	92.9	487.1	8.2	0.59	15.7	2.831	2.822	2.811
SD	0.21	16.2	109.2	1.1	0.27	2.4	0.050	0.060	0.062
	BTem1	Mean1	BLens1	TopPlat1	BotPlat1	AntSI1	PostSI1	CLT	CCT
Mean	2.822	2.821	3.384	2.802	4.225	1.553	-1.533	3.898	530
SD	0.064	0.039	0.056	0.514	0.577	0.412	0.557	0.403	36

Among all the measurements taken from the instruments, the ones that were not normally distributed are: length of first applanation, time of first applanation, length of second applanation, time of highest concavity, non-corrected IOP, inverse concave radius, whole-eye-movement, stress-strain index, corneal biomechanical index, biomechanically corrected IOP for Corvis ST; Brillouin lenticular modulus, top plateau length, anterior slope, posterior slope for BOSS; corneal lens thickness measured using the OCT.

The results of all the correlations are in Table 11.22 (Appendix 11.4). The correlations that were considered statistically significant before Bonferroni correction were:

Table 5.2 Statistically significant correlations between BOSS measurements and parameters measured by ORA, Corvis ST and OCT

Variable 1	Variable 2	Correlation	P-value	R²	Method
Blnf1	CRF	0.246	0.045	0.060	Pearson
Blnf1	A1T	0.350	0.004	0.123	Spearman
Blnf1	IOPnct	0.328	0.007	0.107	Spearman
Blnf1	bIOP	0.318	0.009	0.101	Spearman
BLens1	CLT	-0.299	0.017	0.090	Spearman
TopPlat1	CLT	0.748	0.000	0.559	Spearman
BotPlat1	CLT	0.727	0.000	0.528	Spearman
PostSI1	CLT	0.357	0.004	0.128	Spearman

As can be seen from the table above, the only corneal Brillouin modulus that correlates with parameters measured by other machines is the one measured in the inferior portion of the cornea, that correlates positively with corneal resistance factor, time of first applanation, non-corrected IOP, biomechanically corrected IOP. Although these correlations are statistically significant considering the classic alpha level (0.05), they are not significant anymore if any of the Bonferroni correction is applied.

Among the lens measurements, it is possible to see that there is a negative correlation between lens thickness measured with OCT and Brillouin modulus. Such correlation was, again not enough to overcome Bonferroni correction. The posterior slope showed a statistically significant correlation with lens thickness that was enough to overcome the first level of Bonferroni correction. Both the plateaus showed strong and statistically significant positive correlation with lens thickness, and both surpassed the Bonferroni correction.

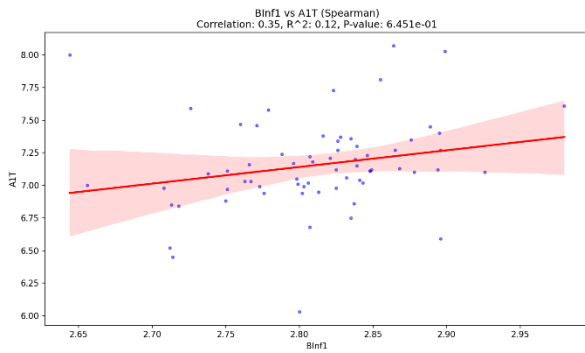


Figure 5.1 Correlation between Brillouin Modulus measured in the inferior part of the corneal and time of the first applanation (Corvis ST)

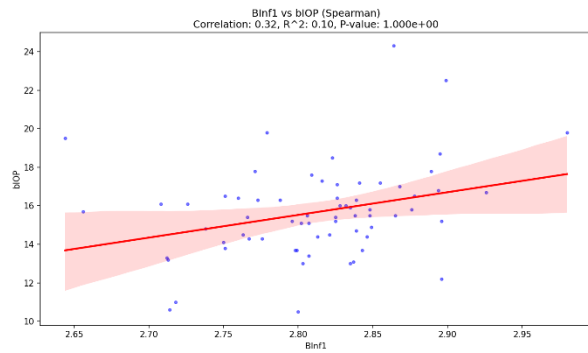


Figure 5.2 Correlation between Brillouin Modulus measured in the inferior part of the corneal and biomechanically corrected IOP (Corvis ST)

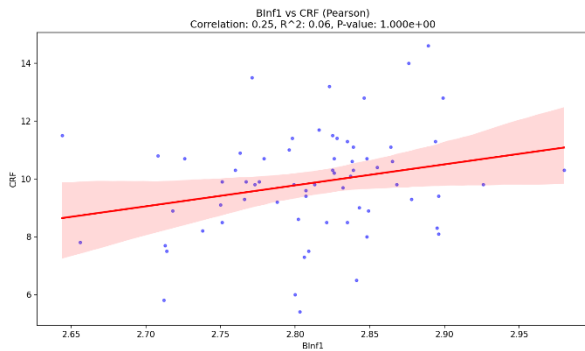


Figure 5.3 Correlation between Brillouin Modulus measured in the inferior part of the corneal and corneal resistance factor (ORA)

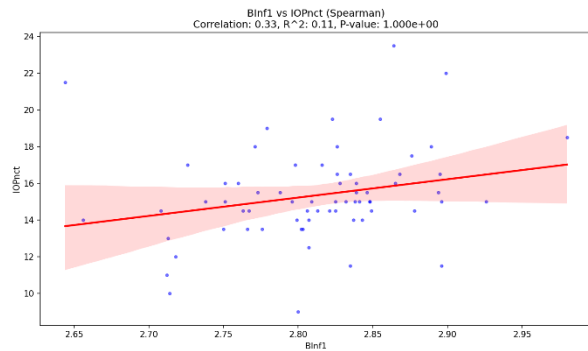


Figure 5.4 Correlation between Brillouin Modulus measured in the inferior part of the corneal and non-corrected IOP (Corvis ST)

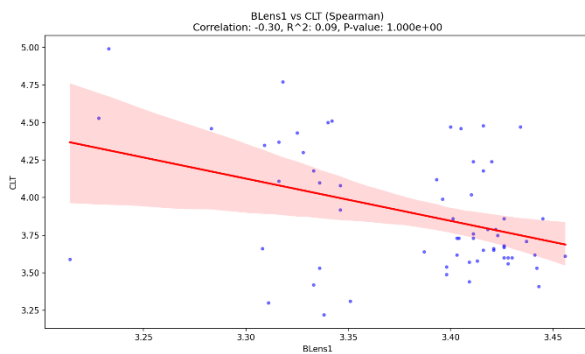


Figure 5.5 Correlation between crystalline lens Brillouin Modulus and central lens thickness (OCT)

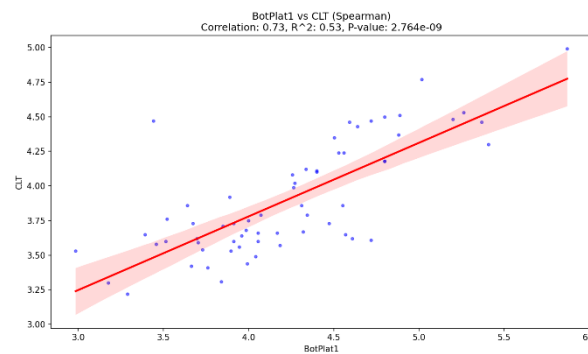


Figure 5.6 Correlation between bottom plateau and central lens thickness (OCT)

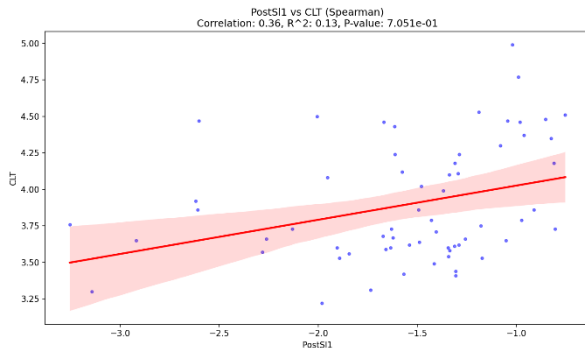


Figure 5.7 Correlation between posterior slope central lens thickness (OCT)

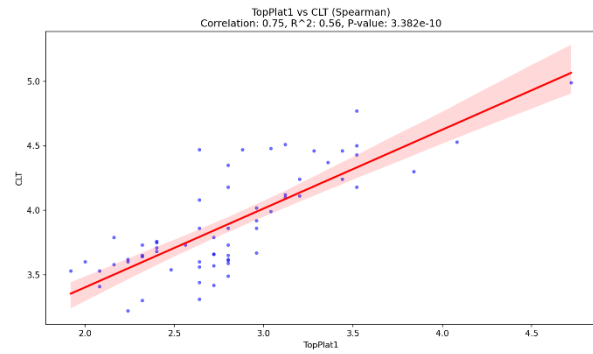


Figure 5.8 Correlation between top plateau and central lens thickness (OCT)

5.4 Discussion

To the best author's knowledge, this is the first study that investigates the relationship between Brillouin modulus with commercially available instruments that measure corneal biomechanical properties. Optical coherence elastography (OCE) does not fall within this definition, as it is not commercially nor clinically available and it is used for research purposes only.

5.4.1 Corneal Measurement

Given that no corneal measurements taken with the BOSS other than inferior ones (superior, nasal, temporal or the average of all of them) correlate with measurements from ORA or Corvis ST, it can be stated that these correlations might be due to chance, especially considering that IOPnct and bIOP are not even corneal measurements, and that thanks to Bonferroni correction it is possible to rule out such findings.

It seems that the BOSS measures a different property than ORA and Corvis ST. Indeed, the latter are non-contact tonometers, that quantify corneal biomechanical features based on displacement created by the air puff, where the IOP play a fundamental role. BOSS measurements, on the contrary, does not consider IOP at all, as the measurement is based on the scattering that happens within the tissue. For these reasons, data from different machine can be considered complementary but not necessarily comparable or correlated.

5.4.2 Lens Measurement

Among the lens measurements, the most interesting is the negative correlation between lens thickness and lens moduli. The explanation is simpler than how it might appear: it is well known that lens becomes thicker with age and, as will be discussed in Chapter 6 the Brillouin lens moduli significantly decreases with age, therefore it is explained the statistically significant correlation.

Something similar happens with posterior slope: the variation in terms of stiffness between nucleus and posterior cortex changes with age and the slope becomes less steep. Being posterior slope negative, it moves towards zero (so a more positive value) and this, joined to a thicker lens, can explain such correlation.

The last two correlations are between lens thickness and length plateaus: both correlations are strong and statistically significant, but to understand if measures can be interchangeable a further analysis is needed.

5.4.3 Confrontation between lens thickness measured using BOSS and OCT

Given the strong and significant correlation measured, a further analysis was performed between BOSS plateaus and the lens thickness measured with the OCT.

Top and Bottom plateau measurements with a vertical offset between -0.05 and 0.05 mm, and with a temporal offset between 0.95 and 1.05 mm were compared with thickness measured 1 mm temporally from the centre of the crystalline lens. The 1 mm offset was measured from the lens axis traced by the software.

From the entire dataset 15 cases were isolated, with the offset features required for this analysis. Two Bland Altman plots were created to compare the Top and Bottom plateaus with the lens thickness measured 1 mm temporally from the centre of the lens.

From the Bland Altman analysis it is visible that the bias is significant in both cases: the Top Plateau measurement is half a millimetre thinner (0.586 mm) than the lens thickness measured using the OCT, while the bottom plateau is almost a millimetre thicker than the OCT measurement. Considering the 95% limit of agreement interval (adding and subtracting 1.96 times standard deviation to the bias values) it appears the Top and Bottom Plateaus do

not match the measurement of the lens thickness done using and OCT and that cannot be used as reference for lens thickness. Plateaus are calculated considering the change of modulus between humours and lens. Bottom plateau is calculated including the transition zone, where the Brillouin modulus start increasing, while the Top Plateau is calculated including only the portion where the Brillouin modulus is constant.

There are two factors that can explain such findings: 1) the measurement of plateaus is made with a movement on the Z-axis and with single scan every 0.1 mm, the entire scan of the lens is 8 mm long, it starts in the aqueous and end in the vitreous. The entire scan takes some time (almost 30 seconds) and during this timeframe it is possible that the patient moves. The offset calculated by the BOSS software, and that was used to compare plateaus with OCT thickness, computes an average of the offset during the measurement. The second factor is related to the system used to calculate of the offset: thanks to the contrast between pupil and iris, the pupil was computed as a perfect circle and the software calculated the centre of the circle. This approximation led to consider the centre of the pupil as the reference for any measurement. In this case the discrepancy lays on the fact that is well known that the centre of the pupil moves (Wyatt 1995), and often the iris is not perfect circle (Basit, Javed et al. 2008).

Such changes create “transition zones” where the Brillouin modulus is increasing, from aqueous to cortex and then to nucleus, and decreasing, from nucleus to cortex (and then vitreous). Using these moduli variations, anterior and posterior slopes are calculated: as the increase and the decrease of the modulus per millimetre.

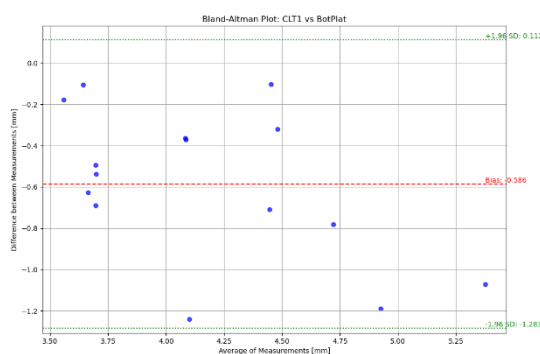


Figure 5.9 Bland Altman Plot Central Lens Thickness (OCT) vs Bottom Plateau

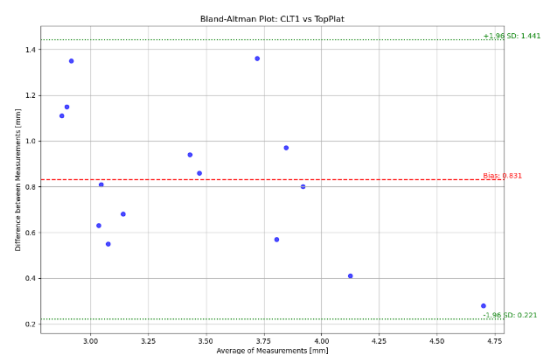


Figure 5.10 Bland Altman Plot Central Lens Thickness (OCT) vs Top Plateau

5.5 Conclusions

Measures from BOSS and other instruments are not interchangeable as each machine evaluates different ocular features. BOSS assesses the longitudinal modulus of transparent tissues but does not correspond with any measurements from the Ocular Response Analyzer (ORA) or Corvis ST. Furthermore, BOSS cannot reliably measure lens thickness due to the high bias observed in its measurements. These findings suggest that BOSS measurements are truly innovative and represent a significant advancement in corneal biomechanics. BOSS is the first instrument capable of detecting localised areas of weakness in the cornea, offering unique insights that other instruments cannot provide.

The following chapter focuses on age-related changes in corneal biomechanics, comparing the differences between younger individuals and those with presbyopia. This exploration is crucial for understanding how corneal properties evolve with age and the implications these changes have for ocular health and the development of age-related eye conditions.

6 Age-Related Changes in Corneal Biomechanics

6.1 Introduction

The biomechanical properties of the cornea are essential for maintaining the structural integrity and optical functionality of the eye. As individuals age, the cornea undergoes changes that affect its elasticity, stiffness, and overall mechanical stability. Understanding these age-related variations not only deepens our knowledge of ocular physiology but also plays a crucial role in improving clinical outcomes and advancing early diagnostic strategies for corneal pathologies.

Despite the increasing interest in assessing corneal biomechanics, a significant gap remains in the literature regarding the specific impact of aging on these parameters. Much of the existing research has focused on younger populations or subjects with ocular pathologies, thereby overlooking the biomechanical alterations in healthy, aged individuals. This gap underscores the need for further investigation into how aging affects corneal mechanical properties.

In this context, the precise evaluation of corneal biomechanics is pivotal for clinical practice. A more detailed understanding of age-related variations can enhance predictive models for surgical outcomes, particularly in refractive surgery and cataract procedures. Comparative analyses of the available measurement technologies – including the ORA, the Corvis ST, and the BOSS – reveal that each instrument offers unique advantages. These insights can facilitate the development of personalized protocols that account for age-specific corneal characteristics (Scarcelli, Kim et al. 2011).

By investigating the biomechanical changes associated with aging, this research aims to bridge the current literature gap and provide valuable data for optimising surgical procedures and refining diagnostic methodologies.

6.1.1 Calculus of sample size

The calculus of the sample size was done using GPower 3.1 (University of Dusseldorf, Dusseldorf, Germany) (Faul, Erdfelder et al. 2007, Faul, Erdfelder et al. 2009). As no data are about age related changes in Brillouin modulus are available in literature, corneal

hysteresis data from (Sharifipour, Panahi-Bazaz et al. 2016) were considered for young (groups 10-19 and 20-29 years) and presbyopes (40-49, 50-59 and 60-69). The sample size calculation was done for the t test family, considering the difference between two groups, two tails, using a priori approach with $\alpha = 0.05$, Power $(1 - \beta) = 0.8$ and calculated effect size $d = 0.86$. The result of the calculation was 44 participants in total, 22 per group.

6.2 Materials and Methods

The current study was done using data from two different groups: young ($n = 23$) and presbyopes ($n = 23$). The inclusion criteria were the age range (19-22 for group Y and above 45 for group P) and the absence of any ocular or systemic pathology. All the participants completed the study. Each participant chose the eye they wanted to be examined.

Participants were required to not have worn contact lenses in the prior 24 hours to avoid any possible influence on corneal biomechanical measurements, that is still unclear. (González-Méijome, Villa-Collar et al. 2008, Cankaya, Beyazyildiz et al. 2012, Peyman, Ghoreishi et al. 2021)

Each participant underwent the entire set of measurement using Ocular Response Analyzer (ORA, Reichert, Inc., Depew, NY, USA), Corneal Visualization Scheimpflug Technology (Corvis ST, OCULUS Optikgerate GmbH, Wetzlar, Germany), Brillouin Optical Scanner System (BOSS, Intelon Optics, Woburn, MA, USA) and Anterior OCT (Heidelberg Engineering GmbH, Heidelberg, Germany) for one eye only, chosen by the participant. The absence of ocular pathology was done during the initial interview and the refractive error was measured with an open field autorefractor (WAM 5500, Grand Seiko, Shigiya Machinery Works LTD, Hiroshima, Japan).

The order of the measurements with ORA, Corvis ST and BOSS was randomised to avoid any bias (the randomised order was selected using a random generator script coded in Python). The measurement of the refractive error was performed before the set of three instruments. The OCT imaging was always done at the end of the experiment. During the BOSS measurement the four dots pattern was used for corneal measurements (each measured point was 2 mm away from corneal centre, up, bottom, nasal and temporal), while for crystalline lens a single axial scan with a 1 mm offset from the lens centre was done. The distance of 1 mm was chosen as rarely the pupil diameter is smaller than 3 mm (Kobashi, Kamiya et al. 2012).

To be considered reliable, each measurement ORA measurement had to have a minimum waveform score of 7 out of 10, any Corvis ST measurement had to display OK as quality specification (QS), while the corneal BOSS measurements had to display “GOOD” (“LOW or “AVERAGE” were not accepted) and lens scan needed to be lower than 3 (BOSS has a reverse scale, so 0 is considered optimum).

After the comparison between the two groups, a second analysis was done correlating data from ORA, Corvis ST and BOSS with age but, due to the extreme narrow distribution of age of the group Y, it was done only for group P.

Data were analysed using JupyterLab from Anaconda Navigator: pandas, seaborn, numpy, scipy.stats and matplotlib packages were used. All the collected data were moved on a spreadsheet and anonymised, then it was load into JupyterLab to be get analysed.

6.3 Results

6.3.1 Differences between Young and Presbyopes

Demographic data of the two groups are presented in Table 6.1.

Table 6.1 Demographics

	Group Y	Group P
Age [years]	19.13 ± 1.06	49.39 ± 7.94
Age Range [years]	19-22	45-67
RE/LE	16 / 7	20 / 3
M/F	7 / 16	12 / 11
Spherical Equivalent Range [D]	-3.88 / 5.38	-3.38 / + 5.63

Groups did not have differences in terms of objective refractive error distribution. Such condition was tested analysing the spherical equivalent of the two groups are show in Figure 6.1

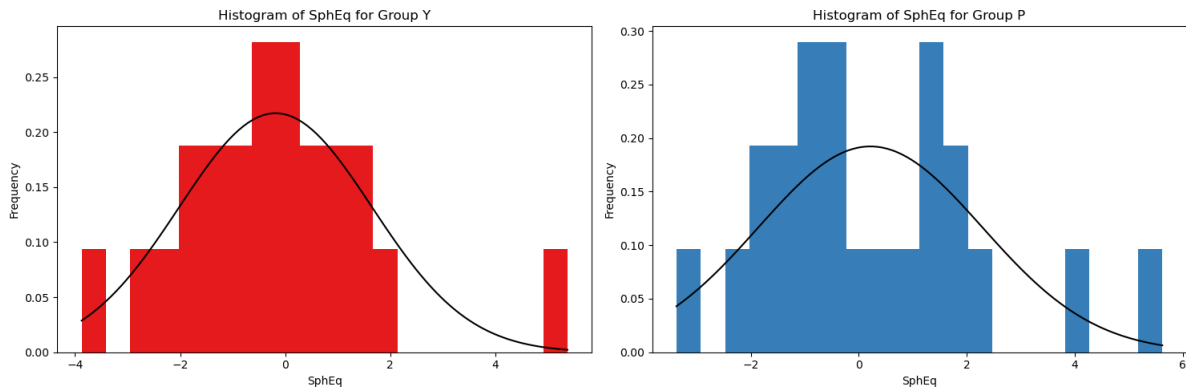


Figure 6.1 Refractive error distribution in terms of Spherical Equivalent for group Y and P

Both young and presbyopes groups had a normal distribution of the mean spherical equivalent (Table 6.2). Because refractive error distribution was normal in both groups, a t-test was conducted to reveal statistically significant differences. The result of the test showed no statistically significant differences between the two groups in terms of refractive error ($t = -0.691$, $p = 0.493$).

Table 6.2 Mean, SD and results of normality test (Shapiro Wilk) for refractive error for groups Y and P

Group	Mean [D]	SD [D]	Shapiro-Wilk test	p-value
Y	-0.182	1.837	0.941	0.187
P	0.217	2.075	0.948	0.271

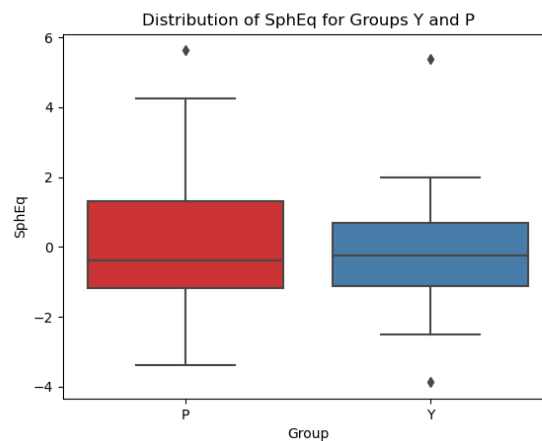


Figure 6.2 Boxplot for Refractive Error (SphEq) for groups P and Y

A series of Shapiro-Wilk test was run to evaluate the distribution of each single parameter measured. The results of these tests are shown in Table 11.23 in Appendix 11.5 alongside the values of mean/median and SD/IQR. Mean and SD are reported if distribution is normal ($p > 0.05$), median and IQR if data were not normally distributed.

Then, according to the distribution, the differences between the two groups were tested using t-test (if both groups showed normally distributed data) or Mann Whitney U (if one of both were not normally distributed). Given the high number of test carried out (41), two levels of Bonferroni correction were carried out: the classic and more conservative one, where the significance level was adjusted dividing alpha by the number of the test carried out ($\alpha = 0,05/41 = 0,0012$) and a less conservative one, that considered the number of the parameter measured by each instrument (4 for the ORA, 25 for the Corvis ST, 10 for the BOSS and two using the OCT). With the second approach the level of significance is different for every instrument: 0,012 for the Ocular Response Analyzer, 0,002 for the Corvis ST, 0,005 for the BOSS and 0,025 for the OCT.

The analysis was done considering each instrument:

- ORA: none of the measured parameter showed a statistically significant difference between young and presbyope.
- Among Corvis ST measured parameters
 - **Length at the First Applanation** (A1L, Figure 6.3), that is higher in younger (2.45 ± 0.30 mm) than in presbyopes (2.10 ± 0.30 mm; t-test $p < 0.001$). Even applying the most conservative Bonferroni correction, it remains statistically significantly higher.
 - **Velocity at the First Applanation** (A1V, Figure 6.4), the value of the young is lower (0.14 ± 0.02 mm/s) that the value of the presbyope group (0.15 ± 0.02 m/s). Despite p value is lower than 0.05 (t-test $p = 0.039$), applying even the least conservative Bonferroni correction ($\alpha = 0.012$) it is not statistically significant anymore.
 - **Velocity at the Second Applanation** (A2V, Figure 6.5), the velocity of the presbyope group (-0.28 ± 0.03) is still higher that velocity of the young group (-0.26 ± 0.03). Again, p value (t-test $p = 0.023$) is smaller than 0.05 but does not reach any significant level if Bonferroni correction is applied.
 - **Highest Concavity Deformation Amplitude** (HCDefoAm, Figure 6.6), the displacement along the Z axis of the corneal apex between the beginning of the air puff and the moment of highest concavity is smaller in the young group (0.98 ± 0.10 mm) compared to the presbyope group (1.06 ± 0.11). The difference was statistically significant (t-test, $p = 0.010$), but not enough if considering Bonferroni correction.
 - **Biomechanical Corrected IOP** (bIOP, Figure 6.7), young group showed a statistically significant (t-test, $p = 0.021$) higher value (16.4 ± 2.7 mmHg) than

older group (14.7 ± 2.0 mmHg). Again, adjusting α to consider Bonferroni correction, the difference was not statistically significant anymore.

- **Whole Eye Movement** (WEM, Figure 6.8), the difference between young (0.31 ± 0.06 mm) and presbyope (median 0.34, IQR 0.06 mm) was statistically significant (Mann Whitney U, as WEM values in P group were not normally distributed, $p = 0.006$) but did not meet criteria after Bonferroni correction was applied.
- Among BOSS measurement, none of the corneal moduli was different between groups. Some changes were measured in the lens parameters:
 - **Lens Modulus** (BLens, Figure 6.9) was lower in the presbyope group (3.351 ± 0.059 GPa) compared to young group (3.411 ± 0.028 GPa). Such difference was statistically significant (Mann Whitney U, $p = 0.002$) even adjusting α for the number of parameters measured with the same instrument (in this case $\alpha = 0.005$), but not if all the parameters measured by all the instruments were considered ($\alpha = 0.0012$).
 - **Top Plateau** (TopPI, Figure 6.10) showed a statistically significant difference (Mann-Whitney U, $p < 0.001$) between the two groups (Y = 2.557 ± 0.325 mm; P = 3.200 ± 0.600 mm). This difference is statistically significant even applying the most conservative Bonferroni correction ($\alpha = 0.0012$).
 - **Bottom Plateau** (BotPI, Figure 6.11) showed a strong statistically significant difference (t-test, $p < 0.001$) between groups Y (3.950 ± 0.437 mm) and P (4.272 ± 0.516 mm). Even applying the most conservative Bonferroni correction ($\alpha = 0.0012$), it remained statistically significant.
 - **Posterior Slope** (PostSI, Figure 6.12): the slope of the transition between lens and vitreous humour was significantly different. The group Y had a statistically significant (Mann Whitney U, $p = 0.015$) steeper posterior slope (-1.481 ± 0.599 GPa/mm) than group P (-1.190 ± 0.643 GPa/mm).
 - **Central Lens Thickness** (CLT, Figure 6.13): a statistically significant difference (t-test, $p < 0.001$) was measured between the two groups, the P group showing thicker lenses (4.35 ± 0.26 mm) than group Y (3.67 ± 0.18 mm).

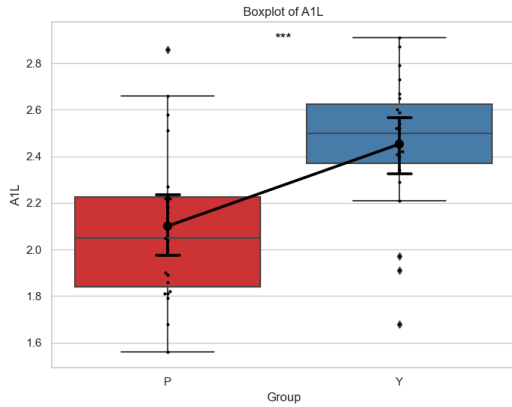


Figure 6.3 Boxplot for Length of First Applanation (Corvis ST)

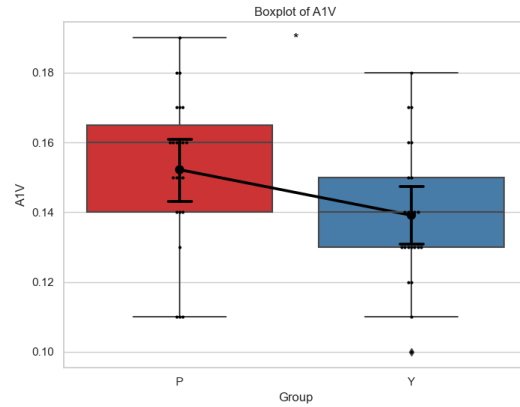


Figure 6.4 Boxplot of Velocity at First Applanation (Corvis ST)

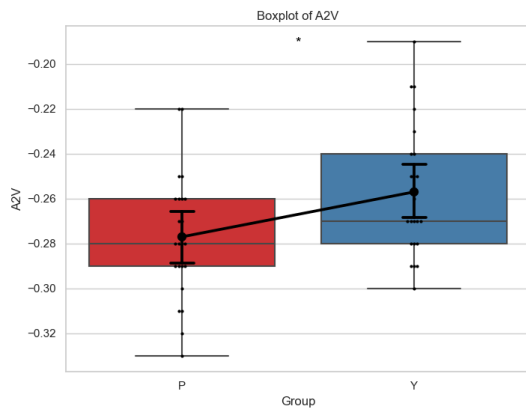


Figure 6.5 Boxplot of Velocity at Second Applanation (Corvis ST)

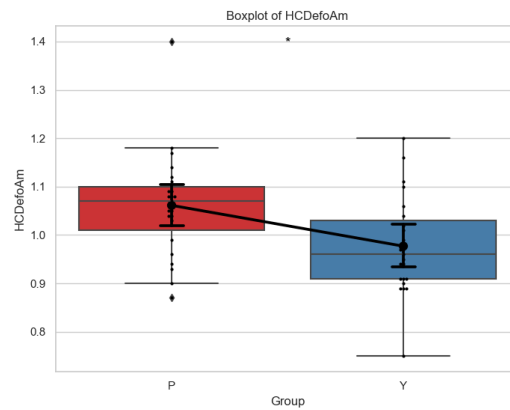


Figure 6.6 Boxplot of Deformation Amplitude during Highest Concavity (Corvis ST)

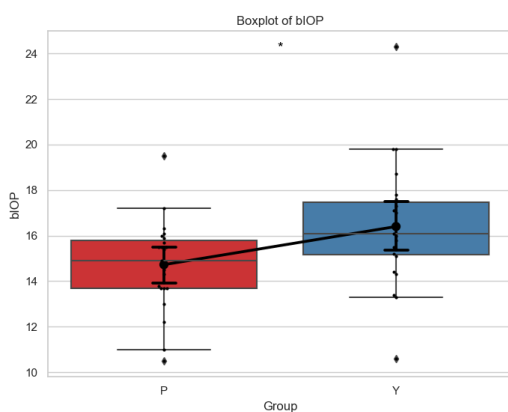


Figure 6.7 Boxplot of Biomechanically Corrected IOP (Corvis ST)

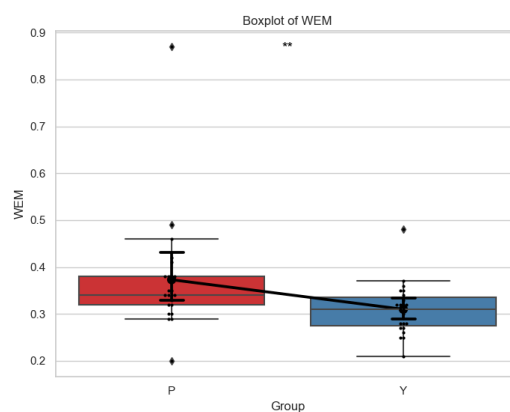


Figure 6.8 Boxplot of Whole-Eye-Movement (Corvis ST)

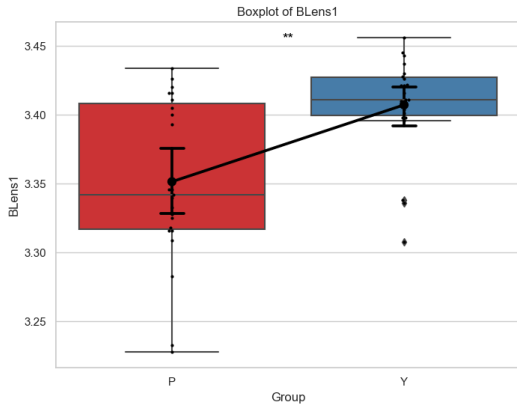


Figure 6.9 Boxplot of Brillouin modulus of the crystalline lens (BOSS)

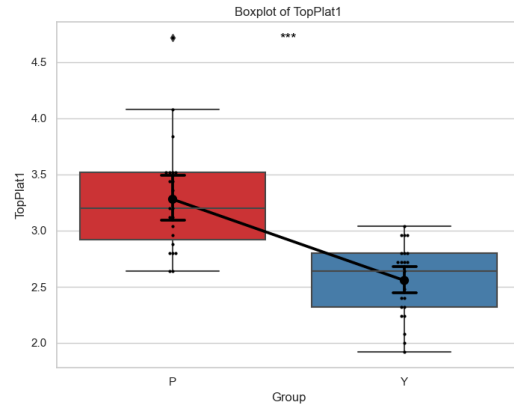


Figure 6.10 Boxplot of Top Plateau (BOSS)

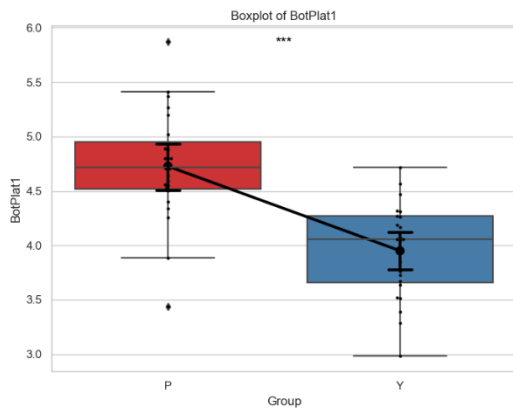


Figure 6.11 Boxplot of Bottom Plateau (BOSS)

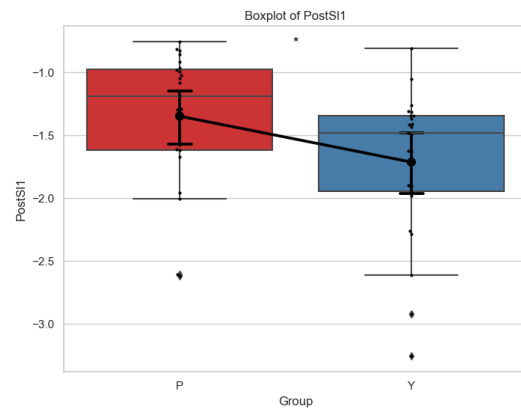


Figure 6.12 Boxplot of Posterior Slope (BOSS)

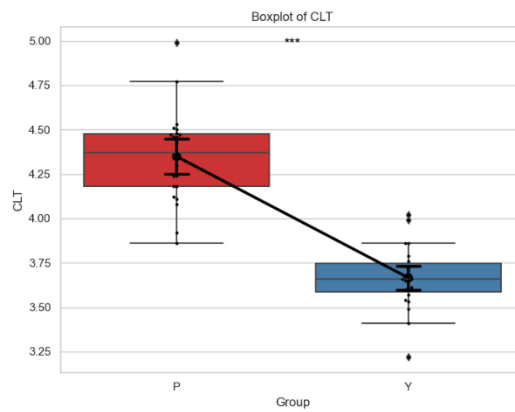


Figure 6.13 Boxplot of Central Lens Thickness (OCT)

6.3.2 Correlation with age for group P

Table 11.24 contains the results of the correlation test with age only for group P. Spearman correlation was used as within group P Age was not normally distributed (Shapiro Wilk stat = 0.91, $p = 0.04$) as can be seen in Figure 6.14.

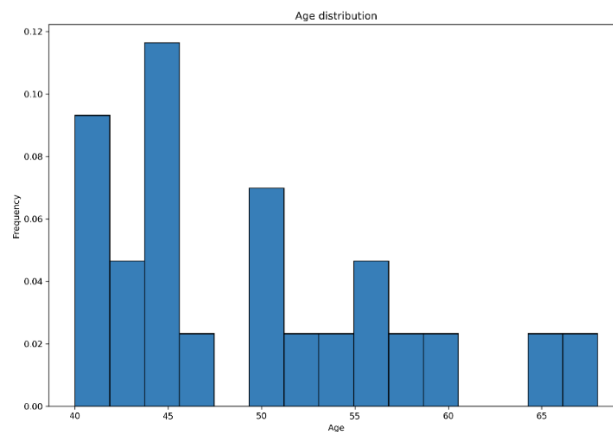


Figure 6.14 Age distribution of P Group

Again, we considered a standard p value (0.05) and two Bonferroni corrections: one strictly related to the instrument and a more conservative one that considered the total number of measurements collected.

The parameters that showed a statistically significant correlation with age were:

- Time of the Second Applanation (A2T, Figure 6.15): negatively correlates with age ($R = -0.44$, $R^2 = 0.19$, $p = 0.035$).
- Brillouin Modulus measured in the temporal side of the cornea (BTem, Figure 6.16): negatively correlates with age ($R = -0.44$, $R^2 = 0.19$, $p = 0.038$).
- Mean of the Brillouin Modulus measured across the cornea (Bmean, Figure 6.17): negatively correlates with age ($R = -0.44$, $R^2 = 0.18$, $p = 0.043$).
- Brillouin Modulus of the Lens (Blens, Figure 6.18): negatively correlates with age ($R = -0.44$, $R^2 = 0.19$, $p = 0.037$).
- Anterior Slope (AntSI, Figure 6.19): positively correlates with age ($R = 0.50$, $R^2 = 0.25$, $p = 0.015$).

None of the above correlations are significant if Bonferroni Correction is considered, both for the most and least conservative approaches.

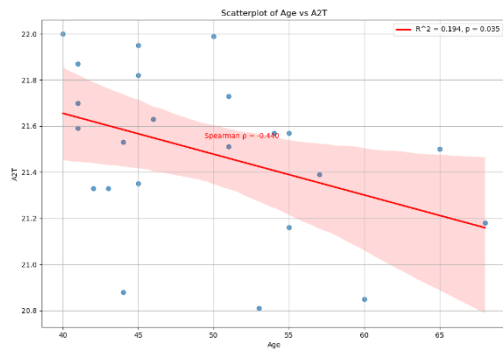


Figure 6.15 Scatterplot, Regression Line and 95% Confidence Interval for Age and Time of Second Applanation (Corvis ST)

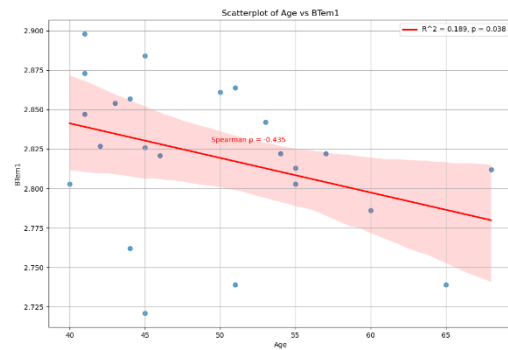


Figure 6.16 Scatterplot, Regression Line and 95% Confidence Interval for Age and Brillouin modulus measured in the temporal cornea (BOSS)

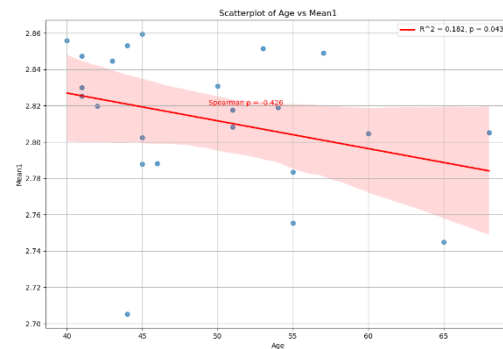


Figure 6.17 Scatterplot, Regression Line and 95% Confidence Interval for Age and Mean Corneal Brillouin modulus (BOSS)

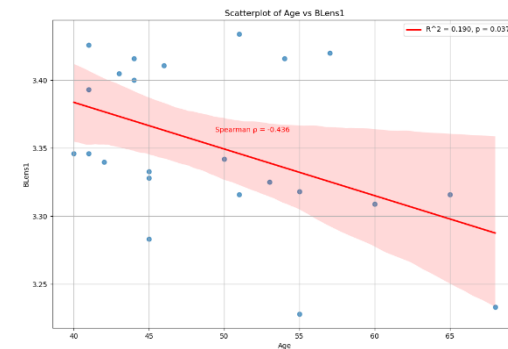


Figure 6.18 Scatterplot, Regression Line and 95% Confidence Interval for Age and Crystalline Lens Brillouin Modulus (BOSS)

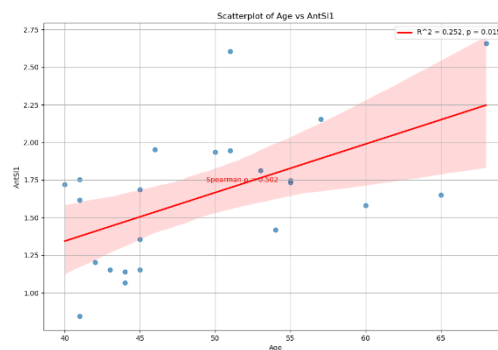


Figure 6.19 Scatterplot, Regression Line and 95% Confidence Interval for Age and Anterior Slop (BOSS)

6.4 Discussion

Most of the measured variables were normally distributed, only Time of the First Applanation, Length of the Second Applanation, Time of Highest Concavity, Inverse Concave Radius, Whole Eye Movement, Integrated Radius, Corvis Biomechanical Index, Mean of Corneal Moduli, Lens Modulus, Top Plateau and Posterior Slope were not normally distributed, for one or both groups, therefore were analysed using Mann Whitney U. All the other parameters were tested for differences between groups using t-test.

6.4.1 ORA

Despite no one of the four parameters measured by the Ocular Response Analyzer showed a statistically significant difference between the two group, it is possible to see that there are some differences between the two groups: IOPg is higher in Group Y and lower in Group P, while IOPcc is lower in Group Y and higher in Group P. IOPg was calibrated to match Goldmann Applanation Tonometry (Ehrlich, Haseltine et al. 2010), while IOPcc consider corneal biomechanical features to correct IOP (Luce 2006). In this case the changes in CH and CRF are not statistically significant although are not far from significance level ($p = 0.072$ and 0.078 , respectively). These changes mean that with aging, cornea becomes less rigid and that therefore dissipates a lower amount of energy. Age related decreases in corneal hysteresis and corneal resistance factor were seen and measured in several studies and some explanation were proposed: alteration in collage cross-linking and cornea hydration that are independent from central thickness or IOP (Kamiya, Shimizu et al. 2009); a global change of the anterior eye, including both biomechanics and IOP, with age, even if IOP changes are minimal, but might have an impact in post refractive surgery stability in elderly patients and create a paradox in corneal ectatic disorders that tend to stabilise with aging (El Massry, Said et al. 2020); some genetic factors can play a role in corneal hysteresis and corneal resistance factor changes: more than 200 gene loci (192 novel) were identified in a recent genome-wide association study (GWAS) that included more than 100000 participants, but did not evaluated age related changes.

ORA values measured in this study are in accordance with data measured in several studies that showed a marked reduction of corneal hysteresis and a milder reduction of corneal resistance factor with age (Rosa, Lanza et al. 2015, El Massry, Said et al. 2020, Simcoe, Khawaja et al. 2020).

Differences between young and presbyopic subjects are often reported as statistically significant in the literature, yet such differences were not observed in the present study. One possible explanation may lie in several methodological and sampling factors that could account for this discrepancy. First, it is important to consider sample size and intra-group variability: a small or homogeneous sample in terms of other parameters (e.g., corneal thickness, intraocular pressure, or systemic characteristics) might not reveal statistically significant differences, even though such differences may be detected in larger and more diverse studies. Additionally, methodological variations—such as differing inclusion criteria, measurement conditions, and statistical approaches—can lead to contrasting results. The literature that reports significant differences often relies on studies in which not all confounding factors were adequately controlled, whereas the present study may have employed more stringent criteria, thereby reducing variance and attenuating the observed differences.

6.4.2 Corvis ST:

Kenia et al. (Kenia, Kenia et al. 2020) investigated the variability of Corvis ST parameters across different age groups, categorising the population into six age ranges: 5-11, 11-20, 21-30, 31-40, 41-50, and over 50 years. They employed analysis of variance to discern differences among these groups, although the absence of post hoc analysis limited insights into specific inter-group differences. However, it is feasible to examine the directional trends of parameters that demonstrated statistically significant differences. Notably, the length at the first applanation (A1L) exhibited a counterintuitive trend, with higher values observed in the oldest group (>50 years, 2.50 ± 0.26 mm) compared to lower values in younger groups (11-20 and 21-30 years, 2.38 ± 0.26 mm and 2.38 ± 0.22 mm, respectively). Contrarily, the present study found a significant difference, with the younger group exhibiting a longer applanation length (2.45 ± 0.30 mm) compared to the older group (2.10 ± 0.33 mm).

Additional parameters that were statistically significant in both studies, velocity at the second applanation (A2V), deformation amplitude at highest concavity (HCDefAm), and biomechanically corrected intraocular pressure (bIOP) demonstrated consistent trends across age groups. These parameters showed higher values in the older group, aligning with the anticipated increase in corneal stiffness (SP-A1 value), which typically corrects for increased intraocular pressure in this demographic. The SP-A1 index, which incorporates corneal load, bIOP, and displacement at first applanation, has been validated as useful in detecting keratoconus (Vinciguerra, Ambrósio et al. 2016). Despite the significant number of

tests conducted, Kenia et al. did not apply a Bonferroni correction, maintaining an alpha level of 0.05 as sufficient for statistical significance.

Furthermore, comparative studies by Liu et al. (Liu, Rong et al. 2020) Eliasy et al. (Eliasy, Chen et al. 2019). explored age-related changes in the Stress Strain Index (SSI) across Chinese, Brazilian, and Italian populations. While these studies found a positive correlation between SSI and age, this investigation did not find statistically significant differences in SSI values, despite observing an increase within the older group ($p = 0.079$, $R^2 = 0.139$, before Bonferroni correction). This discrepancy might be attributed to the variability inherent in a smaller sample size (23 eyes) compared to the larger cohorts in the aforementioned studies (480 and 175 eyes, respectively).

6.4.3 BOSS - Cornea

To date, no studies have explicitly correlated corneal Brillouin modulus with age. Analysis of the collected data indicates that there are no significant differences in Brillouin modulus between the two groups. Two of the measured locations demonstrated an increase in modulus (Nasal and Temporal, with changes of 0.003 GPa and 0.011 GPa, respectively), while two showed a decrease (Superior and Inferior, with changes of -0.008 GPa and -0.025 GPa, respectively). The mean of these measurements reflects a marginal increase of 0.001 GPa. However, none of these differences reached statistical significance.

After analysing the correlation between corneal modulus measurements and age, it is noteworthy that both the mean Brillouin corneal modulus and the Brillouin modulus measured on the temporal side of the cornea exhibit a negative correlation with age. Although these correlations are statistically significant, they are weak and do not retain their significance under the application of the Bonferroni Correction. The observation that only one out of four measured corneal points shows a significant age-related change is peculiar. Typically, in the absence of corneal pathologies such as keratoconus, the cornea is expected to exhibit uniform properties and should not display such inhomogeneities. Moreover, the change observed in the mean of the measurements presents an intriguing contradiction to existing literature: previous research has suggested changes in Brillouin frequency shift (Seiler, Shao et al. 2019, Shao, Eltony et al. 2019), quantifying the increase in 3 and 4 MHz per decade. However, these results were not statistically significant. Considering that these minor frequency shifts correspond to an increase in Brillouin modulus of approximately 1 kPa per decade, which is three orders of magnitude below the instrument's resolution limit of 1

MPa (or 0.001 GPa), it is probable that the observed variations of this study are attributable to random fluctuations rather than substantive changes that the instrument failed to detect.

6.4.4 BOSS - Lens

Among the various lens parameters measured, those showing statistically significant differences between the two groups include the Brillouin modulus of the lens, the top and bottom plateaus, and the posterior slope.

The statistical robustness observed in both plateaus aligns with expectations based on the well-documented age-related thickening of the crystalline lens (Dalziel and Egan 1982, Dubbelman, Van der Heijde et al. 2003). As discussed in Chapter 5, the central lens thickness measured using OCT is approximately 1 mm greater (Bias: 1.087 ± 0.376 mm, 95% limits of agreement: 0.460 to 1.714 mm) compared to measurements from the bottom plateau, which are comparatively smaller (Bias: -0.325 ± 0.376 mm, 95% limits of agreement: -1.062 to 0.413 mm). This discrepancy allows for the interpretation of the top plateau as representing the thickness of the nuclear portion of the lens, while the bottom plateau corresponds to the thickness of the entire crystalline lens (nucleus and cortexes). Such theory is supported by the measurements of the central lens thickness, in Table 5.1, where can be seen that central lens thickness values are closer to bottom plateau, rather than to top plateau.

Given that major age-related changes predominantly occur in the nucleus rather than in the cortex, it is unsurprising that the variations in the bottom plateau are similar to the variation in the top plateau. It should be noted that the measurement of plateau length does not correspond to the central thickness of the crystalline lens, as the BOSS cannot accurately measure this due to excessive reflections that impair the analysis of scattering. All the lens measurements taken with the BOSS were performed at 1 mm temporally from the pupil centre.

Unexpectedly, if the correlations within the elder group were analysed, none reached statistical significance. The correlations were still positive (plateaus length increase with age), but both failed in reaching significance; on the contrary, central lens thickness measured with OCT shows a significant correlation with age in group P, as expected.

The observed difference in the posterior slope between the two groups suggests a reduction in the gradient of change across the posterior cortex. As expected, the cortex is more deformable than the nucleus; however, the region of the cortex that is most susceptible to

deformation is larger, as indicated by the negative slope. A more positive value would suggest a less steep slope, indicating a more gradual, rather than abrupt, change. Notably, this change is not statistically significant when the posterior slope is correlated with age. However, the anterior slope shows a positive correlation with age, indicating that the modulus of the anterior portion of the lens increases with age, particularly after the age of 45.

It is important to note that these values do not provide any information regarding the shape of the crystalline lens. Furthermore, it should be acknowledged that the slopes were computed using limited data from the transition between the aqueous humour and the nucleus of the lens.

Interestingly, the Brillouin modulus of the lens is significantly lower in the elder group than in the younger group. Although this finding may seem counterintuitive - given the common belief that presbyopia is caused by a crystalline lens that becomes less deformable and therefore more rigid—this could be an example of the lens paradox. According to this paradox According to this paradox, as outlined by Dubbelman and Van der Heijde (Dubbelman and Van der Heijde 2001), the growth in the thickness of the crystalline lens is accompanied by a decrease in the refractive index of the nucleus, which changes from 1.433 to 1.417 between the ages of 20 and 70. Such a change is unlikely to affect the measurement significantly, as it creates a variation that is considered negligible (Besner, Scarcelli et al. 2016) and the ratio between the mass density of the lens (ρ) and the square of the refractive index (r) is set to a constant value (0.57).

Similar findings about the plateaus and modulus changes were found in a 2016 study (Besner, Scarcelli et al. 2016), that was the first in vivo study that characterised the lens properties using Brillouin technology: a lower amount of Brillouin modulus for crystalline lens after the age of 45 and a substantial increment in the plateaus length throughout life. In this study it was authors identified the variation in modulus for the central portion of the lens was -4.5 ± 1.4 MPa per year, while no changes were measured for the cortexes (anterior and posterior slopes), after the age of 45.

6.5 Conclusion

This study has extensively examined age-related changes in corneal and lens biomechanics using multiple instruments.

Our findings confirm that corneal biomechanics, as measured by ORA and Corvis ST, subtly but significantly alters with age. While ORA measurements did not reveal statistically significant differences between the groups, there was a notable trend in the behaviour of IOPg and IOPcc, which reflects the intrinsic biomechanical changes within the cornea, potentially due to changes in collagen cross-linking and hydration independent of central thickness or IOP. Such biomechanical degradation may have profound implications on the stability of post-refractive surgery and the progression of corneal ectatic disorders in the elderly.

Significant differences in lens biomechanics were observed with the use of BOSS. Notably, the Brillouin modulus of the lens was found to be lower in the older group, contrary to the conventional expectation that the lens becomes more rigid with age. Furthermore, this study highlights a stronger correlation of lens thickness changes with age, as detected by OCT, suggesting that age primarily influences the nucleus rather than the cortex.

Additionally, expanding the sample size and including more diverse age groups could validate and refine findings, providing a more detailed mapping of biomechanical aging in the human eye. Another possible limitation is related to the measurement of refraction: an open field autorefractor was used, while a combination of axial length and autorefraction would have probably been more precise in terms of characterisation of refractive error.

The integration of biomechanical assessments into routine ophthalmic evaluation could revolutionise the approach to ocular health, paving the way for targeted interventions that are finely tuned to the biomechanical profile of each patient at different ages.

In the following Chapter the changes in terms of ocular biomechanics related to different refractive errors are investigated.

7 Corneal Biomechanics Changes related to Refractive Error

7.1 Introduction

This chapter aims to elucidate the relationships between refractive errors and corneal biomechanical parameters by employing a range of advanced diagnostic tools. Refractive errors—such as hyperopia, emmetropia, and myopia—reflect variations in the eye's ability to focus light on the retina, thereby impacting visual acuity. While numerous studies have focused on the optical aspects of these errors, the underlying biomechanical differences of the cornea among various refractive groups remain less understood. The rationale for this study is based on the hypothesis that the corneal biomechanical properties (e.g., corneal hysteresis and resistance factor) differ among individuals with different refractive statuses, which may influence not only the progression of refractive errors but also the outcomes of refractive surgical interventions.

The primary objective is to quantitatively assess the differences in corneal biomechanics among groups with different refractive errors and to explore the correlations between these biomechanical parameters and the magnitude of refractive error. By integrating data from state-of-the-art diagnostic technologies, this study seeks to provide deeper insights into the structural and functional variations of the cornea, potentially guiding more personalized approaches to refractive error management and treatment in the future.

7.1.1 Sample Size Calculation

The sample size calculation was conducted using GPower 3.1 (University of Dusseldorf, Dusseldorf, Germany) (Faul, Erdfelder et al. 2007, Faul, Erdfelder et al. 2009). For this study, five different groups were identified based on the mean spherical equivalent (MSE) refractive error: hyperopes ($MSE > +0.50$ D), emmetropes (-0.50 D \leq MSE \leq +0.50 D), low myopes (-0.50 D $>$ MSE \geq -3.00 D), medium myopes (-3.00 D $>$ MSE \geq -6.00 D), and high myopes (MSE \leq -6.00 D). As no previous studies have investigated differences in the Brillouin modulus across various refractive errors, data from the Ocular Response Analyzer (ORA) were utilised. Corneal hysteresis data from the study "*Relationship among Corneal Biomechanics, Refractive Error, and Axial Length*" (Buena-Gimeno, España-Gregori et al. 2014) informed the sample size calculation. Using corneal hysteresis data from these

groups, an effect size of 0.44 was calculated, and the sample size was computed with the following settings in GPower: $\alpha = 0.05$, power $(1 - \beta) = 0.8$, across five groups. A total of 65 participants was required (13 participants per group).

7.2 Material and Methods

To refine the age range of the sample, it was determined that only participants aged 19-23 were eligible for this study. The inclusion criteria included the absence of ocular pathology and this specific age range. Participants were required not to wear contact lenses during the 24 hours preceding the experiment.

A total of 45 participants were enrolled in the study, with 44 completing it. The initial target sample size could not be met due to time constraints and participant availability. Participants' refractive errors were measured using an open field autorefractor (WAM 5500, Grand Seiko, Shigiya Machinery Works LTD, Hiroshima, Japan); each eye was measured five times and the mean of these measurements was calculated. Each participant then chose which eye would be included in the study.

Measurements were taken using three different instruments: the Ocular Response Analyzer (ORA, Reichert, Inc., Depew, NY, USA), Corneal Visualization Scheimpflug Technology (Corvis ST, OCULUS Optikgeräte GmbH, Wetzlar, Germany), and the Brillouin Optical Scanner System (BOSS, Intelon Optics, Woburn, MA, USA). The sequence of instrument use was randomised to mitigate potential confounding factors. Following these measurements, an anterior segment tomography was conducted using an Anterior OCT (Heidelberg Engineering GmbH, Heidelberg, Germany).

For the data to be deemed acceptable, measurements taken with the ORA had to have a minimum wavefront score of 7 out of 10. The Corvis ST measurements needed to display 'OK' as a quality specification, and BOSS measurements of the cornea had to be rated 'GOOD' for each scanned point (with 'LOW' or 'Average' scans being rejected). For lens measurements with the BOSS, the quality index had to be lower than 3 on a reverse scale, where 0 is optimal. The scanning pattern employed with the BOSS used a 4-dots configuration, where each point was positioned 2 mm from the computed centre of the pupil: upper (BSup), nasal (BNas), inferior (BInf), and temporal (BTem). The mean of these points

was calculated (Mean). The BOSS lens scan was performed 1 mm temporally from the centre of the pupil to avoid reflections that could impede accurate measurements.

Two analyses were conducted with the collected data: one assessing differences between groups based on refractive errors, and another examining correlation with the mean spherical equivalent (MSE), treated as a continuous variable.

The normality of the distribution within each group was assessed using the Shapiro-Wilk test. Differences among groups were evaluated using either ANOVA or the Kruskal-Wallis test, depending on the normality results. Post hoc analyses were performed using the Tukey test for ANOVA and the Dunn test for Kruskal-Wallis, as appropriate.

Due to the high number of tests conducted, a Bonferroni correction was applied in addition to the classic significance level of $\alpha = 0.05$. Two levels of Bonferroni correction were considered: a more traditional and conservative approach, where alpha is divided by the total number of tests ($\alpha_B = 0.05 \div 42 = 0.00119$) and a less conservative one, which depends on the number of parameters measured by each instrument. The adjusted significance levels were as follow: α_{ORA} ($0.05 \div 4 = 0.0125$); α_{CST} ($0.05 \div 25 = 0.002$); α_{BOSS} ($0.05 \div 10 = 0.005$); α_{OCT} ($0.05 \div 2 = 0.025$).

7.3 Results

7.3.1 Participants

Due to challenges in recruiting participants and time constraints, the final recruitment comprised only 44 patients: 7 in the hyperopic group, 12 in the emmetropic group, 15 in the low myopia group, 9 in the medium myopia group, and 1 in the high myopia group. Owing to the limited representation in the high myopia group, the sole participant was included in the medium myopia group to facilitate a more robust analysis. All the participants were recruited among Aston University undergraduate students, to have a restricted age range and be sure that age did not bias the experiment.

Demographics of the participants are listed in Table 7.1.

Table 7.1 Demographics of participants divided in groups according to the refractive error

	Hyperopia	Emmetropia	Low Myopia	Medium Myopia
Age [years]	19.85 ± 1.14	19.43 ± 0.98	19.20 ± 1.26	19.70 ± 1.06
RE/LE	5 / 2	10 / 3	11 / 4	7 / 3
M/F	1 / 6	4 / 9	6 / 9	2 / 8
SER [D]	1.77 ± 1.65	-0.03 ± 0.19	-1.43 ± 0.76	-4.70 ± 1.71

7.3.2 Differences among groups

The initial analysis involved testing for the normality of distribution within each group. Given the small number of subjects in each group, the Shapiro-Wilk test was employed (Razali, Wah et al. 2011). According to Table 11.25 in the Appendix 11.6.1, most measurements exhibited a normal distribution, with exceptions including: length at first appplanation, time of the first appplanation, length at the second appplanation, time of highest concavity, radius at highest concavity, non-corrected intraocular pressure (IOP), deflection area, inverse concave radius, whole-eye-movement, stress-strain index, biomechanically corrected IOP, Brillouin modulus on the temporal side, Brillouin mean modulus, Brillouin modulus of the lens, bottom plateau, and posterior slope. For all these parameters differences between groups were tested with Kruskal Wallis test. All the other measurements were tested with ANOVA. Results of ANOVA and Kruskal Wallis test are in Table 11.26 in Appendix 11.6.1. For all these non-normally distributed parameters, differences between groups were assessed using the Kruskal-Wallis test. For all other measurements, which conformed to a normal distribution, ANOVA was applied.

The analyses identified several parameters that demonstrated statistically significant differences among the groups:

- **Length at First Appplanation** (A1L, Figure 7.1): Assessed using the Kruskal-Wallis test ($K = 8.901$, $p = 0.002$), a significant difference was noted between the hyperopic and medium myopia groups ($p = 0.019$), as shown by the Dunn post hoc test. The box plot illustrates that myopic eyes are associated with shorter lengths at first appplanation compared to hyperopic eyes.
- **Highest Concavity Radius** (HCR, Figure 7.2): This parameter also showed significant differences (Kruskal-Wallis, $K = 14.743$, $p = 0.002$). The Dunn post hoc test indicated significant differences between the medium myopia and emmetropia

groups ($p = 0.001$), and between medium and low myopia groups ($p = 0.025$). More myopic eyes exhibited lower values of radius.

- **Inverse Concave Radius** (InvRad, Figure 7.3): Significant variation was found (Kruskal-Wallis, $K = 12.049$, $p = 0.007$) with a notable difference between the emmetropia and medium myopia groups ($p = 0.005$), identified by the Dunn post hoc test. The medium myopia group showed higher values of inverse concave radius.
- **Stress-Strain Index** (SSI, Figure 7.4): Showing the most pronounced differences (Kruskal Wallis, $K = 18.945$, $p = 0.00028$), the medium myopia group differed significantly from the other three groups ($p < 0.001$ for all comparisons) as per the post hoc analysis. The stress-strain index in medium myopia is markedly reduced and shows less variability. This parameter passed both Bonferroni corrections.
- **Integrated Radius** (IntRad, Figure 7.5): Evaluated through ANOVA ($F = 4.738$, $p = 0.006$), significant differences were detected between the emmetropia and medium myopia groups ($p = 0.003$), as shown by the Tukey post hoc test, with the medium myopia group presenting a higher value.
- **Brillouin Modulus of the Crystalline Lens** (BLens, Figure 7.6): Another significant finding from the Kruskal Wallis test ($K = 10.896$, $p = 0.012$) was noted between hyperopia and emmetropia groups ($p = 0.0199$) via post hoc analysis. The hyperopic group showed a slightly higher lenticular Brillouin modulus.

Boxplot of differences in Length at First Applanation across Refractive Error groups (Corvis ST)

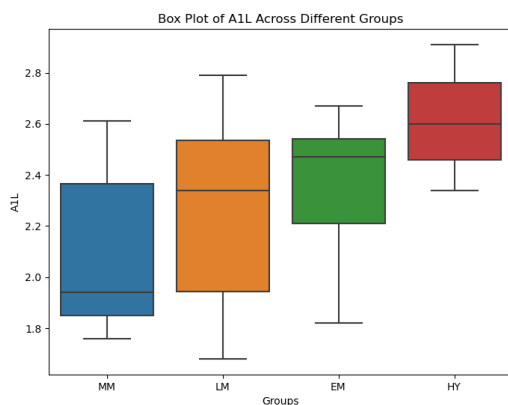


Figure 7.1 Boxplot of differences in Length at First Applanation across Refractive Error groups (Corvis ST)

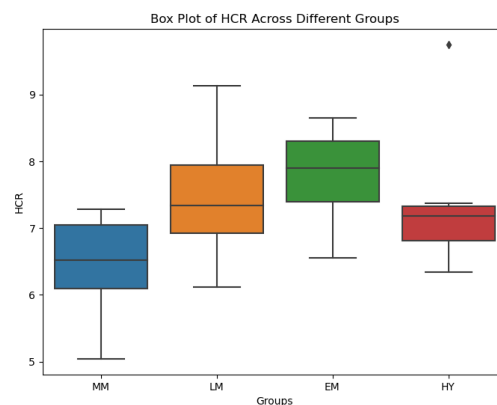


Figure 7.2 Boxplot of differences in Radius at Highest Concavity across Refractive Error groups (Corvis ST)

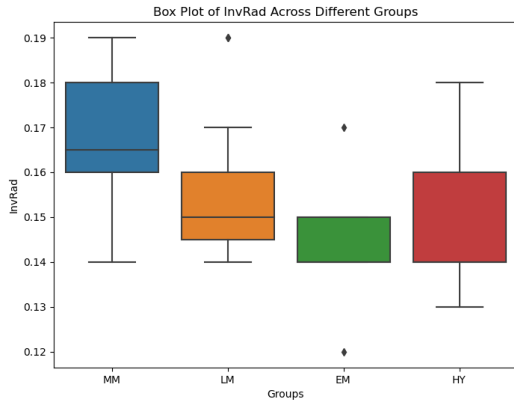


Figure 7.3 Boxplot of differences in Inverse Radius across Refractive Error groups (Corvis ST)

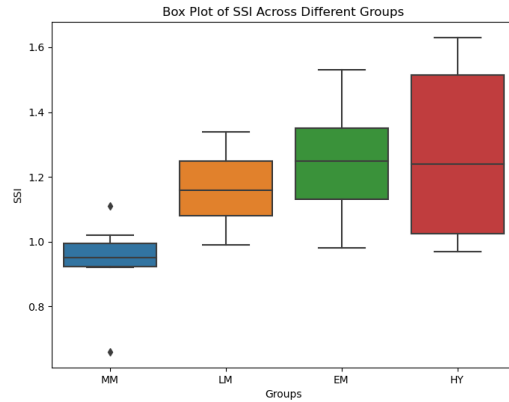


Figure 7.4 Boxplot of differences in Stress-Strain Index across Refractive Error groups (Corvis ST)

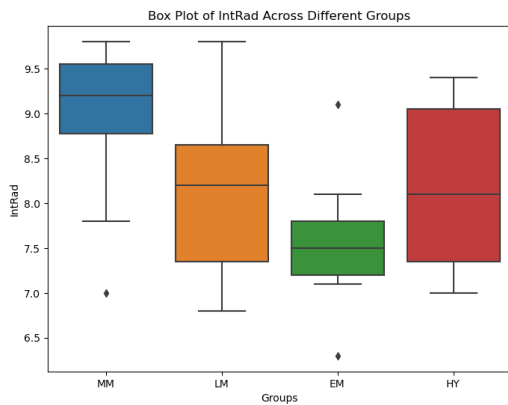


Figure 7.5 Boxplot of differences in Integrated Radius across Refractive Error groups (Corvis ST)

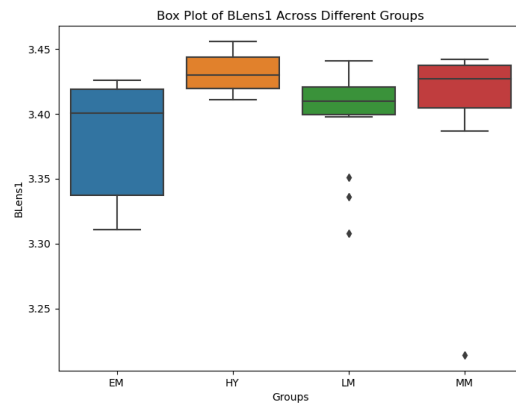


Figure 7.6 Boxplot of differences in Crystalline Lens Modulus across Refractive Error groups (BOSS)

7.3.3 Correlation with Refractive Error

For the second analysis, which explored the correlation between biomechanical parameters and the magnitude of refractive error, it was necessary to test the normality of both sets of variables. The Shapiro-Wilk test indicated that the distribution of refractive error was not normal ($W = 0.938$, $p = 0.018$), as illustrated in Figure 7.7 Refractive error distribution. Given the non-normal distribution of the refractive error, the Spearman correlation coefficient was employed for the analysis. This choice was appropriate as Spearman's method does not assume normality and is thus suited for data that are either ordinal or not normally distributed. This approach ensures a robust analysis of the correlation between refractive error and various biomechanical properties of the eye.

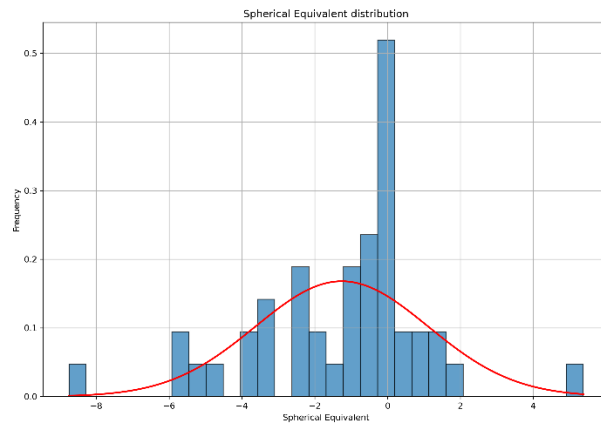


Figure 7.7 Refractive error distribution

The analysis of correlations between biomechanical parameters and the magnitude of refractive error, as detailed in Table 11.27 in Appendix 11.6.2, identified several parameters with statistically significant correlations:

- **Length at First Applanation** (A1L, Figure 7.8) Exhibits a positive, weak correlation ($\rho = 0.360$, $p = 0.015$, $R^2 = 0.130$), suggesting that longer applanation lengths correlate with higher refractive error.
- **Highest Concavity Time** (HCT, Figure 7.9): Shows a positive, weak correlation ($\rho = 0.296$, $p = 0.048$, $R^2 = 0.088$), indicating a slight association between the time of highest concavity and refractive error.
- **Highest Concavity Radius** (HCR, Figure 7.10): Also presents a positive, weak correlation ($\rho = 0.306$, $p = 0.041$, $R^2 = 0.094$), aligning with a minimal increase in radius with higher refractive errors.
- **Deflection Amplitude** (DeflAm, Figure 7.11): Demonstrates a negative, weak correlation ($\rho = -0.305$, $p = 0.041$, $R^2 = 0.093$), indicating that higher deflection amplitudes are associated with lower refractive errors.
- **Deflection Amplitude Ratio** (DeflAmR, Figure 7.12): Has a negative, weak to moderate correlation ($\rho = -0.392$, $p = 0.008$, $R^2 = 0.153$), suggesting a stronger negative relationship with refractive error.
- **Deformation Amplitude Ratio** (DefAR, Figure 7.13): Exhibits a moderate negative correlation ($\rho = -0.430$, $p = 0.003$, $R^2 = 0.185$), implying that greater deformations are linked to lower refractive errors.
- **Inverse Concave Radius** (InvRad, Figure 7.14): Shows a moderate negative correlation ($\rho = -0.429$, $p = 0.003$, $R^2 = 0.184$), suggesting similar trends as deformation amplitude ratio.

- **Whole-Eye-Movement** (WEM, Figure 7.15): Displays a weak positive correlation ($\rho = 0.313$, $p = 0.036$, $R^2 = 0.098$), indicating a slight increase in eye movement with higher refractive errors.
- **Stress Strain Index** (SSI, Figure 7.16): Reveals a moderate positive correlation ($\rho = 0.517$, $p < 0.001$, $R^2 = 0.267$), indicating a substantial relationship where higher SSI values correlate with higher refractive errors (Figure XX16). This parameter also surpassed both the instrument-specific and the classic Bonferroni corrections.
- **Integrated Radius** (IntRad, Figure 7.17): Shows a weak negative correlation ($\rho = -0.321$, $p = 0.032$, $R^2 = 0.103$), suggesting that a larger radius correlates with lower refractive errors.

It is notable that among all these correlations, only the SSI achieved a level of significance robust enough to withstand both Bonferroni corrections. None of the measurements from ORA, BOSS, or OCT reached statistical significance, highlighting specific biomechanical characteristics associated with different refractive errors and providing a focused insight into ocular biomechanics.

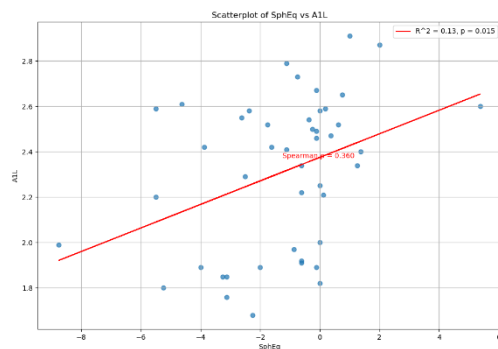


Figure 7.8 Scatterplot and regression line of Refractive Error and Length of First Applanation (Corvis ST)

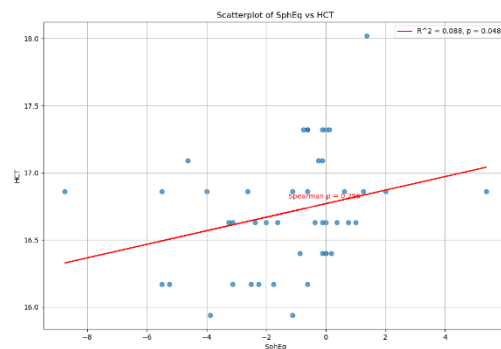


Figure 7.9 Scatterplot and regression line of Refractive Error and Highest Concavity Time (Corvis ST)

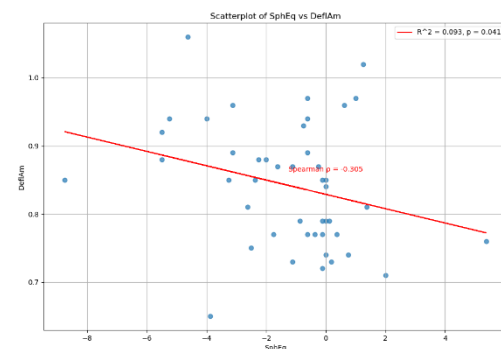
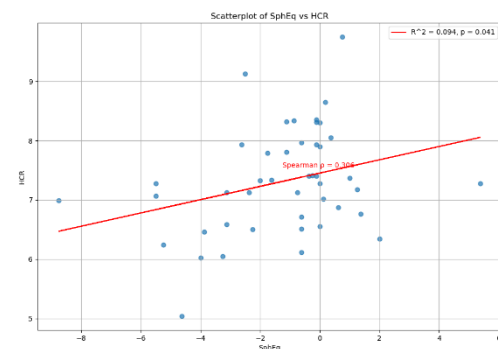


Figure 7.10 Scatterplot and regression line of Refractive Error and Highest Concavity Radius (Corvis ST)

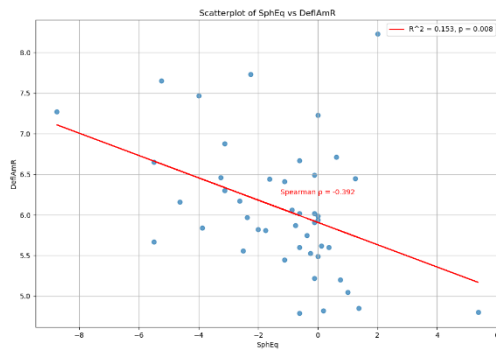


Figure 7.11 Scatterplot and regression line of Refractive Error and Deflection Amplitude (Corvis ST)

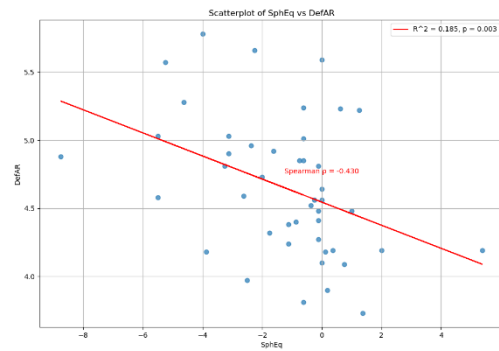


Figure 7.12 Scatterplot and regression line of Refractive Error and Deflection Amplitude Ratio (Corvis ST)

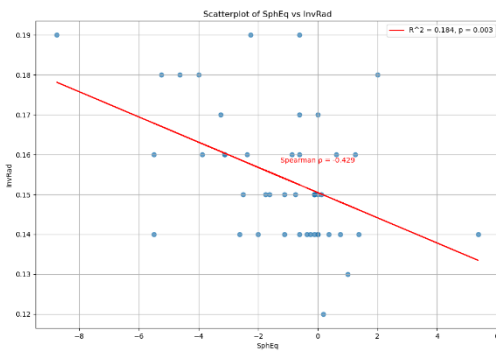


Figure 7.13 Scatterplot and regression line of Refractive Error and Deformation Amplitude Ratio (Corvis ST)

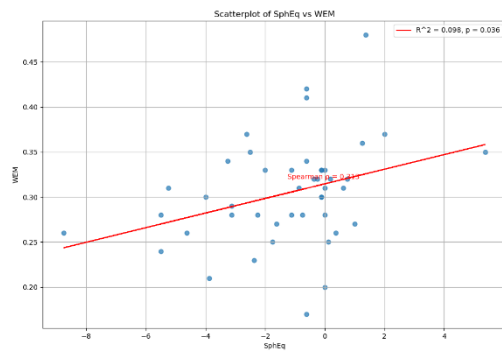


Figure 7.14 Scatterplot and regression line of Refractive Error and Inverse Radius (Corvis ST)

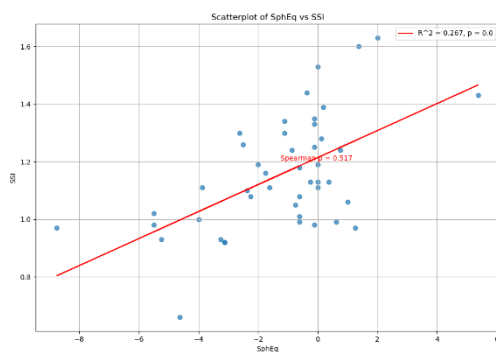


Figure 7.15 Scatterplot and regression line of Refractive Error and Whole-Eye-Movement (Corvis ST)

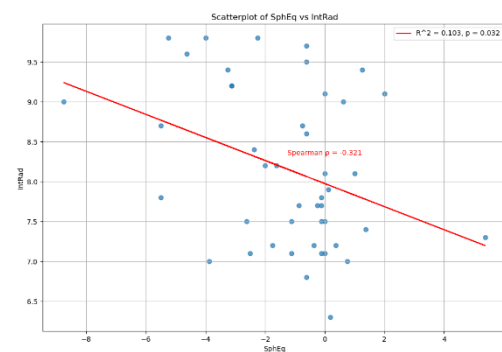


Figure 7.16 Scatterplot and regression line of Refractive Error and Stress-Strain Index (Corvis ST)

Figure 7.17 Scatterplot and regression line of Refractive Error and Integrated Radius (Corvis ST)

7.4 Discussion

7.4.1 ORA

While none of the parameters measured by the Ocular Response Analyzer showed statistically significant differences among the groups, there are noteworthy observations regarding corneal hysteresis and the corneal resistance factor. Corneal hysteresis was observed to be reduced in the low and medium myopia groups compared to emmetropic values, indicating a potential decrease in the viscoelastic properties of the cornea in myopic eyes. Similarly, the corneal resistance factor was lower in the medium myopia, low myopia, and hyperopia groups when compared with emmetropia, further suggesting a potential reduction in corneal biomechanical stability in these conditions.

Interestingly, the hyperopia group exhibited a higher degree of variability in both corneal resistance factor (standard deviation, SD = 3.1 mmHg, almost double that of the other groups) and corneal hysteresis (SD = 2.6 mmHg, 1.5 to 2.4 times the SD of other groups). This variation suggests that hyperopic corneas do not follow a consistent biomechanical pattern and may indicate a more complex interplay of factors influencing corneal properties in hyperopia.

Furthermore, intraocular pressure compensated for corneal characteristics (IOPcc), which adjusts for variables such as corneal hysteresis and resistance factor, was found to be higher in myopic individuals, with greater variability compared to emmetropic or hyperopic subjects.

The correlation analysis, while not yielding statistically significant results, did show clear trends in how intraocular pressure compensated for corneal characteristics (IOPcc) and Goldmann-correlated intraocular pressure (IOPg) vary with different refractive errors. IOPcc and IOPg were observed to increase with the degree of myopia and decrease towards hyperopia, with IOPcc demonstrating a steeper slope. This pattern may reflect the impact of refractive error on the biomechanical properties of the eye, influencing intraocular pressure measurements.

Conversely, corneal hysteresis and corneal resistance factor exhibited opposite trends: increasing with hyperopia and decreasing with myopia. This suggests that the cornea's ability to handle deformation and dissipate energy is compromised in myopic eyes compared to hyperopic ones. The reduction in corneal hysteresis and resistance factor in myopic eyes

has been posited by some researchers to potentially contribute to the onset and progression of myopia. These findings, however, are subject to variability due to factors like the demographic characteristics of the study populations (often Southeast Asian) and the degrees of myopia considered (Del Buey, Lavilla et al. 2014). Furthermore, the association between changes in axial length and corneal biomechanics has been documented (Bueno-Gimeno, España-Gregori et al. 2014), suggesting that as the eye elongates—a typical change in myopia—corneal properties are altered.

The findings of Plakitsi et al (Plakitsi, O'Donnell et al. 2011) which highlighted a reduction in corneal hysteresis in highly myopic eyes compared to those with low to moderate myopia and emmetropes, align somewhat with your study's observations. They also noted a correlation between corneal hysteresis and refractive error, quantifying an increase in hysteresis of 0.13 mmHg per dioptre (D) of refractive change. In contrast, your study observed a more pronounced increase in corneal hysteresis relative to refractive error, quantifying it at 0.413 mmHg per D. This discrepancy could be indicative of methodological differences, variations in the populations studied, or differences in the severity and range of myopia examined between the two studies. Moreover, while Plakitsi et al. found a correlation with corneal hysteresis, they did not observe any correlation between corneal resistance factor and refractive error. The absence of hyperopic participants in their study could limit the applicability of their findings across a broader refractive spectrum, potentially skewing the understanding of how corneal biomechanics interact with refractive error universally.

The study used to calculate the sample size for this experiment (Bueno-Gimeno, España-Gregori et al. 2014) found a consistent reduction in corneal hysteresis with the decrease in hyperopia and increase in myopia. Similar results were observed for the resistance factor, though the reduction was less pronounced and not statistically significant.

A study investigating corneal biomechanical differences among myopes (< -5.00 D), hyperopes (> +3.00 D), and controls (between +1.00 and -1.00 D) reached similar conclusions to this study: corneal hysteresis was reduced in myopes and increased in hyperopes compared to controls. This suggests that excessive axial elongation might influence the rigidity of ocular structures and, consequently, corneal hysteresis. While the corneal resistance factor (CRF) was not affected by refractive error, intraocular pressure (IOPcc and IOPg) was higher in myopic eyes (İnceoğlu, Emre et al. 2018).

A fascinating theory hypothesises that lower values of corneal hysteresis might contribute to the development of refractive errors (Huang, Huang et al. 2011). Animal models have shown

that induced ametropia causes changes in scleral fibril orientation (McBrien, Young et al. 2009) which can affect corneal collagen and potentially lead to both local (reduction in corneal hysteresis) and global (axial elongation) ocular changes. Currently, there is a lack of strong evidence supporting this theory, and it remains unclear whether the reduction in corneal hysteresis is a cause or an effect of refractive error development. This uncertainty is compounded by the fact that the corneal resistance factor, which is generally considered to reflect the overall resistance and elastic behaviour of the cornea, is not affected by refractive error.

7.4.2 Corvis ST

The analysis of the statistically significant differences between groups in the Corvis ST measurements highlighted that only a few parameters showed differences among the groups:

- **Length at the First Appplanation:** The post hoc analysis revealed that the corneas of hyperopic eyes (median 2.60 mm; IQR 0.17 mm) are more deformable than those of moderately myopic eyes (median 1.94 mm; IQR 0.29 mm), as indicated by the greater applanated length. A positive statistically significant correlation was found, suggesting that the applanated portion of the cornea increases with hyperopia and decreases with myopia. Similar findings are reported in the literature, with statistically significant differences observed between groups with different refractive errors (Lu, Hu et al. 2022).
- **Highest Concavity Radius:** Moderately myopic eyes have smaller radii (median 6.53 mm; IQR 0.53 mm) compared to low myopic (median 7.34 mm; IQR 0.67 mm) and emmetropic eyes (median 7.90 mm; IQR 0.52 mm). Interestingly, no differences were found with hyperopic eyes. The correlation with refractive error was positive and statistically significant. Lower values of radius indicate a stiffer and less deformable cornea, as this measurement reflects the curvature of the cornea at its maximum concavity. A shorter radius suggests that the portion of the cornea displaced during maximum concavity is smaller, indicating greater stiffness. Similar findings are reported in the literature (Kenia, Kenia et al. 2020, Sedaghat, Momeni-Moghaddam et al. 2020, Yu, Shao et al. 2020). However, opposite results were found in Chinese children, where high myopes showed flatter curvatures than hyperopes and emmetropes (Lu, Hu et al. 2022)

- **Inverse Concave Radius:** The medium myopia group (median 0.17 mm^{-1} ; IQR 0.01 mm^{-1}) showed a statistically significant difference compared to the emmetropia group (median 0.14 mm^{-1} ; IQR 0.01 mm^{-1}). The inverse radius exhibits a negative statistically significant correlation with refractive error. As the reciprocal of the highest concavity radius, a higher inverse radius value is associated with a stiffer cornea. Therefore, these results align with the findings for length at first applanation and highest concavity radius.
- **Stress-Strain Index:** The medium myopia group (median 0.95; IQR 0.07) showed statistically significant differences compared to all other groups: low myopia (median 1.16; IQR 0.09), emmetropia (median 1.25; IQR 0.13), and hyperopia (median 1.24; IQR 0.24). A positive correlation was also found with the degree of refractive error. The results were robust enough to withstand Bonferroni correction. Interestingly, the interpretation of the stress strain index suggests the opposite of the other Corvis ST parameters: a higher value indicates greater resistance to deformation, thus a stiffer cornea. Similar findings were recently observed in the Indian population, where a higher degree of myopia was associated with lower stress strain index values (Kenia, Kenia et al. 2024). The discrepancy with other measurements could be explained by the fact that the stress strain index is independent of IOP, making it more reflective of corneal structure than other Corvis ST parameters (Eliasy, Chen et al. 2019).
- **Integrated Radius:** The only statistically significant difference in the post hoc analysis was found between medium myopia (9.0 ± 0.9) and emmetropia (7.6 ± 0.7). A negative statistically significant correlation was found with refractive error, suggesting that the integrated radius increases with myopia but remains the same for hyperopes and emmetropes. The integrated radius is the integral under the curve of the concave radius and the inverse concave radius. Although it represents an area, it does not have a unit of measurement. As an integral, it sums the infinitesimal areas beneath the curve representing the inverse concave radius (the reciprocal of the radius of curvature). The result depends on the specific values of the curve. A curve with higher values of the reciprocal of the radius of curvature (indicating a smaller radius of curvature and thus a stiffer cornea) will produce a greater integral value. Therefore, the results align with the highest concavity radius and inverse concave radius: myopia is associated with stiffer corneas, and hyperopia with softer ones. Similar findings are reported in the literature, showing an increase in integrated values associated with more severe myopia (Sedaghat, Momeni-Moghaddam et al. 2020, Kenia, Kenia et al. 2024) or the presence of myopia (Lu, Hu et al. 2022).

- **Highest Concavity Time:** A positive, albeit weak, statistically significant correlation with refractive error was found. Highest concavity time represents the interval between the initiation of the puff of air and the point of highest concavity. A stiffer cornea reaches maximum concavity sooner than a more deformable (and elastic) cornea, which can be deformed more and thus requires more time (Kling and Hafezi 2017, Liu, Pang et al. 2022). Similar correlations have been reported in the literature (Yu, Shao et al. 2020) suggesting that highly myopic corneas reach highest concavity sooner than low myopic corneas.
- **Deflection Amplitude:** A negative statistically significant correlation was found with refractive error. Deflection amplitude measures the movement of the corneal apex while accounting for the overall eye movement, thus isolating the corneal displacement. It is calculated by comparing the superimposed cornea with the actual corneal movement during displacement. A smaller deflection amplitude indicates a stiffer cornea (Bak-Nielsen, Pedersen et al. 2014, Chun, Moon et al. 2020), implying that more myopic eyes have softer corneas. Similar findings are reported in the literature, where higher myopes exhibit greater values of deflection amplitude (Kenia, Kenia et al. 2020).
- **Deflection Amplitude Ratio:** A negative, statistically significant correlation was found with refractive error. The deflection amplitude ratio describes the ratio between the deflection amplitude at the corneal apex and the deflection amplitude 2 mm laterally from the corneal apex. This parameter reflects the uniformity of corneal deformation between the centre and periphery. Similar to deflection amplitude, a stiffer cornea exhibits more uniform displacement within the tissue, resulting in a lower deflection amplitude ratio.
- **Deformation Amplitude Ratio:** A negative, statistically significant correlation was found with refractive error. Deformation amplitude represents the displacement of the corneal apex along the Z-axis, indicating the inward movement caused by the air puff. Unlike deflection amplitude, it does not account for the overall eye movement. The deformation amplitude ratio describes the ratio between the apex and peripheral corneal displacements. The interpretation is similar: a stiffer cornea exhibits higher displacement uniformity compared to a softer cornea.
- **Whole Eye movement:** A positive, statistically significant correlation was found with refractive error. It is computed by considering the movement of the peripheral part of the cornea along the Z-axis. This correlation suggests that myopic eyes exhibit a smaller movement of the whole eye compared to hyperopic eyes, indicating a stiffer structure.

The results present an inherent ambiguity: while parameters such as length at first applanation, highest concavity time, highest concavity radius, inverse radius, integrated radius, and whole eye movement suggest increased stiffness in myopic corneas, others, including the stress strain index, deflection amplitude, deflection amplitude ratio, and deformation amplitude ratio, indicate a reduction in corneal stiffness associated with myopia. This inconsistency may be attributed to the significant dependence of most of these parameters on intraocular pressure (IOP). Notably, the stress strain index, which is independent of IOP, is the only parameter that consistently withstands both levels of Bonferroni correction.

7.4.3 BOSS

7.4.3.1 Cornea

This study is the first to examine the relationship between BOSS measurements and refractive error. None of the measurements of the corneal Brillouin modulus were correlated with the magnitude of the refractive error, and no statistically significant differences were found between the four groups. Interestingly, even though not statistically significant, all the correlations are negative: as the myopic refractive error decreases or the hyperopic refractive error increases, the Brillouin modulus decreases. This finding might be due to chance, as differences between groups do not follow a consistent trend. The mean values across the four corneal locations support the trend observed in the correlations, but again, no statistically significant differences were identified.

7.4.3.2 Lens

Among lenticular parameters the only measurement that showed a statistically significant difference is Brillouin modulus of the lens. Post hoc analysis revealed a statistically significant difference between hyperopes (median 3.430 GPa; IQR 0.014 GPa) and emmetropes (median 3.401 GPa; IQR 0.037 GPa). However, this finding was not confirmed by the correlation analysis, and none of the lens parameters measured using BOSS were correlated with refractive error.

7.4.4 OCT

Central corneal thickness did not show any statistically significant differences among groups, nor did it correlate with refractive error distribution, consistent with previous literature (Chen, Liu et al. 2009, Nangia, Jonas et al. 2010).

Similarly, the crystalline lens did not exhibit any statistical differences. The correlation, although neither strong nor significant, suggests a positive relationship between refractive error and lens thickness: hyperopes tend to have thicker lenses than myopes. Literature findings are inconclusive and inconsistent, largely due to confounding factors such as age, gender, and developmental stage (Shih, Chiang et al. 2009, Hashemi, Pakzad et al. 2018, Wang, Zhu et al. 2022). A recent study investigating lens morphology differences in eyes of patients with unilateral high myopia found no significant differences (Zhang, Zhang et al. 2024). It can be inferred that limited differences in lens thickness are expected among patients with varying refractive errors within a narrow age range, although further studies are necessary to confirm these findings.

7.5 Conclusions

The results of this study highlighted some significant differences between groups with different refractive errors, particularly in parameters measured with the Corvis ST. Parameters such as length at first applanation, highest concavity radius, and the stress-strain index showed statistically significant differences among the groups, suggesting variations in corneal deformability and stiffness associated with different refractive errors.

Despite some limitations, such as the inability to achieve the initially planned sample size, the study provided valuable insights into the biomechanical characteristics of the cornea in relation to refractive errors. The data suggest that myopia is generally associated with increased corneal stiffness, while hyperopia tends to be associated with a more deformable cornea.

In particular, the stress-strain index showed a robust correlation with refractive error, indicating potential use as a biomarker to evaluate the biomechanical properties of the cornea in patients with varying degrees of myopia and hyperopia. However, the variability observed in some parameters suggests that further research is needed to confirm these

findings and deepen the understanding of the interactions between corneal biomechanics and refractive errors.

These results underscore the importance of considering corneal biomechanical properties in the clinical management of refractive errors and in planning refractive surgical interventions. Future studies could benefit from larger sample sizes and greater demographic diversity to confirm and expand upon the conclusions of this study.

7.6 Limitations

Due to recruitment limitations, it was not possible to fulfil the criteria established with the sample size calculation and the groups did not match in numbers. The high myopia group had to be eliminated, and the only participant was included in the medium myopia group.

8 Lens Peripheral Thickness Variations

8.1 Introduction

The final chapter addresses an incidental finding encountered during the investigation detailed in the previous chapters. Specifically, while selecting the most appropriate cases for comparing the measurements of the BOSS plateau with lens thickness evaluated using OCT as described in section 5.4.3, it became apparent that the peripheral thickness of the crystalline lens exhibited variability not only across different meridians but also within individual meridians themselves. Such variations have received limited attention in the ophthalmic literature, despite their potential importance in refining intraocular lens (IOL) power calculations, improving refractive surgery outcomes, and deepening the understanding of accommodative changes that accompany aging. To comprehensively explore the extent and implications of this observation, data from all participants involved in the prior studies were extrapolated and subjected to further analysis.

The human crystalline lens is a transparent, avascular, and biconvex anatomical structure primarily responsible for the eye's ability to accommodate, thereby enabling clear vision at near distances. In adults, typical dimensions of the lens are approximately 9 to 10 mm in equatorial diameter and 4 to 5 mm in axial thickness (Ruan, Liu et al. 2020). While traditionally assumed to exhibit radial symmetry about its optical axis, the lens frequently demonstrates toricity, characterized by differential refractive powers along distinct meridians. Such toricity contributes significantly to variations in optical performance and may be influenced by both anatomical and physiological factors, including zonular tension distribution, capsular elasticity, and lens fibre architecture. Understanding these peripheral thickness variations can thus offer valuable insights into lens biomechanics and optical function, particularly in the context of refractive surgery, presbyopia management, and cataract extraction.

8.2 Materials and Methods

A total of 58 eyes (44 right eyes [OD] and 14 left eyes [OS]) were included in this analysis. Measurements of crystalline lens thickness were acquired using the Anterior OCT device (Heidelberg Engineering GmbH, Heidelberg, Germany), a swept-source optical coherence tomography system designed for anterior segment imaging. All scans were conducted without the use of mydriatic agents, under standardized ambient room lighting conditions.

Following image acquisition, the central lens thickness automatically calculated by the Anterior software was recorded and subsequently used as a reference point, designated as the lens centre. To investigate peripheral lens thickness variability, measurements were manually obtained from OCT images at 1 mm distance from the lens centre along four principal meridians (superior, inferior, nasal, and temporal). For accuracy and consistency, each measurement was carefully extracted by visual inspection of cross-sectional OCT images oriented along the respective meridians.

Statistical analyses and data visualization were performed using Python 3 (Python Software Foundation, Wilmington, DE, USA), employing widely accepted libraries including Pandas for data management, SciPy.stats for statistical testing, NumPy for numerical analysis, and Matplotlib for graphical

Demographics of the patients are reported in Table 8.1.

Table 8.1 Demographics of participants

Age [years]	30 ± 15
RE / LE	44 / 14
M / F	21 / 37
SER [D]	-0.76 ± 2.39

8.3 Results

The descriptive statistics (mean ± standard deviation) of lens thickness at the central and peripheral locations, as well as the results of the Shapiro-Wilk test for normality, are summarized in Table 8.2. Figure 8.1 visually depicts the distribution patterns of peripheral lens thickness measurements at each of the four investigated meridians.

Table 8.2 Mean, SD and Shapiro Wilk results for normality

	Mean [mm]	SD [mm]	Statistic	p-value
Central Lens Thickness	3.89	0.41	0.91	< 0.001
Thickness 1 mm Nasally	3.73	0.41	0.91	< 0.001
Thickness 1mm Temporally	3.76	0.41	0.90	< 0.001
Thickness 1 mm Superiorly	3.79	0.41	0.90	< 0.001
Thickness 1 mm Inferiorly	3.72	0.40	0.90	< 0.001

Since peripheral lens thickness data deviated significantly from a normal distribution (see Table 8.2), non-parametric statistical methods were employed for further analyses.

Friedman's test revealed statistically significant differences in lens thickness among the four peripheral locations ($\chi^2 = 107.12$, $p < 0.001$). Subsequently, a post hoc pairwise comparison using the Wilcoxon signed-rank test, adjusted with Bonferroni correction to account for multiple comparisons, was conducted. Results indicated statistically significant differences (all $p \leq 0.01$ after correction) in lens thickness between each of the four peripheral locations, as detailed in Table 8.3.

Table 8.3 Results of post hoc analysis, with differences along meridians

	Mean Difference	SD	W Statistics	P value	Corrected p-value
Temporal-Nasal	0.03	0.05	267.0	< 0.001	< 0.001
Temporal-Superior	-0.01	0.3	346.5	0.002	0.011
Temporal-Inferior	0.05	0.03	0.0	< 0.001	< 0.001
Nasal-Superior	-0.04	0.03	34.0	< 0.001	< 0.001
Nasal-Inferior	0.02	0.04	343.0	< 0.001	< 0.001
Superior-Inferior	0.07	0.04	3.0	< 0.001	< 0.001

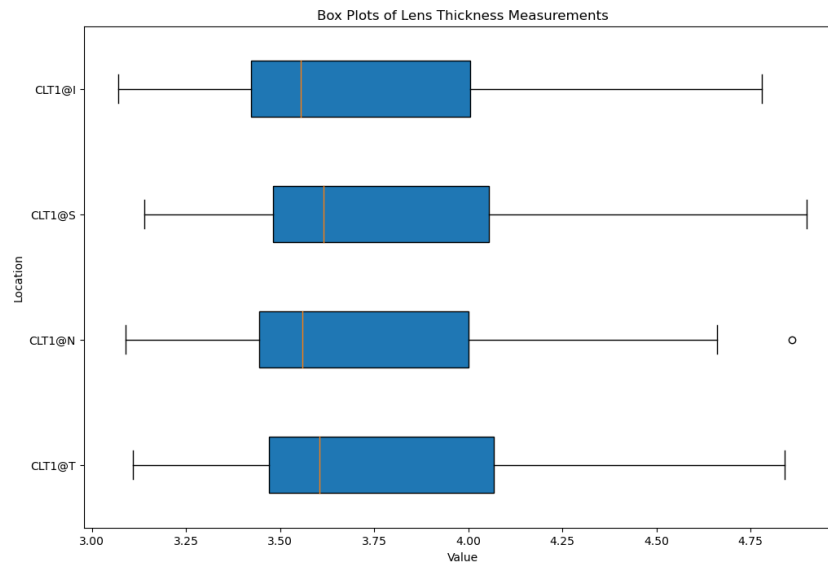


Figure 8.1 Box plot of lens thickness according to location. CLT (Central Lens Thickness) Inferiorly (I), Superiorly (S), Nasally (N) and Temporally (T).

8.4 Discussion

At 1 mm of eccentricity, the crystalline lens exhibited notable asymmetry, with the temporal side measuring 0.03 ± 0.04 mm thicker than the nasal side and the superior aspect measuring 0.07 ± 0.04 mm thicker than the inferior aspect. These observations of regional peripheral differences have not been documented previously. For instance, Ortiz, Pérez-Merino et al. (2012) developed 3D models of the crystalline lens using OCT images; however, their study did not assess differences in peripheral thickness along the same meridian at identical eccentricities. Their findings indicated that the lens surface could be well described by symmetric conoids with deviations from perfect symmetry being minimal (on the order of microns) (Ortiz, Pérez-Merino et al. 2012). Similarly, a study reported that the ratio of lens equatorial diameter to axial thickness remains relatively constant (approximately 2.1 in younger subjects, decreasing to 2.0 with age), suggesting a uniformly expanding and symmetric lens structure (Rosen, Denham et al. 2006).

Several hypotheses may account for the observed peripheral asymmetry:

- 1) **Measurement Error:** Although measurement error is always a consideration, the Anterior OCT has demonstrated high repeatability (Schiano-Lomoriello, Hoffer et al. 2021). Nonetheless, the inability to cross-validate with an additional machine means

that an undetected systematic error cannot be entirely ruled out, even if the Anterior needs to be calibrated every time is turned on.

- 2) **Head Positioning and Instrument Alignment:** The configuration of the chinrest and forehead rest may induce a slight head tilt, potentially causing a corresponding tilt in the lens during measurement. This positional adjustment might contribute to the apparent differences in lens thickness.
- 3) **Convergence Effects:** The proximity of the fixation target—located only a few centimeters away—could induce convergence. A previous work suggests that convergence is accompanied by a slight downward rotation of the eye, which might manifest as the observed asymmetry in thickness (Enright 1989).
- 4) **Accommodation-Induced Changes:** The close distance between the eye and the instrument may provoke a minor degree of accommodation. It has been well documented that accommodative changes are not entirely symmetric. It is well documented that the anterior lens surface tends to become more convex than the posterior surface during accommodation (Koretz, Cook et al. 2002, Esteve-Taboada, Domínguez-Vicent et al. 2017, Gibson, Cruickshank et al. 2018); the posterior surface of the lens tends to show less change on the vertical meridian than on the horizontal one (Leng, Yuan et al. 2014). An analysis of higher-order aberrations during accommodation confirmed the asymmetry between anterior and posterior lenticular changes in terms of curvature (Yuan, Shao et al. 2013). The asymmetry measured during accommodation has never been reported along a single meridian but only across meridians.
- 5) **Differential Zonular Tension and Biomechanical Variability:** Variations in the distribution and mechanical properties of the zonular fibers may produce differential tension across the lens capsule. A study found that the biomechanical forces exerted by the zonules influence lens shape and could lead to localized differences in thickness (Koretz and Handelman 1982). This hypothesis suggests that regional disparities in zonular insertion or tension, potentially due to subtle variations in ciliary muscle activity, may contribute to the asymmetric peripheral measurements.
- 6) **Intrinsic Anatomical Variation:** The asymmetry may represent an intrinsic anatomical feature that has not been previously described. This stable variation, potentially compensated by neural mechanisms to mitigate image degradation from high-order aberrations (Chen, Artal et al. 2007, Sabesan and Yoon 2010), might also be influenced by the natural orientation of human orbits—which typically point temporally to optimize peripheral vision. While this could explain discrepancies along the horizontal meridian, it does not fully account for the vertical differences.

To further elucidate the underlying mechanisms and clinical implications, several strategies for future investigation are recommended:

- **Multi-Device Validation:** Employing additional OCT systems to corroborate the reproducibility of these measurements can help rule out instrument-specific biases.
- **Optimizing Patient Positioning and Open Field OCT:** Investigating alternative chinrest designs and open field OCT systems (currently not available) may reduce the constraints imposed by conventional head stabilization, thereby mitigating potential measurement biases associated with head tilt and effects of ocular accommodation and near fixation. Although there is limited published evidence directly addressing this modification, the approach could offer a more natural viewing environment and improved accuracy.
- **Enhanced Imaging Techniques:** Utilizing advanced imaging modalities (e.g., high-resolution ultrasound biomicroscopy or MRI) may provide more detailed assessments of zonular fibres distribution and lens capsule integrity.
- **Accommodation Control:** Future studies could incorporate cycloplegic protocols or controlled fixation distances to minimize accommodative effects during measurement.

8.5 Conclusions

This chapter has demonstrated that the peripheral thickness of the human crystalline lens exhibits significant asymmetry, with the temporal and superior regions displaying greater thickness compared to the nasal and inferior regions, respectively. These observations challenge the conventional assumption of radial symmetry and underscore the importance of considering regional variations in lens morphology.

The potential benefits of these insights are multifaceted. Clinically, recognizing and quantifying peripheral lens asymmetries could enhance the precision of intraocular lens (IOL) power calculations and improve outcomes in refractive surgery. Furthermore, these findings may contribute to a better understanding of accommodative dynamics and presbyopia development, leading to more targeted therapeutic interventions. From a research perspective, the demonstration of subtle regional differences prompts a reevaluation of current biomechanical models of the lens and may inform the design of future optical imaging studies.

Further studies are needed to understand the nature of the differences in terms of lenticular thickness along the same meridians at the same eccentricity. The use of different OCTs, different setup of forehead rest and chinrest or the use of an open field OCT (not commercially available right now) could help clarifying the unexpected findings.

9 Summary and Future Work

9.1 Summary of Findings

Despite ocular biomechanics only recently becoming quantifiable in clinical settings, substantial progress has been made over the past 20 years. This field has seen remarkable technological advancements and has rapidly expanded, establishing itself as a significant area of study in optometry and ophthalmology. At present, three distinct instruments are commercially available; however, their outputs are not directly comparable, as each device assesses different biomechanical properties. The Ocular Response Analyzer measures corneal viscoelasticity, the Corvis ST evaluates parameters related to air-puff-induced deformation, and the BOSS quantifies the Brillouin modulus, which reflects the longitudinal elastic modulus and may thus be interpreted as an index of corneal stiffness. This diversity in instrumentation underscores the complexity and multifaceted nature of ocular biomechanics, which necessitates a comprehensive approach to fully understand its implications.

The increasing accessibility to machine learning algorithms and computational power has naturally led to the integration of ocular biomechanics data with supervised machine learning algorithms for detecting and diagnosing ocular pathologies. Chapter 2 demonstrated that even traditional indices measured by the Corvis ST could reveal alterations in corneal biomechanics. When these indices are properly combined with a robust algorithm, they can detect keratoconus with a high degree of accuracy. This achievement highlights the potential for machine learning to enhance diagnostic precision and offers a promising avenue for early detection of this condition. While the performance in detecting POAG was lower compared to keratoconus detection, it was still noteworthy, indicating room for further refinement and optimisation of the algorithms. Such refinement could lead to an improvement in pathology detection, that could possibly reach accuracy of the other methods that are currently used to screen for keratoconus or POAG. The superior performance of the Corvis ST compared to the ORA can be attributed to the larger number of indices it measures, providing a broader range of features for characterisation and quantification, thus offering more detailed insights into corneal biomechanics.

Having established that keratoconus and POAG can be detected using machine learning algorithms, attention shifted to the potential confusion keratoconus alterations might cause in a classifier designed to differentiate various types of glaucoma (POAG, NTG, and OHT) from

healthy subjects. Using Orange Data Mining software facilitated the rapid development of a pipeline where models were trained, optimised, and tested with data from patients with keratoconus but without glaucoma. Findings suggest that keratoconus alterations could indeed confound a glaucoma screening tool. This underscores the importance of developing more sophisticated models that can accurately distinguish between different ocular conditions, ensuring that diagnostic tools are both sensitive and specific.

Chapter 4 assessed the repeatability of BOSS measurements, revealing that the Brillouin modulus exhibits excellent repeatability in the crystalline lens, on the contrary repeatability of corneal measurements is low, due to the fewer points measured along the z axis. High repeatability is crucial for ensuring consistent and reliable data, which is fundamental for both clinical practice and research.

Chapter 5 demonstrated that the Brillouin modulus is a novel parameter that does not correlate with any indices measured by other devices, indicating that BOSS data are distinct from other corneal biomechanical data or from OCT data about lens thickness. This finding is significant as it suggests that the Brillouin modulus provides unique information about the biomechanical properties of the eye, which could lead to new insights and potentially new diagnostic criteria.

Age-related analysis in Chapter 6 revealed an unexpected finding: the Brillouin modulus decreases with age, suggesting that the lens becomes softer over time. This finding is contrary to expectations for presbyopia, where lens thickening in the central region counteracts lens softening, leading to presbyopia. Lens growth was confirmed with both BOSS and OCT measurements. These results indicate that while the lens becomes softer with age, its overall thickness increases, which complicates the biomechanical understanding of presbyopia and calls for a reassessment of existing theories.

Chapter 7 highlighted the importance of considering corneal biomechanics as a biomarker for myopia onset and progression, especially considering stress-strain index (SSI) that is independent from IOP measurement. The findings suggest that changes in corneal biomechanics may precede or accompany the development of myopia, making it a valuable target for early intervention strategies. Furthermore, the chapter underscores the need to develop new technologies to quantify scleral biomechanics, as the sclera plays a critical role in the structural integrity of the eye and may significantly influence myopia progression.

Chapter 8 reported an unexpected finding not reported in literature before: along the same meridian (vertical or horizontal), at the same distance from the centre of the crystalline lens

(1 mm), the thickness varies. Along the vertical meridian, the lens is thicker in the superior portion than in the inferior; along the horizontal meridian, it is thicker in the temporal portion than in the nasal portion. This anisotropy in lens thickness could have important implications for understanding the biomechanics of the lens and its role in visual function, and it may influence the development of new optical models and correction strategies.

In summary, the advancements in ocular biomechanics over the past two decades have been significant, driven by technological innovation and the integration of machine learning. These developments have not only improved our understanding of ocular biomechanics but also opened new avenues for diagnosing and managing ocular pathologies, ultimately enhancing patient care.

9.2 Future Research

The fourth industrial revolution and the development of more complex and powerful neural networks will provide even more advanced tools for the early detection and prompt management of ocular pathologies. Future research should address some limitations of the studies presented in this thesis.

Firstly, it is essential to train all models with the updated indices from all available machines, including data from the BOSS. While BOSS has proven effective in detecting keratoconus alterations, no studies have yet explored its application to glaucoma alterations. Investigating the confounding factors due to KC in a screening tool developed for glaucoma would benefit from these updated indices. Moreover, optimising machine learning algorithms, such as SVM, MLP classifiers, Decision Trees, and Random Forests, is crucial. These algorithms were not trained in the present work because the optimisation using Orange Data Mining must be done manually and it is extremely inefficient and time-consuming. Despite this, Orange Data Mining is a powerful learning tool and should be included in undergraduate programmes to educate the next generation of clinicians. These clinicians must have the knowledge to interact with and interpret AI tools, which will become increasingly predominant in healthcare.

Intelon, the company that manufactures BOSS, recently communicated that modifications were made to the measurement process. The system now scans more than 3 to 5 points per location, as the steps between points on the z-axis were modified to increase accuracy.

Additionally, the depth of the scan for the cornea will soon be reduced from 8 mm to 2 mm, allowing for faster measurement, which is crucial for patient comfort. These changes are expected to enhance repeatability and improve the ability to recognise alterations.

The next step in research will be the study of scleral biomechanics to evaluate the effect of scleral rigidity on glaucoma, keratoconus, and the development of refractive errors. This exploration is vital for understanding the broader biomechanical properties of the eye and their implications for various ocular conditions.

10 Bibliography

- Aas, K., M. Jullum and A. J. A. I. Løland (2021). "Explaining individual predictions when features are dependent: More accurate approximations to Shapley values." **298**: 103502.
- Abd Rahman, H. A. and B. W. Yap (2016). Imbalance effects on classification using binary logistic regression. Soft Computing in Data Science: Second International Conference, SCDS 2016, Kuala Lumpur, Malaysia, September 21-22, 2016, Proceedings 2, Springer.
- Abdelgawad, A. E., M. T. Elnaggar, M. E. Abdelsalam and A. K. J. A.-A. I. M. J. Abdullah (2024). "Study of Corneal Biomechanics Using Corneal Visualization by Scheimpflug Technology in Corneas with Tomographic Ectasia Susceptibility." **5**(8): 38.
- Abitbol, O., J. Bouden, S. Doan, T. Hoang-Xuan and D. Gatinel (2010). "Corneal hysteresis measured with the ocular response analyzer ® in normal and glaucomatous eyes." Acta Ophthalmologica **88**(1): 116-119.
- Ahmadi Hosseini, S. M., N. Mohidin, F. Abolbashari, B. Mohd-Ali and C. T. J. I. o. Santhirathelagan (2013). "Corneal thickness and volume in subclinical and clinical keratoconus." **33**: 139-145.
- Alain, S., Y. Lteif, A. É and D. Gatinel "Biomechanical properties of keratoconus suspect eyes." Investigative Ophthalmology and Visual Science.
- Ali, N. Q., D. V. Patel and C. N. J. McGhee "Biomechanical Responses of Healthy and Keratoconic Corneas Measured Using a Noncontact Scheimpflug-Based Tonometer." Investigative Ophthalmology & Visual Science **55**(6): 3651.
- Ali, N. Q., D. V. Patel and C. N. J. McGhee (2014). "Biomechanical responses of healthy and keratoconic corneas measured using a noncontact scheimpflug-based tonometer." Invest Ophthalmol Vis Sci **55**(6): 3651-3659.
- Alkanaa, A., R. Barsotti, O. Kirat, A. Khan, T. Almubrad and S. Akhtar (2019). "Collagen fibrils and proteoglycans of peripheral and central stroma of the keratoconus cornea - Ultrastructure and 3D transmission electron tomography." Sci Rep **9**(1): 19963.
- Alnahedh, T. A. and M. Taha (2024). "Role of Machine Learning and Artificial Intelligence in the Diagnosis and Treatment of Refractive Errors for Enhanced Eye Care: A Systematic Review." Cureus **16**(4): e57706.
- Althnian, A., D. AlSaeed, H. Al-Baity, A. Samha, A. B. Dris, N. Alzakari, A. Abou Elwafa and H. J. A. s. Kurdi (2021). "Impact of dataset size on classification performance: an empirical evaluation in the medical domain." **11**(2): 796.
- Altmann, A., L. Toloşi, O. Sander and T. J. B. Lengauer (2010). "Permutation importance: a corrected feature importance measure." **26**(10): 1340-1347.
- Ambekar, Y., M. Singh, J. T. Zhang, A. Nair, S. R. Aglyamov, G. Scarcelli and K. V. Larin (2020). "Multimodal quantitative optical elastography of the crystalline lens with optical coherence elastography and Brillouin microscopy." Biomedical Optics Express **11**(4): 2041-2051.
- Ambekar, Y. S., M. Singh, G. Scarcelli, E. M. Rueda, B. M. Hall, R. A. Poché and K. V. Larin (2020). "Characterization of retinal biomechanical properties using Brillouin microscopy." Journal of biomedical optics **25**(9).

Ambrósio, R., Jr., B. T. Lopes, F. Faria-Correia, M. Q. Salomão, J. Bühren, C. J. Roberts, A. Elsheikh, R. Vinciguerra and P. Vinciguerra (2017). "Integration of Scheimpflug-Based Corneal Tomography and Biomechanical Assessments for Enhancing Ectasia Detection." *J Refract Surg* **33**(7): 434-443.

Ambrósio, R., Jr., A. P. Machado, E. Leão, J. M. G. Lyra, M. Q. Salomão, L. G. P. Esporcatte, J. B. R. da Fonseca Filho, E. Ferreira-Meneses, N. B. Sena, Jr., J. S. Haddad, A. Costa Neto, G. C. de Almeida, Jr., C. J. Roberts, A. Elsheikh, R. Vinciguerra, P. Vinciguerra, J. Bühren, T. Kohnen, G. M. Kezirian, F. Hafezi, N. L. Hafezi, E. A. Torres-Netto, N. Lu, D. S. Y. Kang, O. Kermani, S. Koh, P. Padmanabhan, S. Taneri, W. Trattler, L. Gualdi, J. Salgado-Borges, F. Faria-Correia, E. Flockerzi, B. Seitz, V. Jhanji, T. C. Y. Chan, P. M. Baptista, D. Z. Reinstein, T. J. Archer, K. M. Rocha, G. O. t. Waring, R. R. Krueger, W. J. Dupps, R. Khoramnia, H. Hashemi, S. Asgari, H. Momeni-Moghaddam, S. Zarei-Ghanavati, R. Shetty, P. Khamar, M. W. Belin and B. T. Lopes (2023). "Optimized Artificial Intelligence for Enhanced Ectasia Detection Using Scheimpflug-Based Corneal Tomography and Biomechanical Data." *Am J Ophthalmol* **251**: 126-142.

Amsler, M. (1946). "Classic keratocene and crude keratocene; Unitary arguments." *Ophthalmologica* **111**(2-3): 96-101.

Anand, A., C. G. De Moraes, C. C. Teng, C. Tello, J. M. Liebmann and R. Ritch (2010). "Corneal hysteresis and visual field asymmetry in open angle glaucoma." *Invest Ophthalmol Vis Sci* **51**(12): 6514-6518.

Ang, G. S., F. Bochmann, J. Townend and A. Azuara-Blanco (2008). "Corneal biomechanical properties in primary open angle glaucoma and normal tension glaucoma." *J Glaucoma* **17**(4): 259-262.

Antonacci, G., T. Beck, A. Bilenca, J. Czarske, K. Elsayad, J. Guck, K. Kim, B. Krug, F. Palombo, R. Prevedel and G. Scarcelli (2020). "Recent progress and current opinions in Brillouin microscopy for life science applications." *Biophys Rev* **12**(3): 615-624.

Aoki, S., Y. Kiuchi, K. Tokumo, Y. Fujino, M. Matsuura, H. Murata, S. Nakakura and R. Asaoka (2020). "Association between optic nerve head morphology in open-angle glaucoma and corneal biomechanical parameters measured with Corvis ST." *Graefes Arch Clin Exp Ophthalmol* **258**(3): 629-637.

Atkinson, G. and A. M. Nevill (1998). "Statistical methods for assessing measurement error (reliability) in variables relevant to sports medicine." *Sports Med* **26**(4): 217-238.

Ayala, M. and E. Chen (2012). "Measuring corneal hysteresis: threshold estimation of the waveform score from the Ocular Response Analyzer." *Graefes Arch Clin Exp Ophthalmol* **250**(12): 1803-1806.

Bak-Nielsen, S., I. B. Pedersen, A. Ivarsen and J. Hjortdal (2014). "Dynamic Scheimpflug-based assessment of keratoconus and the effects of corneal cross-linking." *J Refract Surg* **30**(6): 408-414.

Bak-Nielsen, S., I. B. Pedersen, A. Ivarsen and J. Hjortdal (2014). "Dynamic Scheimpflug-based assessment of keratoconus and the effects of corneal cross-linking." *Journal of Refractive Surgery* **30**(6): 408-414.

Baptista, P. M. L., A. S. Ferreira, N. P. Silva, A. R. M. Figueiredo, I. C. Sampaio, R. V. F. Reis, R. Ambrósio, Jr., P. Menéres, J. N. M. Beirão and M. Menéres (2024). "Scheimpflug-Based Corneal Biomechanical Analysis As A Predictor of Glaucoma in Eyes With High Myopia." *Clin Ophthalmol* **18**: 545-563.

Bartlett, J. W. and C. Frost (2008). "Reliability, repeatability and reproducibility: analysis of measurement errors in continuous variables." *Ultrasound Obstet Gynecol* **31**(4): 466-475.

Basit, A., M. Javed and S. Masood (2008). *Non-circular pupil localization in iris images*. 2008 4th International Conference on Emerging Technologies, IEEE.

- Benassi, P., R. Eramo, A. Giugni, M. Nardone and M. Sampoli (2005). "A spectrometer for high-resolution and high-contrast Brillouin spectroscopy in the ultraviolet." Review of Scientific Instruments **76**(1).
- Bergstra, J. and Y. J. J. o. m. l. r. Bengio (2012). "Random search for hyper-parameter optimization." **13**(2).
- Besner, S., G. Scarcelli, R. Pineda and S. H. Yun (2016). "In vivo brillouin analysis of the aging crystalline lens." Investigative Ophthalmology and Visual Science **57**(13): 5093-5100.
- Bland, J. M. and D. G. Altman (1996). "Measurement error." Bmj **312**(7047): 1654.
- Bland, J. M. and D. J. T. I. Altman (1986). "Statistical methods for assessing agreement between two methods of clinical measurement." **327**(8476): 307-310.
- Bonaccorso, G. (2018). Machine Learning Algorithms: Popular algorithms for data science and machine learning, Packt Publishing Ltd.
- Breiman, L. J. M. I. (2001). "Random forests." **45**: 5-32.
- Brillouin, L. J. A. (1922). "Diffusion de la lumière et des rayons X par un corps transparent homogène." **9**(17): 88-122.
- Bueno-Gimeno, I., E. España-Gregori, A. Gene-Sampedro, A. Lanzagorta-Aresti and D. P. Piñero-Llorens (2014). "Relationship among corneal biomechanics, refractive error, and axial length." Optom Vis Sci **91**(5): 507-513.
- Bukshtab, M., A. Paranjape, M. Friedman and D. Muller (2015). Fast low-noise brillouin spectroscopy measurements of elasticity for corneal crosslinking. Progress in Biomedical Optics and Imaging - Proceedings of SPIE.
- Burgansky-Eliash, Z., G. Wollstein, T. Chu, J. D. Ramsey, C. Glymour, R. J. Noecker, H. Ishikawa, J. S. J. I. o. Schuman and v. science (2005). "Optical coherence tomography machine learning classifiers for glaucoma detection: a preliminary study." **46**(11): 4147-4152.
- Burges, C. J. J. D. m. and k. discovery (1998). "A tutorial on support vector machines for pattern recognition." **2**(2): 121-167.
- Cankaya, A. B., E. Beyazyildiz, D. Ileri and F. Ozturk (2012). "The effect of contact lens usage on corneal biomechanical parameters in myopic patients." Cornea **31**(7): 764-769.
- Castro-Luna, G., D. Jiménez-Rodríguez, A. B. Castaño-Fernández and A. Pérez-Rueda (2021). "Diagnosis of Subclinical Keratoconus Based on Machine Learning Techniques." J Clin Med **10**(18).
- Chen, L., P. Artal, D. Gutierrez and D. R. Williams (2007). "Neural compensation for the best aberration correction." J Vis **7**(10): 9.1-9.
- Chen, M. J., Y. T. Liu, C. C. Tsai, Y. C. Chen, C. K. Chou and S. M. Lee (2009). "Relationship between central corneal thickness, refractive error, corneal curvature, anterior chamber depth and axial length." J Chin Med Assoc **72**(3): 133-137.
- Chi, Z. (1995). MLP classifiers: overtraining and solutions. Proceedings of ICNN'95-International Conference on Neural Networks, IEEE.
- Chun, H., J. I. Moon and Y. J. J. o. t. K. O. S. Jung (2020). "Analysis of Factors Affecting Corneal Deflection Amplitude in Normal Korean Eyes." **61**(5): 538-544.

Cohen, E. J. and J. S. Myers (2010). "Keratoconus and normal-tension glaucoma: a study of the possible association with abnormal biomechanical properties as measured by corneal hysteresis." Cornea **29**(9): 955-970.

Cortes, C. and V. J. M. I. Vapnik (1995). "Support-vector networks." **20**: 273-297.

Costin, B. R., G. P. Fleming, P. A. Weber, A. M. Mahmoud and C. J. Roberts (2014). "Corneal biomechanical properties affect Goldmann applanation tonometry in primary open-angle glaucoma." J Glaucoma **23**(2): 69-74.

Curatolo, A., J. S. Birkenfeld, E. Martinez-Enriquez, J. A. Germann, G. Muralidharan, J. Palací, D. Pascual, A. Eliasy, A. Abass, J. Solarski, K. Karnowski, M. Wojtkowski, A. Elsheikh and S. Marcos (2020). "Multi-meridian corneal imaging of air-puff induced deformation for improved detection of biomechanical abnormalities." Biomed Opt Express **11**(11): 6337-6355.

D'Agostino, R. B., Sr., M. J. Pencina, J. M. Massaro and S. Coady (2013). "Cardiovascular Disease Risk Assessment: Insights from Framingham." Glob Heart **8**(1): 11-23.

Dalziel, C. C. and D. J. Egan (1982). "Crystalline lens thickness changes as observed by pachometry." Am J Optom Physiol Opt **59**(5): 442-447.

Dascalescu, D., C. Corbu, M. Constantin, M. Cristea, C. Ionescu, M. Cioboata and L. Voinea (2015). "Correlations between Corneal Biomechanics and Glaucoma Severity in Patients with Primary Open Angle Glaucoma." Maedica (Bucur) **10**(4): 331-335.

De Moraes, C. V., V. Hill, C. Tello, J. M. Liebmann and R. Ritch (2012). "Lower corneal hysteresis is associated with more rapid glaucomatous visual field progression." J Glaucoma **21**(4): 209-213.

Del Buey, M. A., L. Lavilla, F. J. Ascaso, E. Lanchares, V. Huerva and J. A. Cristóbal (2014). "Assessment of corneal biomechanical properties and intraocular pressure in myopic spanish healthy population." J Ophthalmol **2014**: 905129.

Demšar, J., T. Curk, A. Erjavec, Č. Gorup, T. Hočevar, M. Milutinovič, M. Možina, M. Polajnar, M. Toplak and A. Starič (2013). "Orange: data mining toolbox in Python." the Journal of machine Learning research **14**(1): 2349-2353.

Detry-Morel, M., J. Jamart, F. Hautenuven and S. Pourjavan (2012). "Comparison of the corneal biomechanical properties with the Ocular Response Analyzer® (ORA) in African and Caucasian normal subjects and patients with glaucoma." Acta Ophthalmologica **90**(2): e118-e124.

Dixit, A., J. Yohannan and M. V. J. O. Boland (2021). "Assessing glaucoma progression using machine learning trained on longitudinal visual field and clinical data." **128**(7): 1016-1026.

Dubbelman, M. and G. L. Van der Heijde (2001). "The shape of the aging human lens: curvature, equivalent refractive index and the lens paradox." Vision Res **41**(14): 1867-1877.

Dubbelman, M., G. L. Van der Heijde, H. A. Weeber and G. F. Vrensen (2003). "Changes in the internal structure of the human crystalline lens with age and accommodation." Vision Res **43**(22): 2363-2375.

Ehrlich, J. R., S. Haseltine, M. Shimmyo and N. M. Radcliffe (2010). "Evaluation of agreement between intraocular pressure measurements using Goldmann applanation tonometry and Goldmann correlated intraocular pressure by Reichert's ocular response analyser." Eye (Lond) **24**(10): 1555-1560.

Ehrlich, J. R., N. M. Radcliffe and M. Shimmyo (2012). "Goldmann applanation tonometry compared with corneal-compensated intraocular pressure in the evaluation of primary open-angle Glaucoma." BMC Ophthalmol **12**: 52.

- El Massry, A. A. K., A. A. Said, I. M. Osman, A. S. Bessa, M. A. Elmasry, E. N. Elsayed and N. H. L. Bayoumi (2020). "Corneal biomechanics in different age groups." Int Ophthalmol **40**(4): 967-974.
- Elbendary, A. M. and R. Mohamed Helal (2013). "Discriminating ability of spectral domain optical coherence tomography in different stages of glaucoma." Saudi J Ophthalmol **27**(1): 19-24.
- Eliasy, A., K. J. Chen, R. Vinciguerra, B. T. Lopes, A. Abass, P. Vinciguerra, R. Ambrósio, Jr., C. J. Roberts and A. Elsheikh (2019). "Determination of Corneal Biomechanical Behavior in-vivo for Healthy Eyes Using CorVis ST Tonometry: Stress-Strain Index." Front Bioeng Biotechnol **7**: 105.
- Eltony, A. M., F. Clouser, P. Shao, R. Pineda, 2nd and S. H. Yun (2020). "Brillouin Microscopy Visualizes Centralized Corneal Edema in Fuchs Endothelial Dystrophy." Cornea **39**(2): 168-171.
- Enright, J. T. (1989). "Convergence during human vertical saccades: probable causes and perceptual consequences." J Physiol **410**: 45-65.
- Esteve-Taboada, J. J., A. Domínguez-Vicent, D. Monsálvez-Romín, A. J. Del Águila-Carrasco and R. Montés-Micó (2017). "Non-invasive measurements of the dynamic changes in the ciliary muscle, crystalline lens morphology, and anterior chamber during accommodation with a high-resolution OCT." Graefes Arch Clin Exp Ophthalmol **255**(7): 1385-1394.
- Faul, F., E. Erdfelder, A. Buchner and A. G. Lang (2009). "Statistical power analyses using G*Power 3.1: tests for correlation and regression analyses." Behav Res Methods **41**(4): 1149-1160.
- Faul, F., E. Erdfelder, A. G. Lang and A. Buchner (2007). "G*Power 3: a flexible statistical power analysis program for the social, behavioral, and biomedical sciences." Behav Res Methods **39**(2): 175-191.
- Fawcett, T. J. P. r. I. (2006). "An introduction to ROC analysis." **27**(8): 861-874.
- Fontes, B. M., R. Ambrósio, Jr., D. Jardim, G. C. Velarde and W. Nosé (2010). "Corneal biomechanical metrics and anterior segment parameters in mild keratoconus." Ophthalmology **117**(4): 673-679.
- Fontes, B. M., R. Ambrósio, Jr., G. C. Velarde and W. Nosé "Ocular Response Analyzer Measurements in Keratoconus with Normal Central Corneal Thickness Compared with Matched Normal Control Eyes." Journal of Refractive Surgery **27**(3): 209-215.
- Fujishiro, T., M. Matsuura, Y. Fujino, H. Murata, K. Tokumo, S. Nakakura, Y. Kiuchi and R. Asaoka (2020). "The Relationship Between Corvis ST Tonometry Parameters and Ocular Response Analyzer Corneal Hysteresis." J Glaucoma **29**(6): 479-484.
- Galletti, J. G., T. Pfortner and F. F. Bonthoux (2012). "Improved keratoconus detection by ocular response analyzer testing after consideration of corneal thickness as a confounding factor." Journal of Refractive Surgery **28**(3): 202-208.
- García-Jiménez, A. and A. Consejo (2022). "Suspect glaucoma detection from corneal densitometry supported by machine learning." J Optom **15 Suppl 1**(Suppl 1): S12-s21.
- Gatzioufas, Z. and B. Seitz (2015). "Determination of corneal biomechanical properties in vivo: a review." Materials Science and Technology **31**(2): 188--196.
- Genuer, R., J.-M. Poggi and C. J. P. r. I. Tuleau-Malot (2010). "Variable selection using random forests." **31**(14): 2225-2236.
- Gibson, G. A., F. E. Cruickshank, J. S. Wolffsohn and L. N. Davies (2018). "Optical Coherence Tomography Reveals Sigmoidal Crystalline Lens Changes during Accommodation." Vision (Basel) **2**(3).

- Goldmann, H. and T. Schmidt (1957). "[Applanation tonometry]." *Ophthalmologica* **134**(4): 221-242.
- González-Méijome, J. M., C. Villa-Collar, A. Queirós, J. Jorge and M. A. Parafita (2008). "Pilot study on the influence of corneal biomechanical properties over the short term in response to corneal refractive therapy for myopia." *Cornea* **27**(4): 421-426.
- Goodman, S. N., D. Fanelli and J. P. Ioannidis (2016). "What does research reproducibility mean?" *Sci Transl Med* **8**(341): 341ps312.
- Gouveia, R. M., G. Lepert, S. Gupta, R. R. Mohan, C. Paterson and C. J. Connon (2019). "Assessment of corneal substrate biomechanics and its effect on epithelial stem cell maintenance and differentiation." *Nat Commun* **10**(1): 1496.
- Grise-Dulac, A., A. Saad, O. Abitbol, J. L. Febbraro, E. Azan, C. Moulin-Tyrode and D. Gatinel (2012). "Assessment of corneal biomechanical properties in normal tension glaucoma and comparison with open-angle glaucoma, ocular hypertension, and normal eyes." *J Glaucoma* **21**(7): 486-489.
- Harper, C. L., M. E. Boulton, D. Bennett, B. Marcyniuk, J. H. Jarvis-Evans, A. B. Tullo and A. E. Ridgway (1996). "Diurnal variations in human corneal thickness." *Br J Ophthalmol* **80**(12): 1068-1072.
- Hashemi, H., R. Pakzad, R. Iribarren, M. Khabazkhoob, M. H. Emamian and A. Fotouhi (2018). "Lens power in Iranian schoolchildren: a population-based study." *Br J Ophthalmol* **102**(6): 779-783.
- Hashemi, S., Y. Yang, Z. Mirzamomen, M. J. I. T. o. K. Kangavari and D. Engineering (2008). "Adapted one-versus-all decision trees for data stream classification." **21**(5): 624-637.
- Hastie, T., R. Tibshirani, J. H. Friedman and J. H. Friedman (2009). *The elements of statistical learning: data mining, inference, and prediction*, Springer.
- Hearst, M. A., S. T. Dumais, E. Osuna, J. Platt, B. J. I. I. S. Scholkopf and t. applications (1998). "Support vector machines." **13**(4): 18-28.
- Helmy, H., M. Leila and A. A. Zaki (2016). "Corneal biomechanics in asymmetrical normal-tension glaucoma." *Clin Ophthalmol* **10**: 503-510.
- Herber, R., L. E. Pillunat and F. Raiskup (2021). "Development of a classification system based on corneal biomechanical properties using artificial intelligence predicting keratoconus severity." *Eye Vis (Lond)* **8**(1): 21.
- Herber, R., R. Vinciguerra, B. Lopes, F. Raiskup, L. E. Pillunat, P. Vinciguerra and R. Ambrósio, Jr. (2020). "Repeatability and reproducibility of corneal deformation response parameters of dynamic ultra-high-speed Scheimpflug imaging in keratoconus." *J Cataract Refract Surg* **46**(1): 86-94.
- Hirasawa, K., M. Matsuura, H. Murata, S. Nakakura, Y. Nakao, Y. Kiuchi and R. Asaoka (2017). "Association between Corneal Biomechanical Properties with Ocular Response Analyzer and Also CorvisST Tonometry, and Glaucomatous Visual Field Severity." *Transl Vis Sci Technol* **6**(3): 18.
- Hirneiss, C., A. S. Neubauer, A. Yu, A. Kampik and M. Kernt (2011). "Corneal biomechanics measured with the ocular response analyser in patients with unilateral open-angle glaucoma." *Acta Ophthalmol* **89**(2): e189-192.
- Hocaoğlu, M., C. Kara, E. M. Şen and F. Öztürk (2020). "Relationships between corneal biomechanics and the structural and functional parameters of glaucoma damage." *Arq Bras Oftalmol* **83**(2): 132-140.
- Hon, Y. and A. K. Lam (2013). "Corneal deformation measurement using Scheimpflug noncontact tonometry." *Optom Vis Sci* **90**(1): e1-8.

Hong, K., I. Y. H. Wong, K. Singh and R. T. Chang (2019). "Corneal Biomechanics Using a Scheimpflug-Based Noncontact Device in Normal-Tension Glaucoma and Healthy Controls." Asia Pac J Ophthalmol (Phila) **8**(1): 22-29.

Hong, Y., N. Shoji, T. Morita, K. Hirasawa, K. Matsumura, M. Kasahara and K. Shimizu (2016). "Comparison of corneal biomechanical properties in normal tension glaucoma patients with different visual field progression speed." Int J Ophthalmol **9**(7): 973-978.

Hooker, G. and L. J. a. p. a. Mentch (2019). "Please stop permuting features: An explanation and alternatives." **2**.

Huang, Y., C. Huang, L. Li, K. Qiu, W. Gong, Z. Wang, X. Wu, Y. Du, B. Chen, D. S. Lam, M. Zhang and N. Congdon (2011). "Corneal biomechanics, refractive error, and axial length in Chinese primary school children." Invest Ophthalmol Vis Sci **52**(7): 4923-4928.

Hurmeric, V., A. Şahin, G. Ozge and A. Bayer "The Relationship Between Corneal Biomechanical Properties and Confocal Microscopy Findings in Normal and Keratoconic Eyes." Cornea.

Hussnain, S. A., J. B. Alsberge, J. R. Ehrlich, M. Shimmyo and N. M. Radcliffe (2015). "Change in corneal hysteresis over time in normal, glaucomatous and diabetic eyes." Acta Ophthalmol **93**(8): e627-630.

İnceoğlu, N., S. Emre and M. O. Ulusoy (2018). "Investigation of corneal biomechanics at moderate to high refractive errors." Int Ophthalmol **38**(3): 1061-1067.

Itoh, S. (1998). "Very rapid nonscanning Brillouin spectroscopy using fixed etalons and multichannel detectors." Japanese Journal of Applied Physics Part 1-Regular Papers Short Notes & Review Papers **37**(5b): 3134-3135.

Jayaram, H. (2020). "Intraocular pressure reduction in glaucoma: Does every mmHg count?" Taiwan J Ophthalmol **10**(4): 255-258.

Jia, X., J. Yu, S. H. Liao and X. C. Duan (2016). "Biomechanics of the sclera and effects on intraocular pressure." Int J Ophthalmol **9**(12): 1824-1831.

Jin, K. and J. Ye (2022). "Artificial intelligence and deep learning in ophthalmology: Current status and future perspectives." Adv Ophthalmol Pract Res **2**(3): 100078.

Johnson, R. D., T. N. Myhanh, N. Lee and D. R. Hamilton "Corneal Biomechanical Properties in Normal, Forme Fruste Keratoconus, and Manifest Keratoconus After Statistical Correction for Potentially Confounding Factors." Cornea.

Jung, Y., H. L. Park, S. Oh and C. K. Park (2020). "Corneal biomechanical responses detected using corvis st in primary open angle glaucoma and normal tension glaucoma." Medicine (Baltimore) **99**(7): e19126.

Kaili, Y., X. Liyan, F. Qi, Z. Dongqing and R. Shengwei "Repeatability and comparison of new Corvis ST parameters in normal and keratoconus eyes." Scientific Reports.

Kamiya, K., K. Shimizu and F. Ohmoto (2009). "Effect of aging on corneal biomechanical parameters using the ocular response analyzer." J Refract Surg **25**(10): Da888-893.

Kanellopoulos, A. J. (2012). "Long-term safety and efficacy follow-up of prophylactic higher fluence collagen cross-linking in high myopic laser-assisted in situ keratomileusis." Clin Ophthalmol **6**: 1125-1130.

Kass, M. A., D. K. Heuer, E. J. Higginbotham, C. A. Johnson, J. L. Keltner, J. P. Miller, R. K. Parrish, 2nd, M. R. Wilson and M. O. Gordon (2002). "The Ocular Hypertension Treatment Study: a

randomized trial determines that topical ocular hypotensive medication delays or prevents the onset of primary open-angle glaucoma." Arch Ophthalmol **120**(6): 701-713; discussion 829-730.

Kaushik, S., S. S. Pandav, A. Banger, K. Aggarwal and A. Gupta (2012). "Relationship between corneal biomechanical properties, central corneal thickness, and intraocular pressure across the spectrum of glaucoma." Am J Ophthalmol **153**(5): 840-849.e842.

Kenia, V. P., R. V. Kenia, P. Bendre and O. H. Pirdankar (2024). "Corneal stress-strain index in myopic Indian population." Oman J Ophthalmol **17**(1): 47-52.

Kenia, V. P., R. V. Kenia and O. H. Pirdankar (2020). "Age-related variation in corneal biomechanical parameters in healthy Indians." Indian J Ophthalmol **68**(12): 2921-2929.

Kenia, V. P., R. V. Kenia and O. H. Pirdankar (2020). "Association between corneal biomechanical parameters and myopic refractive errors in young Indian individuals." Taiwan J Ophthalmol **10**(1): 45-53.

Khawaja, A. P., M. P. Y. Chan, D. C. Broadway, D. F. Garway-Heath, R. Luben, J. L. Y. Yip, S. Hayat, K. T. Khaw and P. J. Foster (2013). "Corneal biomechanical properties and glaucoma-related quantitative traits in the EPIC-Norfolk eye study." Investigative Ophthalmology and Visual Science **55**(1): 117-124.

Kirwan, C., O. M. Donal and M. O. Keefe "Corneal Hysteresis and Corneal Resistance Factor in Keratoectasia: Findings Using the Reichert Ocular Response Analyzer." Ophthalmologica.

Kling, S. and F. Hafezi (2017). "Biomechanical stiffening: Slow low-irradiance corneal crosslinking versus the standard Dresden protocol." J Cataract Refract Surg **43**(7): 975-979.

Kobashi, H., K. Kamiya, H. Ishikawa, T. Goseki and K. Shimizu (2012). "Daytime variations in pupil size under photopic conditions." Optometry and Vision Science **89**(2): 197-202.

Koç, M., E. Aydemir, K. Tekin, M. Inanc, P. Kosekahya and K. Hasan "Biomechanical Analysis of Subclinical Keratoconus With Normal Topographic, Topometric, and Tomographic Findings." Journal of refractive surgery.

Komninou, M. A., T. G. Seiler and V. Enzmann (2024). "Corneal biomechanics and diagnostics: a review." Int Ophthalmol **44**(1): 132.

Koo, T. K. and M. Y. Li (2016). "A Guideline of Selecting and Reporting Intraclass Correlation Coefficients for Reliability Research." J Chiropr Med **15**(2): 155-163.

Koretz, J. F., C. A. Cook and P. L. Kaufman (2002). "Aging of the human lens: changes in lens shape upon accommodation and with accommodative loss." J Opt Soc Am A Opt Image Sci Vis **19**(1): 144-151.

Koretz, J. F. and G. H. Handelman (1982). "Model of the accommodative mechanism in the human eye." Vision Res **22**(8): 917-927.

Kotecha, A. (2007). "What biomechanical properties of the cornea are relevant for the clinician?" Surv Ophthalmol **52 Suppl 2**: S109-114.

Krishnan, A., A. Dutta, A. Srivastava, N. Konda and R. K. Prakasam (2025). "Artificial Intelligence in Optometry: Current and Future Perspectives." Clin Optom (Auckl) **17**: 83-114.

Ku, J. Y., H. V. Danesh-Meyer, J. P. Craig, G. D. Gamble and C. N. McGhee (2006). "Comparison of intraocular pressure measured by Pascal dynamic contour tonometry and Goldmann applanation tonometry." Eye (Lond) **20**(2): 191-198.

- Labib, K. M., H. Ghumman, S. Jain and J. S. Jarstad (2024). "Applications of Artificial Intelligence in Ophthalmology: Glaucoma, Cornea, and Oculoplastics." Cureus **16**(11): e73522.
- Lam, A. K., D. Chen and J. Tse (2010). "The usefulness of waveform score from the ocular response analyzer." Optom Vis Sci **87**(3): 195-199.
- Lee, K. M., T. W. Kim, E. J. Lee, M. J. A. Girard, J. M. Mari and R. N. Weinreb (2019). "Association of Corneal Hysteresis With Lamina Cribrosa Curvature in Primary Open Angle Glaucoma." Invest Ophthalmol Vis Sci **60**(13): 4171-4177.
- Lee, R., R. T. Chang, I. Y. Wong, J. S. Lai, J. W. Lee and K. Singh (2016). "Novel Parameter of Corneal Biomechanics That Differentiate Normals From Glaucoma." J Glaucoma **25**(6): e603-609.
- Leite, D., M. Campelos, A. Fernandes, P. Batista, J. Beirão, P. Menéres and A. J. P. C. S. Cunha (2022). "Machine Learning automatic assessment for glaucoma and myopia based on Corvis ST data." **196**: 454-460.
- Leng, L., Y. Yuan, Q. Chen, M. Shen, Q. Ma, B. Lin, D. Zhu, J. Qu and F. Lu (2014). "Biometry of anterior segment of human eye on both horizontal and vertical meridians during accommodation imaged with extended scan depth optical coherence tomography." PLoS One **9**(8): e104775.
- Li, B. B., Y. Cai, Y. Z. Pan, M. Li, R. H. Qiao, Y. Fang and T. Tian (2017). "Corneal Biomechanical Parameters and Asymmetric Visual Field Damage in Patients with Untreated Normal Tension Glaucoma." Chin Med J (Engl) **130**(3): 334-339.
- Li, Z., L. Wang, X. Wu, J. Jiang, W. Qiang, H. Xie, H. Zhou, S. Wu, Y. Shao and W. Chen (2023). "Artificial intelligence in ophthalmology: The path to the real-world clinic." Cell Rep Med **4**(7): 101095.
- Lindsay, S. M., M. W. Anderson and J. R. Sandercock (1981). "Construction and Alignment of a High-Performance Multipass Vernier Tandem Fabry-Perot-Interferometer." Review of Scientific Instruments **52**(10): 1478-1486.
- Liu, G., H. Rong, R. Pei, B. Du, N. Jin, D. Wang, C. Jin and R. Wei (2020). "Age distribution and associated factors of cornea biomechanical parameter stress-strain index in Chinese healthy population." BMC Ophthalmol **20**(1): 436.
- Liu, J. and C. J. Roberts (2005). "Influence of corneal biomechanical properties on intraocular pressure measurement: quantitative analysis." J Cataract Refract Surg **31**(1): 146-155.
- Liu, Q., C. Pang, C. Liu, W. Cheng, S. Ming, W. Du and X. Feng (2022). "Correlations among Corneal Biomechanical Parameters, Stiffness, and Thickness Measured Using Corvis ST and Pentacam in Patients with Ocular Hypertension." J Ophthalmol **2022**: 7387581.
- Lovie, P. J. E. o. s. i. b. s. (2005). "Coefficient of variation."
- Lu, L. L., X. J. Hu, Y. Yang, S. Xu, S. Y. Yang, C. Y. Zhang and Q. Y. Zhao (2022). "Correlation of myopia onset and progression with corneal biomechanical parameters in children." World J Clin Cases **10**(5): 1548-1556.
- Luce, D. (2006). "Methodology for Cornea Compensated IOP and Corneal Resistance Factor for the Reichert Ocular Response Analyzer." Investigative Ophthalmology & Visual Science **47**(13): 2266-2266.
- Luce, D. A. (2005). "Determining in vivo biomechanical properties of the cornea with an ocular response analyzer." J Cataract Refract Surg **31**(1): 156-162.

- Mandalos, A., E. Anastasopoulos, L. Makris, N. Dervenis, V. Kilintzis and F. Topouzis (2013). "Inter-examiner reproducibility of Ocular Response Analyzer using the waveform score quality index in healthy subjects." J Glaucoma **22**(2): 152-155.
- Mangouritsas, G., G. Morphis, S. Mourtzoukos and E. Feretis (2009). "Association between corneal hysteresis and central corneal thickness in glaucomatous and non-glaucomatous eyes." Acta Ophthalmol **87**(8): 901-905.
- Marinescu, M., D. Dascalescu, M. Constantin, V. Coviltir, M. Burcel, D. Darabus, R. Ciuluvica, D. Stanila, V. Potop and C. Alexandrescu (2022). "Corneal Biomechanics - an Emerging Ocular Property with a Significant Impact." Maedica (Bucur) **17**(4): 925-930.
- Markewitz, H. H. (1960). "The so-called Imbert-Fick law." Arch Ophthalmol **64**: 159.
- Matsuura, M., K. Hirasawa, H. Murata, M. Yanagisawa, Y. Nakao, S. Nakakura, Y. Kiuchi and R. Asaoka (2016). "The Relationship between Corvis ST Tonometry and Ocular Response Analyzer Measurements in Eyes with Glaucoma." PLoS One **11**(8): e0161742.
- McBrien, N. A., T. L. Young, C. P. Pang, C. Hammond, P. Baird, S.-M. Saw, I. G. Morgan, D. O. Mutti, K. A. Rose, J. Wallman, A. Gentle, C. F. Wildsoet, J. Gwiazda, K. L. Schmid, E. I. Smith, D. Troilo, J. Summers-Rada, T. T. Norton, F. Schaeffel, P. Megaw, R. W. Beuerman and S. A. McFadden (2009). "Myopia: Recent Advances in Molecular Studies; Prevalence, Progression and Risk Factors; Emmetropization; Therapies; Optical Links; Peripheral Refraction; Sclera and Ocular Growth; Signalling Cascades; and Animal Models." **86**(1): 45-66.
- McGraw, K. O. and S. P. J. P. m. Wong (1996). "Forming inferences about some intraclass correlation coefficients." **1**(1): 30.
- Medeiros, F. A., D. Meira-Freitas, R. Lisboa, T.-M. Kuang, L. M. Zangwill and R. N. Weinreb (2013). "Corneal hysteresis as a risk factor for glaucoma progression: a prospective longitudinal study." Journal of Ophthalmology **120**(8): 1533-1540.
- Medeiros, F. A., L. M. Zangwill, C. Bowd, R. M. Vessani, R. Susanna, Jr. and R. N. Weinreb (2005). "Evaluation of retinal nerve fiber layer, optic nerve head, and macular thickness measurements for glaucoma detection using optical coherence tomography." Am J Ophthalmol **139**(1): 44-55.
- Meek, K. M., S. J. Tuft, Y. Huang, P. S. Gill, S. Hayes, R. H. Newton and A. J. Bron (2005). "Changes in collagen orientation and distribution in keratoconus corneas." Invest Ophthalmol Vis Sci **46**(6): 1948-1956.
- Mendes, M., A. J. P. J. o. I. Pala and Technology (2003). "Type I error rate and power of three normality tests." **2**(2): 135-139.
- Mercer, R. N., G. O. I. V. Waring, C. J. Roberts, V. Jhanji, Y. Wang, J. S. Filho, R. A. Hemings, Jr. and K. M. Rocha "Comparison of Corneal Deformation Parameters in Keratoconic and Normal Eyes Using a Non-contact Tonometer With a Dynamic Ultra-High-Speed Sc heimpflug Camera." Journal of Refractive Surgery **33**(9): 625-631.
- Michelessi, M., E. Lucenteforte, F. Oddone, M. Brazzelli, M. Parravano, S. Franchi, S. M. Ng and G. Virgili (2015). "Optic nerve head and fibre layer imaging for diagnosing glaucoma." Cochrane Database Syst Rev **2015**(11): Cd008803.
- Miki, A., Y. Yasukura, R. N. Weinreb, N. Maeda, T. Yamada, S. Koh, T. Asai, Y. Ikuno and K. Nishida (2020). "Dynamic Scheimpflug Ocular Biomechanical Parameters in Untreated Primary Open Angle Glaucoma Eyes." Invest Ophthalmol Vis Sci **61**(4): 19.
- Moguerza, J. M. and A. Muñoz (2006). "Support vector machines with applications."

- Mohammadzadeh, V., S. Wu, S. Besharati, T. Davis, A. Vepa, E. Morales, K. Edalati, M. Rafiee, A. Martinyan, D. Zhang, F. Scalzo, J. Caprioli and K. Nouri-Mahdavi (2024). "Prediction of Visual Field Progression with Baseline and Longitudinal Structural Measurements Using Deep Learning." Am J Ophthalmol **262**: 141-152.
- Morita, T., N. Shoji, K. Kamiya, F. Fujimura and K. Shimizu (2012). "Corneal biomechanical properties in normal-tension glaucoma." Acta Ophthalmol **90**(1): e48-53.
- Murphy, M. L., O. Pokrovskaya, M. Galligan and C. O'Brien (2017). "Corneal hysteresis in patients with glaucoma-like optic discs, ocular hypertension and glaucoma." BMC Ophthalmol **17**(1): 1.
- Nangia, V., J. B. Jonas, A. Sinha, A. Matin and M. Kulkarni (2010). "Central corneal thickness and its association with ocular and general parameters in Indians: the Central India Eye and Medical Study." Ophthalmology **117**(4): 705-710.
- Narayanaswamy, A., D. H. Su, M. Baskaran, A. C. Tan, M. E. Nongpiur, H. M. Htoon, T. Y. Wong and T. Aung (2011). "Comparison of ocular response analyzer parameters in chinese subjects with primary angle-closure and primary open-angle glaucoma." Arch Ophthalmol **129**(4): 429-434.
- Narayanaswamy, A., D. H. Su, M. Baskaran, A. C. S. Tan, M. E. Nongpiur, H. M. Htoon, T. Y. Wong and T. Aung (2011). "Comparison of ocular response analyzer parameters in Chinese subjects with primary angle-closure and primary open-angle glaucoma." Archives of Ophthalmology **129**(4): 429-434.
- Navia-Vazquez, A., D. Gutierrez-Gonzalez, E. Parrado-Hernandez and J. J. Navarro-Abellan (2006). "Distributed support vector machines." IEEE Trans Neural Netw **17**(4): 1091-1097.
- Nessim, M., S. P. Mollan, J. S. Wolffsohn, M. Laiquzzaman, S. Sivakumar, S. Hartley and S. Shah (2013). "The relationship between measurement method and corneal structure on apparent intraocular pressure in glaucoma and ocular hypertension." Cont Lens Anterior Eye **36**(2): 57-61.
- Nishijima, E., D. Hosaka, S. Ogawa, Y. Itoh, T. Noro, S. Okude, K. Sano, K. Yoshikawa, M. Tatemichi and T. Nakano (2024). "Comparison of Glaucoma Detection Performance of Binocular Perimetry Screening Program Using imo Perimetry With Frequency Doubling Technology." Transl Vis Sci Technol **13**(8): 9.
- Nohara, Y., K. Matsumoto, H. Soejima and N. Nakashima (2022). "Explanation of machine learning models using shapley additive explanation and application for real data in hospital." Comput Methods Programs Biomed **214**: 106584.
- Ortiz, D., D. Piñero, M. H. Shabayek, F. Arnalich-Montiel and J. L. Alió (2007). "Corneal biomechanical properties in normal, post-laser in situ keratomileusis, and keratoconic eyes." Journal of Cataract and Refractive Surgery **33**(8): 1371-1375.
- Ortiz, S., P. Pérez-Merino, E. Gamba, A. de Castro and S. Marcos (2012). "In vivo human crystalline lens topography." Biomed Opt Express **3**(10): 2471-2488.
- Osl, M., C. Baumgartner, B. Tilg and S. Dreiseitl (2008). On the combination of logistic regression and local probability estimates. 2008 Third International Conference on Broadband Communications, Information Technology & Biomedical Applications, IEEE.
- Pal, M. and P. M. Mather (2002). A comparison of decision tree and backpropagation neural network classifiers for land use classification. IEEE International Geoscience and Remote Sensing Symposium, IEEE.
- Park, J. H., R. M. Jun and K. R. Choi (2015). "Significance of corneal biomechanical properties in patients with progressive normal-tension glaucoma." Br J Ophthalmol **99**(6): 746-751.

- Park, K.-D., B. Min, P. Kim, N. Park, J.-H. Lee and J.-S. Chang (2002). "Dynamics of cascaded Brillouin–Rayleigh scattering in a distributed fiber Raman amplifier." Optics letters **27**(3): 155-157.
- Park, K., J. Shin and J. Lee (2018). "Relationship between corneal biomechanical properties and structural biomarkers in patients with normal-tension glaucoma: a retrospective study." BMC Ophthalmol **18**(1): 7.
- Peña-garcía, P., C. Peris-Martínez, A. Abbouda and J. Ruiz-Moreno "Detection of subclinical keratoconus through non-contact tonometry and the use of discriminant biomechanical functions." Journal of Biomechanics.
- Peyman, A., M. Ghoreishi, S. S. Hashemi-Estabragh, M. Mirmohammadkhani, M. Mohammadinia and M. Pourazizi (2021). "Corneal biomechanical properties after soft contact lens wear measured on a dynamic Scheimpflug analyzer: A before and after study." J Fr Ophthalmol **44**(3): 391-396.
- Pillunat, K. R., C. Hermann, E. Spoerl and L. E. Pillunat (2016). "Analyzing biomechanical parameters of the cornea with glaucoma severity in open-angle glaucoma." Graefes Arch Clin Exp Ophthalmol **254**(7): 1345-1351.
- Piñero, D. P., J. L. Alio, R. I. Barraquer, R. Michael and R. Jiménez "Corneal Biomechanics, Refraction, and Corneal Aberrometry in Keratoconus: An Integrated Study." Investigative Ophthalmology & Visual Science **51**(4): 1948.
- Plakitsi, A., C. O'Donnell, M. A. Miranda, W. N. Charman and H. Radhakrishnan (2011). "Corneal biomechanical properties measured with the Ocular Response Analyser in a myopic population." Ophthalmic Physiol Opt **31**(4): 404-412.
- Prata, T. S., V. C. Lima, L. M. Guedes, L. G. Biteli, S. H. Teixeira, C. G. de Moraes, R. Ritch and A. Paranhos, Jr. (2012). "Association between corneal biomechanical properties and optic nerve head morphology in newly diagnosed glaucoma patients." Clin Exp Ophthalmol **40**(7): 682-688.
- Rahmati, S. M., R. Razaghi and A. Karimi (2021). "Biomechanics of the keratoconic cornea: Theory, segmentation, pressure distribution, and coupled FE-optimization algorithm." J Mech Behav Biomed Mater **113**: 104155.
- Raju, G. B., C. Manasa, N. D. Bhavani, J. Amulya and D. Shirisha (2023). Comparative Analysis of Different Machine Learning Algorithms on Different Datasets. 2023 7th International Conference on Intelligent Computing and Control Systems (ICICCS), IEEE.
- Ramesh, P. V., T. Subramaniam, P. Ray, A. K. Devadas, S. V. Ramesh, S. M. Ansar, M. K. Ramesh, R. Rajasekaran and S. J. I. J. o. O. Parthasarathi (2022). "Utilizing human intelligence in artificial intelligence for detecting glaucomatous fundus images using human-in-the-loop machine learning." **70**(4): 1131-1138.
- Randall, J. and J. M. Vaughan (1982). "The measurement and interpretation of Brillouin scattering in the lens of the eye." Proc R Soc Lond B Biol Sci **214**(1197): 449-470.
- Randleman, J. B., J. P. Su and G. Scarcelli (2017). "Biomechanical Changes After LASIK Flap Creation Combined With Rapid Cross-Linking Measured With Brillouin Microscopy." Journal of Refractive Surgery **33**(6): 408-+.
- Raschka, S. and V. Mirjalili (2019). Python machine learning: Machine learning and deep learning with Python, scikit-learn, and TensorFlow 2, Packt publishing ltd.
- Razali, N. M., Y. B. J. J. o. s. m. Wah and analytics (2011). "Power comparisons of shapiro-wilk, kolmogorov-smirnov, lilliefors and anderson-darling tests." **2**(1): 21-33.

- Rei, S., K. Sperlich, M. Hovakimyan, P. Martius, R. F. Guthoff, H. Stolz and O. Stachs (2012). "Ex vivo measurement of postmortem tissue changes in the crystalline lens by Brillouin spectroscopy and confocal reflectance microscopy." IEEE Transactions on Biomedical Engineering **59**(8): 2348-2354.
- Reiss, S., G. Burau, O. Stachs, R. Guthoff and H. Stolz (2011). "Spatially resolved Brillouin spectroscopy to determine the rheological properties of the eye lens." Biomedical Optics Express **2**(8): 2144-2159.
- Ren, S., K. Yang, L. Xu, Q. Fan, Y. Gu, C. Pang and D. Zhao (2023). "Machine learning analysis with the comprehensive index of corneal tomographic and biomechanical parameters in detecting pediatric subclinical keratoconus." Front Bioeng Biotechnol **11**: 1273500.
- Roberts, C. J., A. M. Mahmoud, J. P. Bons, A. Hossain, A. Elsheikh, R. Vinciguerra, P. Vinciguerra and R. Ambrósio, Jr. (2017). "Introduction of Two Novel Stiffness Parameters and Interpretation of Air Puff-Induced Biomechanical Deformation Parameters With a Dynamic Scheimpflug Analyzer." J Refract Surg **33**(4): 266-273.
- Rodríguez-Robles, F., R. Verdú-Monedero, R. Berenguer-Vidal, J. Morales-Sánchez and I. Sellés-Navarro (2023). "Analysis of the Asymmetry between Both Eyes in Early Diagnosis of Glaucoma Combining Features Extracted from Retinal Images and OCTs into Classification Models." Sensors (Basel) **23**(10).
- Roghiyeh, E., E. Jafarzadehpur, H. Hashemi, K. Amanzadeh, S. Fereshteh, A. Yekta and M. Khabazkhoob "Keratoconus diagnosis using Corvis ST measured biomechanical parameter s." Journal of Current Ophthalmology.
- Rosa, N., M. Lanza, M. De Bernardo, G. Signoriello and P. Chiodini (2015). "Relationship Between Corneal Hysteresis and Corneal Resistance Factor with Other Ocular Parameters." Semin Ophthalmol **30**(5-6): 335-339.
- Rosen, A. M., D. B. Denham, V. Fernandez, D. Borja, A. Ho, F. Manns, J.-M. Parel and R. C. J. V. r. Augusteyn (2006). "In vitro dimensions and curvatures of human lenses." **46**(6-7): 1002-1009.
- Ruan, X., Z. Liu, L. Luo and Y. Liu (2020). "The Structure of the Lens and Its Associations with the Visual Quality." BMJ Open Ophthalmol **5**(1): e000459.
- Sabesan, R. and G. Yoon (2010). "Neural compensation for long-term asymmetric optical blur to improve visual performance in keratoconic eyes." Invest Ophthalmol Vis Sci **51**(7): 3835-3839.
- Safavian, S. R., D. J. I. t. o. s. Landgrebe, man, and cybernetics (1991). "A survey of decision tree classifier methodology." **21**(3): 660-674.
- Salomão, M. Q., A. L. Hofling-Lima, F. Faria-Correia, B. T. Lopes, S. Rodrigues-Barros, C. J. Roberts and R. Ambrósio (2018). "Dynamic corneal deformation response and integrated corneal tomography." Indian J Ophthalmol **66**(3): 373-382.
- Salouti, R., A. A. Alishiri, R. Gharebaghi, M. Naderi, K. Jadidi, A. Shojaei-Baghini, M. Talebnejad, Z. Nasiri, S. Hosseini and F. Heidary (2018). "Comparison among Ocular Response Analyzer, Corvis ST and Goldmann applanation tonometry in healthy children." Int J Ophthalmol **11**(8): 1330-1336.
- Salvetat, M. L., M. Zeppieri, C. Tosoni, M. Felletti, L. Grasso and P. Brusini (2015). "Corneal Deformation Parameters Provided by the Corvis-ST Pachy-Tonometer in Healthy Subjects and Glaucoma Patients." J Glaucoma **24**(8): 568-574.
- Santhiago, M. R. and J. B. Randleman (2021). "The biology of corneal cross-linking derived from ultraviolet light and riboflavin." Exp Eye Res **202**: 108355.

- Santodomingo-Rubido, J., G. Carracedo, A. Suzaki, C. Villa-Collar, S. J. Vincent and J. S. Wolffsohn (2022). "Keratoconus: An updated review." Cont Lens Anterior Eye **45**(3): 101559.
- Santos, L. F., M. Á. Sánchez-Tena, C. Alvarez-Peregrina, J.-M. Sánchez-González and C. J. T. Martínez-Perez (2025). "The Role of Artificial Intelligence in Optometric Diagnostics and Research: Deep Learning and Time-Series Forecasting Applications." **13**(2): 77.
- Saraswat, D., P. Bhattacharya, A. Verma, V. K. Prasad, S. Tanwar, G. Sharma, P. N. Bokoro and R. J. I. A. Sharma (2022). "Explainable AI for healthcare 5.0: opportunities and challenges." **10**: 84486-84517.
- Scarcelli, G., S. Besner, R. Pineda, P. Kalout and S. H. Yun (2015). "In vivo biomechanical mapping of normal and keratoconus corneas." JAMA Ophthalmol **133**(4): 480-482.
- Scarcelli, G., S. Besner, R. Pineda and S. H. Yun (2014). "Biomechanical characterization of keratoconus corneas ex vivo with Brillouin microscopy." Invest Ophthalmol Vis Sci **55**(7): 4490-4495.
- Scarcelli, G., P. Kim and S. H. Yun (2011). "In Vivo Measurement of Age-Related Stiffening in the Crystalline Lens by Brillouin Optical Microscopy." Biophysical Journal **101**(6): 1539-1545.
- Scarcelli, G., S. Kling, E. Quijano, R. Pineda, S. Marcos and S. H. Yun (2013). "Brillouin microscopy of collagen crosslinking: noncontact depth-dependent analysis of corneal elastic modulus." Invest Ophthalmol Vis Sci **54**(2): 1418-1425.
- Scarcelli, G., R. Pineda and S. H. Yun (2012). "Brillouin optical microscopy for corneal biomechanics." Invest Ophthalmol Vis Sci **53**(1): 185-190.
- Scarcelli, G. and S. H. Yun (2007). "Confocal Brillouin microscopy for three-dimensional mechanical imaging." Nat Photonics **2**: 39-43.
- Scarcelli, G. and S. H. Yun (2012). "In vivo Brillouin optical microscopy of the human eye." Opt Express **20**(8): 9197-9202.
- Schiano-Lomoriello, D., K. J. Hoffer, I. Abicca and G. Savini (2021). "Repeatability of automated measurements by a new anterior segment optical coherence tomographer and biometer and agreement with standard devices." Sci Rep **11**(1): 983.
- Scornet, E., G. Biau and J.-P. Vert (2015). "Consistency of random forests."
- Sedaghat, M. R., H. Momeni-Moghaddam, R. Ambrósio, Jr., H. R. Heidari, N. Maddah, Z. Danesh and F. Sabzi (2018). "Diagnostic Ability of Corneal Shape and Biomechanical Parameters for Detecting Frank Keratoconus." Cornea **37**(8): 1025-1034.
- Sedaghat, M. R., H. Momeni-Moghaddam, A. Azimi, Z. Fakhimi, M. Ziaei, Z. Danesh, C. J. Roberts, N. Monfared and A. Jamali (2020). "Corneal Biomechanical Properties in Varying Severities of Myopia." Front Bioeng Biotechnol **8**: 595330.
- Seiler, T. G., P. Shao, A. Eltony, T. Seiler and S. H. Yun (2019). "Brillouin Spectroscopy of Normal and Keratoconus Corneas." Am J Ophthalmol **202**: 118-125.
- Seiler, T. G., P. Shao, B. E. Frueh, S. H. Yun and T. Seiler (2018). "The influence of hydration on different mechanical moduli of the cornea." Graefes Arch Clin Exp Ophthalmol **256**(9): 1653-1660.
- Sethi, I. K. J. P. R. (1997). "Structure-driven induction of decision tree classifiers through neural learning." **30**(11): 1893-1904.

- Shah, N. N., C. Bowd, F. A. Medeiros, R. N. Weinreb, P. A. Sample, E. M. Hoffmann and L. M. Zangwill (2006). "Combining structural and functional testing for detection of glaucoma." Ophthalmology **113**(9): 1593-1602.
- Shah, S., M. Laiquzzaman, R. Bhojwani, S. Mantry and I. Cunliffe "Assessment of the Biomechanical Properties of the Cornea with the Ocular Response Analyzer in Normal and Keratoconic Eyes." Investigative Ophthalmology & Visual Science **48**(7): 3026.
- Shah, S., M. Laiquzzaman, R. Bhojwani, S. Mantry and I. Cunliffe (2007). "Assessment of the biomechanical properties of the cornea with the ocular response analyzer in normal and keratoconic eyes." Invest Ophthalmol Vis Sci **48**(7): 3026-3031.
- Shah, S., M. Laiquzzaman, S. Mantry and I. Cunliffe (2008). "Ocular response analyser to assess hysteresis and corneal resistance factor in low tension, open angle glaucoma and ocular hypertension." Clin Exp Ophthalmol **36**(6): 508-513.
- Shah, S., M. Laiquzzaman, I. Yeung, X. Pan and C. Roberts (2009). "The use of the Ocular Response Analyser to determine corneal hysteresis in eyes before and after excimer laser refractive surgery." Contact Lens and Anterior Eye **32**(3): 123-128.
- Shao, P., S. Besner, J. Zhang, G. Scarcelli and S. H. Yun (2016). "Etalon filters for Brillouin microscopy of highly scattering tissues." Opt Express **24**(19): 22232-22238.
- Shao, P., A. M. Eltony, T. G. Seiler, B. Tavakol, R. Pineda, T. Koller, T. Seiler and S. H. Yun (2019). "Spatially-resolved Brillouin spectroscopy reveals biomechanical abnormalities in mild to advanced keratoconus in vivo." Sci Rep **9**(1): 7467.
- Shao, P., T. G. Seiler, A. M. Eltony, A. Ramier, S. J. J. Kwok, G. Scarcelli, R. Pineda and S. H. A. Yun (2018). "Effects of corneal hydration on Brillouin microscopy in vivo." Investigative Ophthalmology and Visual Science **59**(7): 3020-3027.
- Sharifipour, F., M. Panahi-Bazaz, R. Bidar, A. Idani and B. Cheraghian (2016). "Age-related variations in corneal biomechanical properties." J Curr Ophthalmol **28**(3): 117-122.
- Shengwei, R., X. Liyan, F. Qi, G. Yuwei and Y. Kaili "Accuracy of new Corvis ST parameters for detecting subclinical and clinical keratoconus eyes in a Chinese population." Scientific Reports.
- Shih, Y. F., T. H. Chiang and L. L. Lin (2009). "Lens thickness changes among schoolchildren in Taiwan." Invest Ophthalmol Vis Sci **50**(6): 2637-2644.
- Shin, J., J. W. Lee, E. A. Kim and J. Caprioli (2015). "The effect of corneal biomechanical properties on rebound tonometer in patients with normal-tension glaucoma." Am J Ophthalmol **159**(1): 144-154.
- Silverman, R. H., M. S. Patel, O. Gal, A. Sarup, A. Deobhakta, H. Dababneh, D. Z. Reinstein, E. J. Feleppa and D. J. Coleman (2009). "Effect of corneal hydration on ultrasound velocity and backscatter." Ultrasound Med Biol **35**(5): 839-846.
- Simcoe, M. J., A. P. Khawaja, P. G. Hysi and C. J. Hammond (2020). "Genome-wide association study of corneal biomechanical properties identifies over 200 loci providing insight into the genetic etiology of ocular diseases." Hum Mol Genet **29**(18): 3154-3164.
- Singh, R. K., S. Smith, J. Fingert, M. Gordon, M. Kass, T. Scheetz, A. V. Segrè, J. Wiggs, T. Elze and N. Zebardast (2024). "Machine Learning-Derived Baseline Visual Field Patterns Predict Future Glaucoma Onset in the Ocular Hypertension Treatment Study." Invest Ophthalmol Vis Sci **65**(2): 35.
- Steinberg, J., T. Katz, K. Lücke, A. Frings, V. Druchkiv and S. J. Linke "Screening for Keratoconus With New Dynamic Biomechanical In Vivo Scheimpflug Analyses." Cornea **34**(11): 1404-1412.

Steinskog, D. J., D. B. Tjøstheim and N. G. J. M. W. R. Kvamstø (2007). "A cautionary note on the use of the Kolmogorov–Smirnov test for normality." **135**(3): 1151-1157.

Steinwart, I. and A. Christmann (2008). Support vector machines, Springer Science & Business Media.

Sullivan-Mee, M., S. C. Billingsley, A. D. Patel, K. D. Halverson, B. R. Alldredge and C. Qualls (2008). "Ocular response analyzer in subjects with and without glaucoma." Optometry and Vision Science **85**(6): 463-470.

Suthaharan, S., S. J. M. I. m. Suthaharan and a. f. b. d. c. t. w. e. f. e. learning (2016). "Support vector machine." 207-235.

Swain, P. H. and H. J. I. T. o. G. E. Hauska (1977). "The decision tree classifier: Design and potential." **15**(3): 142-147.

Tanaka, H. and T. Sonehara (1995). "New Method of Superheterodyne Light Beating Spectroscopy for Brillouin-Scattering Using Frequency-Tunable Lasers." Physical Review Letters **74**(9): 1609-1612.

Taunk, K., S. De, S. Verma and A. Swetapadma (2019). A brief review of nearest neighbor algorithm for learning and classification. 2019 international conference on intelligent computing and control systems (ICCS), IEEE.

Tavakol, M. and R. Dennick (2011). "Making sense of Cronbach's alpha." Int J Med Educ **2**: 53-55.

Tejwani, S., S. Devi, S. Dinakaran, R. Shetty, P. Meshram, M. Francis and A. Sinha Roy (2016). "Diagnostic Efficacy of Normalization of Corneal Deformation Variables by the Intraocular Pressure in Glaucomatous Eyes." Invest Ophthalmol Vis Sci **57**(3): 1082-1086.

Thomas, R., K. Loibl and R. Parikh (2011). "Evaluation of a glaucoma patient." Indian J Ophthalmol **59 Suppl**(Suppl1): S43-52.

Tian, L., Y.-F. Huang, L.-Q. Wang, H. Bai, Q. Wang, J.-J. Jiang, Y. Wu and M. Gao (2014). "Corneal biomechanical assessment using corneal visualization scheimpflug technology in keratoconic and normal eyes." Journal of ophthalmology **2014**: 147516.

Tian, L., D. J. Wang, Y. Wu, X. L. Meng, B. Chen, M. Ge and Y. F. Huang (2016). "Corneal biomechanical characteristics measured by the CorVis Scheimpflug technology in eyes with primary open-angle glaucoma and normal eyes." Acta Ophthalmologica **94**(5): e317-e324.

Tian, L., H. Yifei, W. Li-qiang, H. Bai, W. Qun, J. Jing-jing, W. Ying and G. Min "Corneal Biomechanical Assessment Using Corneal Visualization Scheimpflug Technology in Keratoconic and Normal Eyes." Journal of Ophthalmology.

Vaughan, J. M. and J. T. Randall (1980). "BRILLOUIN-SCATTERING, DENSITY AND ELASTIC PROPERTIES OF THE LENS AND CORNEA OF THE EYE." Nature **284**(5755): 489-491.

Vinciguerra, R., R. Ambrósio, Jr., A. Elsheikh, C. J. Roberts, B. Lopes, E. Morengi, C. Azzolini and P. Vinciguerra (2016). "Detection of Keratoconus With a New Biomechanical Index." J Refract Surg **32**(12): 803-810.

Vinciguerra, R., S. Rehman, N. A. Vallabh, M. Batterbury, G. Czanner, A. Choudhary, R. Cheeseman, A. Elsheikh and C. E. Willoughby (2020). "Corneal biomechanics and biomechanically corrected intraocular pressure in primary open-angle glaucoma, ocular hypertension and controls." British Journal of Ophthalmology **104**(1): 121-126.

Vinciguerra, R., A. Renato, A. Elsheikh, C. Roberts, T. L. Bernardo, E. Morengi, C. Azzolini and P. Vinciguerra "Detection of Keratoconus With a New Biomechanical Index." Journal of refractive surgery.

Wang, W., S. L. Du and X. L. Zhang (2015). "Corneal Deformation Response in Patients With Primary Open-Angle Glaucoma and in Healthy Subjects Analyzed by Corvis ST." Investigative Ophthalmology & Visual Science **56**(9): 5557-5565.

Wang, X., C. Zhu, X. Hu, L. Liu, M. Liu, Y. Yuan and B. Ke (2022). "Changes in Dimensions and Functions of Crystalline Lens in High Myopia Using CASIA2 Optical Coherence Tomography." Ophthalmic Res **65**(6): 712-721.

Webb, J. N., J. P. Su and G. Scarcelli (2017). "Mechanical outcome of accelerated corneal crosslinking evaluated by Brillouin microscopy." J Cataract Refract Surg **43**(11): 1458-1463.

Wells, A. P., D. F. Garway-Heath, A. Poostchi, T. Wong, K. C. Chan and N. J. I. o. Sachdev (2008). "Corneal hysteresis but not corneal thickness correlates with optic nerve surface compliance in glaucoma patients." Invest Ophthalmol Vis Sci **49**(8): 3262-3268.

Westreich, D., J. Lessler and M. J. J. J. o. c. e. Funk (2010). "Propensity score estimation: neural networks, support vector machines, decision trees (CART), and meta-classifiers as alternatives to logistic regression." **63**(8): 826-833.

Windeatt, T. (2008). Ensemble MLP classifier design. Computational Intelligence Paradigms: Innovative Applications, Springer: 133-147.

Windeatt, T. J. I. T. o. N. N. (2006). "Accuracy/diversity and ensemble MLP classifier design." **17**(5): 1194-1211.

Wu, C. W., T. Y. Huang, Y. C. Liou, S. H. Chen, K. Y. Wu and H. Y. Tseng (2024). "Recognition of Glaucomatous Fundus Images Using Machine Learning Methods Based on Optic Nerve Head Topographic Features." J Glaucoma.

Wu, J. H., T. Nishida, R. N. Weinreb and J. W. Lin (2022). "Performances of Machine Learning in Detecting Glaucoma Using Fundus and Retinal Optical Coherence Tomography Images: A Meta-Analysis." Am J Ophthalmol **237**: 1-12.

Wu, Y., X. Li, X. Yan, B. Rong and H. Li (2018). "Research of diagnostic value of corneal biomechanical parameters based on Corvis ST in keratoconus." Chinese Journal of Experimental Ophthalmology: 130-134.

Wyatt, H. J. (1995). "The form of the human pupil." Vision Research **35**(14): 2021-2036.

Xiong, J., F. Li, D. Song, G. Tang, J. He, K. Gao, H. Zhang, W. Cheng, Y. Song and F. J. O. Lin (2022). "Multimodal machine learning using visual fields and peripapillary circular OCT scans in detection of glaucomatous optic neuropathy." **129**(2): 171-180.

Yang, K., L. Xu, Q. Fan, D. Zhao and S. Ren (2019). "Repeatability and comparison of new Corvis ST parameters in normal and keratoconus eyes." Sci Rep **9**(1): 15379.

Yang, L., K. Qi, P. Zhang, J. Cheng, H. Soha, Y. Jin, H. Ci, X. Zheng, B. Wang, Y. Mei, S. Chen and J. Wang (2024). "Diagnosis of Forme Fruste Keratoconus Using Corvis ST Sequences with Digital Image Correlation and Machine Learning." Bioengineering (Basel) **11**(5).

Yang, Q., Z.-f. Wu, J. Zhong and P. J. J. o. C. U. Yu (2004). "Support Vector Machines Based on Positive Feedback."

- Ye, C., M. Yu, G. Lai and V. Jhanji "Variability of Corneal Deformation Response in Normal and Keratoconic Eyes." Optometry and Vision Science **92**(7): e149-e153.
- Yu, A. Y., H. Shao, A. Pan, Q. Wang, Z. Huang, B. Song, C. McAlinden, J. Huang and S. Chen (2020). "Corneal biomechanical properties in myopic eyes evaluated via Scheimpflug imaging." BMC Ophthalmol **20**(1): 279.
- Yu, Y., F. Zhong-liang, Z. Xiang-hui and C. Wen-fang (2009). Combining classifier based on decision tree. 2009 WASE International Conference on Information Engineering, IEEE.
- Yu, Z., S. Yang, Y. Zhipeng, T. Mi, J. Zhao and Z. Xing-tao "Relationship Among Corneal Stiffness, Thickness, and Biomechanical Parameters Measured by Corvis ST, Pentacam and ORA in Keratoconus." Frontiers in Physiology.
- Yuan, Y., Y. Shao, A. Tao, M. Shen, J. Wang, G. Shi, Q. Chen, D. Zhu, Y. Lian, J. Qu, Y. Zhang and F. Lu (2013). "Ocular anterior segment biometry and high-order wavefront aberrations during accommodation." Invest Ophthalmol Vis Sci **54**(10): 7028-7037.
- Yülek, F., S. Gerçeker, E. Akçay, Ö. Saraç and N. Çağıl (2015). "Corneal biomechanics in steroid induced ocular hypertension." Cont Lens Anterior Eye **38**(3): 181-184.
- Zadnik, K., K. Steger-May, B. A. Fink, C. E. Joslin, J. J. Nichols, C. E. Rosenstiel, J. A. Tyler, J. A. Yu, T. W. Raasch and K. B. Schechtman (2002). "Between-eye asymmetry in keratoconus." Cornea **21**(7): 671-679.
- Zhang, C., A. J. Tatham, R. Y. Abe, A. Diniz-Filho, L. M. Zangwill, R. N. Weinreb and F. A. Medeiros (2016). "Corneal Hysteresis and Progressive Retinal Nerve Fiber Layer Loss in Glaucoma." American Journal of Ophthalmology **166**: 29-36.
- Zhang, H., M. Roozbahani, A. L. Piccinini, O. Golan, F. Hafezi, G. Scarcelli and J. B. Randleman (2019). "Depth-dependent reduction of biomechanical efficacy of contact lens–assisted corneal cross-linking analyzed by Brillouin microscopy." Journal of Refractive Surgery **35**(11): 721-728.
- Zhang, H., M. Roozbahani, A. L. Piccinini, F. Hafezi, G. Scarcelli and J. B. Randleman (2020). "Depth-dependent analysis of corneal cross-linking performed over or under the LASIK flap by Brillouin microscopy." J Cataract Refract Surg.
- Zhang, Y., J. Zhang, A. Jin, X. Tan, K. Ohno-Matsui, X. Han, L. Luo and Y. Liu (2024). "Interocular difference in crystalline lens morphology in children and adolescents with unilateral high myopia." Asia Pac J Ophthalmol (Phila) **13**(1): 100001.

11 Appendix

11.1 General Version of the ML Code

```
# Import libraries
import pandas as pd
import numpy as np
from sklearn.model_selection import train_test_split, RandomizedSearchCV,
GridSearchCV, cross_val_score
from sklearn.preprocessing import StandardScaler, LabelEncoder
from sklearn.neural_network import MLPClassifier
from sklearn.ensemble import RandomForestClassifier
from sklearn.svm import SVC
from sklearn.linear_model import LogisticRegression
from sklearn.naive_bayes import GaussianNB
from sklearn.tree import DecisionTreeClassifier
from sklearn.metrics import accuracy_score, f1_score, precision_score,
confusion_matrix, roc_auc_score, roc_curve
from scipy.stats import f_oneway, uniform, randint
import matplotlib.pyplot as plt
import warnings
from sklearn.exceptions import ConvergenceWarning
import time

# Function to calculate metrics and create ROC
def calculate_metrics_and_plot_roc(model, X_test_scaled, y_test,
title=None, save_as=None):
    # Calculate predictions and probabilities
    y_pred = model.predict(X_test_scaled)
    y_pred_proba = model.predict_proba(X_test_scaled)[:, 1]

    # Evaluation metrics
    accuracy = accuracy_score(y_test, y_pred)
    f1 = f1_score(y_test, y_pred)
    precision = precision_score(y_test, y_pred)
    auc = roc_auc_score(y_test, y_pred_proba)

    # Confusion matrix
    confusionMatrix = confusion_matrix(y_test, y_pred)
    TN = confusionMatrix[1, 1]
    TP = confusionMatrix[0, 0]
    FP = confusionMatrix[0, 1]
    FN = confusionMatrix[1, 0]

    # Sensitivity and specificity
    sensitivity = TP / float(FN + TP) if FN + TP != 0 else 0
    specificity = TN / float(TN + FP) if TN + FP != 0 else 0

    # Metrics printing
    print('Accuracy: ', accuracy)
    print('F1 Score: ', f1)
    print('Precision: ', precision)
    print('AUC: ', auc)
    print('Sensitivity: ', sensitivity)
    print('Specificity: ', specificity)
```

```

print('Confusion Matrix: ', confusionMatrix)

# ROC calculation
fpr, tpr, thresholds = roc_curve(y_test, y_pred_proba)

# Plot ROC
plt.figure()
plt.plot(fpr, tpr, label='ROC curve (area = %0.2f)' % auc)
plt.plot([0, 1], [0, 1], 'k--')
plt.xlim([0.0, 1.0])
plt.ylim([0.0, 1.05])
plt.xlabel('False Positive Rate')
plt.ylabel('True Positive Rate')
plt.title(title if title else 'Receiver Operating Characteristic')
plt.legend(loc="lower right")
if save_as:
    plt.savefig(save_as)
plt.show()
plt.close()

# return the metrics calculated and roc curve data
return {
    'accuracy': accuracy,
    'f1': f1,
    'precision': precision,
    'auc': auc,
    'sensitivity': sensitivity,
    'specificity': specificity,
    'fpr': fpr,
    'tpr': tpr
}

#Function to merge together ROC curves
def plot_combined_roc(roc_data, title, save_as=None):
    plt.figure(figsize=(10, 8))
    for fpr, tpr, auc_value, label in roc_data:
        plt.plot(fpr, tpr, label=f'(Antonacci, Beck et al.) (AUC =
{auc_value:.2f})')
    plt.plot([0, 1], [0, 1], 'k--', lw=2)
    plt.xlim([0.0, 1.0])
    plt.ylim([0.0, 1.05])
    plt.xlabel('False Positive Rate')
    plt.ylabel('True Positive Rate')
    plt.title(title)
    plt.legend(loc="lower right")
    if save_as:
        plt.savefig(save_as)
    plt.show()

# Load dataset
data = pd.read_excel('normal_kc_CST.xlsx')

# Delete columns 'no'
data_cleaned = data.drop(columns=['no'])

```

```

# Separation between features (X) and target (y)
X = data_cleaned.drop(columns=['DIAGNOSIS'])
y = data_cleaned['DIAGNOSIS']

# Labelling ('Normal' a 0 e 'KC' a 1)
le = LabelEncoder()
y = le.fit_transform(y)

# Creation of train and test sets (80% addestramento, 20% test)
X_train, X_test, y_train, y_test = train_test_split(X, y, test_size=0.2,
random_state=42, stratify=y)

# Features normalisation
scaler = StandardScaler()
X_train_scaled = scaler.fit_transform(X_train)
X_test_scaled = scaler.transform(X_test)

#Convert to DataFrame to retain features names
X_train_scaled = pd.DataFrame(X_train_scaled, columns=X_train.columns)
X_test_scaled = pd.DataFrame(X_test_scaled, columns=X_test.columns)

# Models and parameters definition for RandomSearch and GridSearch
models_params = {
    'NaiveBayes': {
        'model': GaussianNB(),
        'params_grid': {},
        'params_dist': {}
    },
    'LogisticRegression': {
        'model': LogisticRegression(random_state=42),
        'params_grid':[
            {'C': [0.001, 0.01, 0.1, 1, 10, 100, 1000], 'solver': ['newton-
cg', 'lbfgs'], 'penalty': ['l2']},
            {'C': [0.001, 0.01, 0.1, 1, 10, 100, 1000], 'solver':
['liblinear'], 'penalty': ['l1', 'l2']},
            {'C': [0.001, 0.01, 0.1, 1, 10, 100, 1000], 'solver': ['saga'],
'penalty': ['l1', 'l2']},
        ],
        'params_dist':[
            {'C': np.logspace(-3, 2, num=100), 'solver': ['newton-cg',
'lbfgs'], 'penalty': ['l2']},
            {'C': np.logspace(-3, 2, num=100), 'solver': ['liblinear'],
'penalty': ['l1', 'l2']},
            {'C': np.logspace(-3, 2, num=100), 'solver': ['saga'],
'penalty': ['l1', 'l2']},
        ],
    },
    'SVM': {
        'model': SVC(random_state=42, probability=True),
        'params_grid': {
            'C': [0.001, 0.01, 0.1, 1, 10, 100, 1000],
            'gamma': ['scale', 'auto', 0.001, 0.01, 0.1, 1, 10, 100],
            'kernel': ['linear', 'rbf', 'poly', 'sigmoid'],
        },
        'params_dist': {
            'C': uniform(0.1, 10),

```



```

best_overall_score = -np.inf
best_overall_params = None
best_overall_model_name = None
best_overall_model = None

# Function to calculate best hyperparameters, train and test
def safe_set_params(model, params):
    try:
        return model.set_params(**params)
    except ValueError:
        return model

performance_dict = {}
time_random_search = {}
time_grid_search = {}

roc_data_grid = []
roc_data_random = []

for model_name, model_params in models_params.items():
    print(f"\n{model_name}")

    if model_params['params_dist']:
        start_time = time.time()
        random_search = RandomizedSearchCV(model_params['model'],

param_distributions=model_params['params_dist'], n_iter=50,
                                                n_jobs=-1, cv=10,
random_state=42, scoring='roc_auc')
        try:
            random_search_result = random_search.fit(X_train_scaled,
y_train)
            print("Best score using RandomSearch: %f using %s" %
(random_search_result.best_score_,
random_search_result.best_params_))
            end_time = time.time()
            elapsed_time = end_time - start_time
            time_random_search[model_name] = elapsed_time

            model_random_search = safe_set_params(model_params['model'],
random_search_result.best_params_)
            model_random_search.fit(X_train_scaled, y_train)

            print('Metrics for the model trained with the best
hyperparameters from RandomSearch:')
            title_random = f"ROC for {model_name} (Random Search)"
            metrics_random =
calculate_metrics_and_plot_roc(model_random_search, X_test_scaled, y_test,
title=title_random, save_as=f"{model_name}_RandomSearch_ROC.png")
            roc_data_random.append((metrics_random['fpr'],
metrics_random['tpr'], metrics_random['auc'], title_random))

            model_random_key = model_name + "_random"
            performance_dict[model_random_key] = {
                'score': random_search_result.best_score_,

```

```

        'params': random_search_result.best_params_,
        **metrics_random
    }
    performance_dict[model_random_key]['model'] =
model_random_search
    except Exception as e:
        logging.error(f"Error during RandomizedSearchCV for
(model_name): {e}")

    try:
        start_time = time.time()
        grid_search = GridSearchCV(model_params['model'],
param_grid=model_params['params_grid'],
                                n_jobs=-1, cv=10, scoring='roc_auc')
        grid_search_result = grid_search.fit(X_train_scaled, y_train)
        print("Best score using GridSearch: %f using %s" %
(grid_search_result.best_score_,
grid_search_result.best_params_))
        end_time = time.time()
        elapsed_time = end_time - start_time
        time_grid_search[model_name] = elapsed_time

        model_grid_search = safe_set_params(model_params['model'],
grid_search_result.best_params_)
        model_grid_search.fit(X_train_scaled, y_train)
        print('Metrics for the model trained with the best hyperparameters
from GridSearch:')
        title_grid = f"ROC for {model_name} (Grid Search)"
        metrics_grid = calculate_metrics_and_plot_roc(model_grid_search,
X_test_scaled, y_test, title=title_grid,
save_as=f"{model_name}_GridSearch_ROC.png")
        roc_data_grid.append((metrics_grid['fpr'], metrics_grid['tpr'],
metrics_grid['auc'], title_grid))

        model_grid_key = model_name + "_grid"
        performance_dict[model_grid_key] = {
            'score': grid_search_result.best_score_,
            'params': grid_search_result.best_params_,
            **metrics_grid
        }
        performance_dict[model_grid_key]['model'] = model_grid_search #
Salva il modello addestrato qui
    except Exception as e:
        logging.error(f"Error during GridSearchCV for {model_name}: {e}")

plot_combined_roc(roc_data_grid, title="Combined ROC for Grid Search ",
save_as="Combined_GridSearch_ROC.png")
plot_combined_roc(roc_data_random, title="Combined ROC for Randomized
Search", save_as="Combined_RandomSearch_ROC.png")

# Creation of performances table
df = pd.DataFrame.from_dict(performance_dict, orient='index')
df['Time Random Search'] = df.apply(lambda row:
time_random_search[row.name.replace('_random', '')] if '_random' in
row.name else None, axis=1)

```

```

df['Time Grid Search'] = df.apply(lambda row:
time_grid_search[row.name.replace('_grid', '')] if '_grid' in row.name else
None, axis=1)

# save to excel
df.to_excel('performance_results.xlsx')

# Update the best_overall_model after RandomSearchCV
if random_search_result.best_score_ > best_overall_score:
    best_overall_score = random_search_result.best_score_
    best_overall_params = random_search_result.best_params_
    best_overall_model_name = model_name + " (Random Search)"
    best_overall_model = model_random_search

# Update the best_overall_model after GridSearchCV
if grid_search_result.best_score_ > best_overall_score:
    best_overall_score = grid_search_result.best_score_
    best_overall_params = grid_search_result.best_params_
    best_overall_model_name = model_name + " (Grid Search)"
    best_overall_model = model_grid_search

#Print best model during learning
print(f"The best model during learning is {best_overall_model_name}
with a score of {best_overall_score:.4f}.")
print(f"The best hyperparameters are: {best_overall_params}")

best_test_auc = 0
best_test_auc_model_key = None
for model_key, performance in performance_dict.items():
    if performance['auc'] > best_test_auc:
        best_test_auc = performance['auc']
        best_test_auc_model_key = model_key

print(f"The model with the best AUC score on test set is
{best_test_auc_model_key} with a score of {best_test_auc:.4f}")

# Load libraries for PFI
from sklearn.inspection import permutation_importance
import matplotlib.pyplot as plt
import seaborn as sns

# Extract the best model
best_model = performance_dict[best_test_auc_model_key]['model']

# Calculate Permutation Feature Importance
result = permutation_importance(best_model, X_test_scaled, y_test,
n_repeats=10, random_state=42, n_jobs=-1, scoring='roc_auc')

# Extract importance feature

```

```

importances = result.importances_mean
std_devs = result.importances_std
features = X_test.columns

# Create a dataframe with importance feature
importance_df = pd.DataFrame({
    'Feature': features,
    'Importance': importances,
    'Std Dev': std_devs
})

# Print the DataFrame
print(importance_df)

# Plot feature importances with error bars
plt.figure(figsize=(10, 6))
sns.barplot(x='Importance', y='Feature', data=importance_df, xerr=std_devs,
            capsize=0.2)
plt.title('Permutation Feature Importances with Confidence Intervals')

plt.savefig('permutation_feature_importances.png')

plt.show()

#import libraries for SHAP
import shap

# extract the best model
best_model = performance_dict[best_test_auc_model_key]['model']

print(best_model)

original_column_names = X_test.columns

if not isinstance(X_test_scaled, pd.DataFrame):
    X_test_scaled = pd.DataFrame(X_test_scaled,
                                columns=original_column_names)

#define classes
class_names = ["Normal", "KC"]

# Stratif distribution
if len(X_test_scaled) > 100:
    X_subset, _, y_subset, _ = train_test_split(X_test_scaled, y_test,
                                                test_size=len(X_test_scaled)-100, stratify=y_test, random_state=42)
else:
    X_subset = X_test_scaled
    y_subset = y_test

# Calculate SHAP values
background = shap.sample(X_train_scaled, 100) if len(X_train_scaled) > 100
else X_train_scaled

# Create an explainer using KernelExplainer
explainer = shap.KernelExplainer(best_model.predict_proba, background,
                                columnn_jobs=-1)

```

```
# Compute SHAP values on test set. Note that you might need to use a subset
of test set, as KernelExplainer can be slow.
shap_values = explainer.shap_values(X_subset[:100])

# Display the summary plot
shap.summary_plot(shap_values, X_subset, show=False)
plt.title("Impact of each predictor on output")
plt.savefig('summary_plot.png')
plt.show()

# Display the scatter plot
shap.summary_plot(shap_values[1], X_subset[:100], plot_type="dot",
show=False)
plt.title("Effect of each predictor on KC prediction")
plt.savefig('summary_scattered_plot_2.png')
```

11.2 Results ML to detect KC and POAG

11.2.1 KC

11.2.1.1 Corvis

Table 11.1 Corvis ST considering CCT

Algorithm	Learning Score	Accuracy	F1	Precision	AUROC	Sensitivity	Specificity	Time
NaiveBayes_grid	0.908	0.875	0.915	0.942	0.957	0.704	0.942	15.9
LogisticRegression_random	0.915	0.927	0.952	0.946	0.977	0.864	0.946	2.3
LogisticRegression_grid	0.914	0.938	0.959	0.947	0.977	0.905	0.947	1.1
SVM_random	0.947	0.938	0.959	0.959	0.990	0.870	0.959	4.3
SVM_grid	0.949	0.938	0.959	0.947	0.987	0.905	0.947	224.0
DecisionTree_random	0.890	0.885	0.922	0.956	0.917	0.714	0.956	1.9
DecisionTree_grid	0.896	0.927	0.952	0.958	0.921	0.833	0.958	3.7
RandomForest_random	0.958	0.938	0.959	0.959	0.980	0.870	0.959	71.6
RandomForest_grid	0.962	0.938	0.959	0.959	0.980	0.870	0.959	73.0
MLPClassifier_random	0.943	0.958	0.973	0.973	0.975	0.913	0.973	47.6
MLPClassifier_grid	0.952	0.938	0.958	0.972	0.970	0.840	0.972	419.3

Table 11.2 Corvis ST excluding CCT

Algorithm	Learning Score	Accuracy	F1	Precision	AUROC	Sensitivity	Specificity	Time
NaiveBayes_grid	0.889	0.854	0.903	0.915	0.945	0.680	0.915	20.6
LogisticRegression_random	0.915	0.906	0.940	0.921	0.952	0.850	0.921	2.7
LogisticRegression_grid	0.916	0.906	0.940	0.921	0.971	0.850	0.921	1.2
SVM_random	0.949	0.917	0.945	0.945	0.983	0.826	0.945	4.4
SVM_grid	0.948	0.917	0.945	0.945	0.985	0.826	0.945	161.5
DecisionTree_random	0.907	0.885	0.921	0.970	0.938	0.700	0.970	1.9
DecisionTree_grid	0.907	0.885	0.921	0.970	0.938	0.700	0.970	4.0
RandomForest_random	0.953	0.896	0.931	0.944	0.977	0.760	0.944	61.1
RandomForest_grid	0.959	0.938	0.959	0.947	0.983	0.905	0.947	66.6
MLPClassifier_random	0.952	0.917	0.944	0.958	0.984	0.800	0.958	44.0
MLPClassifier_grid	0.953	0.927	0.951	0.971	0.946	0.808	0.971	346.7

11.2.1.2 ORA

Table 11.3 ORA including CCT

Algorithm	Learning Score	Accuracy	F1	Precision	AUROC	Sensitivity	Specificity	Time
NaiveBayes_grid	0.908	0.905	0.943	0.904	0.947	0.909	0.904	19.2
LogisticRegression_random	0.887	0.857	0.917	0.857	0.904	0.857	0.857	1.9
LogisticRegression_grid	0.888	0.893	0.936	0.892	0.905	0.900	0.892	1.0
DecisionTree_random	0.899	0.893	0.934	0.914	0.824	0.786	0.914	1.4
DecisionTree_grid	0.900	0.821	0.885	0.906	0.828	0.550	0.906	3.0
RandomForest_random	0.923	0.893	0.936	0.892	0.829	0.900	0.892	60.9
RandomForest_grid	0.924	0.893	0.936	0.892	0.828	0.900	0.892	69.4
MLPClassifier_random	0.909	0.905	0.943	0.904	0.845	0.909	0.904	43.1
MLPClassifier_grid	0.907	0.905	0.943	0.904	0.904	0.909	0.904	307.8

Table 11.4 ORA excluding CCT

Algorithm	Learning Score	Accuracy	F1	Precision	AUROC	Sensitivity	Specificity	Time
NaiveBayes_grid	0.878	0.881	0.929	0.890	0.894	0.818	0.890	20.0
LogisticRegression_random	0.857	0.857	0.917	0.857	0.842	0.857	0.857	2.0
LogisticRegression_grid	0.857	0.857	0.915	0.867	0.845	0.778	0.867	0.9
DecisionTree_random	0.872	0.845	0.902	0.909	0.767	0.611	0.909	1.5
DecisionTree_grid	0.880	0.833	0.896	0.896	0.758	0.588	0.896	3.2
RandomForest_random	0.883	0.869	0.923	0.868	0.782	0.875	0.868	67.4
RandomForest_grid	0.883	0.869	0.923	0.868	0.766	0.875	0.868	65.0
MLPClassifier_random	0.889	0.857	0.914	0.877	0.718	0.727	0.877	33.1
MLPClassifier_grid	0.893	0.845	0.908	0.865	0.772	0.700	0.865	294.8

11.2.2 POAG

11.2.2.1 Corvis ST

Table 11.5 Corvis ST including Central Corneal Thickness and IOP

	Learning Score	accuracy	f1	precision	auc	sensitivity	specificity	Time
NaiveBayes_grid	0.801	0.701	0.491	0.609	0.779	0.730	0.609	17.8
LogisticRegression_random	0.839	0.680	0.563	0.541	0.759	0.767	0.541	2.5
LogisticRegression_grid	0.840	0.680	0.587	0.537	0.758	0.786	0.537	1.3
SVM_random	0.889	0.763	0.676	0.649	0.824	0.833	0.649	7.8
SVM_grid	0.894	0.753	0.676	0.625	0.830	0.842	0.625	327.2
DecisionTree_random	0.791	0.691	0.595	0.550	0.746	0.789	0.550	1.6
DecisionTree_grid	0.791	0.691	0.595	0.550	0.746	0.789	0.550	3.6
RandomForest_random	0.892	0.701	0.613	0.561	0.803	0.804	0.561	71.5
RandomForest_grid	0.896	0.711	0.622	0.575	0.796	0.807	0.575	78.6
MLPClassifier_random	0.881	0.753	0.667	0.632	0.803	0.831	0.632	49.9
MLPClassifier_grid	0.888	0.784	0.720	0.659	0.807	0.875	0.659	396.3

Table 11.6 Corvis ST including Central Corneal Thickness, but not IOP

	Learning Score	accuracy	f1	precision	auc	sensitivity	specificity	Time
NaiveBayes_grid	0.811	0.701	0.491	0.609	0.777	0.730	0.609	20.9
LogisticRegression_random	0.818	0.691	0.545	0.563	0.716	0.754	0.563	2.3
LogisticRegression_grid	0.819	0.691	0.545	0.563	0.718	0.754	0.563	1.2
SVM_random	0.884	0.763	0.685	0.641	0.808	0.845	0.641	7.5
SVM_grid	0.885	0.773	0.703	0.650	0.809	0.860	0.650	254.9
DecisionTree_random	0.806	0.660	0.522	0.514	0.690	0.742	0.514	1.4
DecisionTree_grid	0.806	0.660	0.522	0.514	0.690	0.742	0.514	3.4
RandomForest_random	0.891	0.711	0.611	0.579	0.803	0.797	0.579	62.9
RandomForest_grid	0.895	0.701	0.613	0.561	0.803	0.804	0.561	72.0
MLPClassifier_random	0.876	0.742	0.667	0.610	0.805	0.839	0.610	41.5
MLPClassifier_grid	0.871	0.753	0.684	0.619	0.791	0.855	0.619	326.1

Table 11.7 Corvis ST including IOP, but not Central Corneal Thickness

	Learning Score	accuracy	f1	precision	auc	sensitivity	specificity	Time
NaiveBayes_grid	0.795	0.691	0.464	0.591	0.773	0.720	0.591	16.5
LogisticRegression_random	0.837	0.691	0.583	0.553	0.772	0.780	0.553	2.1
LogisticRegression_grid	0.837	0.691	0.583	0.553	0.773	0.780	0.553	1.1
SVM_random	0.885	0.784	0.727	0.651	0.830	0.889	0.651	7.3

SVM_grid	0.891	0.784	0.727	0.651	0.831	0.889	0.651	245.6
DecisionTree_random	0.808	0.701	0.603	0.564	0.699	0.793	0.564	1.3
DecisionTree_grid	0.808	0.722	0.597	0.606	0.736	0.781	0.606	3.1
RandomForest_random	0.892	0.732	0.629	0.611	0.811	0.803	0.611	62.2
RandomForest_grid	0.892	0.742	0.658	0.615	0.822	0.828	0.615	69.4
MLPClassifier_random	0.885	0.763	0.685	0.641	0.823	0.845	0.641	45.3
MLPClassifier_grid	0.890	0.773	0.694	0.658	0.811	0.847	0.658	300.1

Table 11.8 Corvis ST excluding IOP and Central Corneal Thickness

	Learning score	accuracy	f1	precision	auc	sensitivity	specificity	Time
NaiveBayes_grid	0.797	0.691	0.464	0.591	0.771	0.720	0.591	14.6
LogisticRegression_random	0.824	0.660	0.492	0.516	0.741	0.727	0.516	2.0
LogisticRegression_grid	0.826	0.649	0.452	0.500	0.745	0.710	0.500	1.1
SVM_random	0.881	0.773	0.694	0.658	0.817	0.847	0.658	7.1
SVM_grid	0.886	0.773	0.711	0.643	0.813	0.873	0.643	224.3
DecisionTree_random	0.807	0.660	0.560	0.512	0.699	0.768	0.512	1.8
DecisionTree_grid	0.807	0.660	0.560	0.512	0.699	0.768	0.512	3.7
RandomForest_random	0.896	0.722	0.630	0.590	0.802	0.810	0.590	62.9
RandomForest_grid	0.898	0.711	0.622	0.575	0.814	0.807	0.575	70.9
MLPClassifier_random	0.874	0.763	0.701	0.628	0.810	0.870	0.628	41.5
MLPClassifier_grid	0.882	0.753	0.667	0.632	0.818	0.831	0.632	294.7

11.2.2.2 ORA

Table 11.9 ORA including IOP and Central Corneal Thickness

	Learning score	accuracy	f1	precision	auc	sensitivity	specificity	Time
NaiveBayes_grid	0.774	0.841	0.683	0.636	0.858	0.917	0.636	14.0
LogisticRegression_random	0.789	0.866	0.686	0.750	0.892	0.894	0.750	1.8
LogisticRegression_grid	0.789	0.866	0.686	0.750	0.893	0.894	0.750	0.9
DecisionTree_random	0.720	0.768	0.537	0.500	0.701	0.867	0.500	1.4
DecisionTree_grid	0.720	0.768	0.537	0.500	0.701	0.867	0.500	3.6
RandomForest_random	0.777	0.817	0.571	0.625	0.790	0.864	0.625	58.5
RandomForest_grid	0.810	0.829	0.611	0.647	0.797	0.877	0.647	65.6
MLPClassifier_random	0.804	0.854	0.684	0.684	0.827	0.905	0.684	37.0
MLPClassifier_grid	0.812	0.878	0.722	0.765	0.845	0.908	0.765	292.1

Table 11.10 ORA including Central Corneal Thickness, excluding IOP

	Learning score	accuracy	f1	precision	auc	sensitivity	specificity	Time
NaiveBayes_grid	0.769	0.780	0.526	0.526	0.804	0.857	0.526	15.5
LogisticRegression_random	0.781	0.805	0.429	0.667	0.846	0.822	0.667	1.7
LogisticRegression_grid	0.781	0.805	0.429	0.667	0.846	0.822	0.667	0.8
DecisionTree_random	0.725	0.805	0.500	0.615	0.754	0.841	0.615	1.4
DecisionTree_grid	0.751	0.817	0.516	0.667	0.779	0.843	0.667	3.3
RandomForest_random	0.783	0.805	0.500	0.615	0.759	0.841	0.615	59.3
RandomForest_grid	0.782	0.829	0.563	0.692	0.767	0.855	0.692	62.5
MLPClassifier_random	0.812	0.854	0.647	0.733	0.834	0.881	0.733	31.2
MLPClassifier_grid	0.813	0.854	0.647	0.733	0.833	0.881	0.733	258.8

Table 11.11 ORA including IOP, excluding Central Corneal Thickness

	Learning score	accuracy	f1	precision	auc	sensitivity	specificity	Time
NaiveBayes_grid	0.766	0.829	0.650	0.619	0.856	0.902	0.619	19.4
LogisticRegression_random	0.793	0.866	0.686	0.750	0.894	0.894	0.750	2.1
LogisticRegression_grid	0.792	0.866	0.686	0.750	0.894	0.894	0.750	0.9
DecisionTree_random	0.741	0.829	0.611	0.647	0.770	0.877	0.647	1.6
DecisionTree_grid	0.751	0.793	0.452	0.583	0.745	0.829	0.583	3.3
RandomForest_random	0.773	0.841	0.606	0.714	0.828	0.868	0.714	61.5
RandomForest_grid	0.777	0.829	0.611	0.647	0.835	0.877	0.647	86.0
MLPClassifier_random	0.802	0.854	0.667	0.706	0.882	0.892	0.706	38.0
MLPClassifier_grid	0.808	0.866	0.718	0.700	0.876	0.919	0.700	383.0

Table 11.12 ORA excluding IOP and Central Corneal thickness

	Learning score	accuracy	f1	precision	auc	sensitivity	specificity	Time
NaiveBayes_grid	0.768	0.793	0.514	0.563	0.822	0.848	0.563	20.8
LogisticRegression_random	0.782	0.854	0.647	0.733	0.875	0.881	0.733	2.1
LogisticRegression_grid	0.781	0.854	0.647	0.733	0.876	0.881	0.733	0.9
DecisionTree_random	0.725	0.805	0.500	0.615	0.719	0.841	0.615	1.6
DecisionTree_grid	0.751	0.817	0.516	0.667	0.758	0.843	0.667	3.1
RandomForest_random	0.761	0.780	0.471	0.533	0.787	0.836	0.533	59.0
RandomForest_grid	0.761	0.829	0.563	0.692	0.793	0.855	0.692	61.5
MLPClassifier_random	0.792	0.866	0.703	0.722	0.850	0.906	0.722	26.4
MLPClassifier_grid	0.796	0.866	0.686	0.750	0.858	0.894	0.750	243.3

11.2.2.3 GAT

Table 11.13 GAT including central corneal thickness

	Learning score	accuracy	f1	precision	auc	sensitivity	specificity	Time
NaiveBayes_grid	0.592	0.663	0.298	0.583	0.634	0.674	0.583	16.7
LogisticRegression_random	0.613	0.643	0.054	0.500	0.636	0.646	0.500	1.6
LogisticRegression_grid	0.613	0.643	0.146	0.500	0.637	0.652	0.500	0.8
DecisionTree_random	0.654	0.673	0.429	0.571	0.624	0.701	0.571	1.4
DecisionTree_grid	0.654	0.673	0.429	0.571	0.624	0.701	0.571	3.2
RandomForest_random	0.657	0.663	0.233	0.625	0.696	0.667	0.625	57.7
RandomForest_grid	0.680	0.724	0.526	0.682	0.631	0.737	0.682	67.9
MLPClassifier_random	0.694	0.673	0.448	0.565	0.678	0.707	0.565	26.8
MLPClassifier_grid	0.691	0.653	0.414	0.522	0.674	0.693	0.522	257.8

Table 11.14 GAT excluding Central corneal thickness

	Learning score	accuracy	f1	precision	auc	sensitivity	specificity	Time
NaiveBayes_grid	0.395	0.673	0.158	1.000	0.535	0.663	1.000	14.7
LogisticRegression_random	0.500	0.643	0.000	0.000	0.500	0.643	0.000	1.7
LogisticRegression_grid	0.500	0.643	0.000	0.000	0.500	0.643	0.000	0.8
DecisionTree_random	0.565	0.673	0.158	1.000	0.575	0.663	1.000	1.6
DecisionTree_grid	0.565	0.673	0.158	1.000	0.575	0.663	1.000	3.0
RandomForest_random	0.575	0.673	0.200	0.800	0.591	0.667	0.800	56.6
RandomForest_grid	0.568	0.673	0.158	1.000	0.572	0.663	1.000	58.7
MLPClassifier_random	0.610	0.673	0.158	1.000	0.560	0.663	1.000	17.6
MLPClassifier_grid	0.605	0.673	0.158	1.000	0.590	0.663	1.000	125.6

11.3 Repeatability

11.3.1 Correlation Difference-Mean value for Intrasection Repeatability

Table 11.15 Correlation tested according to Kolmogorov Smirnov test

Measure	Mean Normality p-value	Difference Normality p-value	Method	Correlation Coefficient	Correlation p-value
BSup	0.88	0.55	Pearson	-0.08	0.54
BNas	0.73	0.82	Pearson	-0.09	0.48
BInf	0.76	0.73	Pearson	0.03	0.82
BTem	0.67	0.47	Pearson	0.06	0.64
Mean	0.74	0.95	Pearson	-0.12	0.35
BLens	0.00	0.07	Spearman	0.20	0.11
TopPlat	0.20	0.62	Pearson	0.06	0.62
BotPlat	0.45	0.83	Pearson	0.00	0.99
AntSI	0.81	0.66	Pearson	-0.10	0.41
PostSI	0.27	0.09	Pearson	0.15	0.23

Table 11.16 Correlation tested according to Shapiro Wilk test

Measure	Mean Normality p-value	Difference Normality p-value	Method	Correlation Coefficient	Correlation p-value
BSup	0.62	0.15	Pearson	-0.08	0.54
BNas	0.18	0.52	Pearson	-0.09	0.48
BInf	0.37	0.76	Pearson	0.03	0.82
BTem	0.88	0.01	Spearman	0.00	0.99
Mean	0.41	0.56	Pearson	-0.12	0.35
BLens	0.00	0.00	Spearman	0.20	0.11
TopPlat	0.00	0.10	Spearman	0.05	0.67
BotPlat	0.06	0.04	Spearman	-0.01	0.91
AntSI	0.79	0.14	Pearson	-0.10	0.41

PostSI	0.00	0.00	Spearman	0.24	0.06
--------	------	------	----------	------	------

11.3.2 Correlation Difference-Mean value for Intrasession Repeatability

Table 11.17 Correlation tested according to Kolmogorov Smirnov test

Measure	Mean Normality p-value	Difference Normality p-value	Method	Correlation Coefficient	Correlation p-value
BSup	0.92	0.83	Pearson	-0.20	0.11
BNas	0.79	0.88	Pearson	-0.17	0.18
BInf	0.95	0.98	Pearson	-0.07	0.58
BTem	0.89	0.92	Pearson	0.00	1.00
Mean	0.59	1.00	Pearson	-0.14	0.29
BLens	0.09	0.09	Pearson	-0.11	0.41
TopPlat	0.11	0.58	Pearson	-0.19	0.14
BotPlat	0.24	0.94	Pearson	-0.04	0.79
AntSI	0.53	0.72	Pearson	-0.24	0.06
PostSI	0.18	0.59	Pearson	0.23	0.07

Table 11.18 Correlation tested according to Shapiro Wilk test

Measure	Mean Normality p-value	Difference Normality p-value	Method	Correlation Coefficient	Correlation p-value
BSup	0.01	0.59	Spearman	-0.14	0.28
BNas	0.24	0.39	Pearson	-0.17	0.18
BInf	0.51	0.66	Pearson	-0.07	0.58
BTem	0.96	0.75	Pearson	0.00	1.00
Mean	0.47	0.96	Pearson	-0.14	0.29
BLens	0.00	0.01	Spearman	-0.12	0.34
TopPlat	0.00	0.27	Spearman	-0.17	0.19
BotPlat	0.02	0.40	Spearman	0.02	0.90
AntSI	0.03	0.00	Spearman	-0.07	0.56

PostSI	0.00	0.42	Spearman	0.16	0.20
--------	------	------	----------	------	------

11.3.3 Bland Altman analysis for time of the day

Table 11.19 Bland Altman analysis results for TimeD subgroups

Measure	Group	Mean	SD	Upper COR Limit	Lower COR Limit	COR Interval
BSup	A	-0.029	0.088	0.143	-0.201	0.343
	B	0.019	0.068	0.152	-0.115	0.267
	C	-0.032	0.064	0.094	-0.158	0.252
BNas	A	-0.050	0.099	0.144	-0.244	0.389
	B	0.014	0.089	0.188	-0.160	0.348
	C	0.050	0.067	0.181	-0.082	0.263
BInf	A	-0.016	0.094	0.168	-0.201	0.370
	B	0.022	0.090	0.198	-0.154	0.352
	C	0.059	0.075	0.205	-0.087	0.292
BTem	A	0.034	0.072	0.175	-0.107	0.282
	B	0.048	0.073	0.191	-0.095	0.286
	C	0.001	0.096	0.188	-0.186	0.374
Mean	A	-0.015	0.069	0.120	-0.150	0.270
	B	0.026	0.055	0.134	-0.083	0.217
	C	0.019	0.046	0.109	-0.070	0.179
BLens	A	0.005	0.056	0.115	-0.105	0.220
	B	0.008	0.055	0.115	-0.100	0.215
	C	0.007	0.074	0.152	-0.137	0.288

Table 11.20 Bland Altman analysis results for TimeDABS subgroups

Measure	Group	Mean	SD	Upper COR Limit	Lower COR Limit	COR Interval
BSup	A	0.019	0.068	0.152	-0.115	0.267
	B	-0.030	0.081	0.129	-0.189	0.317
BNas	A	0.014	0.089	0.188	-0.160	0.348

	B	-0.019	0.101	0.180	-0.218	0.398
BInf	A	0.022	0.090	0.198	-0.154	0.352
	B	0.007	0.095	0.194	-0.179	0.373
BTem	A	0.048	0.073	0.191	-0.095	0.286
	B	0.023	0.082	0.183	-0.136	0.320
Mean	A	0.026	0.055	0.134	-0.083	0.217
	B	-0.004	0.065	0.122	-0.131	0.253
BLens	A	0.008	0.055	0.115	-0.100	0.215
	B	0.006	0.062	0.128	-0.116	0.244

11.4 Relationship with other instruments

Table 11.21 Results of Normality test (Shapiro Wilk) for clinical measurements

Instrument	Parameter	Statistic	P-value	Instrument	Parameter	Statistic	P-value
CST	A1L	0.954	0.015	ORA	IOPcc	0.975	0.190
	A1V	0.966	0.061		IOPg	0.981	0.397
	A1T	0.949	0.008		CH	0.976	0.230
	A2L	0.849	0.001		CRF	0.983	0.504
	A2V	0.969	0.090	BOSS Cornea	BSup1	0.97	0.103
	A2T	0.988	0.793		BNas1	0.98	0.351
	HCT	0.95	0.009		Blnf1	0.983	0.476
	HCPD	0.969	0.097		BTem1	0.982	0.423
	HCR	0.992	0.934		Mean1	0.984	0.524
	HCDefoAm	0.972	0.131	BOSS Lens	BLens1	0.856	< 0.001
	CCTcor	0.99	0.869		TopPlat1	0.943	0.004
	IOPnct	0.944	0.005		BotPlat1	0.989	0.800
	ArcL	0.969	0.088		AntSI1	0.964	0.047
	DeflAm	0.985	0.613	PostSI1	0.904	< 0.001	
	DeflAmR	0.976	0.227	CLT	CLT	0.933	0.002
	DeflAr	0.984	0.529	CCT	CCT	0.987	0.752
	DefAR	0.982	0.426				
	InvRad	0.942	0.004				
	WEM	0.751	< 0.001				
	SSI	0.963	0.042				
SP-A1	0.982	0.461					
ARTh	0.973	0.146					
IntRad	0.976	0.218					
CBI	0.939	0.003					
biOP	0.944	0.005					

Table 11.22 Correlations between measurements from different instruments

Var 1	Var 2	Corr	P-value	Test	Adj P-value	Var 1	Var 2	Corr	P-value	Test	Adj P-value
BSup1	IOPcc	-0.06	0.65	Pear	1	Blnf1	HCR	0.03	0.83	Pear	1
BSup1	IOPg	0.03	0.78	Pear	1	Blnf1	HCDefoAm	-0.23	0.06	Pear	1
BSup1	CH	0.18	0.14	Pear	1	Blnf1	CCTcor	-0.03	0.78	Pear	1
BSup1	CRF	0.15	0.22	Pear	1	Blnf1	IOPnct	0.33	0.01	Spearm	1
BNas1	IOPcc	0.11	0.37	Pear	1	Blnf1	ArcL	0.01	0.94	Pear	1

BNas1	IOPg	0.13	0.29	Pear	1		Blnf1	DeflAm	-0.16	0.20	Pear	1
BNas1	CH	0.02	0.89	Pear	1		Blnf1	DeflAmR	0.10	0.43	Pear	1
BNas1	CRF	0.09	0.46	Pear	1		Blnf1	DeflAr	-0.17	0.17	Pear	1
Blnf1	IOPcc	0.11	0.38	Pear	1		Blnf1	DefAR	-0.04	0.74	Pear	1
Blnf1	IOPg	0.21	0.10	Pear	1		Blnf1	InvRad	0.04	0.73	Spear	1
Blnf1	CH	0.16	0.20	Pear	1		Blnf1	WEM	-0.11	0.37	Spear	1
Blnf1	CRF	0.25	0.04	Pear	1		Blnf1	SSI	-0.13	0.31	Spear	1
BTem1	IOPcc	0.16	0.18	Pear	1		Blnf1	SP-A1	0.12	0.31	Pear	1
BTem1	IOPg	0.13	0.29	Pear	1		Blnf1	ARTh	-0.07	0.57	Pear	1
BTem1	CH	-0.09	0.47	Pear	1		Blnf1	IntRad	-0.02	0.88	Pear	1
BTem1	CRF	0.01	0.93	Pear	1		Blnf1	CBI	0.01	0.91	Spear	1
Mean1	IOPcc	0.13	0.28	Pear	1		Blnf1	biOP	0.32	0.01	Spear	1
Mean1	IOPg	0.20	0.11	Pear	1		BTem1	A1L	0.06	0.64	Spear	1
Mean1	CH	0.09	0.47	Pear	1		BTem1	A1V	0.01	0.94	Pear	1
Mean1	CRF	0.19	0.13	Pear	1		BTem1	A1T	0.02	0.89	Spear	1
BSup1	A1L	-0.15	0.22	Spear	1		BTem1	A2L	0.17	0.16	Spear	1
BSup1	A1V	0.12	0.33	Pear	1		BTem1	A2V	0.11	0.36	Pear	1
BSup1	A1T	0.15	0.22	Spear	1		BTem1	A2T	0.00	0.97	Pear	1
BSup1	A2L	-0.07	0.57	Spear	1		BTem1	HCT	-0.08	0.53	Spear	1
BSup1	A2V	0.08	0.49	Pear	1		BTem1	HCPD	-0.07	0.58	Pear	1
BSup1	A2T	-0.01	0.92	Pear	1		BTem1	HCR	0.02	0.88	Pear	1
BSup1	HCT	-0.14	0.25	Spear	1		BTem1	HCDefoAm	-0.08	0.54	Pear	1
BSup1	HCPD	-0.09	0.49	Pear	1		BTem1	CCTcor	0.01	0.93	Pear	1
BSup1	HCR	-0.04	0.75	Pear	1		BTem1	IOPnct	-0.01	0.92	Spear	1
BSup1	HCDefoAm	-0.08	0.53	Pear	1		BTem1	ArcL	-0.19	0.11	Pear	1
BSup1	CCTcor	0.10	0.40	Pear	1		BTem1	DeflAm	-0.01	0.92	Pear	1
BSup1	IOPnct	0.09	0.46	Spear	1		BTem1	DeflAmR	0.00	0.99	Pear	1
BSup1	ArcL	0.06	0.65	Pear	1		BTem1	DeflAr	0.06	0.63	Pear	1
BSup1	DeflAm	-0.08	0.52	Pear	1		BTem1	DefAR	0.05	0.67	Pear	1
BSup1	DeflAmR	0.01	0.92	Pear	1		BTem1	InvRad	0.03	0.80	Spear	1
BSup1	DeflAr	-0.10	0.44	Pear	1		BTem1	WEM	-0.02	0.85	Spear	1
BSup1	DefAR	0.00	0.97	Pear	1		BTem1	SSI	-0.19	0.13	Spear	1
BSup1	InvRad	0.07	0.59	Spear	1		BTem1	SP-A1	-0.01	0.93	Pear	1
BSup1	WEM	0.00	0.97	Spear	1		BTem1	ARTh	-0.04	0.75	Pear	1
BSup1	SSI	-0.05	0.69	Spear	1		BTem1	IntRad	0.03	0.81	Pear	1
BSup1	SP-A1	0.01	0.94	Pear	1		BTem1	CBI	0.08	0.52	Spear	1
BSup1	ARTh	0.05	0.67	Pear	1		BTem1	biOP	0.00	0.99	Spear	1
BSup1	IntRad	0.03	0.84	Pear	1		Mean1	A1L	-0.02	0.89	Spear	1
BSup1	CBI	-0.03	0.79	Spear	1		Mean1	A1V	-0.03	0.81	Pear	1
BSup1	biOP	0.12	0.31	Spear	1		Mean1	A1T	0.24	0.05	Spear	1
BNas1	A1L	0.05	0.71	Spear	1		Mean1	A2L	0.02	0.86	Spear	1
BNas1	A1V	-0.02	0.87	Pear	1		Mean1	A2V	0.21	0.09	Pear	1
BNas1	A1T	0.11	0.39	Spear	1		Mean1	A2T	-0.10	0.43	Pear	1
BNas1	A2L	0.06	0.62	Spear	1		Mean1	HCT	-0.18	0.15	Spear	1

BNas1	A2V	0.23	0.07	Pear	1		Mean1	HCPD	-0.15	0.24	Pear	1
BNas1	A2T	-0.07	0.55	Pear	1		Mean1	HCR	0.05	0.67	Pear	1
BNas1	HCT	0.01	0.92	Spear	1		Mean1	HCDefoAm	-0.18	0.14	Pear	1
BNas1	HCPD	-0.10	0.41	Pear	1		Mean1	CCTcor	0.05	0.71	Pear	1
BNas1	HCR	0.12	0.32	Pear	1		Mean1	IOPnct	0.19	0.12	Spear	1
BNas1	HCDefoAm	-0.09	0.46	Pear	1		Mean1	ArcL	-0.06	0.65	Pear	1
BNas1	CCTcor	0.06	0.65	Pear	1		Mean1	DeflAm	-0.16	0.19	Pear	1
BNas1	IOPnct	0.09	0.45	Spear	1		Mean1	DeflAmR	0.02	0.89	Pear	1
BNas1	ArcL	0.00	0.99	Pear	1		Mean1	DeflAr	-0.14	0.27	Pear	1
BNas1	DeflAm	-0.18	0.14	Pear	1		Mean1	DefAR	-0.03	0.78	Pear	1
BNas1	DeflAmR	-0.07	0.59	Pear	1		Mean1	InvRad	0.00	0.97	Spear	1
BNas1	DeflAr	-0.17	0.18	Pear	1		Mean1	WEM	0.02	0.86	Spear	1
BNas1	DefAR	-0.11	0.39	Pear	1		Mean1	SSI	-0.06	0.64	Spear	1
BNas1	InvRad	-0.08	0.52	Spear	1		Mean1	SP-A1	0.06	0.64	Pear	1
BNas1	WEM	0.22	0.07	Spear	1		Mean1	ARTh	-0.03	0.83	Pear	1
BNas1	SSI	0.20	0.10	Spear	1		Mean1	IntRad	-0.02	0.88	Pear	1
BNas1	SP-A1	0.02	0.84	Pear	1		Mean1	CBI	-0.04	0.77	Spear	1
BNas1	ARTh	0.00	1.00	Pear	1		Mean1	biOP	0.15	0.23	Spear	1
BNas1	IntRad	-0.08	0.52	Pear	1		BSup1	CCT	0.09	0.49	Pear	1
BNas1	CBI	-0.05	0.71	Spear	1		BNas1	CCT	0.08	0.53	Pear	1
BNas1	biOP	0.02	0.85	Spear	1		Blnf1	CCT	-0.07	0.61	Pear	1
Blnf1	A1L	0.02	0.87	Spear	1		BTem1	CCT	0.06	0.65	Pear	1
Blnf1	A1V	-0.16	0.19	Pear	1		Mean1	CCT	0.05	0.67	Pear	1
Blnf1	A1T	0.35	0.00	Spear	0.57		BLens1	CLT	-0.30	0.02	Spear	1
Blnf1	A2L	-0.12	0.35	Spear	1		TopPlat1	CLT	0.75	0.00	Spear	0.00
Blnf1	A2V	0.12	0.34	Pear	1		BotPlat1	CLT	0.73	0.00	Spear	0.00
Blnf1	A2T	-0.16	0.19	Pear	1		AntSl1	CLT	0.11	0.39	Spear	1
Blnf1	HCT	-0.24	0.05	Spear	1		PostSl1	CLT	0.36	0.00	Spear	0.62
Blnf1	HCPD	-0.13	0.30	Pear	1							

11.5 Age Analysis

Table 11.23 Results of normality test, mean/median, SD/IQR, and test for differences between groups Y and P.

Variable	p-value Group Y	p-value Group P	Mean Median (Group Y)	SD/IQR (Group Y)	Mean Median (Group P)	SD/IQR (Group P)	Test	p-value
IOPcc	0.59	0.43	15.9	3.6	16.3	2.9	t-test	0.656
IOPg	0.18	0.11	15.4	3.6	14.7	3.1	t-test	0.502
CH	0.63	0.09	10.4	1.9	9.5	1.5	t-test	0.072
CRF	0.50	0.15	10.4	2.0	9.4	1.7	t-test	0.078
A1L	0.13	0.35	2.45	0.30	2.10	0.33	t-test	0.000
A1V	0.39	0.11	0.14	0.02	0.15	0.02	t-test	0.039
A1T	0.19	0.01	7.22	0.35	7.05	0.18	Mann-Wh	0.067
A2L	0.00	0.10	1.95	0.30	1.94	0.24	Mann-Wh	0.373
A2V	0.16	0.64	-0.26	0.03	-0.28	0.03	t-test	0.023
A2T	0.50	0.28	21.45	0.47	21.49	0.35	t-test	0.748
HCT	0.22	0.02	16.71	0.49	16.86	0.46	Mann-Wh	0.099
HCPD	0.43	0.09	4.73	0.30	4.85	0.28	t-test	0.154
HCR	0.51	0.86	7.54	0.91	7.58	0.97	t-test	0.881
HCDefoAm	0.35	0.06	0.98	0.10	1.06	0.11	t-test	0.010
CCTcor	0.98	0.90	521	40	527	40	t-test	0.605
IOPnct	0.54	0.07	15.7	2.8	14.9	2.5	t-test	0.326
ArcL	0.40	0.09	-0.12	0.02	-0.14	0.03	t-test	0.068
DeflAm	0.27	0.90	0.82	0.10	0.88	0.11	t-test	0.064
DeflAmR	0.06	1.00	5.93	0.86	6.19	0.69	t-test	0.272
DeflAr	0.74	0.52	2.91	0.49	3.17	0.53	t-test	0.090
DefAR	0.07	0.69	4.48	0.49	4.71	0.45	t-test	0.112
InvRad	0.04	0.58	0.15	0.02	0.16	0.02	Mann-Wh	0.158
WEM	0.07	< 0,001	0.31	0.06	0.34	0.06	Mann-Wh	0.006
SSI	0.22	0.07	1.23	0.18	1.29	0.23	t-test	0.309
SP-A1	0.28	0.28	93.16	15.99	93.95	18.08	t-test	0.876
ARTh	0.94	0.27	472	72	491	144	t-test	0.564
IntRad	0.04	0.93	7.50	1.25	8.16	1.25	Mann-Wh	0.350
CBI	0.54	0.03	0.63	0.24	0.61	0.57	Mann-Wh	0.404

bIOP	0.20	0.44	16.4	2.7	14.7	2.0	t-test	0.021
BSup	0.61	0.08	2.824	0.055	2.816	0.047	t-test	0.581
BNas	0.39	0.07	2.819	0.056	2.822	0.057	t-test	0.850
BInf	0.64	0.23	2.817	0.064	2.792	0.064	t-test	0.180
BTem	0.49	0.33	2.810	0.061	2.821	0.047	t-test	0.497
Mean	0.38	0.04	2.818	0.038	2.819	0.051	Mann-Wh	0.843
BLens	0.00	0.07	3.411	0.028	3.351	0.059	Mann-Wh	0.002
TopPlat	0.27	0.04	2.557	0.325	3.200	0.600	Mann-Wh	0.000
BotPlat	0.89	0.72	3.950	0.437	4.727	0.516	t-test	0.000
AntSI	0.82	0.33	1.496	0.358	1.647	0.457	t-test	0.219
PostSI	0.01	0.01	-1.481	0.599	-1.190	0.643	Mann-Wh	0.015
CLT	0.70	0.44	3.67	0.18	4.35	0.26	t-test	0.000
CCT	0.74	0.73	528	39	534	38	t-test	0.606

Table 11.24 Correlation between age and parameters measured with ORA, Corvis ST, BOSS and OCT for group P

Variable	Spearman Correlation	Spearman p-value	R²
IOPcc	0.29	0.173	0.09
IOPg	0.11	0.632	0.01
CH	-0.39	0.063	0.16
CRF	-0.22	0.322	0.05
A1L	0.02	0.921	0.00
A1V	-0.02	0.920	0.00
A1T	-0.05	0.834	0.00
A2L	0.08	0.702	0.01
A2V	-0.08	0.725	0.01
A2T	-0.44	0.035	0.19
HCT	-0.23	0.290	0.05
HCPD	-0.11	0.618	0.01
HCR	0.05	0.821	0.00
HCDefoAm	-0.21	0.346	0.04

CCTcor	-0.15	0.491	0.02
IOPnct	-0.02	0.925	0.00
ArcL	-0.02	0.936	0.00
DeflAm	0.02	0.942	0.00
DeflAmR	0.12	0.578	0.01
DeflAr	0.05	0.810	0.00
DefAR	0.07	0.758	0.00
InvRad	0.13	0.546	0.02
WEM	-0.16	0.455	0.03
SSI	0.37	0.079	0.14
SP-A1	-0.10	0.638	0.01
ARTh	0.05	0.815	0.00
IntRad	0.02	0.930	0.00
CBI	0.01	0.972	0.00
blOP	-0.11	0.625	0.01
BSup1	-0.28	0.190	0.08
BNas1	-0.26	0.224	0.07
BInf1	-0.22	0.317	0.05
BTem1	-0.44	0.038	0.19
Mean1	-0.43	0.043	0.18
BLens1	-0.44	0.037	0.19
TopPlat1	0.35	0.104	0.12
BotPlat1	0.32	0.141	0.10
AntSI1	0.50	0.015	0.25
PostSI1	0.34	0.117	0.11
CLT	0.43	0.040	0.19
CCT	-0.12	0.587	0.01

11.6 Refractive Error Analysis

11.6.1 Groups

Table 11.25 Results of Normality test, Mean and SD for groups

Measure	Group	Statistic	p-value	Mean/Median Value		SD/IQR Value	
IOPcc	MM	0.89	0.16	Mean	16.1	SD	5.0
	LM	0.94	0.43	Mean	16.3	SD	4.5
	EM	0.95	0.65	Mean	15.7	SD	2.6
	HY	0.84	0.11	Mean	14.4	SD	2.8
IOPg	MM	0.90	0.23	Mean	14.8	SD	4.7
	LM	0.94	0.40	Mean	15.1	SD	4.7
	EM	0.92	0.27	Mean	15.6	SD	2.8
	HY	0.92	0.44	Mean	13.7	SD	4.0
CH	MM	0.95	0.62	Mean	9.8	SD	1.5
	LM	0.97	0.84	Mean	9.8	SD	1.1
	EM	0.92	0.27	Mean	10.8	SD	1.7
	HY	0.94	0.64	Mean	10.5	SD	2.6
CRF	MM	0.88	0.12	Mean	9.7	SD	1.4
	LM	0.97	0.85	Mean	9.8	SD	1.5
	EM	0.95	0.57	Mean	10.8	SD	1.8
	HY	0.98	0.94	Mean	9.9	SD	3.1
A1L	MM	0.84	0.05	Median	1.94	IQR	0.52
	LM	0.95	0.49	Mean	2.28	SD	0.34
	EM	0.87	0.05	Median	2.47	IQR	0.33
	HY	0.94	0.60	Mean	2.61	SD	0.22
A1V	MM	0.87	0.11	Mean	0.15	SD	0.02
	LM	0.96	0.69	Mean	0.15	SD	0.02
	EM	0.92	0.24	Mean	0.14	SD	0.01
	HY	0.89	0.25	Mean	0.14	SD	0.02
A1T	MM	0.74	0.00	Median	7.07	IQR	0.27
	LM	0.96	0.61	Mean	7.15	SD	0.32
	EM	0.85	0.03	Median	7.29	IQR	0.22
	HY	0.82	0.07	Mean	7.05	SD	0.40
A2L	MM	0.84	0.05	Median	1.91	IQR	0.16
	LM	0.86	0.03	Median	1.93	IQR	0.21
	EM	0.68	0.00	Median	1.92	IQR	0.08
	HY	0.87	0.19	Mean	2.19	SD	0.44
A2V	MM	0.96	0.83	Mean	-0.28	SD	0.03
	LM	0.94	0.43	Mean	-0.27	SD	0.02
	EM	0.97	0.94	Mean	-0.27	SD	0.02
	HY	0.87	0.18	Mean	-0.25	SD	0.04

A2T	MM	0.85	0.06	Mean	21.48	SD	0.49
	LM	0.97	0.86	Mean	21.47	SD	0.39
	EM	0.90	0.13	Mean	21.31	SD	0.30
	HY	0.93	0.52	Mean	21.73	SD	0.49
HCT	MM	0.90	0.20	Mean	16.54	SD	0.39
	LM	0.91	0.13	Mean	16.63	SD	0.46
	EM	0.82	0.01	Median	16.63	IQR	0.69
	HY	0.63	0.00	Median	16.86	IQR	0.12
HCPD	MM	0.88	0.13	Mean	4.81	SD	0.31
	LM	0.97	0.90	Mean	4.83	SD	0.15
	EM	0.96	0.79	Mean	4.64	SD	0.20
	HY	0.92	0.47	Mean	4.76	SD	0.44
HCR	MM	0.92	0.34	Mean	6.49	SD	0.68
	LM	0.98	0.92	Mean	7.47	SD	0.82
	EM	0.96	0.68	Mean	7.73	SD	0.61
	HY	0.76	0.02	Median	7.18	IQR	0.51
HCDefoAm	MM	0.90	0.23	Mean	1.03	SD	0.12
	LM	0.93	0.29	Mean	1.00	SD	0.11
	EM	0.96	0.81	Mean	0.95	SD	0.05
	HY	0.93	0.54	Mean	1.02	SD	0.12
CCTcor	MM	0.93	0.48	Mean	517	SD	42
	LM	0.94	0.35	Mean	518	SD	31
	EM	0.94	0.49	Mean	533	SD	29
	HY	0.91	0.38	Mean	517	SD	50
IOPnct	MM	0.66	0.00	Median	15.3	IQR	1.0
	LM	0.94	0.36	Mean	15.2	SD	2.4
	EM	0.80	0.01	Median	16.0	IQR	2.5
	HY	0.95	0.76	Mean	14.2	SD	2.9
ArcL	MM	0.94	0.55	Mean	-0.12	SD	0.02
	LM	0.93	0.32	Mean	-0.12	SD	0.02
	EM	0.92	0.22	Mean	-0.13	SD	0.02
	HY	0.96	0.78	Mean	-0.12	SD	0.03
DeflAm	MM	0.89	0.18	Mean	0.89	SD	0.11
	LM	0.95	0.59	Mean	0.85	SD	0.07
	EM	0.93	0.32	Mean	0.79	SD	0.05
	HY	0.88	0.21	Mean	0.85	SD	0.13
DeflAmR	MM	0.96	0.78	Mean	6.64	SD	0.68
	LM	0.93	0.25	Mean	6.02	SD	0.66
	EM	0.93	0.37	Mean	5.82	SD	0.59
	HY	0.85	0.12	Mean	5.90	SD	1.29
DeflAr	MM	0.78	0.01	Median	3.20	IQR	0.44
	LM	0.95	0.52	Mean	2.98	SD	0.33
	EM	0.94	0.44	Mean	2.76	SD	0.23
	HY	0.91	0.38	Mean	3.13	SD	0.67

DefAR	MM	0.97	0.92	Mean	5.00	SD	0.46
	LM	0.98	0.98	Mean	4.66	SD	0.49
	EM	0.88	0.07	Mean	4.48	SD	0.42
	HY	0.87	0.21	Mean	4.45	SD	0.58
InvRad	MM	0.92	0.34	Mean	0.17	SD	0.01
	LM	0.83	0.01	Median	0.15	IQR	0.02
	EM	0.85	0.02	Median	0.14	IQR	0.01
	HY	0.89	0.28	Mean	0.15	SD	0.02
WEM	MM	0.99	0.99	Mean	0.28	SD	0.04
	LM	0.98	0.96	Mean	0.31	SD	0.07
	EM	0.83	0.02	Median	0.31	IQR	0.04
	HY	0.91	0.40	Mean	0.35	SD	0.07
SSI	MM	0.83	0.03	Median	0.95	IQR	0.07
	LM	0.95	0.61	Mean	1.16	SD	0.11
	EM	0.97	0.92	Mean	1.25	SD	0.16
	HY	0.88	0.23	Mean	1.27	SD	0.28
SP-A1	MM	0.95	0.66	Mean	88.9	SD	14.3
	LM	0.94	0.43	Mean	90.8	SD	14.0
	EM	0.95	0.64	Mean	99.6	SD	12.1
	HY	0.97	0.90	Mean	87.2	SD	21.1
ARTh	MM	0.96	0.75	Mean	494.7	SD	104.1
	LM	0.95	0.50	Mean	481.1	SD	94.8
	EM	0.92	0.29	Mean	494.2	SD	84.6
	HY	0.98	0.96	Mean	453.0	SD	56.2
IntRad	MM	0.85	0.06	Mean	9.0	SD	0.9
	LM	0.93	0.24	Mean	8.1	SD	1.0
	EM	0.93	0.39	Mean	7.6	SD	0.7
	HY	0.89	0.26	Mean	8.2	SD	1.0
CBI	MM	0.89	0.18	Mean	0.68	SD	0.24
	LM	0.94	0.44	Mean	0.64	SD	0.23
	EM	0.96	0.72	Mean	0.53	SD	0.22
	HY	0.89	0.30	Mean	0.67	SD	0.26
bIOP	MM	0.77	0.01	Median	16.4	IQR	1.9
	LM	0.93	0.30	Mean	16.0	SD	2.3
	EM	0.70	0.00	Median	16.4	IQR	1.2
	HY	0.97	0.89	Mean	15.1	SD	2.7
BSup1	MM	0.91	0.29	Mean	2.849	SD	0.038
	LM	0.89	0.08	Mean	2.838	SD	0.056
	EM	0.95	0.62	Mean	2.838	SD	0.052
	HY	0.93	0.56	Mean	2.825	SD	0.059
BNas1	MM	0.91	0.29	Mean	2.810	SD	0.067
	LM	0.96	0.64	Mean	2.832	SD	0.072
	EM	0.92	0.26	Mean	2.823	SD	0.050
	HY	0.91	0.42	Mean	2.812	SD	0.066

BInf1	MM	0.98	0.98	Mean	2.837	SD	0.036
	LM	0.91	0.15	Mean	2.809	SD	0.066
	EM	0.94	0.51	Mean	2.836	SD	0.056
	HY	0.90	0.33	Mean	2.803	SD	0.077
BTem1	MM	0.79	0.01	Median	2.847	IQR	0.050
	LM	0.98	0.97	Mean	2.808	SD	0.086
	EM	0.87	0.07	Mean	2.831	SD	0.063
	HY	0.95	0.72	Mean	2.831	SD	0.060
Mean1	MM	0.82	0.02	Median	2.847	IQR	0.032
	LM	0.97	0.91	Mean	2.822	SD	0.036
	EM	0.82	0.02	Median	2.836	IQR	0.040
	HY	0.92	0.50	Mean	2.818	SD	0.053
BLens1	MM	0.60	0.00	Median	3.427	IQR	0.033
	LM	0.80	0.00	Median	3.410	IQR	0.022
	EM	0.82	0.02	Median	3.401	IQR	0.082
	HY	0.93	0.52	Mean	3.432	SD	0.017
TopPlat1	MM	0.92	0.38	Mean	2.536	SD	0.344
	LM	0.94	0.39	Mean	2.555	SD	0.271
	EM	0.92	0.29	Mean	2.633	SD	0.332
	HY	0.95	0.76	Mean	2.434	SD	0.360
BotPlat1	MM	0.67	0.00	Median	3.928	IQR	0.124
	LM	0.96	0.68	Mean	3.993	SD	0.438
	EM	0.90	0.16	Mean	3.906	SD	0.429
	HY	0.90	0.30	Mean	3.936	SD	0.452
AntSI1	MM	0.96	0.83	Mean	1.499	SD	0.311
	LM	0.97	0.89	Mean	1.429	SD	0.323
	EM	0.91	0.20	Mean	1.684	SD	0.442
	HY	0.96	0.84	Mean	1.366	SD	0.450
PostSI1	MM	0.98	0.94	Mean	-1.393	SD	0.266
	LM	0.98	0.93	Mean	-1.628	SD	0.501
	EM	0.86	0.04	Median	-1.500	IQR	0.657
	HY	0.70	0.00	Median	-1.494	IQR	0.439
CLT	MM	0.98	0.95	Mean	3.586	SD	0.080
	LM	0.93	0.38	Mean	3.647	SD	0.169
	EM	0.97	0.87	Mean	3.658	SD	0.263
	HY	0.95	0.74	Mean	3.653	SD	0.145
CCT	MM	0.94	0.65	Mean	517	SD	37
	LM	0.93	0.36	Mean	527	SD	35
	EM	0.91	0.19	Mean	540	SD	28
	HY	0.93	0.58	Mean	523	SD	47

Table 11.26 Results of test among groups

Measure	Test Used	Statistic	p-value	Sig_0.05	Bonf_Inst	Bonf_All
IOPcc	ANOVA	0.383	0.766	No	No	No
IOPg	ANOVA	0.332	0.802	No	No	No
CH	ANOVA	1.046	0.382	No	No	No
CRF	ANOVA	0.797	0.503	No	No	No
A1L	Kruskal-Wallis	8.901	0.031	Yes	No	No
A1V	ANOVA	1.135	0.346	No	No	No
A1T	Kruskal-Wallis	3.936	0.268	No	No	No
A2L	Kruskal-Wallis	3.010	0.390	No	No	No
A2V	ANOVA	1.679	0.186	No	No	No
A2T	ANOVA	1.638	0.195	No	No	No
HCT	Kruskal-Wallis	3.615	0.306	No	No	No
HCPD	ANOVA	1.361	0.268	No	No	No
HCR	Kruskal-Wallis	14.743	0.002	Yes	No	No
HDefoAm	ANOVA	1.602	0.204	No	No	No
CCTcor	ANOVA	0.572	0.637	No	No	No
IOPnct	Kruskal-Wallis	4.807	0.186	No	No	No
ArcL	ANOVA	0.100	0.960	No	No	No
DeflAm	ANOVA	2.831	0.050	No	No	No
DeflAmR	ANOVA	2.402	0.081	No	No	No
DeflAr	Kruskal-Wallis	6.506	0.089	No	No	No
DefAR	ANOVA	2.827	0.050	No	No	No
InvRad	Kruskal-Wallis	12.049	0.007	Yes	No	No
WEM	Kruskal-Wallis	7.165	0.067	No	No	No
SSI	Kruskal-Wallis	18.945	0.000	Yes	Yes	Yes
SP-A1	ANOVA	1.552	0.216	No	No	No
ARTh	ANOVA	0.389	0.761	No	No	No
IntRad	ANOVA	4.738	0.006	Yes	No	No
CBI	ANOVA	1.012	0.397	No	No	No
biOP	Kruskal-Wallis	2.251	0.522	No	No	No
BSup1	ANOVA	0.292	0.831	No	No	No
BNas1	ANOVA	0.278	0.841	No	No	No
BInf1	ANOVA	0.906	0.447	No	No	No
BTem1	Kruskal-Wallis	1.408	0.704	No	No	No
Mean1	Kruskal-Wallis	1.149	0.765	No	No	No
BLens1	Kruskal-Wallis	10.896	0.012	Yes	No	No
TopPlat1	ANOVA	0.585	0.628	No	No	No
BotPlat1	Kruskal-Wallis	0.458	0.928	No	No	No
AntSI1	ANOVA	1.421	0.251	No	No	No
PostSI1	Kruskal-Wallis	2.488	0.477	No	No	No
CLT	ANOVA	0.272	0.845	No	No	No
CCT	ANOVA	0.742	0.534	No	No	No

11.6.2 Continuous Distribution of Refractive Error

Table 11.27 Correlation between Refractive Error and parameters measured by ORA, Corvis ST, BOSS, OCT

Variable	Correlation Coefficient	R ²	p-value	Sig_0.05	Bonf_Inst	Bonf_All
IOPcc	-0.174	0.030	0.252	No	No	No
IOPg	-0.026	0.001	0.863	No	No	No
CH	0.214	0.046	0.157	No	No	No
CRF	0.096	0.009	0.530	No	No	No
A1L	0.360	0.130	0.015	Yes	No	No
A1V	-0.271	0.073	0.072	No	No	No
A1T	0.166	0.028	0.276	No	No	No
A2L	0.218	0.048	0.150	No	No	No
A2V	0.204	0.042	0.178	No	No	No
A2T	0.017	0.000	0.913	No	No	No
HCT	0.296	0.088	0.048	Yes	No	No
HCPD	-0.249	0.062	0.099	No	No	No
HCR	0.306	0.094	0.041	Yes	No	No
HCDefoAm	-0.212	0.045	0.161	No	No	No
CCTcor	0.117	0.014	0.445	No	No	No
IOPnct	0.058	0.003	0.704	No	No	No
ArcL	0.027	0.001	0.858	No	No	No
DeflAm	-0.305	0.093	0.041	Yes	No	No
DeflAmR	-0.392	0.153	0.008	Yes	No	No
DeflAr	-0.158	0.025	0.300	No	No	No
DefAR	-0.430	0.185	0.003	Yes	No	No
InvRad	-0.429	0.184	0.003	Yes	No	No
WEM	0.313	0.098	0.036	Yes	No	No
SSI	0.517	0.267	0.000	Yes	Yes	Yes
SP-A1	0.111	0.012	0.468	No	No	No
ARTh	-0.025	0.001	0.870	No	No	No
IntRad	-0.321	0.103	0.032	Yes	No	No
CBI	-0.140	0.020	0.359	No	No	No
biOP	-0.026	0.001	0.864	No	No	No
BSup1	-0.128	0.016	0.409	No	No	No
BNas1	-0.069	0.005	0.657	No	No	No
BInf1	-0.046	0.002	0.767	No	No	No
BTem1	-0.089	0.008	0.564	No	No	No
Mean1	-0.165	0.027	0.284	No	No	No
BLens1	0.085	0.007	0.583	No	No	No
TopPlat1	0.075	0.006	0.630	No	No	No
BotPlat1	0.018	0.000	0.908	No	No	No
Height1	0.085	0.007	0.583	No	No	No
AntSI1	0.009	0.000	0.955	No	No	No

PostSI1	-0.185	0.034	0.229	No	No	No
CLT	0.253	0.064	0.115	No	No	No
CCT	0.137	0.019	0.399	No	No	No